THESIS
5
2004
V.1
56954764

This is to certify that the
dissertation entitled

Quantitative Microstructural Investigation
of Damaged Concrete

presented by

Mohamed Farouk Elzafraney

has been accepted towards fulfillment
of the requirements for the

Doctoral degree in Civil Engineering

Major Professor's Signature

April 27, 2004

Date

MSU is an Affirmative Action/Equal Opportunity Institution

LIBRARY
Michigan State
University

PLACE IN RETURN BOX to remove this checkout from your record.
TO AVOID FINES return on or before date due.
MAY BE RECALLED with earlier due date if requested.

DATE DUE	DATE DUE	DATE DUE

6/01 c:/CIRC/DateDue.p65-p.15

QUANTITATIVE MICROSTRUCTURAL INVESTIGATION OF DAMAGED CONCRETE

VOLUME I

By

Mohamed Farouk Elzafraney

A DISSERTATION

Submitted to
Michigan State University
in partial fulfillment of the requirements
for the degree of

DOCTOR OF PHILOSOPHY

Department of Civil and Environmental Engineering

2004

ABSTRACT

QUANTITATIVE MICROSTRUCTURAL INVESTIGATION OF DAMAGED CONCRETE

By

Mohamed Farouk Elzafraney

A comprehensive approach has been developed for quantitative analysis of concrete microcrack and void systems. The proposed approach aims to establish solid bases for development of concrete microstructure-property relationships, which can provide substantial insight into the behavior and failure modes of concrete. Throughout the research study, more than 200,000 images were captured through environmental scanning electron microscopy (ESEM) and fluorescent microscopy. Specimen preparation, image acquisition and processing, and quantitative analysis of images constitute the steps involved in microstructural analysis of concrete. Specimen preparation for ESEM involves Wood's metal impregnation. For fluorescent microscopy, a two-step ink/epoxy impregnation was developed in the research study. Prepared surfaces would yield sharp contrasts between features of interest (microcracks and voids) and the body of concrete. After acquisition of microscopic images, image processing functions were performed to alter gray scale images into binary images, and to refine such images for the purpose of quantitative analysis. Mathematical expressions were developed for distinguishing microcracks from void, and for comprehensive quantification of microcrack and void systems. Stereological relationships were employed for quantification of spatial (3-D) microcrack/void characteristics based on planar (2-D) measurements. Statistical sampling

schemes were developed for determining the adequate number of specimens and images for deriving statistically viable conclusions, and also for comparative evaluation of different sub-regions within the concrete system. The proposed approach was used to determine the effects of different mechanical, thermal and weathering phenomena on concrete microstructure and engineering properties, and to develop preliminary microstructure-property relationships. The system was also applied toward the field application of quantitative microstructural investigation methodology to rigid pavement and reinforced concrete bridge deck system.

The research study emphasized investigation of microcrack propagation under mechanical, thermal and environmental damage phenomena, and the impact of microcrack growth on concrete performance characteristics. The laboratory and field test data validated the analytical and experimental tools developed in the study for quantitative microstructural investigation of concrete. The approach developed in the study constitutes a valuable research tool, and can also contribute toward forensic studies and health assessment of deteriorated and damaged concrete-based infrastructure systems.

DEDICATION

To every desperate in the whole world, every person thinks that there is impossible, every creature thinks that the sun will not rise again, every human being in the middle of the road, everyone keeps trying, everyone believes in saying "never say never", every hardworker, everyone thinks that despotism never ends, every truth seeker, Victor Hugo and les miserables

To the hope, the faith, the destiny, the real, the commitment, the fact, the system, the order, the light, the white, the rest, health, the triumph, the peace, future, confidence, patience, oddity, life, love, to justice and mercy

To civil engineers, architects, students, journals, papers, technology, to scientists and researchers

To skies, ground, mountains, deeps, wind, power, fire, water, beauty, deserts, forests, falls, floods, volcanoes, hurricanes, hail, storms, lightning, thunders, snow, rain, dust, mites, molds, pollens, insects, heaven, hell, concrete, to houses and homeless and all refugees

To my family

To every Noga cares about me

To everyone hopes that tomorrow never dies

To everyone who wants to see the light at the end of the tunnel.

ACKNOWLEDGEMENTS

I would like to express my thanks and profound gratitude to Prof. Parviz Soroushian for his effective guidance, continuous support, and tremendous patience. The completion of this work is highly indebted to his intellectual inspiration, care and consideration and the long time he spent with me.

I would like also to express my faithful thanks to members of the guidance committee: Prof. Ronald S. Harichandran, Prof. Neeraj J. Buch, and Prof. Gerald D. Ludden for their great encouragement, precious guidance, valuable discussions and helpful advice.

Special thanks for Ali Nossoni and Siavosh Ravanbakhsh for the role that they have played in initiation and successful undertaking of this work.

The financial support of Egyptian Government and U.S. Air Force for my graduate study and the research work is sincerely acknowledged.

TABLE OF CONTENTS

Chapter 1. Introduction 1
1.1 Preface 1
1.2 Definition of the Problem 2
1.3 Research Objectives 3
1.4 Significance of the Research 4
1.5 Research Methodology 5

Chapter 2. Concrete Microstructure: Literature Review 8
2.1 Preface 8
2.2 Structure of Concrete Phases 10
2.2.1 Aggregate Phase 10
2.2.1.1 Structure of the Aggregate Phase 10
2.2.1.2 Effect of Aggregate Phase on Concrete Properties and Performance 11
2.2.2 Binding Medium Phase 15
2.2.2.1 Structure of the Binding Medium Phase 15
2.2.2.2 Solids in the Binding Medium Phase and its Effect on Concrete Properties and Performance 16
2.2.2.3 Voids in the Binding Medium Phase 18
2.2.2.4 Types of Voids and their Effects on Concrete Properties 19
2.2.3 Structure of the Interfacial Transition Zone (ITZ) 26
2.2.3.1 Concrete Microcracks 28
2.2.3.2 Causes of Microcrack Propagation 29
2.2.3.3 Effect of (ITZ) and Microcracks on Concrete Properties and Performance 44

Chapter 3. Methodologies for Concrete Image Processing Automation 52
3.1 Preface 52
3.2 Criterion to Distinguish between Microcracks and Voids (Shape Analysis) 53
3.3 Criterion for Noise Removal (Size Analysis) 59
3.4 Selection of the Magnification Factor 65
3.5 Conclusions 69

Chapter 4. Specimen Preparation for Automated Features Detection 70
4.1 Feature Detection Techniques 70
4.1.1 Preface 70
4.1.2 Current Techniques Used for Detection of Concrete Features 70
4.1.2.1 Photo-Elastic Coating Techniques 70
4.1.2.2 Interferometry Techniques 71

4.1.2.3 Stereo-Photogrammetry Techniques 71
4.1.2.4 Acoustic Emission Techniques 72
4.1.2.5 Neutron Radiography Techniques 73
4.1.2.6 Mercury Intrusion Porosimetry Techniques 74
4.1.2.7 Infrared Thermography Techniques 75
4.1.2.8 X-Ray Techniques 75
4.1.2.9 Scanner Techniques 76
4.1.2.10 Microscopy Techniques 76
4.1.3 Selection of the Feature Detection Technique 81
4.1.3.1 Environmental Scanning Electron Microscopy 81
4.1.3.2 Fluorescent Microscopy 89
4.2 Specimen Preparation 90
4.2.1 Preface 91
4.2.2 Objective of Specimen Preparation 93
4.2.3 Existing Specimen Preparation Techniques 91
4.2.4 Description of the Proposed Specimen Preparation Techniques 94
4.2.4.1 Specimen Preparation for ESEM (Wood's Metal Impregnation) 94
4.2.4.2 Specimen Preparation for Fluorescent Microscopy (Ink-Epoxy Impregnation) 99
4.3 Conclusions 108

Chapter 5. Image Processing and Analysis 109
5.1 Preface 109
5.2 Image Processing 111
5.2.1 Image Processing Functions 112
5.2.1.1 Digitization 112
5.2.1.2 Discrimination and Thresholding 112
5.2.1.3 Morphological Operations 120
5.2.2 Detachment of Intersecting and/or Connected Microcracks and Voids 141
5.3 Image Analysis 144
5.3.1 Image Analysis Formula (Models) 148
5.3.1.1 Microcrack Planar (2-D) Measurements 148
5.3.1.2 Void Planar (2-D) Measurements 158
5.3.1.3 Aggregate Planar (2-D) Measurements 165
5.3.1.4 Fibers Planar (2-D) Measurements 169
5.4 Conclusions 170

Chapter 6. Stereological Interpretations & Relationships 172
6.1 Stereology 172
6.1.1 Preface 172
6.1.2 Basic Stereological Relationships 172
6.1.3 Stereological Treatment of Oriented Features 175
6.1.3.1 System of Lines in Plane 179

6.1.3.2 System of Lines in Space 185
6.1.3.3 System of surfaces in Space 185
6.1.4 Stereological Relationships 188
6.1.4.1 Microcrack Spatial (3-D) Measurements ... 188
6.1.4.2 Void Spatial (3-D) Measurements 193
6.1.4.3 Aggregate Spatial (3-D) Measurements 200
6.1.4.4 Fibers Spatial (3-D) Measurements 203
6.2 Statistical Analysis 205
6.2.1 Preface 205
6.2.2 The Sampling Scheme 205
6.2.2.1 Preliminary Sub-regioning 206
6.2.2.2 Coring and Sectioning 206
6.2.2.3 Image Acquisition and Microstructural Analysis 210
6.2.2.4 Assessment of the Required Number of Images, Cores and Sub-regions 210
6.2.3 Application of the Proposed Sampling Scheme 214
6.2.4 Results and Discussion 216
6.3 Conclusions 228

Chapter 7. Qualitative Microstructural Analysis of Concrete 230
7.1 Preface 230
7.2 Experimental Program 231
7.2.1 Concrete Mixture and Specimens 231
7.2.2 Testing Plan 233
7.3 Microstructural Investigation Scheme 234
7.4 Performance Test Results 237
7.5 Results of Microstructural Investigation 246
7.6 Discussion 248
7.7 Conclusions 255

Chapter 8. Quantitative Microstructural Analysis of Concrete 257
8.1 Preface 257
8.2 Experimental Program 258
8.3 Microstructural Analysis Scheme 262
8.4 Microstructural Analysis Results 263
8.4.1 Analogy between Unreinforced (Unrestrained) and Reinforced (Restrained) Normal-Strength Concrete Specimens 263
8.4.1.1 Planar (2-D) Measurements 263
8.4.1.2 Spatial (3-D) Measurements 275
8.4.2 Analogy between Unrestrained (Unreinforced) and Restrained (Unreinforced) Normal-Strength Concrete Specimens 284
8.4.2.1 Planar (2-D) Measurements 284
8.4.2.2 Spatial (3-D) Measurements 290

8.4.3 Analogy between Normal-Strength and Relatively High-Strength Concrete 295
8.4.3.1 Planar (2-D) Measurements 295
8.4.3.2 Spatial (3-D) Measurements 301
8.5 Discussion 306
8.6 Conclusions 308

Chapter 9. Field Applications 311
9.1 Rigid Pavement Application 311
9.1.1 Preface 311
9.1.2 Pavement Description 311
9.1.3 Pavement Sub-regioning and Coring 314
9.1.4 Experimental Methodology 316
9.1.5 Microstructural Investigation 317
9.1.6 Mechanical Test Results and Discussion 318
9.1.7 Microstructural Data and Discussion 319
9.1.7.1 Planar (2-D) Measurements 320
9.1.7.2 Spatial (3-D) Measurements 325
9.1.8 Assessment of the Adequacy of the Number of Cores and Sub-regions 329
9.2 Reinforced Concrete Bridge Deck 332
9.2.1 Preface 332
9.2.2 Description of the Bridge 332
9.2.3 Sub-regioning and Coring of the Bridge Deck 336
9.2.4 Experimental Methodology 337
9.2.5 Microstructural Investigation and Discussion 339
9.2.6 Mechanical Test Results and Discussion 340
9.2.7 Microstructural Data and Discussion 341
9.2.7.1 Planar (2-D) Measurements 341
9.2.7.2 Spatial (3-D) Measurements 344
9.2.8 Assessment the Adequacy the Number of Cores and Sub-regions 352
9.3 Conclusions 354

Chapter 10. Development of Concrete Microcrack-Property Relationships . 357
10.1 Preface 357
10.2 Experimental and Microstructural Analysis Program 358
10.3 Experimental Results 360
10.4 Results of Microstructural Analysis 361
10.5 Microcrack-Property Relationships 370
10.6 Verification of the Developed Models 377
10.7 Conclusions 381

Chapter 11. Summary and Conclusions 383

Literature Cited 397

LIST OF TABLES

Table 3.1 Statistical Summary of Formfactor Measurements for Microcracks and Voids 56
Table 3.2 Visual Vs. Automated Measurements of Microcracks and Voids 58
Table 3.3 Lengths of Noise, Microcracks, and Voids at the Proposed Magnifications 62
Table 3.4 The Errors (%) Associated With Different Threshold Length Values for Distinguishing Noise 62
Table 5.1 Comparison Between Manual and Automatic Low Threshold Levels for ESEM Concrete Micrographs 116
Table 5.2 Comparison between Manual and Automatic Low Threshold levels for Fluorescent Concrete Micrographs 116
Table 5.3 Errors in Calculated Crack Width by The Proposed Equation 152
Table 6.1 Relationship of Measured (O) and Calculated (□) Quantities 173
Table 6.2 Expressions Relevant to Three-Dimensional Features in Space 177
Table 6.3 Equations for Systems of Lines in a Plane 184
Table 6.4 Equations for Systems of Lines in a Space 185
Table 6.5 Equations for Systems of Surfaces in Space 186
Table 6.6 Equations for Partially Oriented Systems of Surfaces in Space 188
Table 6.7 Nomenclature Used in Schwartz-Saltykov Method 195
Table 6.8 Crack Length Per Unit Area (1/mm) of Section (X-Y) for Mixture I (3 Replicated Scans) 217
Table 6.9 Crack Length Per Unit Area (1/mm) of Section (Y-Z) for Mixture I (3 Replicated Scans) 218
Table 6.10 Crack Length Per Unit Area (1/mm) of Section (X-Y) for Mixture II (3 Replicated Scans) 219
Table 6.11 Crack Length Per Unit Area (1/mm) of Section (Y-Z) for Mixture II (3 Replicated Scans) 220
Table 6.12 Statistical Analysis of Crack Length Per Unit Area (1/mm) for Mixture I ..222
Table 6.13 Statistical Analysis of Crack Length Per Unit Area (1/mm) for Mixture II .223
Table 6.14 Microcrack Specific Surface Area (3 Replicated Scans) 225
Table 7.1 The Post-Damage Test Program for Concrete Mixtures 235
Table 8.1 Summary of Specimens and Damaging Effects of Normal-Strength Concrete in the Experimental Program 260
Table 8.2 Summary of Damaging Effects and Specimens of High-Strength Concrete in the Experimental Program 261
Table 8.3 Results of Statistical Analysis for Unreinforced (Unrestrained) Normal-Strength Specimens (Planar Measurements) (Changes for Undamaged Condition in Percent) 273
Table 8.4 Results of Statistical Analysis for Reinforced (Unrestrained) Normal-Strength Specimens (Planar Measurements) (Changes from Undamaged Condition in Percent) 274
Table 8.5 Results of Statistical Analysis for Unreinforced (Unrestrained) Normal-Strength Specimens (Spatial Measurements)

(Changes from Undamaged Condition in Percent) 282
Table 8.6 Results of Statistical Analysis for Reinforced (Unrestrained) Normal Strength Specimens (Spatial Measurements) (Changes from Undamaged Conditions in Percent) 283
Table 8.7 Results of Statistical Analysis for Unrestrained (Unreinforced) and Restrained (Unreinforced) Normal-Strength Specimens (Planar Measurements) (Percent Changes Vs. Undamaged Condition) 289
Table 8.8 Results of Statistical Analysis for Unrestrained (Unreinforced) and Restrained (Reinforced) Normal-Strength Specimens (Spatial Measurements) (Percent Changes Vs. Undamaged Condition) 294
Table 8.9 Results of Normal-Strength and Relatively High-Strength Specimens 300
Table 8.10 Results of Statistical Analysis for Normal-Strength (Unreinforced / Unrestrained) and Relatively High-Strength Concrete (Spatial Measurements) (Percent Changes Vs. Undamaged Condition) 306
Table 9.1 Tests Performed on Pavement Sub-regions 317
Table 9.2 Mechanical and Transport Properties of Concrete Cores 319
Table 9.3 Planar (2-D) Measurements for Top Sub-region 321
Table 9.4 Planar (2-D) Measurements for Bottom Sub-region 323
Table 9.5 Required Number of Cores Per Sub-region for Microstructural Investigation 331
Table 9.6 Details of Test Plan 339
Table 9.7 Mechanical and Test properties of Concrete Cores 341
Table 9.8 Planar (2-D) Measurements 342
Table 9.9 Comparison of The Required and Actual Number of Cores Per Sub-region for Microcrack Analysis 353
Table 10.1 Changes (%) in Flexural Strength and Permeability Caused by Different Damaging Effects 361
Table 10.2 Changes (%) in Planar Measurements for Mix I 365
Table 10.3 Changes (%) in Planar Measurements for Mix II 366
Table 10.4 Changes (%) in Spatial Measurements for Mix I 368
Table 10.5 Changes (%) in Spatial Measurements for Mix II 369
Table 10.6 Correlation Coefficients between Changes in Spatial Microcrack Characteristics and the Corresponding Changes in Flexural Strength and Permeability 371
Table 10.7 Errors in Prediction of the Developed Modes for Mixtures I and II 377

LIST OF FIGURES

Figure 1.1	Schematic Presentation of stage I of the Research Study	6
Figure 2.1	Different Scales of Concrete Observation	8
Figure 2.2	Effect of Aggregate Content on Stiffness of Concrete and Mortar	11
Figure 2.3	Possible Toughening Mechanisms Operating in a Fibrous Concrete	13
Figure 2.4	Crack Propagation under Compression	14
Figure 2.5	Diagrammatic Presentation of Bleeding in Freshly Deposited Concrete	15
Figure 2.6	SEM Micrograph of Isolated Plates of CH in Different Orientations (A&B)	18
Figure 2.7	Air-Void Gradation, Compared with Aggregates, Cement and Some Mineral Additives	20
Figure 2.8	Effects of Capillary Porosity on Compressive Strength Under Different Damaging Conditions	21
Figure 2.9	Effect of Air Entrained Voids on Concrete Durability at Different Water/Cement Ratios	24
Figure 2.10	Different Types of Water in Concrete	25
Figure 2.11	Structure of Interfacial Transition Zone	26
Figure 2.12	SEM Micrograph of an Area Around Grain in Ordinary Concrete	28
Figure 2.13	Identification of Concrete Microcracks	29
Figure 2.14	Diagrammatic Presentation of the Stress-Strain Behavior of Concrete under Uniaxial Compression	30
Figure 2.15	SEM for Normal-Strength Concrete Specimen Subjected to Uniaxial Compression	31
Figure 2.16	SEM for High-Strength Concrete Specimen Subjected to Uniaxial Compression	32
Figure 2.17	The Relationship between Creep of the Specific Crack Area and the axial Creep	33
Figure 2.18	Typical Stress-Strain Diagrams for Concrete Loaded in Uniaxial Tension	35
Figure 2.19	Schematic Illustration of the Fracture Process Zone	37
Figure 2.20	The Stress-Deformation Relation Under Cyclic Tensile Load .	38
Figure 2.21	SEM Micrograph for Concrete Specimens Before and After Freeze-Thaw Deterioration	39
Figure 2.22	Microcrack Pattern Due to Shrinkage	41
Figure 2.23	Microcrack Pattern in Case of Alkali-Aggregate Reaction ...	43
Figure 2.24	An Optical Micrograph of a Concrete Specimen Damaged by Alkali-Aggregate reaction	44
Figure 2.25	The Relation between Microcracking Growth and Stress-Strain Behavior	45

Figure 2.26	Idealization of Stresses Around a Single Aggregate Particle Embedded in a Continuous Matrix, and Hypothesized Failure Mode	46
Figure 2.27	Hypothesized Micromechanisms, Explaining the Effect of Initial Anisotropy in Concrete	48
Figure 2.28	SEM Micrograph Showing Deposition of Ettringite in Microcracks	49
Figure 2.29	Effect of Microcracking in Creep	50
Figure 3.1	Concrete Images Captured by Environmental Scanning Electron and Fluorescent Microcopy	54
Figure 3.2	Histogram of Formfactor Measurements for Microcracks	56
Figure 3.3	Histogram of Formfactor Measurements for Voids	57
Figure 3.4	Comparison between Formfactor Measurements for Microcracks and Voids	57
Figure 3.5	Visual Vs. Automated Formfactor Measurements	59
Figure 3.6	The Effect of Applying Image Processing Functions to Remove Noise	61
Figure 3.7	Errors in Applying the Three Selected Limit Values	63
Figure 3.8	Flowchart Presentation of the Criteria for Distinction of Microcracks, Voids and Noise	64
Figure 3.9	ESEM Micrograph of Concrete Captured at Different Magnification Factors	66
Figure 3.10	Concrete Images Captured Using ESEM and Fluorescent Microscopy at Different Magnification Factors	68
Figure 4.1	Ultrasonic Test Configurations for Concrete Specimens	72
Figure 4.2	Neutron Radiography of Concrete Specimen	74
Figure 4.3	Resolution of an Optical microscope, a High Quality Flatbed Scanner, and Ordinary Flatbed Scanner	77
Figure 4.4	Topographic Image of Concrete Sample	79
Figure 4.5	General View of the Environmental Scanning Electron Microscopy Used in the Investigation	83
Figure 4.6	Cross-Section Through the Optical Column Console	84
Figure 4.7	Plastic Scintillating BSE Detector with Actual Positioning in ESEM	86
Figure 4.8	Backscattered Electron Signal	86
Figure 4.9	SEM Micrograph Captured by ESEM in Two Different Techniques	88
Figure 4.10	General View of the Fluorescent Microscope Used in the Investigation	90
Figure 4.11	Digitized Images of Concrete Specimens Impregnated with Red Dye	93
Figure 4.12	Cutting the Specimen	95
Figure 4.13	Grinding the Specimen After Cutting	96
Figure 4.14	Steel Container Used for Wood's Metal Specimen Preparation	96
Figure 4.15	Placing the Concrete Specimen in the Pressure Chamber	97

Figure 4.16	Final Lapping of the Concrete Specimen	97
Figure 4.17	Concrete Micrographs Before and After Specimen Preparation by Wood's Metal	98
Figure 4.18	Fluorescent Micrographs of Concrete Specimen Impregnated with Fluorescent Epoxy Dye	100
Figure 4.19	Fluorescent Micrograph of Concrete Specimen Subjected to Two-Stage Impregnation with Ink Followed by Fluorescent Epoxy	101
Figure 4.20	Lapping of Concrete Specimen	103
Figure 4.21	Specimen Cleaning in Ultrasonic Bath	103
Figure 4.22	Vacuum Drying of Concrete Specimen	104
Figure 4.23	Ink (or Fluorescent Epoxy) Impregnation	104
Figure 4.24	Nitrogen Pressure Application	106
Figure 4.25	Fluorescent Micrographs of Concrete Specimens Prepared by Conventional and the New (Two-Stage) Specimen Preparation Technique	107
Figure 5.1	An Overview in the Steps Involved in Image Processing and Analysis	110
Figure 5.2	Effect of Applying Thresholding Function on Gray Image	113
Figure 5.3	Threshold Levels for Both manual and Automatic Threshold Functions for ESEM Concrete Micrographs	117
Figure 5.4	Threshold Levels for Both Manual and Automatic Threshold Functions for Fluorescent Concrete Micrographs ...	117
Figure 5.5	Comparison between Manual and Automatic (Factorization) Threshold Function on ESEM Concrete Micrographs	118
Figure 5.6	Comparison between Manual and Automatic (Factorization) Threshold Function on Fluorescent Concrete Micrographs	119
Figure 5.7	Applying Erosion Function on Fluorescent and ESEM Concrete Micrographs	121
Figure 5.8	Applying Dilation Function on Fluorescent and ESEM Concrete Micrographs	122
Figure 5.9	Applying Opening Function on Fluorescent and ESEM Concrete Micrographs	124
Figure 5.10	Applying Closing Function on Fluorescent and ESEM Concrete Micrographs	125
Figure 5.11	Opening and Closing Operations on Binary Pixels	126
Figure 5.12	Applying Hole-Fill Function on Fluorescent and ESEM Concrete Micrographs	128
Figure 5.13	Proposed Image Processing Scenarios	132
Figure 5.14	Effect of Applying Different Image Processing Scenarios on Fluorescent Gray Scale Concrete Micrographs at Magnification 125X	134
Figure 5.15	Effect of Applying Different Image Processing Scenarios on ESEM Gray Scale Concrete Micrographs at Magnification 250X	136

Figure 5.16	Applying Opening Operation on Fluorescent Concrete Micrographs at Different Number of Iterations	137
Figure 5.17	Applying Opening Operation on ESEM Concrete Micrographs at Different Number of Iterations	138
Figure 5.18	Applying Closing Operation on Fluorescent Concrete Micrograph at Different Number of Iterations	139
Figure 5.19	Applying Closing Operation on ESEM Concrete at Different Number of Iterations	140
Figure 5.20	Image Processing Scenario for Detachment of Intersecting Microcracks and Voids as well as Connected Voids	142
Figure 5.21	Image Processing Scenario for Detachment of Intersecting Microcracks and Voids as well as Connected Voids	143
Figure 5.22	Box Counting Method	145
Figure 5.23	Microcrack Mapping for Manual Measuring	145
Figure 5.24	Original Microtomographic Image of the Lime Silica Brick	146
Figure 5.25	Logarithmic Image Processing Approach	147
Figure 5.26	Two Cracks Have the Same Length and Different Perimeter	149
Figure 5.27	The Difference between Crack Breadth and Width	151
Figure 5.28	Comparison between Measured and Calculated Crack Width	153
Figure 5.29	Schematic Presentation of Crack Angle of Orientation (ω_C)	155
Figure 5.30	Schematic Presentation of Point Intersections	157
Figure 5.31	Schematic Presentation of the Assumptions Used in Spacing Computations	161
Figure 6.1	Schematic Presentation of Basic Stereological Expressions	176
Figure 6.2	Example of Isometric System of Lines	178
Figure 6.3	Examples of Completely Oriented System of Lines in a Plane	178
Figure 6.4	Example of Partially Oriented System of Lines	179
Figure 6.5	Applying Rose of Orientation Manually on Tillite Specimen.	183
Figure 6.6	Using Rose of Orientation to Determine Fiber Orientation	183
Figure 6.7	Classification of Partially Oriented System of Lines	187
Figure 6.8	Schematic Presentation of the Relationship between Projected and Actual Crack widths	192
Figure 6.9	Example of Concrete System Divided to Sub-regions	207
Figure 6.10	Example of Coring Concrete System	207
Figure 6.11	Sectioning of Concrete Cores	209
Figure 6.12	Required Number of Cores for Undamaged Specimens (Mix I) at Different Magnification Levels (Average of ESEM and Fluorescent Microscopy)	226
Figure 6.13	Required Number of Cores for damaged Specimens (Mix I) at Different Magnification Levels (Average of ESEM and Fluorescent Microscopy)	226
Figure 6.14	Required Number of Cores for Undamaged Specimens (Mix II) at Different Magnification Levels (Average of ESEM and Fluorescent Microscopy)	227

Figure 6.15	Required Number of Cores for Damaged Specimens (Mix II) at Different Magnification Levels (Average of ESEM and Fluorescent Microscopy)	227
Figure 7.1	Sectioning Directions for Microscopic Investigation	236
Figure 7.2	Damaging Effects on Flexural Strength of Normal-Strength Concrete (Means & Standard Errors)	237
Figure 7.3	Damage Normal-Strength Concrete Specimen After Exposure to Elevated Temperature	238
Figure 7.4	Damaging Effects of Compression on Flexural Strength of High-Strength Concrete (Means & Standard Errors)	239
Figure 7.5	Splitting Tensile Strength Test Results Prior to and After Exposure to Peak Compressive Stress (Means & Standard Errors)	240
Figure 7.6	Damaging Effects of Compression on Impact Resistance (Means & Standard Errors)	241
Figure 7.7	Effect of Repeated Freeze-Thaw Cycles on Compressive Strength of Normal-Strength Concrete (Means & Standard Errors)	242
Figure 7.8	Damaging Effect on Chloride Permeability (Means & Standard Errors)	243
Figure 7.9	Effects of Restraint Condition and Exposure Temperature on Flexural Strength of Normal-Strength Concrete (Means & Standard Errors)	245
Figure 7.10	Effects of Restraint Condition on Compressive Strength of Fiber Reinforced Concrete (Means & Standard Errors)	245
Figure 7.11	Micrographs of Normal-Strength Concrete	251
Figure 7.12	Micrographs of High-Strength Concrete	253
Figure 7.13	Scanning Electron Micrographs for Fiber Reinforced Concrete	254
Figure 8.1	Planar (2-D) Measurements for Unreinforced (Unrestrained) Normal-Strength Specimens in Horizontal Section (X-Y) ...	267
Figure 8.2	Planar (2-D) Measurements for Reinforced (Unrestrained) Normal-Strength Specimens in Horizontal Section (X-Y) ...	271
Figure 8.3	Spatial (3-D) Measurements for Unreinforced (Unrestrained) Normal-Strength Specimens	278
Figure 8.4	Spatial (3-D) Measurements for Reinforced (Unrestrained) Normal-Strength Specimens	281
Figure 8.5	Planar (2-D) Measurements for Unrestrained (Unreinforced) Normal-Strength Specimens in Horizontal Section (X-Y) (Average of Three Magnification Levels)	285
Figure 8.6	Spatial (3-D) Measurements for Unrestrained and Restrained (Unreinforced) Normal-Strength Specimens (Average of Three Magnification Levels)	293
Figure 8.7	Planar (2-D) Measurements for Normal-Strength (Unreinforced -Unrestrained) and Relatively High-Strength	

	Concrete Specimens in Horizontal Section (X-Y) (Average of Three Magnification Levels)	299
Figure 8.8	Spatial (3-D) Measurements for Normal-Strength (Unreinforced-Unrestrained) and Relatively High-Strength Concrete Specimens (Average of Three Magnification Levels)	305
Figure 9.1	Different Views of the Concrete Damage Conditions	314
Figure 9.2	Sub-regioning and Coring Configuration of the Concrete Pavement	315
Figure 9.3	Spatial (3-D) Measurements for Horizontal and Vertical Sub-regions (Means & Standard Errors)	328
Figure 9.4	Changes in Specific Surface Area Vs. Changes in Permeability	329
Figure 9.5	General view of the Bridge	333
Figure 9.6	Typical Surface Cracks of the Bridge Deck	335
Figure 9.7	Sub-regioning and Coring Configurations, and Surface Crack Patterns of the Deck	338
Figure 9.8	Spatial (3-D) Measurements for All Sub-regions (Means & Standard Errors)	348
Figure 9.9	Spatial (3-D) Measurements for Cores Extracted Over/Near and Far From Cracks (Means & Standard Errors)	351
Figure 10.1	Flexure Strength of Mix I (Normal-Strength) After Different Damaging Effects	362
Figure 10.2	Permeability of Mix I (Normal-Strength) After Different Damaging Effects	363
Figure 10.3	Flexure Strength of Mix II (Relatively-High Strength) After Different Damaging Effects	363
Figure 10.4	Permeability of Mix II (Relatively-High Strength) After Different Damaging Effects	364
Figure 10.5	Examples of Strong and Weak Correlations between Changes in Flexural Strength/Permeability and Microcrack Characteristics for Mix I (Normal-Strength)	372
Figure 10.6	Examples of Strong and Weak Correlations between Changes in Flexural Strength/Permeability and Microcrack Characteristics for Mix II (Relatively High-Strength)	373
Figure 10.7	Trends between Changes in Flexural Strength/Permeability and Microcrack Characteristics for Mix I (Normal-Strength)	374
Figure 10.8	Trends between Changes in Flexural Strength/Permeability and Microcrack Characteristics for Mix II (Relatively High-Strength)	375
Figure 10.9	Comparison between Modified Theoretical and Developed Experimental Models	380

NOTATION

A_A = Feature area fraction
A_{AC} = Crack area fraction
A_{AC1} = Crack area fraction on the first (horizontal) section
A_{AC2} = Crack area fraction on the second (vertical) section
A_{Ag} = Aggregate area fraction.
A_{AV} = Void volume fraction
AE = Acoustic emission technique
A_{gg} = Aggregate angularity
A_{iC} = Area of each individual crack.
A_{icm} = Mean of the area of each individual crack in the section of interest.
A_{ig} = Area of each individual aggregate particle
A_{iv} = Area of each individual void
$(A_{Sev})_{av}$ = Mean value of the ellipsoid voids aspect ratio in the section of interest.
A_{sg} = Aggregate particles aspect ratio
A_{SV} = Void aspect ratio
A_{Sf} = Aspect ratio of fibers
$(A_{Sf})_{av}$ = Mean value of fibers aspect ratio in the whole section of interest
Bi = Bismuth
BSED = Back scattered electron detector
Cd = Cadmium
CI_{fs} = Complexity index of fibers in space
C_{Ig} = Complexity index of aggregate in plane
CI_{gS} = complexity index of aggregate in space
CL_n = Number of pixels to distinguish between cracks and voids
C_{Sv} = Void compactness
d_{if} = Diameter of each individual fiber
d_{Lv} = Void equivalent diameter
d_{mfs} = Fibers mean diameter in space
d_{mgs} = Mean diameter of aggregates in space
d_{mvp} = Mean diameter of voids in plane
d_{mvs} = Mean diameter of voids in space
d_v = Diameter of individual void in the section of interest.
d_{vn} = Diameter of "n" voids in the section of interest
E = The mean value of the reciprocals of aggregate disk lengths on plane section
ESEM = Environmental scanning electron microscopy
f = the fraction of the connected pipes
F_{Fv} = Void form factor
FLR = Fluorescent liquid replacement technique
G = The mean value of the width-to-length ratios of aggregate disc sections
GSED = Gaseous secondary detector
h = Acceptable error (precision) or half the maximum acceptable confidence interval
h_{if} = Height of each individual fiber.
h_{mf} = Mean height of fibers in section of interest

I = Insignificant difference between crack length per unit area for both sections horizontal and vertical

I1 = Insignificant difference between crack length per unit area for the first (horizontal) section (perpendicular to the direction of loading)

I2 = Insignificant difference between crack length per unit area for the second (vertical) section [Perpendicular to the first (horizontal) section)]

ITZ = Interfacial transition zone

i = Total number of sub-regions in the whole structure

j = Total number of cores per sub-region

K = Number of size classes

K(q) = Shape factor for the ellipsoid voids

L = Dimension of the section of interest

$\bar{L}_3$ = Mean intercept length of three-dimensional bodies

L_A = Feature length per unit area

$(L_A)_{or}$ = The length per unit area of the parallel (oriented) lines of the system

L_{AC} = Crack length per unit area

L_{AC1} = Crack length per unit area of the first (horizontal) section (perpendicular to the direction of loading).

L_{AC2} = Crack length per unit are of the second (vertical) section [Perpendicular to the first (horizontal) section)]

$(L_{ev})_{av}$ = The average major axis for the ellipsoid voids

L_g = Length of any individual aggregate particle in the section of interest.

L_{gn} = Length of "n" aggregate particles in the section of interest.

L_{iC} = Length of each individual crack.

L_{ig} = Length of each individual aggregate particle

L_{iv} = Length (longest diameter) of each individual void

L_L = Feature lineal fraction

L_n = Object length

L_V = Feature length per unit volume

l = Constant length of short test lines thrown randomly on microstructure

m = The mean value of the reciprocals of the void circle diameters on the test section, or m_n = Numerator degree of freedom

MSE = Mean square error of specific surface area

n = Average number of cores required at the designated percent level of confidence

N_{Af} = Number of fibers per unit area

N_{Ag} = Number of aggregate particles per unit area of section of interest.

N_{AV} = Number of voids per unit area

n_g = Number of aggregate particles in the section of interest

N_{Ig} = Nonequiaxiality Index of each individual aggregate particle

N_{iv} = Total number of voids in the whole section

N_L = number of interceptions of features per unit length

N_{LC} = Number of cracks through length (L)

N_{SC} = Total number of cracks in the section of interest

N_V = Number of features per unit volume

N_{Vg} = Number of aggregate particles per unit volume

N_{Vf} = Number of fibers per unit volume

N_{VV} = Number of voids per unit volume
n_v = Number of voids in the section of interest
P = Number of intersections with surfaces make by l-lines
P_A = Number of feature points per unit test area
P_{AC} = Crack perimeter per unit area
P_{AV} = Void perimeter per unit area
Pb = Lead
P_{iC} = Perimeter of each individual crack
P_{iv} = Perimeter of each individual void
P_L = Number of point intersections per unit length of test line
$(PL)_{iav}$ = Average (PL) value for each individual aggregate
$(PL)i\perp$ or $(PL)i\amalg$ = Number of point intersections per unit length of superimposed array of equally spaced parallel test lines oriented in a predetermined direction for each individual aggregate particle running perpendicular and parallel to the preferred orientation of aggregates.
$(PL)t\perp$ or $(PL)tII$ = Total number of point intersections per unit length of superimposed array of equally spaced parallel test lines oriented in a predetermined direction. Subscripts "$\perp$"and "*II*" refer to test lines running perpendicular and parallel to the preferred orientation of cracks.
$(PL)ts\perp$ or $(PL)tsII$ = Total number of point intersections in space per unit length of superimposed array of equally spaced parallel test lines oriented in a predetermined direction. Subscripts "$\perp$"and "*II*" refer to test lines running perpendicular and parallel to the preferred orientation of cracks
$(P_L)_\perp$ = The number of intersections per unit length of the test array aligned in a direction perpendicular to the orientation axis
$(P_L)_\parallel$ = The number of intersections per unit length of the test array aligned in a direction parallel to the orientation axis
P_P = Feature point fraction
p = number of (end) points of l-lines that fall in phase of interest
$Q_{\alpha,i,i(j-1)}$ = Studentized range distribution
q = Shape coefficient for ellipsoid voids
r = Preliminary number of sub-region in the structure
S = External surface area of individual feature
S1 = Significant difference between crack length per unit area for the first (horizontal) section (perpendicular to the direction of loading)
S2 = Significant difference between crack length per unit area for the second (vertical) section [Perpendicular to the first (horizontal) section)]
Sd. Dv. = Standard deviation
SEM = Scanning electron microscopy
Sn = Tin
S_{SV} = Voids specific surface
S_V = Feature specific surface area
$S_{V\alpha}$ = Specific surface area of α-objects
S_{VC} = Specific surface area of cracks
S_{Vf} = Specific surface area of fibers
S_{Vg} = Specific surface area of aggregate

S_{VV} = Specific surface area of voids

$\overline{S}_{\alpha}$ = Mean surface area of α-objects

s = Significant difference between crack length per unit area for both sections horizontal or vertical

T_{CP} = Crack tortuosity in plane

T_{CP1} = Crack tortuosity in plane in the first section (perpendicular to direction of loading)

T_{CP2} = Crack tortuosity in plane in the second section (perpendicular to the first section)

T_{CS} = Crack tortuosity in space

t_{mg} = Mean thickness of aggregate particles

R_{Sv} = Void roundness

V = Volume of individual feature

V_{if} = Volume of each individual fiber

V_V = Feature volume fraction

V_{VC} = Crack volume fraction

V_{Vev} = volume fraction of the ellipsoid voids

V_{vg} = Aggregate volume fraction

V_{Vf} = Fibers volume fraction

V_{VV} = Void volume fraction

$V_{V\alpha}$ = Volume fraction of α-objects

$\overline{V}_{\alpha}$ = Mean volume of α-objects

W = Width of object

W_{CP} = Crack width per unit area in plane

W_{CP1} = Crack width per unit area in the first section (perpendicular to direction of loading)

W_{CP2} = Crack width per unit area in the second section (perpendicular to the first section)

W_{CS} = Crack width per unit volume in space

$(W_{ev})_{av}$ = The average minor axis for ellipsoid voids

$(W_{ev})_{max}$ = The minor axis of the ellipsoid voids in the largest size class

W_{iC} = Width of each individual crack

W_{ig} = Width of each individual aggregate particle

W_{vc} = Width (shortest diameter) of each individual void

$\overline{w}$ = Average half-crack aperture

z = Percentile of standard normal distribution

λ_{CP1} = Crack spacing in plane

λ_{CP1} = Spacing in plane through length (L)

$\lambda_{CPdiagonal}$ = Diagonal crack spacing in plane

λ_{cpx} = Crack spacing in X direction.

λ_{cpy} = Crack spacing in Y direction

λ_{CS} = Crack spacing in space

λ_{fs} = Fibers spacing in space

λ_{gs} = Aggregate spacing in space

λ_{VP} = Void spacing in plane

λ_{VS} = Void spacing in space

Γ_g = Width/length ratio of any individual aggregate particle in the section of interest
Γ_{gn} = Width/length ratio of "n" aggregate particle in the section of interest
ω = The numerical value used for comparison
ω_C = Angle of orientation of cracks in plane
Ω = Feature degree of orientation
Ω_{CP} = Crack degree of orientation in plane
Ω_{CS} = Crack degree of orientation in space
Ω_{gs} = Aggregate degree of orientation in space
β = The required power of the test, or the risk of making a type II error
β_1 = The dimensionless shape coefficient that relates the object volume and its mean cross-sectional area.
β_2 = Dimensionless shape coefficient that relates the object volume to its mean cross-sectional area
σ = Population standard deviation (for specific surface area of cracks within each sub-region)
α = The level at which the risk of making a Type I error is to be controlled
α_i = Numerical coefficient
μ_i = Mean of the specific surface area of cracks
μ_{k+1} = Mean of specific surface area of the successor sub-region
$\delta\mu$ = The difference of means of specific surface areas for two sub-regions in the whole structure
ν = Denominator degree of freedom
∂F = Change (%) in concrete flexural strength
∂S_{VC} = Change (%) in microcrack specific surface area
∂V_{VC} = Change (%) in microcrack volume faction
∂W_{CS} = Change (%) in microcrack width
$\partial \rho$ = Change (%) in concrete permeability
$\partial \lambda_{CS}$ = Change in (%) in microcrack spacing in space
ϕ = Porosity
∇ = Difference between maximum and minimum means of crack specific surface area
Δ = The ratio of maximum void diameter to the total number of voids in the group

CHAPTER 1

INTRODUCTION

1.1 PREFACE

Concrete has been used in construction for several centuries, perhaps first by ancient Egyptians and Romans. Concrete offers distinct economic, energy and environmental advantages which have led to its predominant position in modern civil engineering construction. These advantages also promise that, in the foreseeable future, concrete will continue to be the mainstay of construction and the backbone of the modern civilization.

Although the exterior appearance of concrete looks likes a solid rock, its interior comprises diverse void and microcrack systems which govern various aspects of mechanical, durability and physical characteristics. Concrete is susceptible to attack by environmental and load effects which tend to propagate microcracks and undermine its performance characteristics (strength, durability, transport properties, etc.). Microcrack growth, besides chemical changes, is a primary means of concrete deterioration under weathering and load effects. Hence, microscopic evaluation of the microcrack system provides powerful tools for assessing concrete behavior and failure modes. Microscopic investigations of concrete, however, are generally conducted qualitatively, and thus tend to lack sufficient, reliability and thoroughness. Such qualitative investigations relay heavily on the judgment and experience of the investigator for assessment the microscopic observations. Quantitative investigations of concrete would enable development of scientific basis for damage processes and failure modes of concrete under

load and environmental effects. Thus investigation of concrete microstructure (microcracks and voids), particularly in a quantitative manner, is considered to be a key probe for a deep understanding of concrete problems and behavior. It is now established that concrete cracks are mainly formed due to the coalescence of microcracks which exist in the interfacial zone (ITZ) before exposure to external load or environmental effects. These internal microcracks result from movement mismatch between aggregate particles and cement paste.

1.2 DEFINITION OF THE PROBLEM

Microcrack growth coalescence constitutes a primary mean of concrete cracking and failure under diverse load and environmental effects. Quantitative assessment of the microcrack system in concrete is thus critical to development of a thorough and fundamentally sound understanding of concrete behavior and failure mechanisms. Quantitative information on microcrack systems would also enable development of microstructure-property relationships which relate changes in quantified microcrack attributes to corresponding changes in concrete engineering properties under load and environmental effects. Such relationships allow practical use of quantitative microstructural analysis towards condition assessment of concrete systems. These achievements would be possible by a departure from today's predominantly qualitative to a new quantitative means of concrete microstructural analysis. Quantitative investigation of microcrack system, when complemented with statistical analyses, provides reliable data on concrete microcrack attributes and thus health conditions. When we measure we know better.

1.3 RESEARCH OBJECTIVES

The fundamental objectives of the research are to develop a quantitative approach to investigation of concrete microcracks, to validate the proposed approach thorough concrete mixtures as well as field investigations, and to develop the basis for realistic relationships between quantified microstructural (microcrack and void) attributes and characteristics of concrete based on laboratory tests. The quantitative approach established the different criteria and parameters for sampling, specimen preparation, features (microcracks vs. voids) detection, image processing and analysis, stereological interpretations and statistical analysis. The results will provide a deep insight into the damaged behavior and deterioration process of concrete under different types of loading, and also provide a basis for condition assessment of concrete durability under different environmental conditions. These methodologies are developed and applied toward developing deep insight into the damage and deterioration processes of concrete under different load and environment effects. The research adopted scientific principles from the fields of microscopy, image processing, image analysis, stereology, and statistics together with some fundamental aspects of concrete technology in order to develop an integrated system for quantitative microstructural investigation of concrete. The research study also applied this system toward better understanding of concrete materials and structures, which is a pre-requisite to effective improvement of concrete materials. The objectives can be summarized as follows:

1- Developing a comprehensive system for quantitative microstructural investigation of concrete.

2- Validating and refining microstructural quantification system through concrete mixtures as well as field applications.

3- Developing microstructure-property relationships for determination of the engineering properties of concrete in terms of quantified microstructural attributes.

1.4 SIGNIFICANCE OF THE RESEARCH

The proposed approach yields valuable insight into concrete deterioration and failure processes, provides a quantitative basis for the assessment of damage to concrete systems under load and environmental effects, and yields fundamental microstructure–property relationships for concrete. Such relationships would be of great value in devising strategies to:

1- Assess the health conditions of existing concrete–based infrastructure in light of aging and environmental effects, and various external applied loads.

2- Develop enhanced concrete materials, and devise improved models for simulating concrete performance.

3- Control the quality of new construction.

1.5 RESEARCH METHODOLOGY

The proposed research study was implemented in three major stages:

Stage (I): Development of a Comprehensive System for Quantitative Microstructural Investigation of Concrete.

Development of the required comprehensive approach can be achieved by conducting the following steps:

i) Establishment of the criteria, and parameters for automation of image processing and analysis

ii) Sampling schemes and specimen preparation for detection of microcrack and void systems

iii) Acquisition, processing and analysis of microscopic images

iv) Stereological interpretations and statistical analysis

Figure 1.1 summarizes steps of Stage I of the research study.

Stage (II): System Verification and Refinement Through Concrete Mixtures as well as Large-Scale Field Applications

i) Quantification of concrete microcrack characteristics through normal-strength and high-strength concrete mixtures.

ii) Assessment of the health conditions and damage distribution of a deteriorated rigid pavement.

iii) Assessment of the health conditions and damage distribution of a deteriorated reinforced concrete bridge deck.

(a) Criteria for Software Automation

(b) Sampling and Sectioning

(c) Specimen Preparation

(d) Image Acquisition

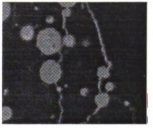

(e) Image processing and Analysis

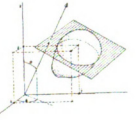

(f) Stereological Interpretations

ϑ	Γ	Π	ς	Ν
5	5%	4	ι	Ξ
-6	ɜ	6	-0.8	-3

(g) Statistical Analysis

Figure 1.1 Schematic Representation of Stage I of The Research Study

Stage (III) Development of Relationships Between Engineering Properties of Concrete and of Quantified Microstructural Attributes.

i) Establish theoretically viable microcrack attributes influencing different engineering properties of concrete.

ii) Develop empirical relationships for changes in key microcrack attributes under different damage phenomena and the corresponding changes in different engineering properties of concrete.

CHAPTER 2

CONCRETE MICROSTRUCTURE: LITERATURE REVIEW

2.1 PREFACE

Most classical limit models are based on the assumption that the material can be represented as a continuum. The behavior described is independent of the structure of the material. The only geometrical ingredients considered are those reflecting on the size and shape of the structure that was considered. Concrete is a multi-scale material.[1] Figure 2.1 shows the different scales of concrete observation.

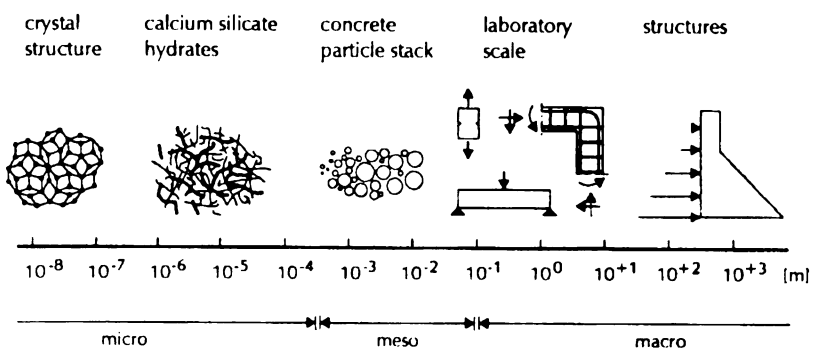

Figure 2.1 Different Scales of Concrete Observation[1]

The smallest structural feature in Figure 2.1 is the atomic structure of cement and aggregates (with observations made at the nanometer scale). At the micrometer scale,

where individual cement grains can be distinguished, the unhydrated cement grains are observed; in the hardened state, calcium silicate hydrates and calcium hydroxide are visible at the micrometer scale. The complex pore structure becomes visible as well at this scale. Upon increasing the scale to 10^{-3} m (meso scale), individual sand and aggregate particles can be distinguished. The 10^{+1} m macro scale covers the laboratory scale (mechanical) test specimens. Even larger scales, i.e. up to 10^{+2} to 10^{+3}, cover civil engineering structures. At the micro-level, the internal structure of cement and hardened cement paste is the most important structural feature. At the macro-level, no internal material structure is recognized, except for reinforced concrete where the reinforcement structure is normally taken into account. According to the above three-level approach, concrete is considered to be heterogeneous, inelastic and multiphase material. With regard to the mechanical behavior, concrete is considered to be a three-phase compsite.[2] The three phases of concrete are:

1- Aggregate particles phase.

2- Binding medium phase (hydrated cement paste "hcp" or mortar) phase and,

3- Interfacial transition zone (ITZ) phase.

The importance of studying concrete at different levels or phases is due to the fact that concrete behavior at one level can be explained in terms of the structure observed at a lower level. For instance, at the micro-level, knowledge of the structure of calcium-silicate hydrate, the pore-structure of the hydrated cement and the interaction between the cement and water (in different forms) helps explain the creep and shrinkage phenomena in concrete. Moreover, knowledge of mechanical behavior of the interfacial transition zone, which plays an important role when the concrete is observed at the meso-level, can

be obtained by considering in detailed structure of hardened cement paste. At the meso-level, studying interactions between matrix and aggregates, as well as mutual interactions between aggregates, provides better understanding of the mechanical behavior of concrete.

2.2 STRUCTURE OF CONCRETE PHASES

2.2.1 Aggregate Phase

2.2.1.1 *Structure of the Aggregate Phase*

The aggregate phase typically comprises about three-quarters of the volume of concrete. Aggregate type, maximum size, gradation, surface texture and shape have an influence on the engineering properties of concrete. Various undesirable constituents might also be identified in the aggregate phase, including clay, mica, gypsum, pyrite and alkali-reactive materials. Being generally stronger than the other two phases of concrete, the aggregate phase has no direct influence on the strength of concrete[3] except in the case of some highly porous and weak aggregates such as lightweight aggregate particles from pumice which are highly cellular aggregate particles. They can cause a noticeable reduction in concrete strength. Aggregate selection is very important in producing high performance concrete using a well-graded combination of fine and coarse aggregates. Aggregate grading affects the packing density of concrete, and experiments show that the packing density has a major effect on workability, permeability and strength of hardened concrete. The size, shape, texture and mineralogy of aggregate also significantly affect the microstructure and properties of hydrated cement paste in the transition zone. Equi-dimensional particles are desirable and can be obtained by crushing either dense

limestone or igneous rocks of plutonic type. Gravel from glacial deposits also is a suitable coarse aggregate. A nominal maximum size of 12 or 19 mm (½ or ¾ in) most commonly used. Natural quartzitic sands of relatively coarse size (fineness modulus of about 3.0), free from silt and clay, should be used as fine aggregate. Ideally, coefficient of thermal expansion and elastic modulus of the aggregate and hydrated cement paste should be the same. A mismatch is probably a primary cause of microcracking which increase the permeability and reduces the durability of concrete.[4]

2.2.1.2 *Effect of Aggregate Phase on Concrete Properties and Performance*

Aggregates have a particularly significant effect on the stiffness of concrete. Aggregate volume fraction has a direct effect on concrete modulus of elasticity as shown in Figure 2.2.

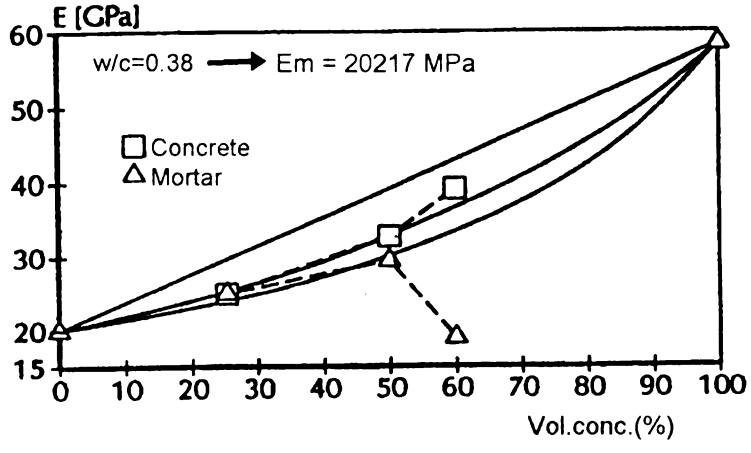

Figure 2.2 Effect of Aggregate Content on Stiffness of Concrete and Mortar[1]

Initial bleeding, segregation and shrinkage cracking occur preferably under the larger aggregate particles in the concrete. Consequently, weak zones will develop in the concrete. The effect of aggregate on concrete stiffness depends mainly on the stiffness of the aggregate itself. Using lightweight aggregate can produce lightweight concrete with low modulus of elasticity, while using normal aggregate can produce concrete with higher modulus of elasticity. The initial stiffness of concrete can also be affected when the direction of loading is changed with respect to the direction of casting.[1]

Aggregates also have an effect on crack path and propagation. Microcracking usually occurs at aggregate/mortar interfaces which represent weak zones due to bleeding on the bottom surfaces of aggregates. The influence of aggregate particle on crack propagation in fibrous concrete is shown in Figure 2.3, which indicates that occurrence of aggregates in the matrix can produce many different and alternative paths of microcracks, such as crack face pinning, crack branching, or crack deflection.[5]

The failure shape and sequence of concrete can also be affected by aggregate particles. If the stiffness of aggregate particles is more than that of the matrix (normal-strength concrete case), microcracks tend to propagate through the matrix/aggregate interfaces around aggregate particles, which constitute the path of least resistance. In case the stiffness of aggregate particles is equal or less than that of the matrix, microcracks tend to propagate through aggregate particles, creating shorter fracture surfaces.[6] Figure 2.4 compares crack propagation paths in normal and high strength concrete

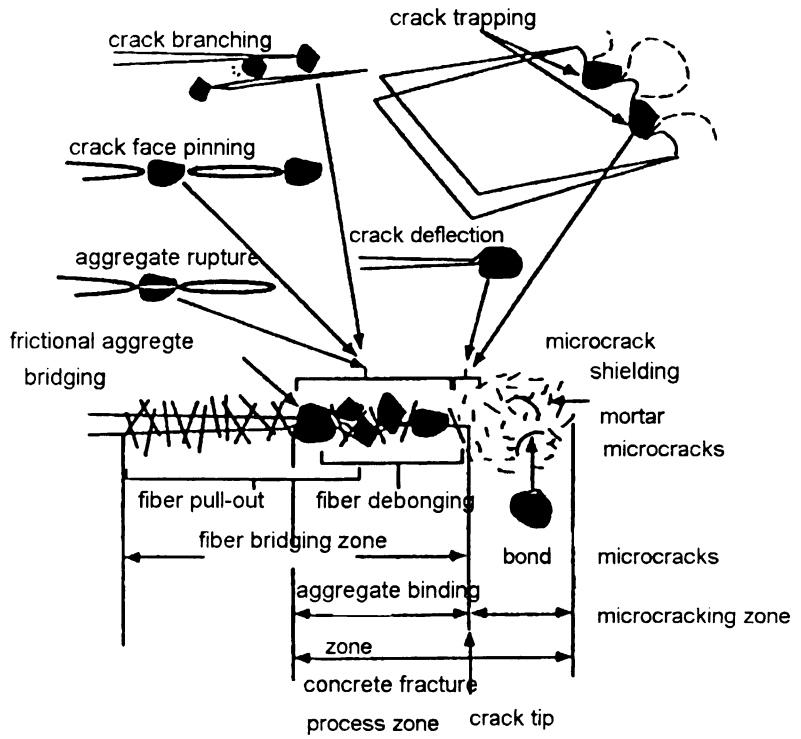

Figure 2.3 Possible Toughening Mechanisms Operating in a Fibrous Concrete[5]

The aggregate phase also has an effect on concrete durability. The size and the shape of coarse aggregates can affect the strength of concrete in an indirect way. It is obvious from Figure 2.5 that the larger the size of aggregate in concrete and the higher the proportion of elongated and flat particles, the greater will be the tendency for water films to accumulate under the aggregate surface and weaken the interface zone. This phenomenon is known as internal bleeding.

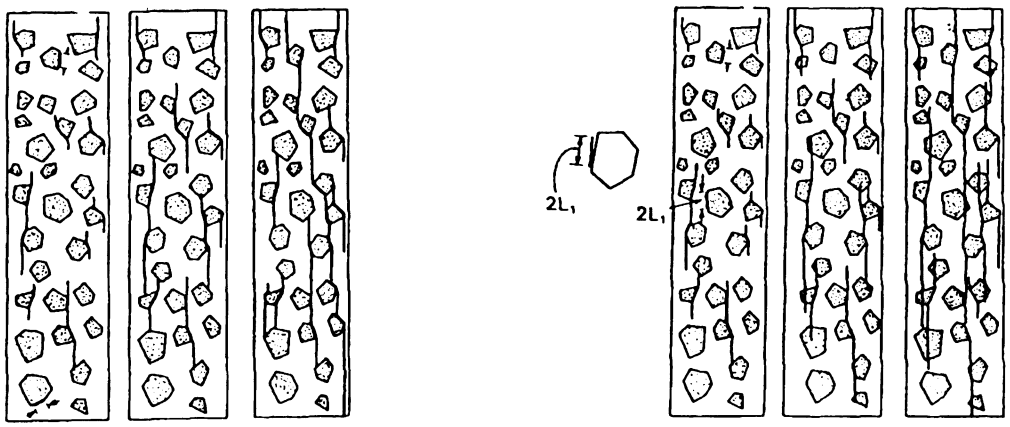

(a) Normal-Strength Concrete (b) High-Strength Concrete

Figure 2.4 Crack Propagation Under Compression[6]

Aggregates also have a significant beneficial effect on the dimensional stability of concrete, since aggregates resist the dimensional movement of concrete.

Chemical reactions of aggregates in concrete can affect the performance of concrete structures. Most of these reactions may result in serious damage to concrete due to abnormal internal expansions that may produce cracking, displacement of elements within larger structural entities, and loss of strength. The most common example of these reactions is alkali-silica reactivity or alkali-aggregate reaction, which involves a reaction between alkalis in cement and silica in aggregate.

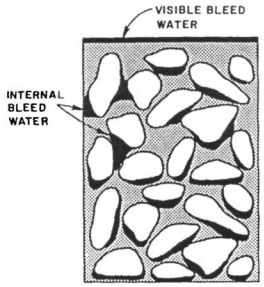

Figure 2.5 Diagrammatic Presentation of Bleeding in Freshly Deposited Concrete[3]

2.2.2 Binding Medium Phase

2.2.2.1 *Structure of the Binding Medium Phase*

The four principal cement constituents (C_3S, C_2S, C_3A and C_4AF) are hydraulic and thus react with water on mixing to form a range of hydrated phases. When Portland cement is dispersed in water, the calcium sulfate and the high-temperature compounds of calcium tend to go into solution, and the liquid phase gets rapidly saturated with various ionic species. As a result of combinations between calcium, sulfate, aluminate and hydroxyl ions within a few minutes of cement hydration, first the needle-shaped crystals of calcium sulfoaluminate hydrated make their appearance; a few hours later, large prismatic crystals of calcium hydroxide and very small fibrous crystals of calcium silicate hydrates begin to

fill the empty space formerly occupied by water and the dissolving particles. After some days, depending on the alumina-to-sulfate ratio of the Portland cement, ettringite may become unstable and decompose to form the monosulfate hydrate, which has hexagonal-plate morphology. Hexagonal-plate morphology is also the characteristics of calcium aluminate hydrates.[7] Using scanning electron microscope; four principal solid phases can be identified in hydrated cement paste.

2.2.2.2 *Solids in the Binding Medium Phase and its Effect on Concrete Properties and Performance*

A) Calcium Silicate Hydrate (C-S-H)

The calcium silicate hydrate phase (C-S-H) makes up 50 to 60 percent of the volume of solids in a completely hydrated cement paste and is, therefore, most important in determining the properties of the paste. The (C-S-H) is composed of irregular forms of different shapes and sizes. Calcium silicate hydrate is considered to be the continuous solid matrix of the hydrated system and therefore is of a particular importance. (C-S-H) is considered to be the main source of strength gain in concrete because calcium silicate hydrate is composed of small crystals and possesses enormous surface area and adhesive capability. The crystals tend to adhere strongly not only to each other, but also to low-surface area solids such as calcium hydroxide, anhydrous clinker grains, and fine and coarse aggregate particles, thereby positively affecting concrete strength. Spacing between calcium silicate hydrate sheets can also affect concrete durability; it also affects its fire resistance due to the existing of interlayer water, which is strongly held by hydrogen bonding. Spacing between (C-S-H) sheets can also affect both creep and

shrinkage of concrete provided that the interlayer water is lost. The more the spacing between sheets the more concrete dimensional instability.

B) Calcium Hydroxide (CH)

Calcium hydroxide crystals constitute 20 to 25 percent of the volume of the solids in hydrated paste. It tends to form large crystals with a distinctive hexagonal–prism morphology.[8] Figure 2.6 shows an SEM micrograph of calcium hydroxide crystals in different orientations. Calcium hydroxide has a little effect on concrete strength due to its low surface area; in general, it has an adverse effect on concrete strength. The presence of considerable amounts of calcium hydroxide in hydrated Portland cement has an adverse effect on concrete chemical resistance to acidic solutions because of the higher solubility of calcium hydroxide when compared with (C-S-H). Since calcium hydroxide crystals do not lose moisture during drying, and hence do not shrink, they may act to restrain the deforming calcium silicate hydrate.

C) Calcium Sulfoaluminates

Calcium sulfoaluminate compounds, which form needle-shaped prismatic crystals occupy 15 to 20 percent of the solids volume in hydrated cement paste, and therefore play only a relatively minor role in structure-property relationships. Due to the small percentage of calcium sulfoaluminate, it does not have a significant effect on concrete strength. The presence of the monosulfate hydrate in concrete makes it more vulnerable to sulfate attack.

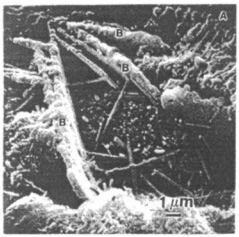

Figure 2.6 SEM Micrograph of Isolated Plates of CH in Different Orientations (A&B)[8]

D) Unhydrated Clinker Grains

Depending on the particle size distribution of anhydrous cement and the degree of hydration, some unhydrated clinker grains may be found in the microstucure of hydrated cement paste.

2.2.2.3 *Voids in the Binding Medium Phase*

A fresh concrete mix is typically compacted using vibration in order to improve the packing of aggregates and cement paste, and to minimize the residual content of entrapped air. In spite of the compacting effort, concrete retains some entrapped air. In fresh concrete, such entrapped air forms bubbles which range in size from microscopic

spheres (the size of cement clinker grains) to irregularly shaped gas pockets (the size of coarse aggregate particles or larger).[9] After hardening of concrete, the entrapped and entrained air bubbles are fixed in place and become air voids. Figure 2.7 compares the air void size distribution in concrete with those of aggregates, cement, and silica fume. The other main type of voids that can be found in concrete is capillary pores. The cement paste that forms in concrete has a pore structure different from that in plain paste.[9,10] The paste in concrete is more porous, and the majority of extra pores have larger diameters than those in plain paste. The paste that forms in mortar has a pore structure which is more analogous to that in concrete than in plain paste.

2.2.2.4 *Types of Voids and Their Effects on Concrete Properties*

A) Capillary Voids

Capillary voids represent the space that was not filled by the solid components of hydrated cement paste. In well-hydrated, low-water cement ratio pastes, at early stages of hydration, the capillary voids may range from 10 to 50 nm; in high water- cement ratio pastes, at early stages of hydration, the capillary voids may be as large as 3 to 5 μm.[3] Capillary porosity is one of the most significant features of concrete microstructure. Most concrete properties, including strength, modulus of elasticity, permeability and toughness are affected by changes in capillary porosity.[11] Capillary voids are not easy to observe under microscopes as they are both well dispersed and their dimensions are at or beyond the working limit of observation. In practice this qualitative observations are made by impregnating concrete with fluorescent epoxy and visually estimating the amount of fluorescence which is then related to water-cement ratio.

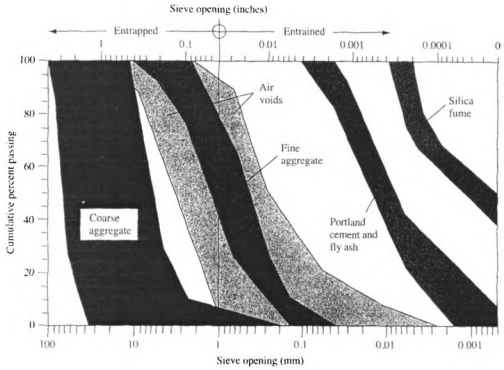

Figure 2.7 Air-Void Gradation, Compared with Aggregates, Cement and Some Mineral Additives[10]

Concrete strength and permeability are two sides of the same coin in the sense that both are closely related to the capillary porosity or solid /space ratio. The strength of hardened cement paste and concrete as well as that of any brittle material decreases rapidly with an increasing in porosity. Capillary pores damage strength properties through:[12] (a) reducing the quantity of solid materials; (b) lowering the number of bonds; and (c) pronouncing stress concentrations (the sharper the pore, the greater the stress concentration). Figure

2.8 shows the trends observed in the effects of capillary porosity on compressive strength.

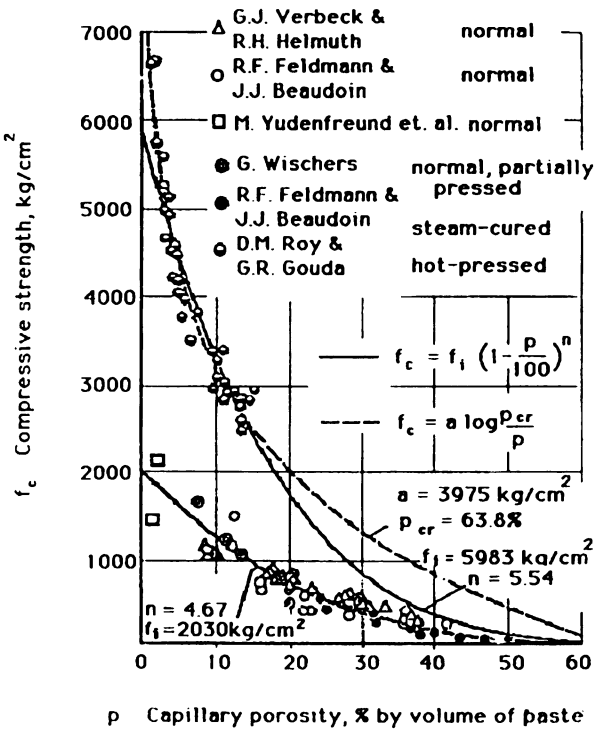

Figure 2.8 Effects of Capillary Porosity on Compressive Strength Under Different Conditions[12]

The pore size distribution, not the total capillary porosity, is considered to be a better criterion for evaluating the effects of capillary voids on concrete properties. Capillary voids larger than 50 nm, referred to as macropores, are assumed to be detrimental to strength and impermeability, while voids smaller than 50 nm, referred to as micropores,

are assumed to be more important to drying shrinkage and creep. The water in large capillary voids (50 nm), which may be considered as free water, does not cause any volume changes, while the water held by capillary tension in small capillaries (5 to 50 nm) may cause shrinkage of concrete. The relation between permeability and porosity is considered to be exponential,[3,13] which means that larger pores exert on pronounced effects on permeability. In hydrated cement paste, a direct relationship was noted between the permeability and the volume of pores larger than about 100 nm. This is probably because that pore systems comprising mainly of small pores tend to become discontinuous.

B) Air Voids

The main difference between capillary pores and air voids is that capillary pores are elongated (and partially inter-related) spaces filled with water while air voids are independent, roughly spherical pores formed by entrapment or entertainment of air. Hence, an important difference is in their minimum dimensions.[10] The difference between entrapped air voids and entrained air voids is that entrapped air voids are trapped during mixing while entrained air voids are produced by admixtures which have a foaming or air-entraining action in the plastic cement paste. Entrained air voids are typically finer and more spherical than entrapped air voids. The investigation of concrete under microscope showed that there is no direct contact between air voids and gravel; the air voids are surrounded by the matrix (cement paste and sand).[14]

i) Entrained Air Voids

Entrained air voids are characteristically spherical in shape; mostly range in diameter between 10 μm and 1 mm. Also, in contrast to the entrapped air voids, the entrained air voids usually exhibit a sensibly uniform distribution throughout the concrete matrix, except near to concrete surfaces and for poorly mixed concrete. The advantages of entrained air voids induced increasing in workability, improving in cohesion and reduced bleeding. In hardened concrete, the prospects for durability are generally improved by a reduction in permeability, with resistance to freezing and thawing cycles and de-icing chemicals notably enhanced.[6] A saturated cement paste containing no entrained air expands due to the generation of hydraulic pressure, with increasing air entertainment, the tendency to expand decreases because the entrained air voids provide escape boundaries for release of hydraulic pressure. Figure 2.9 illustrates the effect of air entraining voids on concrete durability. Air-entertainment lowers the density of concrete; some loss of compressive strength could also be observed with air entrainment which is, at least partially, compensated for by improved workability which allows lowering of water-cement ratio and consequent proportional lowering of strength.

ii) Entrapped Air Voids

Entrapped air voids are typically irregular in shape, and mainly greater than 1mm in diameter. The size distribution and disposition is also irregular within the concrete, with a tendency for increase in both size and number towards surfaces. The entrapped air voids are formed during concrete mixing. The content of entrapped air voids should be reduced

as the degree of compaction improves. Larger and irregularly shaped entrapped air voids become more common with increasing cement content.

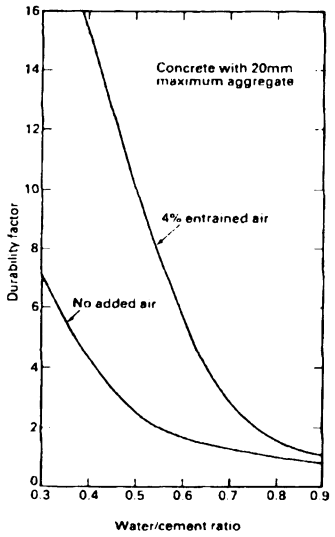

Figure 2.9 Effect of Air-entrained Voids on Concrete Durability at Different Water/Cement Ratios[6]

From examination of the air void system in a thin section it is possible to characterize the parameters of the system and also to observe if they contain calcium hydroxide or any other products. Spacing between entrained air voids is considered to be an important factor for enhancing the freeze-thaw resistance of concrete. Since the spacing between entrapped air voids is fairly large compared to the spacing between entrained air voids, the entrapped voids do not have any effect on concrete resistance to freezing and thawing. Entrapped air voids are relatively large and thus capable of adversely affecting concrete strength and impermeability.

C) Water Voids

Depending on the environmental humidity and the porosity of the paste, the unreacted cement paste is capable of holding a large amount of water at the time of the concrete maturation. Water voids are irregular in shape, generally elongated and usually very large (several mm in size). Typically found beneath particles of coarse aggregate or reinforcing bars, their interior surfaces have a granular appearance instead of the usually glazed luster of air voids. Four types of water can be distinguished in concrete microstructure:[15] (as shown in Figure 2.10).

1- Chemically combined water, water present in the crystalline phases of cement paste such as C-S-H.

2- Interlayer water, water present in the gel, whether in layers themselves or in the interlayer spaces (the distinction is difficult to make).

3- Adsorbed water, monolayer water, of which most will be on the surface of the micropores.

4- Capillary water, water present in either micropores or larger pores.

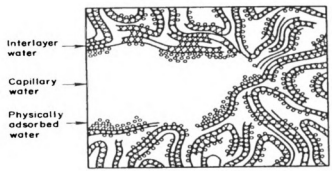

Figure 2.10 Different Types of Water in Concrete[3]

2.2.3 Structure of the Interfacial Transition Zone Phase (ITZ)

The transition zone typically ranges from 10 to 40 μm thick, and is generally weaker than either of the other two phases of concrete; therefore, it has a disproportionate influence on the mechanical behavior of concrete compared to its size.[1,3] The transition zone is formed by accumulation of water films around large aggregate particles. Next, calcium, sulfate, hydroxyl and aluminate ions produced by the dissolution of calcium sulfate and calcium aluminate compounds combine to form ettringite and calcium hydroxide. These crystalline products in the vicinity of coarse aggregate consist of relatively larger crystals and therefore form a more porous framework than in the bulk of cement paste. Structure of the interfacial transition zone is shown in Figure 2.11.

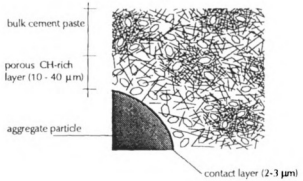

Figure 2.11 Structure of the Interfacial Transition Zone[1]

Other researchers[16,17] acclaimed that the ITZ surrounding aggregate grains in concrete can be objectively designated as a volume from which Portland cement particles have been preferentially excluded on a statistical basis. The effects of such statistical exclusion are manifested, even after most of the cement is hydrated, in a well-defined gradient marking the reduced content of residual unhydrated cement with decreasing distance from the aggregate surface as shown in Figure 2.12. Over time, in the presence of moisture, the interfacial pore space originally associated with the wall effect in ordinary concrete becomes mostly filled up by deposits of calcium hydroxide and by deposits of C-S-H passing through solution, leading to the retention of only a modest residual extra average pore content within the ITZ. Hence the existence of the ITZ around aggregates can have only marginal effects on both mechanical properties and on performance after continued exposure to moisture over time.

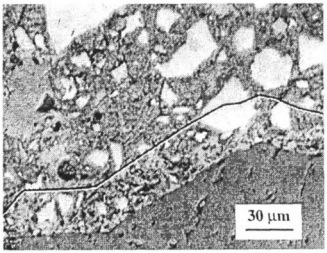

Figure 2.12 SEM Micrograph of an Area Around a Sand Grain in Ordinary Concrete[16]

2.2.3.1 *Concrete Microcracks*

Concrete microcracks can be detected, even prior to any loads or environmental effects[18], in the interfacial transition zone (ITZ) by using a powerful microscope. It is well known that even before the application of external load, microcracks already exist in the transition zone between mortar and coarse aggregate due to the shrinkage and thermal mismatch between aggregate particles and matrix[3]. The number and width of these microcracks in a concrete specimen would depend, among other factors, on bleeding characteristics, strength of the transition zone, and the curing history of concrete. Under ordinary curing conditions (when a concrete element is subjected to drying or thermal shrinkage effects), due to differences in their thermal and hygral movements, differential strains and thus interfacial stresses will be set up between the matrix and coarse aggregates, causing microcrack for mortars in the transition zone. When concrete is subjected to externally imposed structural loads or damaging environmentally effects, tensile stress-concentrations will appear at the interface between aggregate and matrix due to differences in elastic modulus and also because of the pre-existing of interfacial microcracks. As a result, concrete macrocracks will occur and develop first in the interface zone (and then into the paste) under load and environmental effects. Experimental results[1-3,19] confirm that microcracks initiate at the interfaces, and subsequently propagate into the matrix and form continuous macrocracks. In the presence of propagating large cracks (as shown in Figure 2.13), microcrack propagation and interconnection occurs ahead of the propagating crack tip.

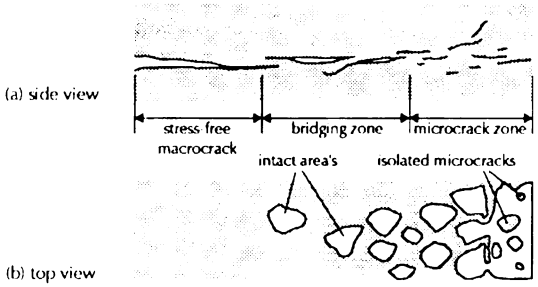

Figure 2.13 Identification of Concrete Microcracks[1]

2.2.3.2 *Causes of Microcracks Propagation*

A) Loading

i) Compressive Load

Under a steadily increasing compressive stress, which is assumed to be uniformly distributed over the specimen cross-section, a nonlinear stress-strain diagram is found as shown in Figure 2.14, where stages of concrete behavior can be distinguished. As noted earlier, even before the application of external load, microcracks already exist in the transition zone between the mortar matrix and coarse aggregates in concrete. The number and width of these cracks in a concrete specimen would depend on bleeding characteristics, strength of the transition zone, and the curing history of concrete. From Figure2.14,[3] it is shown that below about 30% of ultimate load, the transition zone cracks remain stable; therefore, the stress-strain curve remains linear (Stage 1). Above about 30% of the ultimate load, as the stress increases, the transition zone microcracks begin to

increase in length, width and numbers; therefore, the curve begins to deviate appreciably from a straight line (Stage 2). Until about 50% of the ultimate stress, a stable system of microcracks may be assumed to exist in the transition zone. At about 60% of the ultimate load cracks begin to form in the matrix. With further increase in stress up to about 75% of ultimate load (Stage 3), not only will the crack system in the transition zone become unstable but also the proliferation and propagation of cracks in matrix will increase causing the stress-strain curve to bend considerably toward the horizontal at about 75%-80% of the ultimate load (Stage 4).

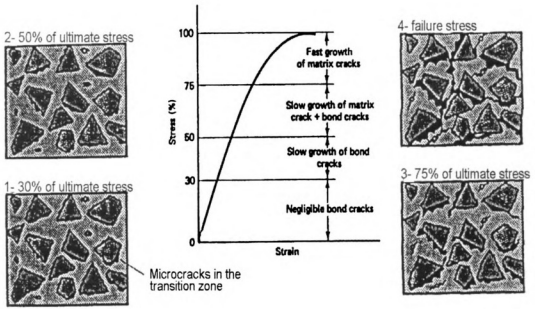

Figure 2.14 Diagrammatic Presentation of The Stress-Strain Behavior of Concrete Under Uniaxial Compression[3]

The rate of strain energy release seems to reach the critical value necessary for spontaneous crack growth under sustained stress and the material will strain to failure (i.e. with increasing stress very high strains are developed), indicating that the crack system is becoming continuous due to rapid propagation of microcracks in both the matrix and the transition zone. Figure 2.15 shows an scanning electron microscopy (SEM) micrograph of a normal concrete failed under compression;[20] microcracks are observed to form not only in the interface zone but also throughout the cement paste.

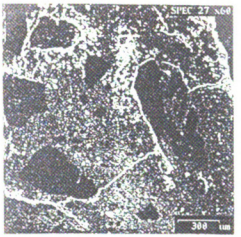

Figure 2.15 SEM for Normal-Strength Concrete Specimen Subjected to Uniaxial Compression[20]

Although under uniaxial compressive load most microcracks appear to have been propagated through the cement paste and along the interfacial transition zone, there are other microcracks that appear to have been generated from voids as a result of local tensile stress tangential to the void boundary. These cracks usually originated near

maximum compression.[18] Compared to normal-strength concrete, high-strength concrete behaves more like a homogeneous material, with its stress-strain curve remaining closer to linearity at higher stress/strength ratios. The amount and degree of microcracking in the interfacial transition zone (ITZ) between cement paste and aggregate cause a more brittle mode of fracture and less volumetric dilation. Figure 2.16 shows an SEM micrograph of a high-strength concrete specimen failed under compression.[20] From the image it can be shown that the microcracks occurred trough both cement paste and aggregates.

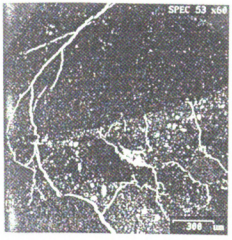

Figure 2.16 SEM for High-Strength Concrete Specimen Subjected to Uniaxial Compression[20]

Adding mineral admixtures such as fly ash or silica fume has an effect on stress-strain curve[21]. The stress-strain curve for pastes with fly ash is less linear and begins to deviate from linearity at about 60% -70% of the ultimate strength. This is probably related to the

increased microcracking between the fly ash particles and hydrates with increasing load level. Inspection of pastes containing fly ash and subjected to uniaxial compressive stresses under SEM showed that microcracks propagate generally around fly ash particles through interfaces between fly ash particles and the matrix of hydrates. In order to study the propagation of microcracks under sustained compression, the relationship between crack propagation and axial creep has been investigated[22] by plotting the increase (creep) of specific crack area against the axial creep at different stress-strength ratios as shown in Figure 2.17.

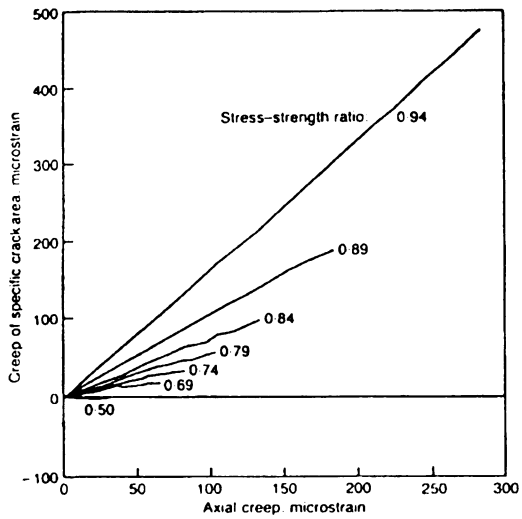

Figure 2.17 The Relationship between Creep of The Specific Crack Area and the Axial Creep[21]

At stresses lower than about 50% of compressive strength, propagation of microcracks under sustained loads is practically negligible. The lines obtained are horizontal, lying on

the axial creep axis. Beyond this stage, the gradient of the line increases with increasing stress, but the line tends to bend towards the axial creep axis until the sustained stress exceeds a certain threshold, beyond which it begins to bend towards the crack axis. This threshold stress was found to be around 80% to 95% of compressive strength.[22] It was also found that the nucleation and propagation of microcracks constitute the mechanisms of concrete damage, and the total crack length per unit volume can be deemed as the damage parameter.[23] It is also reported that the resulting microcracks under concentric compressive load appeared to be uniformly distributed throughout the specimen while the resulting microcracks under eccentric compressive load exist through the full length of the specimen but are almost collinear with the line of action of the load; in some cases few longitudinal microcracks along the side away from the eccentric load were observed.[24]

ii) Tensile Load

When a concrete specimen is subjected to uniaxial tension, a stress-deformation diagram as shown in Figure 2.18 is observed. The relation has essentially the same shape as the compressive stress-strain curve. From the figure, it is shown that the fracture process of concrete specimen under uniaxial tension load is composed of three stages, distributed damage during loading of the sample to about 80% of the pre-peak load, formation of microcrack localization during the loading period between 80% of load from pre-peak to post-peak regions, and major crack propagation in the post-peak region after the load drops below 80% of the peak load. During this period of rapid crack propagation, the largest energy release occurs, yielding a steep drop in the stress-strain curve.[25]

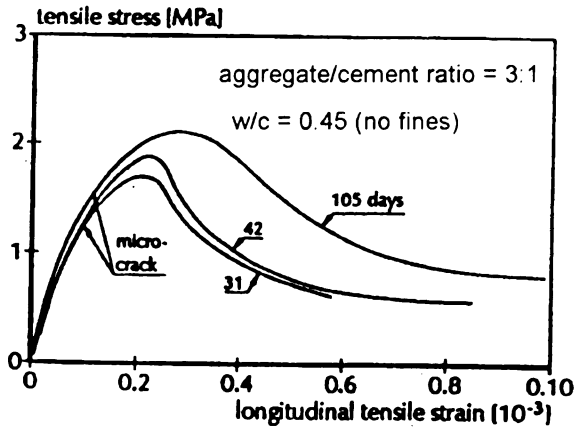

Figure 2.18 Typical Stress-Strain Diagrams for Concrete Loaded in Uniaxial Tension[1]

It is proposed that the number of microcracks in concrete specimens subjected to uniaxial tension can be obtained by dividing the energy required to open a microcrack during the multiple cracking process by the energy required to form a new microcrack.[26] The rational for this is that alters the energy state during the multiple cracking process will also alter the energy state associated with the formation of new cracks. However, the elasticity theory predicts that cracks will be initiated if actual stresses exceed the strength of the material. The eventual propagation of initial cracks cannot be determined by this theory[27] since it will predict infinitely high stresses at the sharp crack tip; therefore, microcracks propagation must be described by fracture mechanics. The fracture mechanics theory addresses the stress singularity problem by using stress intensity factors of fracture energy; microcracks are assumed to propagate when the maximum tension stress intensity factor, obtained at any crack tip in mixed mode, reaches the mode I

fracture toughness of the material containing the crack tip.[28] Microcracks will therefore follow the shortest route in a homogeneous medium or the boundary between a strong grain and the weaker paste. The microcrack may eventually take a shortcut through a strong grain if the path through the grain is significantly smaller than that along the boundary.[29] It is observed that the orientation of the majority of microcracks in concrete specimens subjected to tensile load is inclined to the loading direction. This provides an indication that although the major cracks of concrete specimens subjected to tension developed perpendicular to the loading direction, the microcracks developed in a different way.[30,31]

iii) Fatigue Load

Fatigue is a complex phenomenon associated with cyclic loading history, stress range, initial defects in concrete, and many other mechanical and environmental factors.[32] Fracture of quasi-brittle materials such as concrete is governed by the existence of a fracture zone. The fracture process zone refers to a region ahead of a crack tip, which consists of a microcracking zone and a bridging zone[33] as shown in Figure 2.19 In the microcracking zone, initiation of microcracks and their growth are dominant. The bridging zone is a part of macrocrack along which stress is transmitted by aggregate or fiber reinforcement.

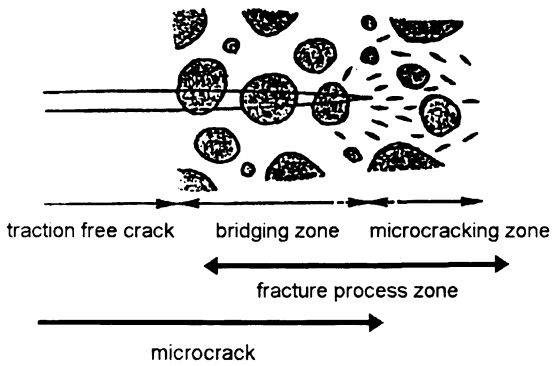

Figure 2.19 Schematic Illustration of The Fracture Process Zone[32]

The width of fracture zone increases with increasing maximum aggregate size provided that the stiffness and strength of aggregate is larger than that of cement matrix, because the size of microcrack overlaps is governed by the aggregate size.[34] The post-peak cyclic behavior of concrete in tension has been investigated and ploted[35] as shown in Figure 2.20 It is shown from the figure that the cyclic tension-softening behavior is complex and includes many characteristics, one of which may be responsible for fatigue crack growth.

The fatigue strain of concrete can be divided into three parts: irreversible strain caused by cyclic creep under the action of average stress, irreversible strain caused by fatigue microcracks, and fatigue strain range[29]. It is also reported that the unilateral behavior of damaged concrete is related to the change in sign of the applied load [36] and most of concrete specimens failed under fatigue loads in the splitting mode.[37]

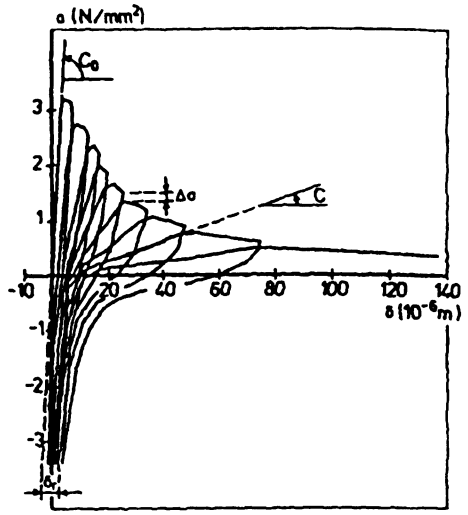

Figure 2.20 The Stress-Deformation Relation Under Cyclic Tensile Load[35]

B) Environmental Effects and Dimensional Movements

i) Frost and Freeze-Thaw

Hardened concrete may be damaged by frost action particularly if it is subjected to freeze-thaw cycles typical of the northern temperature latitudes. It is reported that when concrete specimens are subjected to freeze-thaw cycles, the number of microcracks is increased compared to the sound specimens.[38] Figure 2.21 shows images taken at 50X for concrete specimens before and after exposure to freeze-thaw cycles. This figure shows that there are clearly more numerous microcracks in the cement paste subjected to freeze-thaw cycles, with most microcracks passing through paste and following the boundaries of larger aggregate particles.

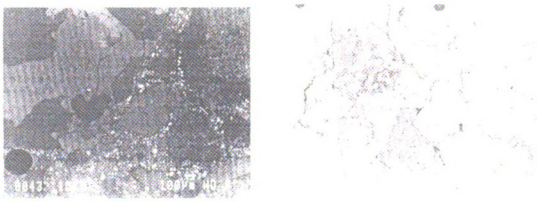

Figure 2.21 SEM Micrograph for Concrete Specimen Before and After Freeze-Thaw Deterioration[38]

It is also reported that after exposure to freeze-thaw cycles, the measured microcracks densities correlated fairly well with the measured durability factors. In most deteriorated concrete specimens subjected to freeze-thaw cycles, microcracks form patterns with average grid size of 400-500 μm and widths ranging from 1 to10 μm were observed.[39]

The use of de-icer salts in freeze-thaw conditions can lead to scaling. The damage usually starts with a superficial flaking of the surface layers resulting from development of irregular microcracks sub-parallel to the exposed surface. As damage becomes more severe, significant spalling of exposed surfaces occur along edges.[10] The difference in damage between freeze-thaw and salt-scaling is detected based on the distribution of microcracks. Concrete specimens which are subjected to freeze-thaw cycles contain

uniformly distributed microcracks, while salt-scaling damage appears in the form of localized zones of substantial deterioration.[40]

ii) Shrinkage

The loss of moisture from concrete or mortar either during setting or after hardening leads to a volume shrinkage of cement paste which, if in sufficient magnitude, may lead to the development of microcracks.[10] Shrinkage of cement paste creates radial and tangential stresses in the paste as well as in the aggregate. Stresses in the particle will be in hydrostatic compression, whereas stresses in the cement paste will be in compression radially and in tension tangentially. No shear stresses will be generated due to rational symmetry. The stress level will be independent of the aggregate size, but will vary with the distance to center of grain.[41] The tangential tensile stresses generated in cement by the shrinkage paste may eventually exceed the tensile strength of cement paste. This will lead to initiation of cracks in the paste at the boundary of aggregates where stresses are highest. Microcracks in the paste radiate from the surface of the aggregate into the paste as shown in Figure 2.22.

Shear stresses are generated along the interface and will be highest near the crack where a connection between the aggregate and the paste would prevent relaxation of the strains and stresses. In addition to existing tensile stresses, shear stresses form shear cracks at the boundary, although compression stresses in the radial direction are transferred across the crack.

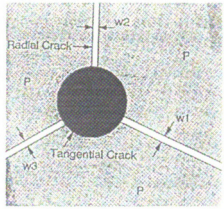

Figure 2.22 Microcracks Pattern Due to Shrinkage[41]

For high-strength concrete, microcracking is shown to increase especially with silica fume addition. This may be attributed to increased brittleness and decreased creep relaxation.[42] Adding fibers to concrete can significantly improve resistance to drying shrinkage of cracking by reducing the number of microcracks created in concrete and by arresting propagation of microcracks. Fibers with high elastic modulus, bond strength, fibers count and surface area (e.g., processed cellulose fibers) are particularly effective in the suppression and stabilization of microcracks.[43]

iii) Corrosion of Steel Reinforcement

Corrosion of steel reinforcement is the most common cause of the deterioration of concrete structures. There are two kinds of rebar corrosion,[44] chloride-induced corrosion and carbonation-induced corrosion; chloride-induced corrosion is generally the more serious one. Chlorides may exist in concrete at the time of mixing or can penetrate into

the hardened concrete later on. For the case of chloride in the surrounding environmental penetrating into concrete, a sufficient quantity of chloride ions must first be accumulated. Next, a localized breakdown of the passive film on steel occurs by the action of these accumulated chloride ions, creating a galvanic cell. The local active areas behave as anodes, while the remaining passive areas become cathodes where reduction of dissolved oxygen takes place. As steel increases its state of oxidation, the volume of the corrosion products increases. The volume of final corrosion product, $Fe(OH)_3.3H_2O$, is six and a half times that of the original Fe.[45] This expansion resulting from corrosion of reinforcement causes microcracking and spalling inside concrete; bonding between steel and concrete is also lost and the steel reinforcement itself is weakened. The first indications of reinforcement corrosion are fine microcracks, followed by unsightly brown rust stains reflecting the pattern of the underlying reinforcement on concrete surfaces.[10] As damage progresses, staining becomes more severe, cracks widen and propagate, and segments of concrete overlying the corroding steel are spalled off.

iv) Alkali-Aggregate Reaction

The alkali-aggregate reaction is the expansive reaction of sodium and potassium alkalis in the pore solution of concrete with minerals in aggregates. The principal source of alkalis is the cement itself, but any source of sodium or potassium can contribute to the reaction provided that the alkali can move into the pore solution of concrete and create the necessary hydroxyl ion concentrations required.[46] Alkali-aggregate reactions lead to expansion of the reactive grain. The reactions and expansions take place after diffusion of alkali and water into the aggregate, thus causing eigenstresses in the aggregate in addition

to the stress fields caused by overall expansion of the grain. Eigenstresses can lead to cracking of the paste similar to overall expansion of the aggregate, leading to formation of microcracks in the cement paste.[41] A typical microcrack pattern for an aggregate and cement paste affected by alkali-aggregate reaction is shown in Figure 2.23.

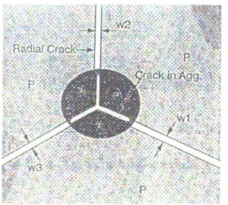

Figure 2.23 Microcrack Pattern in Case of Alkali-Aggregate Reaction[41]

If concrete specimens suffering from alkali-aggregate reaction are subjected to external loading, surface of microcracking will be magnified and the number of microcracks in the weakened matrix of concrete will be increased. It is also noticed that concrete specimens which suffer from alkali-aggregate reaction contain microcracks in both coarse aggregate and concrete matrix, that can cause bond failure throughout the cement-aggregate interfaces.[47] An optical micrograph of concrete specimen suffering from alkali-aggregate reaction is shown in Figure 2.24.

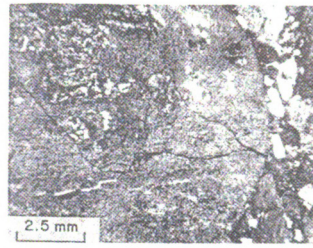

Figure 2.24 An Optical Micrograph of Concrete Specimen Damaged by Alkali-Aggregate Reaction[47]

2.2.3.3 *Effect of (ITZ) and Microcracks on Concrete Properties and Performance*

A) Effect of Microcracks on Strength and Stress-Strain Behavior

The structure of transition zone, especially the volume of microcracks and voids, has a great influence on both the stiffness and elastic modulus of elasticity of concrete. In a composite material, the transition zone serves as a bridge between mortar matrix and coarse aggregate particles.[20] Even when the individual components are of high stiffness, the composite may provide relatively low stiffness because of the broken bridges (microcracks and voids in the transition zone), which do not permit stress transfer. Characteristics of the transition zone also influence the durability of concrete. The existence of microcracks in transition zone, at interfaces with steel and coarse aggregate, is the primary reason that concrete is more permeable than the corresponding hydrated

cement paste. In general, microcracks, void spaces and oriented calcium hydroxide crystals are relatively more common in the transition zone than in the bulk cement paste; therefore they play a very important role in determining the stress-strain behavior of concrete.

It is well known that due to differential drying shrinkage and thermal mismatch between aggregate and matrix, tensile stress concentration will appear in the interfacial transition zone (ITZ) between aggregate and matrix. The relation between microcrack growth and stress-strain behavior of concrete is shown in Figure 2.25. From the figure it can be shown that microcracks generally initiate at the interface between aggregate and matrix, propagate into the matrix under load and eventually form continuous network of macrocracks around the peak of stress-strain curve (at large strains).[1]

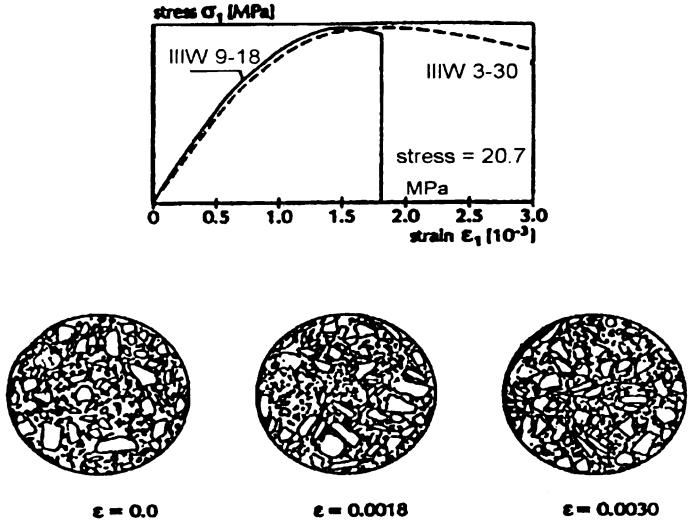

Figure 2.25 The Relation Between Microcracking Growth and Stress-Strain Behavior[1]

In fact, tensile stress concentrations will appear around any type of heterogeneity in the material structure. The simplest case is a single void or aggregate embedded in a continuous matrix. Figure 2.26 depicts the processes taking place around a single particle under load.

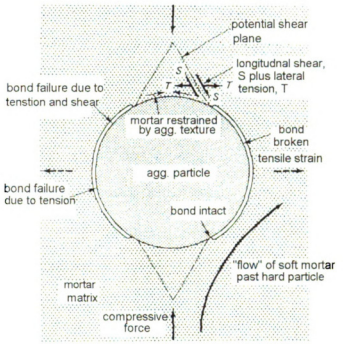

Figure 2.26 Idealization of Stresses Around a Single Aggregate Particle Embedded in a Continuous Matrix, and Hypothesized Failure Mode[19]

Figure 2.26 shows a stiff aggregate particle embedded in a soft matrix, with two interfacial microcracks developed due to differential shrinkage. Because the matrix has a lower stiffness than the aggregate, the matrix material tends to flow around the particle. Microcracks in the interfacial zone between cement and aggregate are stable; initially, and propagate only when the external load is increased to a certain level. Because of the mismatch in Poisson's ratio, the matrix material above and below the particle is confined,

i.e., a state of triaxial compression develops above and below the aggregate particle. Shear forces exist at the interface as indicated in the Figure 2.26. Fracture mechanisms can be qualitatively expressed by the following sequence at events. First, there are the de-bonding microcracks, most likely nucleated during the hardening of the concrete. Next, depending of the flow of paste around the aggregate particle, the de-bonding microcracks might be subjected to lateral splitting loads and propagate. The propagation stage stops as soon as the triaxially loaded cores are reached, and failure can proceed only through extension of shear cracks through the paste.[19] The energy for crack extension comes either from the work of external forces or from changes in the strain energy stored in concrete. This effect, combined with the arresting effect of aggregate particles, explains the extensive microcracking that takes place under load (rather than the growth of a single crack through the concrete), and also justifies the nonlinearity of the stress-strain curve of concrete. The extent of branch cracking tends to be increased by more irregularly shaped aggregate particles.

Occurrence of microcracks can also provide some changes in both peak stress and peak strain of concrete. At the meso-level, the mechanism is shown in Figure 2.27. When loading is applied parallel to the direction of casting, the orientation of the initial weak layers or microcracks is very unfavorable to propagation in a compressive stress field in the direction of casting. Under loads perpendicular to casting direction, cracks are oriented more favorably, and crack propagation may proceed much faster. The delayed and accelerated crack growth for parallel and perpendicular loads, respectively, seems to yield differences in peak strain but not so much in peak stress.

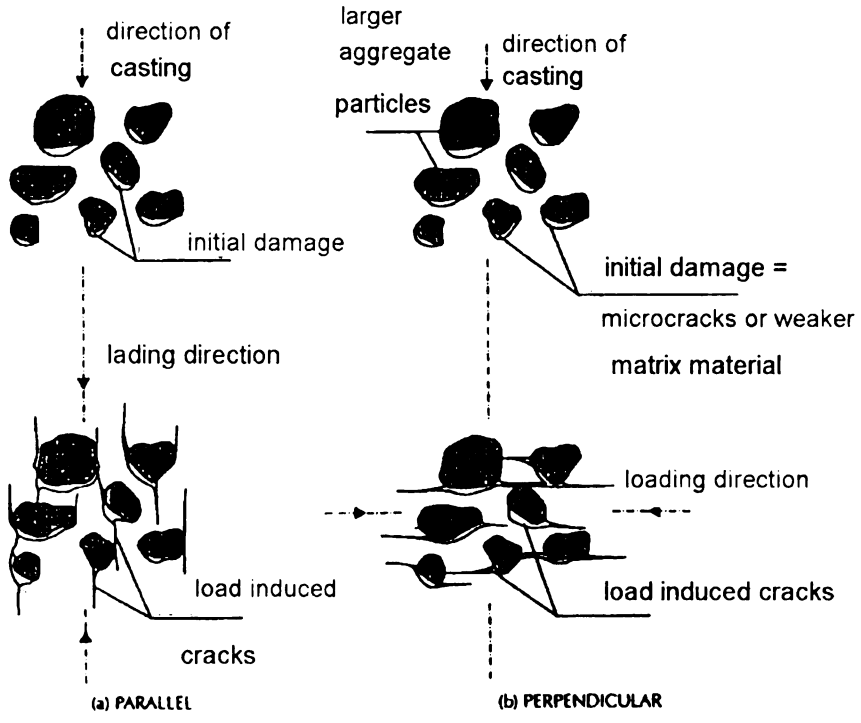

Figure 2.27 Hypothesized Micromechanisms, Explaining the Effect of Initial Anisotropy in Concrete[1]

B) Effect of Microcracks on Creep and Mass Transport Properties

Since initial microcracking may occur due to differential shrinkage, bleeding and segregation during casting, weak layers develop preferentially under the larger aggregate particles. Load-induced microcracks appear mostly at the paste-aggregate interface and then extend into the matrix as load increases. Substantial growth of microcracks occurs at stress levels between 75 and 90 percent of maximum compressive strength. Failure occurs when extensive microcracking leads to collapse of all the remaining load paths and disintegration of the internal matrix. Prior to failure, microcracks may provide an

interconnected system of "voids" that are larger than typical capillaries and create a potential path for ingress of gasses, liquids, and dissolved solids. Microcracks can thus affect mass transport properties of concrete. For higher load levels, however, mass transport properties may be increased by 20 percent or more.[48]

Concretes made with ASTM Type III cement generally show more microcracking than concretes made with other types of cement. This is due to rapid formation of C-S-H gel from Type III cement which increases the density of early-age shrinkage microcracks. Due to the formation of such microcracks, ettringite is believed to preferentially nucleate and grow in pre-existing mcirocracks.[49] The sulfate ions released from internal sources, i.e. C-S-H complex, will likely migrate to the nearest crack. Nucleation of ettingite in microcracks is sufficient to create supersaturation conditions necessary for forming ettringite, as shown in Figure 2.28.

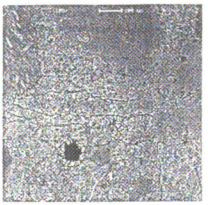

Figure 2.28 SEM Micrograph Showing Deposition of Ettringite in Microcracks[49]

Due to the accumulation of ettringite in microcracks, crack opening processes and, as a result, concrete expansion can be observed.

Creep in concrete has two different sources: microcracking and stress-induced shrinkage. Previous studies[50,51] indicated that there is a strong correlation between the basic creep of concrete to the total number of microcracks created in concrete. The effect of stress-induced shrinkage on concrete creep increases with time, while microcracking effect can be decomposed further, as shown in Figure 2.29. From the figure, it appears that the microcracking effect increases from the very beginning, reaches its maximum in about 10 days, and then decreases. This is because moisture distribution gradually approaches a uniform state. However, even after a longtime, the microcracks that have developed in the early drying process close only partly, which must be explained by irreversibility of crack openings.

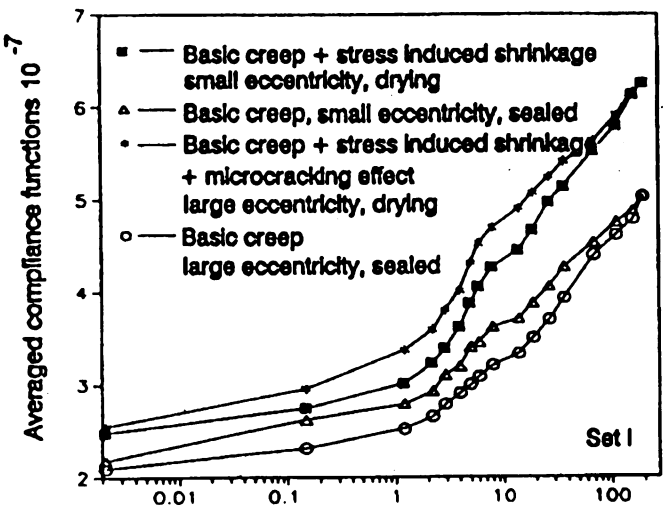

Figure 2.29 Effect of Microcracking on Creep[51]

C) Effect of Microcracks on Concrete Durability

The overall quality of concrete, especially its low permeability, reflects strongly on concrete durability. Reasonably, high cement content, low water/cement ratio and proper compaction and curing of fresh concrete are among the important factors that contribute to low permeability. Existence of tensile microcracking in concrete promotes the diffusion of aggressive agents from concrete cover to its internal structure. Tensile microcracking reduces the time that is necessary for aggressive agents to reach the internal structure of concrete through the concrete cover.[52] The kinetics of CO_2 penetration through concrete is often used to characterize durability characteristics of concrete because concrete carbonation is one of a major cause of reinforcement corrosion. Occurrence of microcracks in concrete facilitates penetration of CO_2 through concrete which contributes to corrosion of reinforcing steel. Concrete microcracks can also allows for chloride ions to reach the embedded steel reinforcement more quickly and thus reduces the service life of reinforced concrete. The past studies[53,54] have shown that the development of reinforcement corrosion is of steel reinforcement not as much influenced by the width of microcracks as it is by the frequency of microcracks.[55] For a specified range of microcrack widths normally found in concrete structures, increasing the frequency of microcracking generally increases the maximum corrosion level; for a given structure, increasing the number of microcracks increases the amount of corrosion in steel reinforcement.

CHAPTER 3

METHODOLOGIES FOR CONCRETE IMAGE PROCESSING AUTOMATION

3.1 PREFACE

Image processing and analysis require iterative application of a relatively large number of functions. Recent progress in image acquisition, processing and analysis techniques has made powerful tools available for microstructural characterization of different material systems. These techniques are now used, for instance, in the field of metallurgy to objectively quantify the microstructure and to offer a better understanding of metal charactrization.[56]

Development of statistically reliable quantitative data on concrete microstructure requires the acquisition, processing and analysis of a relatively large number of microscopic images. Automation of image processing and analysis steps can facilitate practical use of modern image analysis schemes in quantitative microstructural analysis of concrete (and development of microstructure–property relationships for concrete). The diversity and complexity of general image processing/analysis routines implies that efforts towards automation of these non-ties should be tailored towards key microstructural features of concrete. Some image elements of the automation process concern distinction between microcracks/voids, and noise removal. Selection of the key attributes of features (microcracks, voids) to be quantified and the magnification factors which best highlight these features are also key decisions which should be made in light of the particular microstructure and microstructure–property relationships of concrete. Throughout the

research study, automated image acquisition, processing, and analysis routines were performed in the context of Visilog 5.3® software system.

3.2 CRITERION TO DISTINGUISH BETWEEN MICROCRACKS AND VOIDS (SHAPE ANALYSIS)

Microcracks and voids are key microstructure features of concrete that can be resolved by microscopy techniques. The microscopic images of concrete shown in Figure 3.1, obtained through environmental scanning electron and fluorescent microscopy, indicate that both microcracks and voids are generally present in concrete images. Microcracks and voids have different effects on engineering properties; efforts to quantify these two features should thus start with distinction of microcracks from voids; their key attributes can then be quantified separately.

The shape of objects is recognized in complex ways by our visual system. Instead of using numerical values, human being eye rotates objects to the same orientation before making comparisons and deciding that features are the same or different. A particularly interesting and revealing characteristic of the visual matching of patterns occurs when similar objects in different orientation are viewed. The length of time required to make a decision as to whether objects are the same is directly proportional to their angular deviation.[57] The proposed approach, however, distinguishes microcracks from voids quantitatively, based on distinct aspects of their geometry.

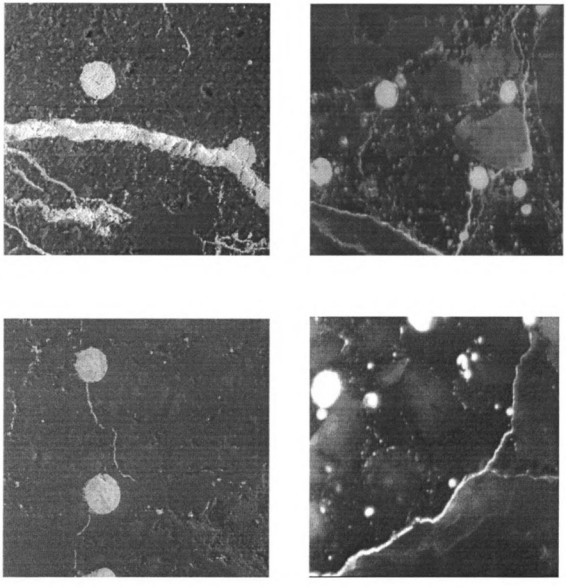

(a) ESEM Images (b) Fluorescent Images

Figure 3.1 Concrete Images Captured by Environmental Scanning Electron and Fluorescent Microscopy

Microcracks when compared with voids are elongated features with relatively high aspect (length to width) ratios. The "formfactor" (shapefactor) that distinguishes microcracks from voids is as follows:

$$Formfactor = \frac{Length\ of\ the\ object}{Width\ of\ the\ object} \qquad \text{.....(3.1)}$$

In order to determine the threshold value of formfactor (above which the object is a microcrack), 300 (environmental scanning electron and fluorescent) microscopic images of concrete were used as training image set. The images were captured at different magnifications (125X, 250X, and 500X), using different concrete mixtures. Microcracks and voids were distinguished visually; their corresponding formfactors (aspect ratios) were measured using a standard (Visilog 5.3®) image analysis software.

Total of 471 microcracks and 1172 voids were analyzed in the 300 selected images. A summary of the formfactor measurements is presented in Table 3.1. Histograms of formfactor measurements for microcracks and voids are presented in Figure 3.2 and Figure 3.3 respectively. Figure 3.4 presents mean of formfactor measurement for microcracks and voids.

Table 3.1 Statistical Summary of Formfactor Measurements for Microcracks and Voids

Statistics	Formfactor Values	
	Microcracks	Voids
Mean	73.044	1.3829
Median	80.23	1.114
Minimum value	5.6463	1.0
Maximum value	107.1	2.9631

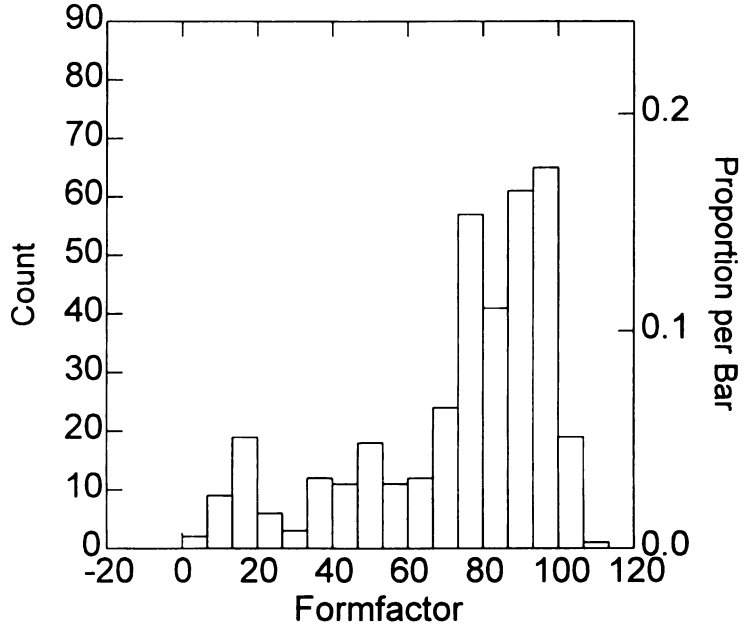

Figure 3.2 Histogram of Formfactor Measurements for Microcracks

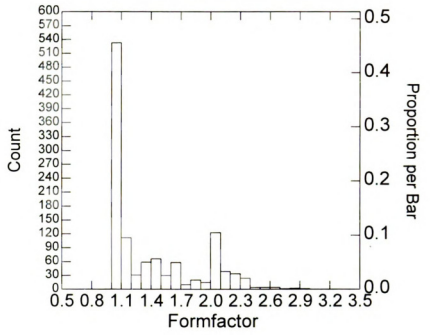

Figure 3.3 Histogram of Formfactor Measurements for Voids

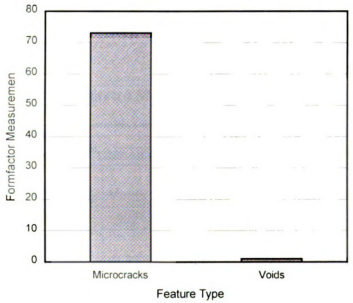

Figure 3.4 Comparison between Formfactor Measurements for Microcracks and Voids

Based on the formfactor measurements presented above, the formfactor value 3.5 is selected to be the limit to distinguish microcracks and voids. Microcracks are considered to have formfactor values greater than or equal to 3.5 while voids are considered to have formfactor values less than 3.5.

In order to validate the proposed criteria for distinction of microcracks and voids, the approach was applied to another training set of 100 images which include a total number of 439 microcracks and voids. Table 3.2 and Figure 3.5 compare the automated and visual counts of microcracks and voids. The number of automatically distinguished microcracks and voids differ form the visually identified ones by 6.38% and 3.02% respectively. These differences are considered to be reasonably small in light of the advantages of automated approach in terms of efficiency and speed of operations.

Table 3.2 Visual Vs. Automated Measurements of Microcracks and Voids

	Proposed Criterion		Visual Distinguishing		Error (%)	
Statistics	Microcracks	Voids	Microcracks	Voids	Microcracks	Voids
Number	132	307	141	298	-6.38	3.02
Formfactor values (average)	33.3	2.22	35.7	1.99	-6.60	11.4
Minimum value	3.64	1.01	3.53	1.01	3.32	0.00
Maximum value	44.7	1.63	44.7	1.58	0.00	3.03

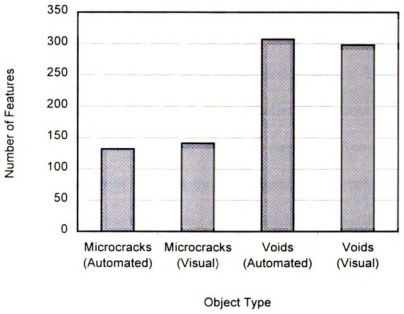

Figure 3.5 Visual Vs. Automated Formfactor Measurements

3.3 CRITERION FOR NOISE REMOVAL (SIZE ANALYSIS)

Despite all precautions taken into account during specimen preparation, still there is a large probability that captured images may contain noise from different sources. Noise can result from left over impregnating agent on the surface of the lapped specimen, uneven distribution of light under microscope, improper adjustment of the brightness and contrast of microscope, or improperly impregnated microcracks and voids. Image processing functions can be employed to remove most of the noise as shown in Figure 3.6. In order to complement the noise-removal effect of image processing functions, a criterion is developed throughout the research study to identify noise based on their distinctly small size when compared with features of interest (microcracks and voids).

After evaluating different size and shape variables, the length (the largest dimension) is chosen to distinguish noise from microcracks and voids. Length measurements of three different magnifications (using 150 training images set of each magnification) are summarized in Table 3.3 (noise, microcracks and voids are identified visually in this case). Size analysis indicated that features smaller than about 30 pixels in length are mostly noise; this threshold number of pixels can range from 25 to 35, the errors in distinguishing noise (with different threshold number of pixels) are also in identifying microcracks and voids for the training images used here are introduced in Table 3.4 and Figure 3.7. Depending on the magnification level and probably sample preparation conditions, the threshold length (in number of pixels) for distinguishing noise from microcracks and voids should be selected based on visual observations of the impact of such noise removal criteria on images.

The criteria introduced above for distinction of microcracks from voids and also noise from these features of interest are illustrated in Figure 3.8. Notations (L_n) and (W) refer to the length and width of features, respectively, and (CL_n) refers to the selected number of pixels for distinguishing noise from microcracks and voids.

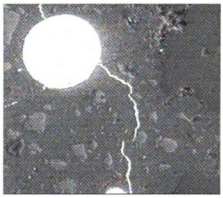

(a) The Original "Gray" Image

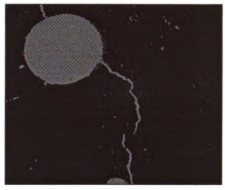

(b) The Binary Image
"Contains Some Noise"

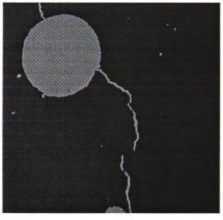

(c) The Image After Applying
Opening Function
"Some Noise Still Remaining"

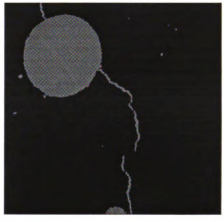

(d) The Image after Applying
Hole-Fill Function
"Some Noise Still Remaining"

Figure 3.6 The Effect of Applying Image Processing Functions to Remove Noise

Table 3.3 Lengths of Noise, Microcracks, and Voids at the Proposed Magnifications

Length (pixels)	Magnification (125 X)			Magnification (250 X)			Magnification (500 X)		
	Noise	Micro-cracks	Voids	Noise	Micro-cracks	Voids	Noise	Micro-cracks	Voids
Minimum value	2	18.4	8	2.82	29	6.72	2	29	35.5
Maximum value	106	478	612	82	756	906	165	948	745
Mean value	15.5	97.7	107	16.8	130	205	24.4	198	271

Table 3.4 The Errors (%) Associated with Different Threshold Length Values for Distinguishing Noise

Error (%)	Magnification (125X)			Magnification (250X)			Magnification (500X)		
	Noise	Micro-cracks	Voids	Noise	Micro-cracks	Voids	Noise	Micro-cracks	Voids
At 25 pixels	20.9	5.95	22	21.45	1.61	22.22	28.8	1.78	2.1
At 30 pixels	8.14	8.33	22	14.19	1.75	22.22	24.2	1.88	1.13
At 35 pixels	7.55	11.9	22	4.93	7	25.9	19.86	1.88	1.25

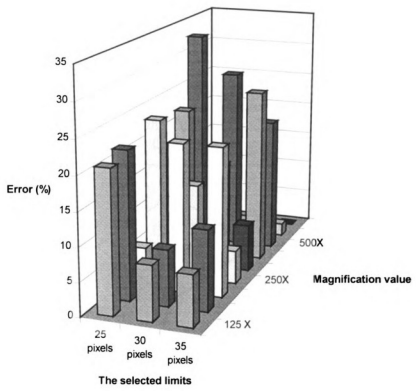

Figure 3.7 Errors in Applying The Three Selected Limit Values

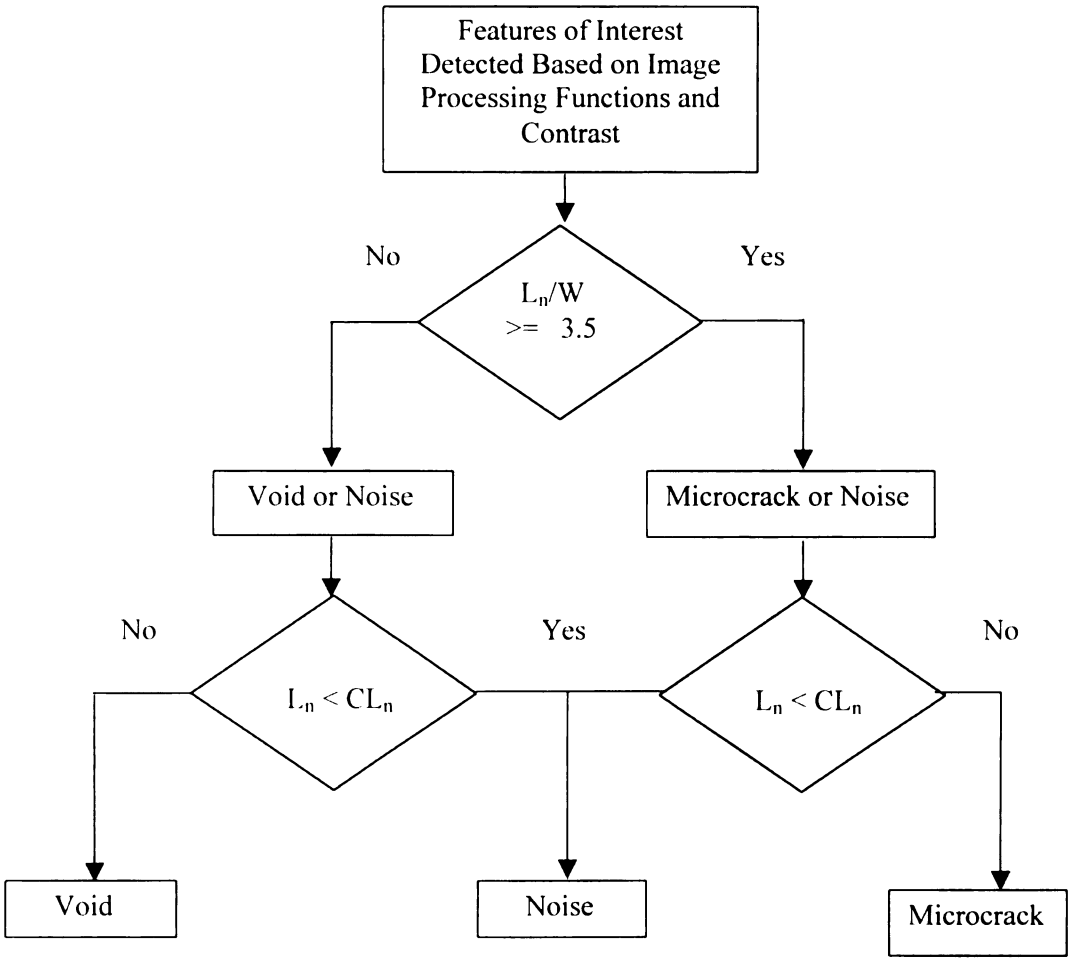

Figure 3.8 Flowchart of The Criteria for Distinction of Microcracks, Voids, and Noise

3.4 SELECTION OF THE MAGNIFICATION FACTOR

The magnification factor for microscopic analysis of materials should be selected to cover the smallest and also the largest features of interest. A minimum number of pixels should be covered by the smallest features to adequately define them. The largest features, on the other hand, should not cover too many pixels so that there would be a relatively small probability of their intersecting the edge of the field. Features larger than about 10% of the total area of the image are at some risk from these limitations. For a 512×512 image (with 262,144 pixels), the requirement that the largest and the smallest features should cover 40,000 and 100 pixels, respectively, implies that the area of features can vary by a factor of about 400 and the linear dimensions by a factor of only 20. Concrete cracks and voids cover broad linear dimensions ranging from sub-micron levels to few millimeters. So it is not possible to cover this broad range of dimensions with a single magnification factor. Therefore different magnification factors may be used for a comprehensive quantitative investigation of microcracks and voids system of concrete . The other consideration which should be taken into account for selection the magnification factors is the microscope capabilities. While environmental scanning electron microscopes (ESEM) can provide magnification values up to 60,000X optical microscopes may have strict limitations with respect to the magnification factor.[24] The particular scanning electron microscopy used in the study does not provide a full coverage of the screen with the range of magnifications low as of 125X, as shown in Figure 3.9. Furthermore, at very low magnifications, few macrocracks may be captured and quantified while the focus of the study is on quantification of microcracks. While there are no particular criteria for selection of the magnification factor in concrete

microsocopy,[58] magnification factor of 125X to 500X are generally considered reasonable for investigation of concrete microcracks system.

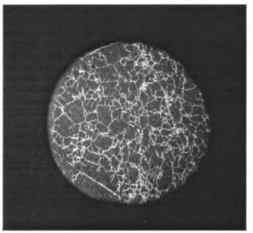

(a) Magnification 45X

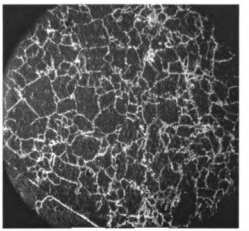

(b) Magnification 75X

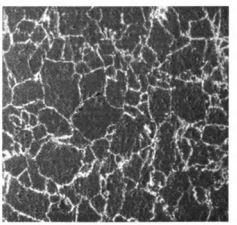

(c) Magnification 125X

Figure 3.9 ESEM Micrograph of Concrete Captured at Different Magnification Factors

The highest magnification factor used for microscopic of concrete was 500X. Most features that are of interest and can be highlighted using our sample preparation schemes can be detected at this magnification. At magnifications much higher than 500X, features of interest could be greatly affected by minor changes in such microscopy functions as well as the levels of brightness and contrast; this is especially distinct in fluorescent microscopy (versus scanning electron microscopy). The level of effort (i.e., number of images to be captured and analyzed) also increases with the magnification level, limiting the practical value of magnification factor far greater than 500X. The intermediate magnification factor 250X (between 125X and 500X) is used to detect fine features occasionally missed at 125X magnification.

Figure 3.10 shows typical concrete micrographs captured by both environmental scanning electron microscopy (ESEM) and fluorescence microscopy at the three-selected magnification factors (125X, 250X, and 500X).

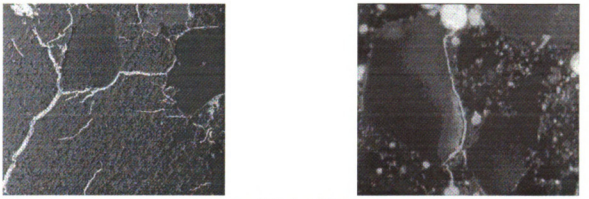

Magnification (125X)

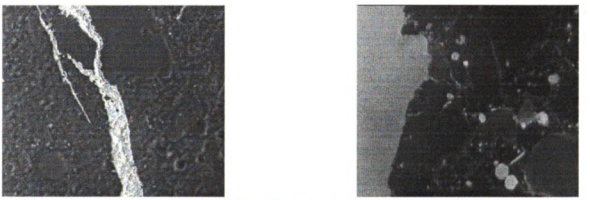

Magnification (250X)

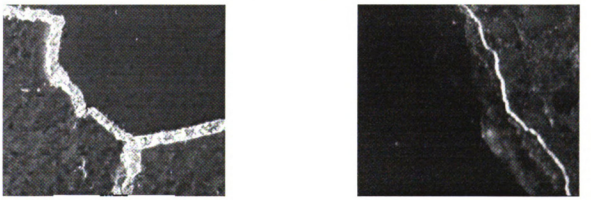

Magnification (500X)

(a) ESEM Images (b) Fluorescent Images

Figure 3.10 Concrete Images Captured Using ESEM and Fluorescent Microscopy at Different Magnification Factors

3.5 CONCLUSIONS

1- Criteria were developed to distinguish between microcracks and voids and to identify noise in concrete microscopy images. Formfactor (length–width ratio) of "3.5" was found to distinguish microcracks from voids at magnifications 125X, 250X, and 500X. Recognizing and filtering out noise (produced due to poor specimen preparation and/or setting of instrumentation) from concrete micrographs was carried out by comparing the length of features of interest with noise and addressing the critical length of the noise. The critical length ranged from 25 pixels to 35 pixels based upon the used magnification factor.

2- Different parameters and variables were selected to capture concrete images for further image processing and analysis such as magnification factor. Magnification values 125X, 250X, and 500X were selected for image acquisition.

CHAPTER 4

SPECIMEN PREPARATION FOR AUTOMATED FEATURES DETECTION

4.1 FEATURE DETECTION TECHNIQUES

4.1.1 Preface

A very important aspect of qualitative and/or quantitative microstructural analysis involves detection of objects or features of interest (microcracks and voids). Common feature detection techniques may be divided into direct and indirect methods although the distinction is not always clear.[1] Direct techniques include all optical and scanning microscopy techniques as well as X-ray measurements. Impregnation and coloring (dyeing) methods can enhance distinction of objects that are studied with different viewing techniques. Indirect techniques include acoustic emission, ultrasonic pulse velocity measurements, and various kinds of interferometry methods.

4.1.2 Current Techniques Used for Detection of Concrete Features

4.1.2.1 *Photo-Elastic Coating Techniques*

Photo-elastic layers of reflecting foil or plate can be glued to the surface of a concrete specimen, or alternatively, they can be cast as a fluid layer which solidifies with time. The layer has always a certain thickness, which is most uniform when plate material is glued to the specimen. Most of applications of photo-elastic coatings are related to finding elastic solutions for elements with complex shapes and/or complicated boundary conditions. After gluing, crack growth can be detected when the specimen is illuminated under polarized light and viewed through a polarization filter. For crack detection in

brittle solids, the method has been considered as not being very effective, and has not applied very much.[1]

4.1.2.2 *Interferometry Techniques*

The Interferometry techniques can be used to measure surface deformations of specimens under load. Traditionally, visible light has been used to illuminate the specimens, but more accurate results are obtained nowadays using monochromatic laser beams. Moiré Interferometry is a method where two girds, one obtained from the unloaded specimen and the other from the loaded specimen, interfere. It should be noted that cracking is indicated by subsequent strain-contours in the Moiré method. More accurate than the Moiré interferometry method are laser interferometry and laser holographic interferometry. The principle of the laser technique is similar to Moiré interferometry, and fringe patterns are obtained by superimposing the image of distorted specimen on a reference pattern.[1]

4.1.2.3 *Stereo-Photogrammetry Technique*

This technique has been used mainly for visualizing tension cracking. In compression, many distributed cracks nucleate and grow throughout the specimen's volume, and seem to develop into a localized deformation zone in the post-peak regime. A noted disadvantage of stereo-photogrammetry is that data processing is a cumbersome and time-consuming activity. It should be mentioned that at present the stereo-photogrammetry technique could only be used for large-deformation measurements like shear band development in concretes and soils. For measurements of isolated

microcracking, impregnation and/or coloring using dye in combination with optical observations seems to be more effective.[1]

4.1.2.4 *Acoustic Emission Techniques*

Acoustic technique is a microseismic wave generated by microcracking, microsliding and other microscopic changes in a material. Two different approaches can be distinguished, namely the acoustic emission technique (AE) where the elastic wave generated by the rapid release of energy from crack processes are measured with piezoelectric transducers,[59] or alternatively the ultrasonic pulse technique in which the deflection and reflection of acoustic signals by discontinuities in the specimen are studied in order to obtain insight into the internal crack structure of the material.[60,61]. Figure 4.1 shows ultrasonic test setup for a concrete specimen.

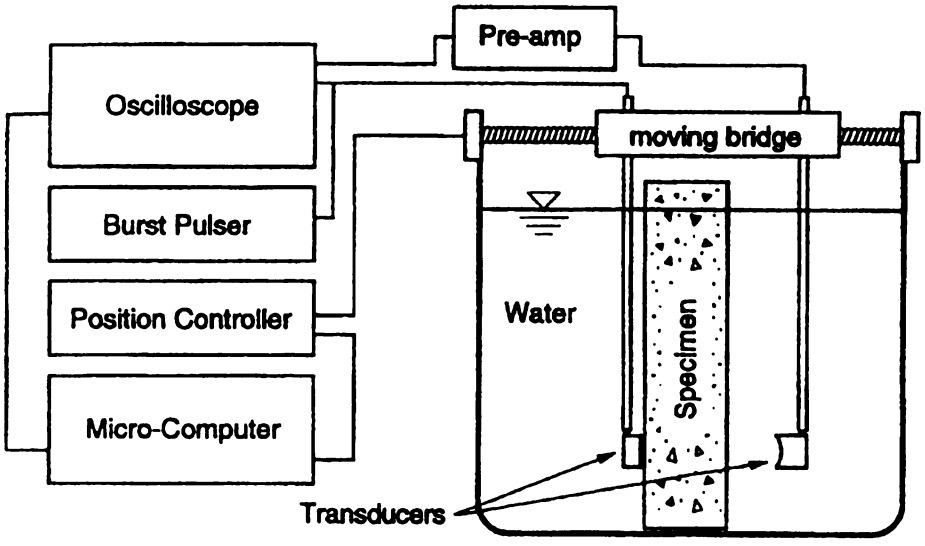

Figure 4.1 Ultrasonic Test Configurations for Concrete Specimen[60]

The main problem in (AE) studies is, however, that the physical mechanism underlying the acoustic signals is not all clear. In general (AE) techniques seem suitable for gathering information about the interior crack processes in a specimen under load. Past studies have shown that the ultrasonic pulse technique can possibly be used to locate cracks and to investigate the crack growth mechanisms.[62] For example, the departure and arrival times at a great number of different transducers can be measured and, through reverse analysis, the location and width of a crack could be determined. The technique is also used, by observing different velocities in different directions, to confirm that crack growth in concrete under uniaxial compression is highly anisotropic. The acoustic emission technique has also been used to detect reinforcing steel corrosion in concrete. The method depends on the fact that when corrosion products are formed on a corroding rebar, they swell and apply pressure to the surrounding concrete. Microcracks will be generated during the expansion process when the pressure is high enough to break the interface layer. The growth of microcracks is directly related to the amount of corrosion products on a corroding rebar. Thus, by detecting the (AE) event rate and their amplitude, the degree of corrosion can be interpreted.[63]

4.1.2.5 *Neutron Radiography Techniques*

Neutron radiography is usually used to analyze the internal damage in concrete caused by externally applied loads (i.e. to record the incidence of microcracking resulting from applied loads). The output of this technique is a black and white photograph indicating the presence of microcracks as white lines on a dark background, which can be analyzed by a number of techniques to obtain quantitative microcrack data. The cumulative length

of microcracks can be measured directly from the radiographs.[48] Figure 4.2 shows a neutron radiograph of concrete; neutron radiography technique has been used successfully to detect microcracks in concrete specimens subjected to compression loads. The effects of load eccentricity on concrete microcracking has been studied using the neutron radiography technique.[24]

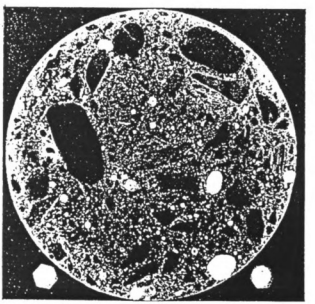

Figure 4.2 Neutron Radiography of Concrete Specimen[48]

4.1.2.6 *Mercury Intrusion Porosimetry Techniques*

Mercury intrusion porosimetry is used extensively for determining capillary pore size distribution within concrete. The concrete specimen has to be dry in order to obtain accurate results. This technique is effective for characterization of capillary pores[64], but the problem is that the volume of "bottleneck" pores will be included in the fine porosity

since the pore size is derived from the pressure needed to squeeze mercury through constrictions; as a result an error may be produced.

4.1.2.7 *Infrared Thermography Techniques*

This non-destructive technique is mainly developed to study damage processes in concrete.[1] Infrared thermography uses a photovoltaic detector in combination with advanced electronics to detect the energy radiated by the specimen during microcracking. All matter radiates energy in the form of charged particles that are accelerated constantly. The temperature of materials increases when the acceleration of particles is larger. This detection system translates the radiated energy into a real-time thermal picture, in which temperature variations of 0.2°C are visible.

4.1.2.8 *X-Ray Techniques*

X-ray diffraction spectrometry is commonly used long time ago for direct identification of crystalline phases in substances.[10] X-ray techniques was used in 1960 for crack detection[1] but only the largest cracks could be made visible. More recently, the technique has been used for studying internal crack growth around reinforcing bars. A contrast medium is needed for concrete. Experiments with different types of barium sulfate and organic iodine showed that an aqueous solution of the latter (440mg/ml) could be effective for the purpose of crack detection. Injection holes are essential to bring the contrast medium into the specimen's interior. The results clearly show the growth of fine cracks initiate from the lugs (deformation) at the reinforcing bars.

4.1.2.9 *Scanner Techniques*

Scanners are mainly used for the purpose of void analysis in concrete. Throughout the use of scanners, digital images of concrete surfaces are used to produce new images, where each pixel is classified as air void, hardened cement paste, or aggregate. Specimen surface preparation is needed for effective scanning.[65] Special precautions should be taken to ensure that the polished surface and the glass flatbed scanner surface are both free of any stray particles of lint or dust that may prevent the sample from resting perfectly flat upon the scanner. The main disadvantage of using scanners for image analysis is that they cannot produce images with high-resolution quality. Figure 4.3 compares the performance of an ordinary flatbed scanner, a high quality flatbed scanner, and an optical microscope. It is obvious that the resolution of scanners is inferior to that of optical microscope.

4.1.2.10 *Microscopy Techniques*

While other techniques can provide easy and high resolution views of features of interest, microscopy techniques seem to provide the best means of detecting features, especially in concrete materials. Different microscopy techniques are used for detection of features in concrete.[10] These techniques are introduced in the following:

A) Optical Microscopy

Conventional optical microscopes are simple to use and have broad laboratory applications. The most common type of optical microscope, is the low-power stereo microscope.[10]

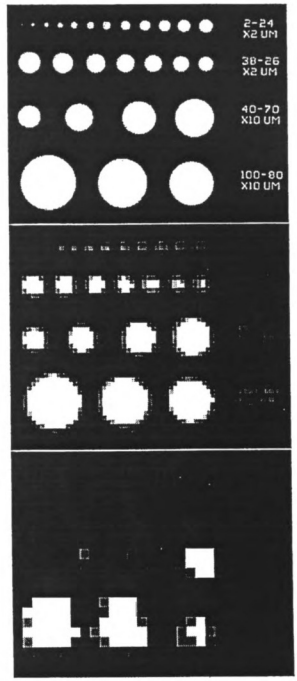

Figure 4.3 Resolution of an Optical Microscope, a High Quality Flatbed Scanner, and an Ordinary Flatbed Scanner[65]

For manipulative procedures, the stereo microscope with its crisp, erect image is an excellent tool. Thus it is commonly used in concrete petrography and air void analysis. Optical microscopes have the advantage that wet specimens can be viewed. The field of view is, however, very small and, the distance between the optics and the specimen surface is also generally rather small, which makes direct observation of cracking rather tedious.[1] In order to view specimens from larger distances, universal polarizing microscope may be used. The polarizing microscope is designed to analyze light transmitted through or reflected from substances; this requires strain-free optics aligned with the optic axis of the microscope.

B) Confocal Microscopy

The most common type of confocal microscope is the tandem scanning microscope.[66] It consists of a Nipkow disk drilled with hundreds of holes (50 μm diameter). Screening of the sample is realized in confocal microscopy by the disk rotation. At any time, several holes are lightened by a white source for the sample surface to receive incident beams. The reflected rays will pass back through the disk only if their meeting point with the material is exactly situated in the focus plane. In this condition, at each position of the stage, the sensor (CCD camera) observes the level line situated in the focusing plane, i.e., the intersection of this plane with the sample surface. Relief of the sample is then acquired by moving the programmable stage step-by-step along the z axis. The observed surface is then associated with a topographic image as shown in Figure 4.4.

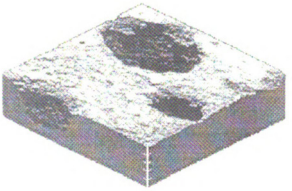

Figure 4.4 Topographic Image of Concrete Sample[66]

C) Acoustic Microscopy

The acoustic microscopy operates by launching ultrasound rays into the material specimen and detecting the reflected specular rays. The acoustic probe consists of a piezoelectric transducer (ZnO film) located on top of a sapphire lens. The acoustic signals are generated in a pulse mode to enable the transducer to function both as transmitter and receiver. The acoustic waves generated by the transducer are channeled through the sapphire lens and a coupling fluid, typically water, and brought to focus on the sample. The waves reflected by the specimen return through the sapphire lens to the transducer, where they are detected.[67] Further development of specimen preparation techniques is necessary for practical use of acoustic microscopy.

D) Fluorescent Microscopy

Fluorescent microscopy involves exciting the specimen to fluoresce by absorption of the

shorter wave length of light, usually ultraviolet light, and observing this fluorescence under microscope. If the detail of interest does not fluorescence naturally, which is often the case; it is preferentially stained with a fluorescent dye or stain. Traditional use of dye in concrete has the disadvantage that it can obscure fine detail of interest in voids and cracks;[10] traditional use of fluorescent microscopy has been restricted to the estimation of porosity, outlining porous areas and very fine microcracks which may not be otherwise observable.[64]

E) Scanning Electron Microscopy

Both conventional scanning electron microscope (SEM) and environmental scanning electron microscope (ESEM) are now widely used in various branches of science. Both (SEM) and (ESEM) have two modes of operation that are of importance. The first of these is the ability to produce images of surfaces in the range of 50X to 50,000X[10] with sufficient depth of field to give a three-dimensional effect. The second is to use the electron beam production of X-rays which allow analysis of volumes as small as 1μm in diameter. However, the electron beam only penetrates a few microns below the surface so that analyses are essentially restricted to surface material, and accuracy is thus vitally dependent on the quality of the polished surface. It should be noted that this is not an analysis of mineral phases as in X-ray diffraction, but an analysis of elements.[10]

Scanning electron microscopy has been successfully used to investigate the fracture surface of concrete.[68] The main difference between (SEM) and (ESEM) is that scanning wet specimens becomes a problem in case of (SEM), but not (ESEM) which requires a much lower vacuum is needed and thus a substantial part of the surface moisture remains

in specimen and allows for studying concrete specimens under wet conditions.[1]

4.1.3 Selection of the Feature Detection Technique

Microscopy is the chosen technique to be used for the research study because observation of features provides a reliable means of identifying and quantifying the features of interest (microcracks and voids) within the complex microstructure of concrete. Alternative techniques are limited in their resolution (which is required for image processing and analysis), sensitivity in detection of features, and the ability to distinguish between different features (microcracks and voids). Other techniques also require special and strict precautions and additional sensitive tools. Microscopy is also amendable in mass production, allowing processing a relatively large number of samples which is essential for production of statistically viable quantitative data on concrete microstructure. Both ESEM and fluorescence microscopy techniques were used throughout this investigation.

4.1.3.1 *Environmental Scanning Electron Microscopy*

Environmental scanning electron microscopy is now used extensively in materials science and has many applications in cement and concrete petrography. ESEM provides concrete researchers with a tremendously powerful tool capable of providing vivid images of the concrete microstructure at diverse maginifications.[10] Images from ESEM are monochrome since they rely on the electron or X-ray flux resulting from the beam/specimen interaction.[64] ESEM allows examination of surfaces of practically any specimen, wet or dry, insulating or conducting, because it allows the introduction of a

gaseous environment in the specimen chamber.[69] The great advantage of ESEM (compared to conventional scanning electron microscope) is that a much lower vacuum is needed; therefore, a substantial part of the surface moisture remains in the specimen and allows for investigation of the structure under moist conditions. Therefore, ESEM provides the capability to evaluate concrete specimens in ambient condition; this eliminates any potential damage to concrete samples associated with the drying process needed in conventional SEM imaging. Figure 4.5 shows a general view of the ESEM used throughout the study.

A) ESEM Components

ESEM is composed of two main parts, column console and control console. The optics column console generates, directs and focuses the electron beam which strikes the surface of the specimen. The control console is used to operate the ESEM.[70]

The column console consist of electron gun, the source of the primary electron beam, (typical accelerating voltage of 20KV was used for image acquisition throughout the study), beam alignment coils (used to direct the primary beam in both the X and Y axes), condenser lens (causes the electron beam to converge and pass through a focal point, stigmator, used to compensate for astigmatism for optimum performance and resolution), scan coils (used to accomplish the movement of the beam electrons to scan the specimen), objective lens (used to focus the electron beam by further demagnifying and converging it at the specimen surface), and image shift coils, used to accomplish the

control for beam shifting and directing). The column console is connected to the specimen chamber.

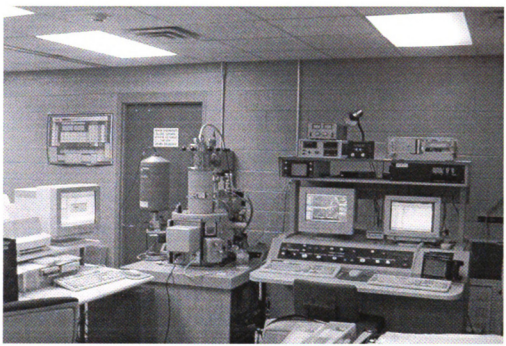

Figure 4.5 General View of Environmental Scanning Electron Microscopy Used in The Investigation

The specimen chamber is a multi-faceted cylindrical assembly located below the electron optics column. Most modern ESEM chambers can take samples as large as 200×200×75 mm.[10] The specimen stage is attached to the inside of the specimen chamber door. The specimen stage is a computer-controlled mechanical device which allows the sample under study to be moved relative to the electron beam. Figure 4.6 shows a cross section

through the column console.

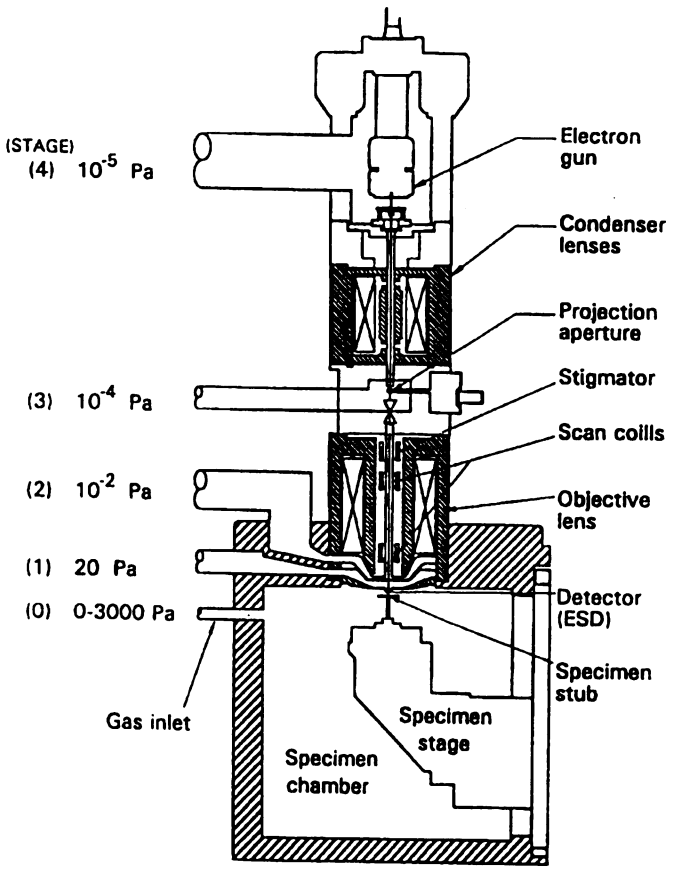

Figure 4.6 Cross-Section Through The Column Console[69]

The control console consists of front panel (that allows direct control over the most often used parameters such as magnification, focus, stigmation, brightness, contrast, grab, and/or acquire, etc.), display monitor (which displays a menu-driven, interactive software

interface which is integrated with the specimen image and related graphics), and user interface control computer (which is the primary hardware/software between the user and the computer-controlled functions of the ESEM).

II – Principles of ESEM Operation

ESEM, as other optical instruments, generates information about the state of a material from the interaction of a finely focused beam of electrons striking the specimen; if measures signals resulting from the electron beam/specimen interaction.[69] The source of electron beam is an electron gun, which operates in a high vacuum environment, and which comprises a heated cathode and other electrodes. The electron gun extracts, controls and focuses the axially symmetric beam of electrons, which is then reduced in diameter (demagnified) and deflected by the optics in the lower column. Imaging with secondary electrons under ESEM pressure conditions is made by the Gaseous Secondary Detector (GSED). The GSED uses principles of gas ionization to collect and amplify the picoampere-level imaging signals originating from beam-specimen interaction.

III- Backscattered Electron Detector

The backscattered electron detector (BSED) is used to detect backscattered electrons from a sample. The primary use of the BSED is to show atomic number contrast between materials. In order to apply BSED, a plastic scintillating BSE detector should be fitted in the ESEM as shown in Figure 4.7. The primary or incident beam will penetrate the sample and be scattered, the extent of which will depend on beam energy and material density. Figure 4.8 illustrates how backscattered electrons are generated from the sample.

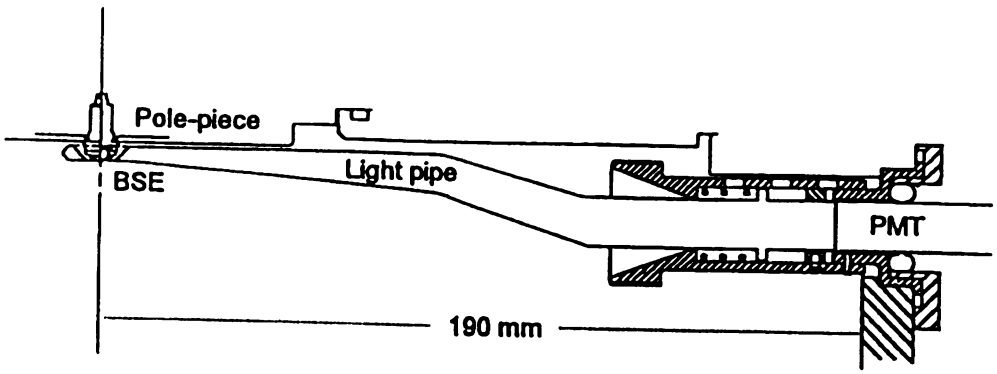

Figure 4.7 Plastic Scintillating BSE Detector with Actual Positioning in ESEM[69]

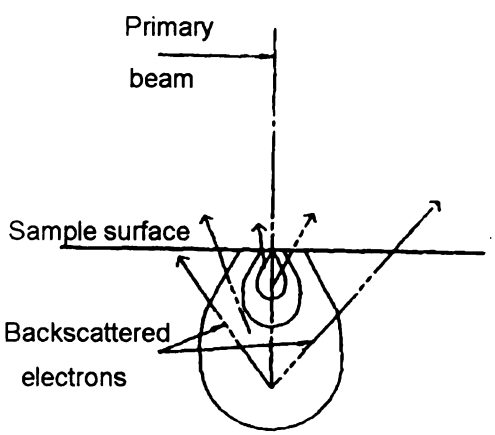

Figure 4.8 Backscattered Electron Signal[70]

Higher acceleration voltages and lower atomic numbers will produce deeper penetration and a larger excitation volume, thus yielding less signal than when lower voltages are used with materials containing high number contrast.[70] Therefore, BSE technique can be considered the ideal technique to detect differences in materials composition. As the average atomic number of Wood's metal is much higher than cement paste and aggregates, impregnated microcracks and voids which are impregnated with Wood's metal can be easily discriminated in BSE images. As a result, the BSE technique can be used in order to capture images of concrete rather than GSED technique. Figure 4.9 presents a comparison in the resolution of concrete images captured by ESEM following both GSED and BSED techniques.

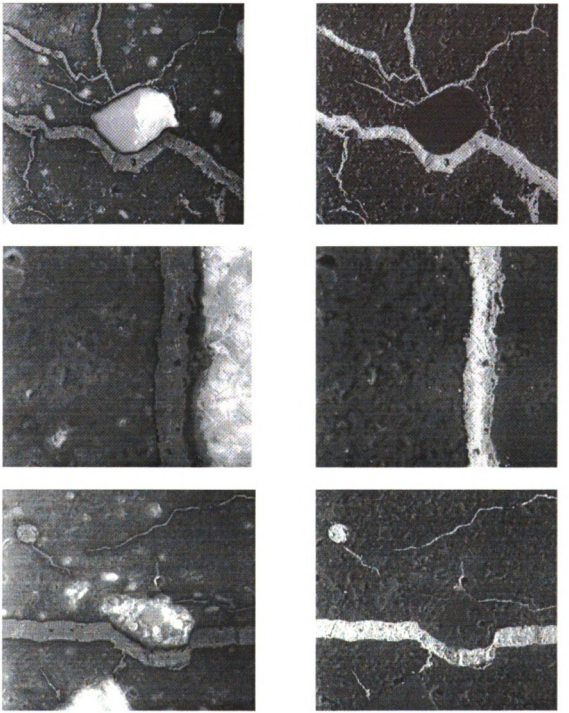

(a) GSED Technique (b) BSED Technique

Figure 4.9 SEM Micrograph Captured by ESEM in Two Different Techniques

4.1.3.2 *Fluorescent Microscopy*

Fluorescent microscope provides a simpler and lower-cost alternative to ESEM for quantitative microstructural investigation of concrete. Fluorescent microscope, unlike ESEM, does not require a specimen chamber or a certain pressure to capture images. There are currently different methods of using fluorescent microscopy in concrete petrography. Areas of high porosity can be highlighted using florescent microscopy after injection of fluorescent epoxy into concrete specimens. Since concrete materials of high water/cement ratio have higher capillary porosity, they would incorporate more fluorescent epoxy after injection; the intensity of fluorescent light under microscope thus reflects (when compared with standard samples) on water/cement ratio of concrete.[10] Crack systems can also be delineated under fluorescent microscope (after fluorescent epoxy injection of cracked concrete). Another application of fluorescent microscopy in concrete petrography involves detection of alkali-silica gel. The used applications of fluorescent microscopy, for investigation of concrete microcracks and voids systems, were carried out by "solvent yellow 43" fluorescent dye in conjunction with a 100 W quartz halogen source (which produce the required shorter wavelengths). A wide band BG12 excitation filter was used, which transmits in the blue around 350-460 nm; a k510 suppression filter was used which transmits only above 500 nm and isolates the fluorescent. Three different magnification factors were used throughout the investigation: 125X, 250X and 500X; these magnification factors were common between fluorescent and scanning electron microscopy. Figure 4.10 presents a general view of the fluorescent microscope used in this investigation.

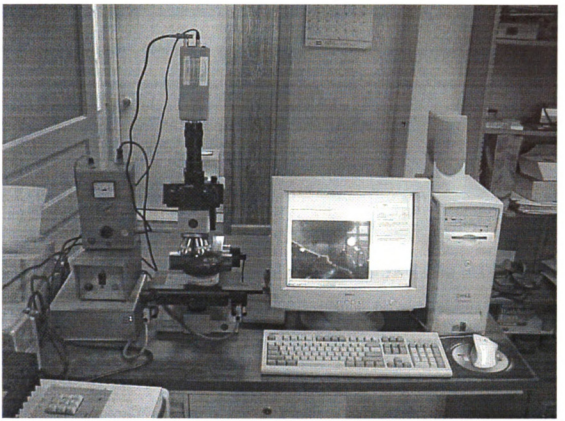

Figure 4.10 General View of the Fluorescent Microscope Used in The Investigation

4.2. SPECIMEN PREPARATION

4.2.1 Preface

Specimen preparation for the purpose of highlighting the features of interest within concrete (microcracks and voids) is of extreme importance; poor specimen preparation can lead to erroneous diagnoses of the concrete distress mechanism. Because of the rather rough character of concrete, that aspect is often neglected. However, since most of measurements are in the micron range, a very good specimen preparation is of utmost importance. This is even more important in the proposed application concerning

quantitative (in lieu of qualitative) microstructural investigation of concrete. Erroneous specimen preparation could fail to highlight some microcracks/voids or could leave residues which are confused with microcracks/voids, thereby yielding erroneous quantitative data on concrete microcracks and voids system.

4.2.2 Objective of Specimen Preparation

The objectives of specimen preparation are as follows:

1- Provide a finely ground and polished surface which yield crisp and conspicuous images and sharp edges with good differentiation between phases and objects (microcracks and voids).

2- Selectively stain particular phases and objects (microcracks and voids) in order to facilitate their identification.

4.2.3 Existing Specimen Preparation Techniques

Basically, selection of specimen preparation method depends on the type of objects to be detected and the type of microscopy technique. For environmental scanning electron microscopy (ESEM) or conventional scanning electron microscopy (SEM), an effective sample preparation technique involves impregnation of concrete with Wood's metal.[10,20] This approach provides a good contrast between features of interest (cracks and voids), which are filed with Wood's metal, ant the background. There are concerns that Wood's metal impregnation may lead to incorrect diagnoses of concrete components, for example, in the case of analyses of concrete damaged by delayed ettringite formation;[71] However, most of studies suggest that Wood's metal impregnation is an effective means

of preparing concrete samples for scanning electron microscopy. In the case of fluorescent microscopy, the most common specimen preparation technique involves epoxy impregnation, which has been used for qualitative analysis of concrete microstructure.[10,72] Despite the fact that epoxy impregnation is effective in highlight more porous areas, it cannot fill microcracks easily and accurately. Therefore, the epoxy impregnation technique has been used generally for qualitative assessment of the porosity of cement paste, and not for investigation of microcracks. Given the inadequate contrast generated by conventional epoxy dye impregnation, other techniques have been developed for improving the contrast between microcracks or voids and the cement paste or mortar. One technique[73] involves polishing and cleaning of the concrete surface, which is then impregnated with a red dye diluted in an ethanol solution. After a first impregnation, the red dye is let to penetrate the sample for 5 minutes, after which the second impregnation is performed. The excess dye is then removed after another 5 minutes by polishing the sample under water using diamond paste. This technique has some disadvantages, mainly polishing of specimen should be carefully controlled since insufficient polishing will leave an excess of colored dye and microcracks will not be easily discernible during cracks observations. On the other hand, an excessive polishing will contribute to removal of the colored dye from impregnated cracks, and will affect subsequent identification and analysis of microcracks. The red dye used in this sample preparation technique tends to penetrate aggregate pores and, as a result, identification of the crack network can be problematic especially for very porous zones. These deficiencies are detrimental to the quality of images produced using this sample preparation technique (Figure 4.11).

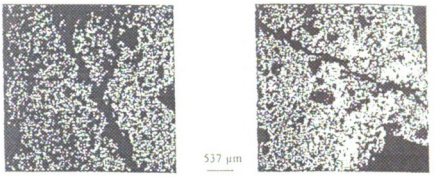

Figure 4.11 Digitized Images of Concrete Specimens Impregnated with Red Dye[73]

The fluorescent liquid replacement technique (FLR) is proposed for specimen preparation for fluorescent microscopy.[74] The technique essentially involves slow replacement of pore water by ethanol. For the purpose of implementing this sample preparation technique, the concrete specimen should be cut and polished, then immersed in a solution of ethanol and fluorescent dye for 4 days. During the four days of immersion, the fluorescent solution replaces the free water in concrete specimen. After removing from the solution, excess fluorescent dye is removed by repolishing. Ethanol is allowed to evaporate until the surface appears dry. The surface is then covered with a thin coat of fluorescent epoxy. Excess epoxy is squeezed away by pressing the coated surface of the specimen against a plane surface. The main drawback of this technique is that it takes very long period of time (4 to 5 days) to prepare only one specimen.

4.2.4 Description of the Proposed Specimen Preparation Techniques

4.2.4.1 *Specimen Preparation for ESEM (Wood's Metal Impregnation)*

The preparation starts by cutting the specimen into 50.8 mm (2 in) thick slices using a suitable electrical saw as shown in Figure 4.12. The sections should provide the maximum planar dimensions allowed by the original specimen size, steel container dimensions, and microscope chamber and travel stage. The cut sections may need to be ground by 1000 grits grinder machine in order to remove surface irregularities produced by the saw as shown in Figure 4.13. The cut sections are then washed using liquid soap and tap water in order to remove any debris attached to the specimen during the cutting or grinding process. The sections are then dried in an electrical oven at 65° C (150° F) for 24 hours to remove any water inside the specimen that may encumber the impregnation process. The dried sections are placed in a steel mold for the purpose of Wood's metal impregnation. The diameter of the steel container is 140 mm (5.5 in), and its height is (54 mm (10 in). This particular container has movable perforated steel shelves to accommodate multiple sections as shown in Figure 4.14. Wood's metal is added to the steel container at12 times the weight of concrete sections. The used Wood's metal melts at 70° C (158° F) and is solid in dry air at room temperature 20° C (68° F); it consists of 50% bismuth (Bi), 25% lead (Pb), 12.5% cadmium (Cd), and 12.5% tin (Sn). The Wood's metal has a Young's modulus of 9.7 GPa (1,400,000 psi), a density of 9.67 g/cm^3 (600 lb/ft^3), and does not go through any volume change during hardening. The container incorporating concrete sections and Wood's metal is placed inside a pressure chamber as shown in Figure 4.15. The pressure chamber should have capabilities for vacuum and pressured nitrogen gas application and also for heating. The air inside the chamber is

removed by turning the vacuum on to 6.65 KPa (0.95 psi) for 30–40 minutes. Next, the chamber is heated (under vacuum) to 93° C (200° F) for 1–2 hours in order to allow for Wood's metal melting. Subsequently, vacuum is turned off (with heat still on), and the chamber is subjected to nitrogen gas at pressure of 1.94–2 MPa (280–300 psi) for 3 – 4 hours in order to allow Wood's metal to penetrate the concrete. After turning the pressure and heat off, the specimen is let to cool down to room temperature while concrete sections are immersed in Wood's metal. Once the chamber reaches room temperature; 6 mm (0.25 in) is cut off the surface layer of the specimen in the required direction by electrical saw in order to expose an impregnated concrete surface. The specimen is then polished using polishing machine and consecutive sets of 320, 600, 1200, and 4000 grit (5–7 minutes each at 300 rpm) silicon carbide abrasive papers to obtain a smooth surface suiting ESEM investigation as shown in Figure 4.16.

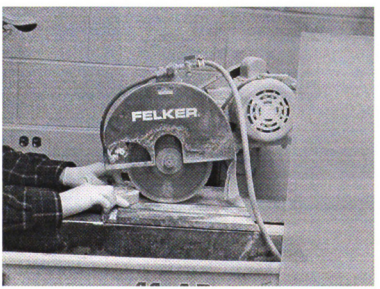

Figure 4.12 Cutting The Specimen

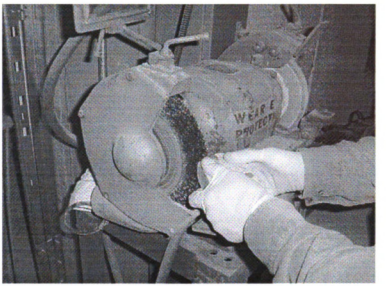

Figure 4.13 Grinding The Specimen After Cutting

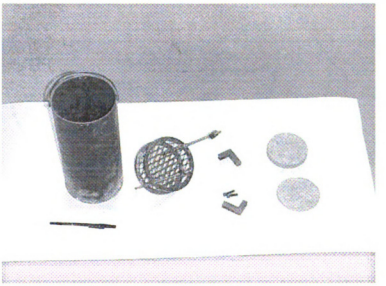

Figure 4.14 Steel Container Used for Wood's Metal Specimen Preparation

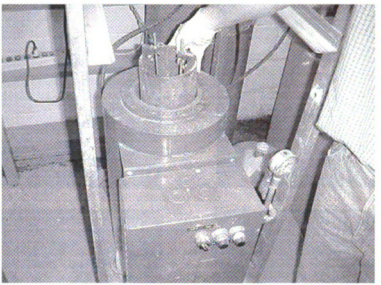

Figure 4.15 Placing The Concrete Specimen in The Pressure Chamber

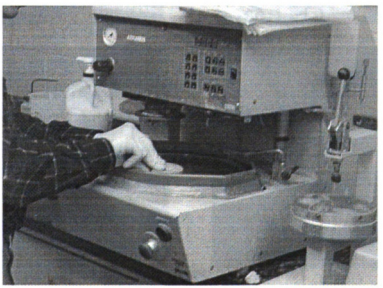

Figure 4.16 Final Lapping of The Concrete Specimen

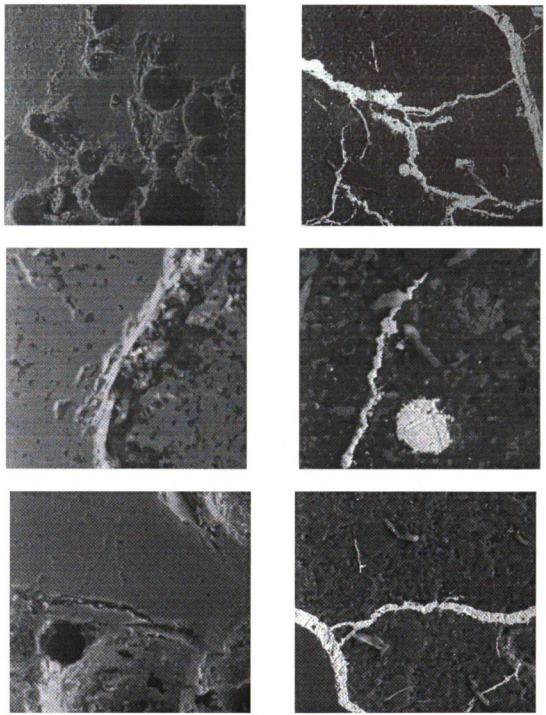

(a) Before (b) After

Figure 4.17 Concrete Micrographs Before and After Specimen Preparation by Wood's Metal

The proposed approach showed good results for concrete specimen preparation, since the captured images showed the deep penetration of Wood's metal in both very small voids and very thick microcracks and also distinctive contrast between both microcracks and voids and the background (mortar or cement paste) which can produce ease application of image processing functions and measurements with high precision. Figure 4.17 shows a comparison between concrete images captured by ESEM for concrete specimens prepared by means of the proposed approach. Form the images it can be easily noticed the difference in contrast between the concrete specimens prepared by the proposed technique and other specimens that not subjected to any specimen preparation.

4.2.4.2 *Specimen Preparation for Fluorescent Microscopy*

(Ink-Epoxy Impregnation)

As explained earlier, conventional fluorescent microscopic techniques have been employed for qualitative investigation of concrete materials impregnated with fluorescent epoxy. Figure 4.18 presents fluorescence micrograph of a concrete impregnated only with one stage fluorescent epoxy dye.

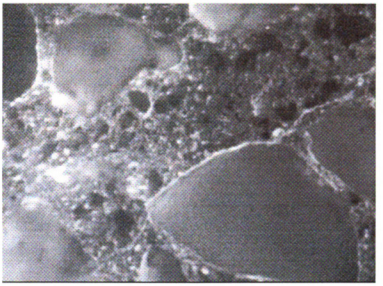

Figure 4.18 Fluorescence Micrograph of Concrete Specimen Impregnated with Fluorescent Epoxy Dye

From the figure, it can be shown conventional methods of fluorescent epoxy impregnation stain capillary pores as well as air voids and microcracks. It would this be difficult to distinguish features of interest (microcracks and voids) from the body of concrete. A two-stage impregnation technique has been devised to resolve this problem. For this purpose, fine pores (capillary pores in hydrated cement paste and aggregate pores) are not first impregnated with black ink (Parker Quink); subsequently, microcracks and air voids are impregnated with fluorescent epoxy. The low viscosity of ink and its ability to harden in this thickness result in filling of capillary pores but not microcracks and air voids in the first stage of impregnation. Figure 4.19 shows a concrete specimen impregnated using the two-stage technique; it can be shown that two-stage impregnation

technique yields a reasonable sharp contrast between features of interest (microcracks and voids) and body of concrete.

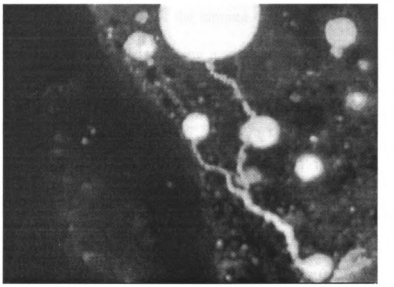

Figure 4.19 Fluorescent Micrograph of Concrete Specimen Subjected to Two-Stage Impregnation with Ink Followed by Fluorescent Epoxy

The proposed approach can be described as follows:

Stage I- Ink Impregnation

The first stage starts by cutting the specimen to 20-30 mm (0.8–1 in) slices with the required cross-sectional dimensions using a suitable electrical saw (trying to maximize cross-sectional areas, given overall specimen dimensions and microscope travel stage dimensions). The specimen may be ground using a grinder in order to remove surface irregularities produced by the saw as shown in Figure 4.13. During all the sawing and

grinding operations, special care should be taken to keep specimen surfaces moist. Once specimen surface is then lapped using an abrasive liquid comprising of 30 g (0.067 lb) vehicle 101 (Lapmaster Intl. Div.), 50 g (0.11 lb) aluminum oxide powder 1800, (Lapmaster Intl. Div.), and 450 g (0.99 lb) tap water under 0.021 MPa (3.0 psi) pressure as shown in Figure 4.20. At the end of the lapping operation, the specimen should be carefully cleaned to remove any debris using a sponge with a 50% solution of an all-purpose cleaner followed by rinsing with water at low and then high speeds. The specimen should then be cleaned in ultrasonic bath (43 KHz frequency) for 20-30 minutes in order to remove any fine particles entrapped inside the voids or the microcracks as shown in Figure 4.21. The specimen then dried in oven at 60°C (140°F) for 3-4 hours, and placed in a plastic container within a glass flask connected to the vacuum pump. Vacuum - drying of the specimen at 2.66 KPa (0.38 psi) for at least one hour (as shown in Figure 4.22) will substantially remove air from voids and microcracks. The vacuum is then turned and, from a container connected to the glass flask, black ink (60% by weight of Parker Quink – 40% water is allowed into the plastic container holding the specimen inside the flask in order to impregnate the specimen as shown in Figure 4.23. The specimen is then moved to a pressure chamber (while kept immersed in ink and covered with a wooden plate in order to prevent splashing of ink when the pressure is introduced using nitrogen gas). The specimen should be subjected to nitrogen gas at pressure of 1.94 MPa (280 psi) for 18-24 hours in order to facilitate impregnation of the capillary pores system within cement paste (and aggregates) with ink. The final step in the fist stage of sample preparation to turn the pressure off, remove the sample from pressure chamber, and place it in oven at 60°C (140°F) for 24 hours to dry the ink.

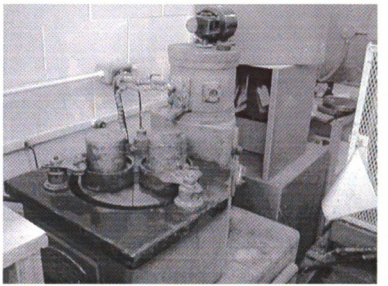

Figure 4.20 Lapping of Concrete Specimen

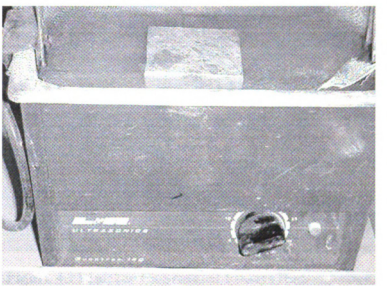

Figure 4.21 Specimen Cleaning in Ultrasonic Bath

Figure 4.22 Vacuum Drying of Concrete Specimen

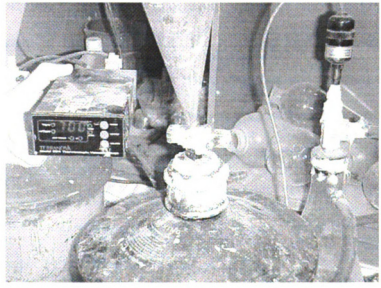

Figure 4.23 Ink (or Fluorescent Epoxy) Impregnation

Stage II- Epoxy Impregnation

The second stage starts by placing the specimen in a plastic container within a glass flask connected to vacuum source. The specimen should be subjected to a vacuum of 2.66 KPa (0.38 psi) for one hour substantially to remove air from the microcracks and the voids. The fluorescent epoxy solution is prepared by adding 3.0 g (0.106 oz) of fluorescent dye (solvent yellow 43) [AAKASH Chemicals & Dye-Stuffs, Inc.] to 30.6 g (0.0674lb) (of "DER" 736 Polyglycol diepoxide/epoxy resin) "modifier" and mixing them together, and then mixing 200 g (0.44lb) of "NSA" (455 ml Noneylsuccinic Anhydride modified), followed by 76.8 g of "ERL" 4221 Vinylcyclophene Dioxide "UC. D." "monomer" and 6 g (0.2 oz) of "DMAE" (2-Dimethylaminoethnol) "epoxy accelerator–catalyst" [SPI-CHEM Supplies]. The solution is poured in glass container connected to a glass flask. After turning off the vacuum, the fluorescent epoxy is allowed to impregnate the specimen as shown in Figure 4.23. With the specimen kept immersed in fluorescent epoxy, the specimen is placed in the pressure chamber and covered by a perforated wooden plate to prevent splashing of fluorescent epoxy dye when nitrogen pressure is applied. After closing the pressure chamber lid, the specimen is subjected to nitrogen pressure of 1.94 MPa (280 psi) for 3 – 4 hours to allow for epoxy penetration into the concrete microcracks and voids as shown in Figure 4.24. The pressure is turned off and the specimen is placed in the electrical oven at 65.5°C (150° F) for 18-24 hours. The final step in the second stage is to lap the specimen surface using a lapping machine and the previously described abrasive liquid under 0.021 MPa (3.0 psi) pressure to remove the thin film of the epoxy dye from the specimen surface to be ready for fluorescent microscopy investigation

The main advantage of this two-stage specimen impregnation, when compared with conventional fluorescent epoxy impregnation, is that ink fills and blocks capillary pores so that microcracks and air voids are highlighted with a reasonable sharp contrast against the body of concrete. In conventional (one-stage) method of specimen preparation, the capillary pores system is also highlighted through fluorescent epoxy impregnation, which is detrimental to the contrast between microcracks/air voids and body of concrete as shown in Figure 4.25, which compares fluorescent micrographs of specimens prepared using either the conventional technique or the new two-stage method. It can be shown that the advantage of two-stage specimen preparation is in producing sharp (crisp) contrast between microcracks/air voids against the body of the concrete.

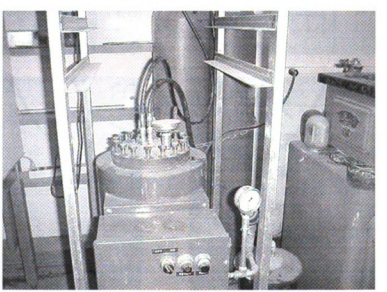

Figure 4.24 Nitrogen Pressure Application

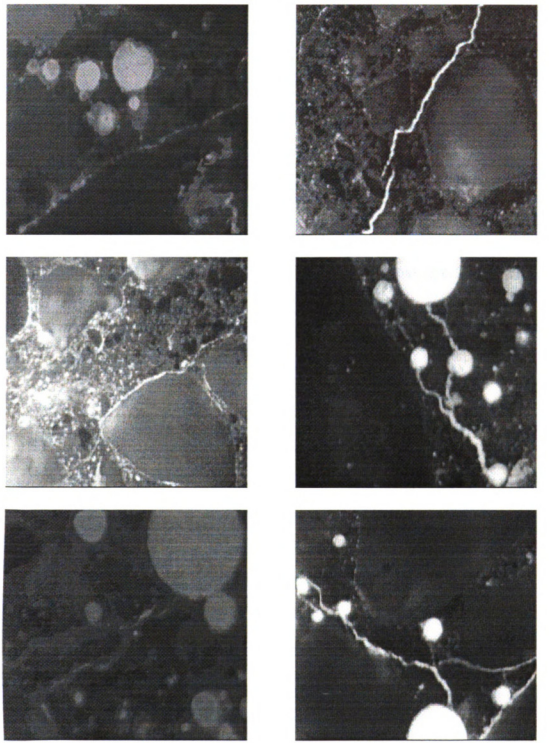

(a) Conventional (b) Two-Stage

Figure 4.25 Fluorescent Micrographs of Concrete Specimens Prepared by Conventional and The New (Two-Stage) Specimen Preparation Techniques

4.3 CONCLUSIONS

1- A refined specimen preparation technique was developed to prepare concrete specimens for SEM investigation by Wood's metal impregnation. The refined method allows to effectively impregnate more than one specimen in the same time.

2- A new two-stage specimen preparation method was developed to prepare concrete specimens for fluorescent microscopy investigation. This two-stage approach first impregnates concrete with ink, which is cured to fill capillary pores; subsequently, microcracks and voids are impregnated with fluorescent epoxy dye. The results showed good contrast between microcracks/voids and the body of concrete.

CHAPTER 5

IMAGE PROCESSING AND ANALYSIS

5.1 PREFACE

Like word processing, image processing manipulates images, rearranges them, and may make them more useful, but it does not reduce (or increase) the amount of data present.[75] The aim of image processing is to extract feature topology from the digitized images of the investigated material in order to extract quantitative information on features and phases of interest from these images. The purpose of image processing in the current research is to transform the captured images from gray scale images into binary scale images, enhance the contrast between the features of interest and the background, and to get rid of the noise in the images in order to extract the quantitative measurements of features of interest from concrete micrographs. Generally, the features of interest in microstructural investigation of concrete are microcracks, voids, aggregate, and fibers. Throughout the study, Mathematical expressions were proposed for the different features of interest, while the analysis was applied only on microcracks. There are four fundamental tasks involved in the digital image processing and analysis. These tasks can be briefly categorized as:[76]

1- Image acquisition through the digitizing instrument.

2- Image enhancement by means of removing the speckle (noise) in addition to contrast improvement.

3- Image segmentation, defined as the differentiation of the features of interest from the background.

4- Feature measurements, i.e. characterization of the features in a quantitative way.

Figure 5.1 presents a hierarchical view of image processing and analysis steps involved throughout the research study.

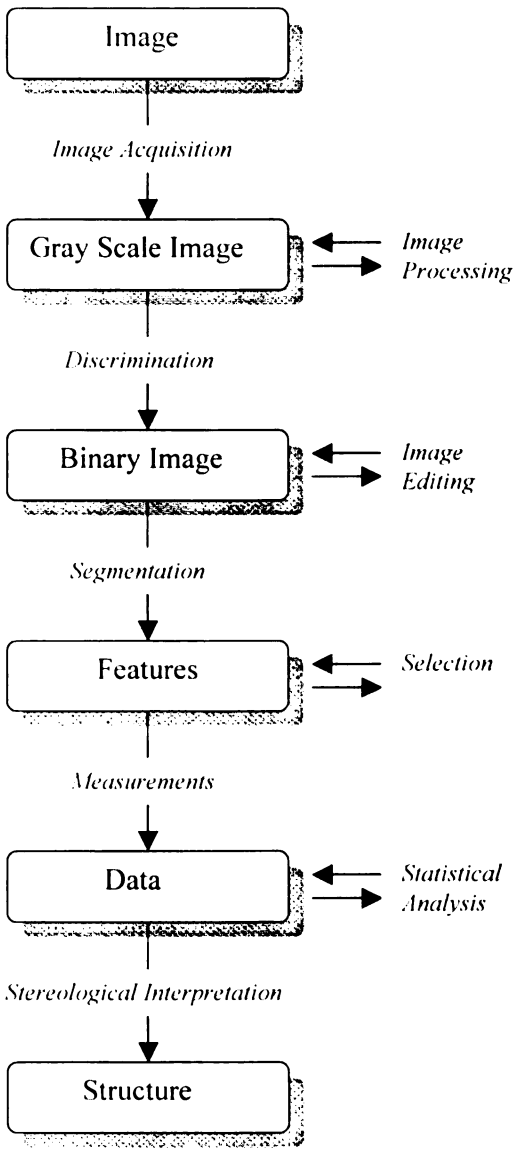

Figure 5.1 An Overview of the Steps Involved in Image Processing and Analysis

The basic step in image processing is capturing images (acquisition) by digitization from the environmental scanning electron microscopy for treatment with computers. In order to cope with the enormous amount of image data, images must be saved and transmitted in the tightest possible code. It may be necessary to correct known disturbances in the image (image restoration). Likewise, brightness and contrast of the image can be optimized. Another important operation is noise reduction in non-clear images. A whole chain of processing steps would then be necessary to analyze and identify objects of interest. First, adequate filtering procedures must be applied in order to distinguish the phases and features of interest from other objects and the background. Then the phases and features of interest have to be separated from the background (segmentation). This process yields a binary image. With the exact geometric shape of the phase/feature known at this stage, the required quantitative information can be extracted.

5.2 IMAGE PROCESSING

Latest developments in microscopy and image processing techniques have facilitated efforts towards investigation of the concrete microstructure.[10,75] Given the complexity and heterogeneity of the concrete structure, development of statistically reliable quantitative information about concrete microstructure requires acquisition, processing and analysis of a relatively large number of microscopic images. Automation of image processing and analysis procedures can facilitate practical use of modern image analysis schemes in quantitative microstructural analysis of concrete towards development of valuable structure-property relationships for concrete. Proper image processing and analysis techniques involve diverse and complex routines; practical use of these

techniques with concrete requires tailoring of such routines to suit concrete microstructure. The work reported herein establishes Image processing and analysis routines for removal of noise, distinction of microcracks from voids and detachment of connected microcracks and voids in concrete micrographs.

5.2.1 Image Processing Functions

5.2.1.1 *Digitization*

Digitization means sampling of gray values at a discrete set of points, which can be represented by a matrix of rectangular basis cells. Environmental scanning electron microscopy commonly has several detectors, capable of producing images with the various signals produced when the incident electron beam strikes the specimen surface. The signal produced by ESEM is a voltage. For storage in the computer, this must be digitized, and this requires an analog to digital converter.[77] The used image analysis system has square image matrices (640×640), any point on this 2D is called a pixel. A pixel represents the gray value of the corresponding grid position. The total number of pixels defines the image resolution for all subsequent activities. The number of bits used to store the brightness information defines the "depth" of the image. Since computer storage is often organized in bytes (8 bits), this produces a capacity for 256 brightness or gray levels.

5.2.1.2 *Discrimination and Thresholding*

Segmentation is a process through which the image is partionated into meaningful regions by using only the intensity of the pixels. When segmentation is applied to a gray

image, the gray level intensity of the pixels which satisfy a given condition are set to one and the rest are set to zero. The converted image is referred to as a binary image where the pixels values can be presented by a single bit signaling a true or false situation (feature of interest or not). Segmentation by brightness thresholding is the simplest approach where a contrast gray level is used as the threshold value, therefore, it is widely used method of converting a gray scale image to a binary (black and white) one as shown in Figure 5.2.

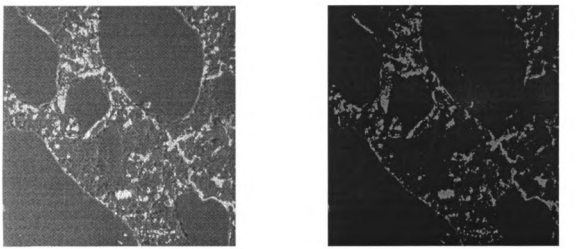

(a) Gray Image (b) Binary Image

Figure 5.2 Effect of Applying Thresholding Function on Gray Image

Discrimination with threshold values is much more efficient than any edge following or region growing method because it works on the entire image at once. Hence the time required is fixed, regardless of the complexity of the image, and very short. Also, the

resulting binary image is a pixel-based representation of features of interest, and is easier for most measurements operations than the boundary representation that results from the location and identification of edges.[78,79] In the simplest version of brightness discrimination, there are two threshold methods; manually and automatically and three different types of thresholding; threshold by factorization, threshold by entropy, and threshold by moment.[78] All pixels whose brightness values lie between these thresholds are considered to be part of the features of interest (microcracks and voids), and all others are considered to be background. In other words, microcracks/voids and cement paste are separated.

Due to the large variations in intensities between images taken from the same section and also due to the large variations of intensities between sections of the concrete specimens, the magnitude of threshold varies from image to image and for the purpose of automation, applying automatic threshold throughout the research study is considered to be the best solution for such large variation. A comparative study is done to check the ability of using automatic threshold rather than manual threshold and also to determine the suitable auto-threshold type for each specimen preparation technique and its microscopy type. One hundred images (containing microcracks and voids) were captured from specimens prepared by the pre-described specimen preparation techniques by both ESEM and fluorescent microscopy at different magnifications (125X, 250X, and 500X) as a training image set and both manual and automatic threshold functions were applied. The low threshold level is set to be zero (default value) for automatic threshold and the program determines automatically the best threshold level for the image. Throughout manual threshold, the optimum high threshold level is determined by comparing the

original (gray) image and the image after applying the manual threshold (binary) image. When the features (microcracks and voids) are correctly highlighted and the most distinction between microcracks and or voids and concrete background is obtained (are well separated from the body of concrete); this value is considered to be the optimum manual threshold level. The three different types of automatic threshold function are applied on the same image, the high threshold level for each type is obtained directly from Visilog 5.3® software throughout applying automatic threshold. Results of the comparison are illustrated in Tables 5.1 and 5.2 and Figures 5.3 and 5.4.

Statistical analysis (comparison of means) between the low gray level of manual threshold function and the three types of automatic threshold functions showed that there is no significant difference between manual threshold and automatic threshold (factorization) function for both ESEM and fluorescent micrographs.

Statistical analysis also showed that there is a significant difference between manual threshold and automatic threshold (entropy and moment) at 95% and 98% level of confidence respectively for ESEM micrographs and at 91% and 98% level of confidence for fluorescent micrographs.

The effect of applying manual, and automatic (factorization for ESEM micrographs), (entropy for fluorescent micrographs) threshold functions on some of the captured images is shown in Figures 5.5 and 5.6.

Table 5.1 Comparison Between Manual and Automatic Low Threshold Levels for ESEM Concrete Micrographs

Comparison	Threshold Function			
	Manual	Automatic		
		Factorization	Entropy	Moment
Minimum	101	107	68	73
Maximum	183	225	181	201
Mean	145	153	101	110
Std. Dev.	27.7	23.9	26.6	21.8

Table 5.2 Comparison between Manual and Automatic Low Threshold Levels for Fluorescent Concrete Micrographs

Comparison	Threshold Function			
	Manual	Automatic		
		Factorization	Entropy	Moment
Minimum Value	76	88	99	61
Maximum Value	201	238	244	241
Mean Value	186	197	222	165
Std. Dev.	31.2	33.7	38.8	35.6

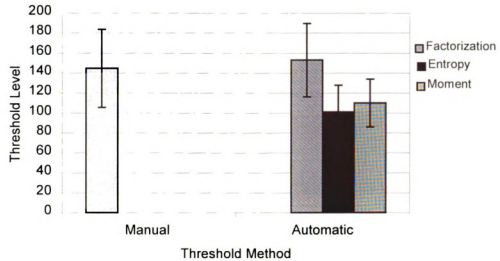

Figure 5.3 Threshold Levels for Both Manual and Automatic Threshold Functions for ESEM Concrete Micrographs

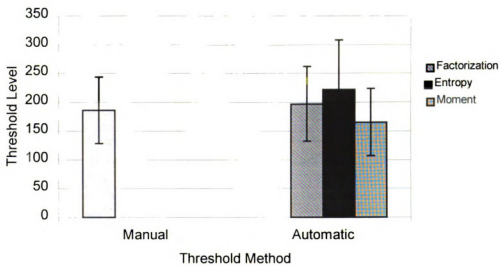

Figure 5.4 Threshold Levels for Both Manual and Automatic Threshold Functions for Fluorescent Concrete Micrographs

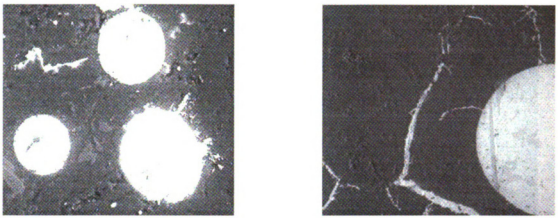

(a) Original Gray Images

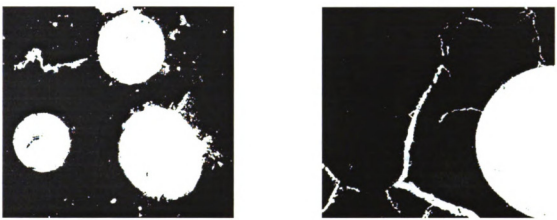

(b) Manual Threshold Function

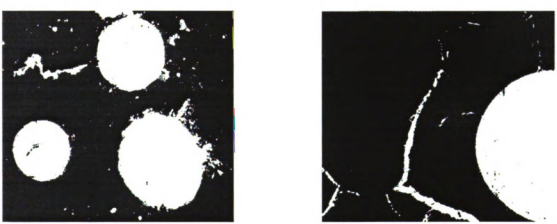

(c) Auto-Threshold Function

Figure 5.5 Comparison between Manual and Automatic (Factorization) Threshold Function on ESEM Concrete Micrographs

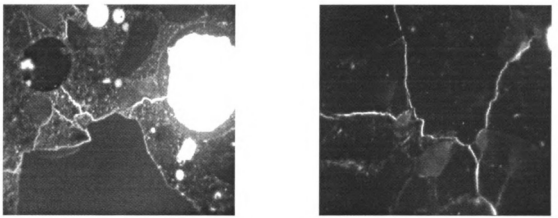

(a) Original Gray Images

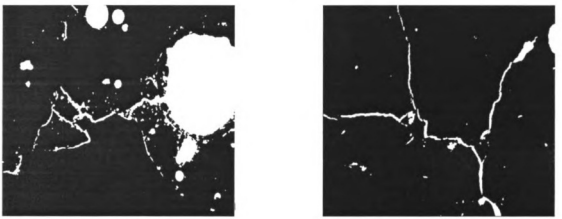

(b) Manual Threshold Function

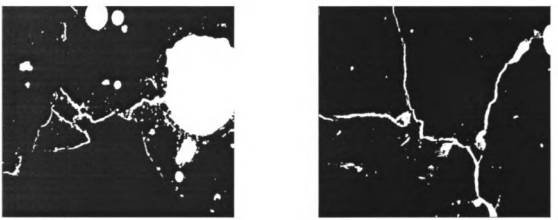

(c) Auto-Threshold Function

Figure 5.6 Comparison between Manual and Automatic (Factorization) Threshold Function on Fluorescent Concrete Micrographs

5.2.1.3 *Morphological Operations*

After applying segmentation process (threshold function), pixels belong to the features of interest may be known. Prior to performing the quantification step, another class of neighborhood operations may be applied to refine the form of objects. Such operators, which relate pixels in a small neighborhood, are versatile and powerful tools that combine pixels of binary images with logical operations of Boolean algebra. These operators cause dilation or erosion of objects. Dilation has different effects, including filling of small holes or cracks and smoothing of contour lines. Erosion caused disappearance of objects smaller than mask governs the effect of operators; for example, an erosion operation works hide a net which has holes in the shape of the mask. All objects smaller than the hole will slip through and disappear from the image. So in its simplest form, erosion consists of examining each binary pixel and changing it from "on" to "off" if it has any neighbors that are off. It is important to specify which neighbors are considered. Visilog 5.3® software usually uses all 8 neighbors in the case of square pixels by default. Erosion reduces feature all around their periphery. It is a global operation working on the entire image at once. The effect of applying erosion function with different number of iterations on binary ESEM and fluorescent concrete micrographs is illustrated in Figure 5.7.

Dilation is the converse of erosion. Mathematically, dilation is performed by change any "off" pixel to "on" if it has at least one "on" neighbor. This cases features to grow (or dilate) in size, which will fill in small breaks in features, internal voids, or small indentations along the feature surface. The effect of dilation function was illustrated in Figure 5.8

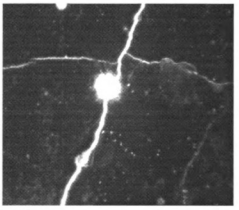

Original Image 250 X

Original Image 125X

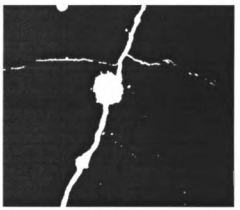

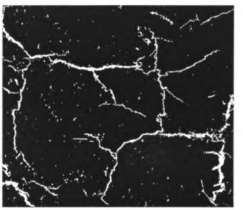

Binary Images

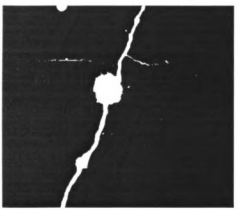

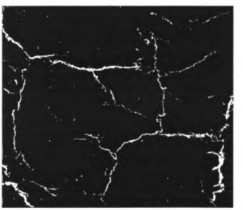

Eroded Images

(a) Fluorescent

(b) ESEM

Figure 5.7 Applying Erosion Function on Fluorescent and ESEM Concrete Micrographs

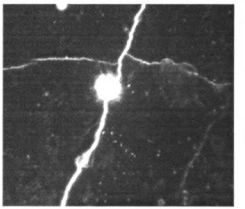

Original Image 250 X

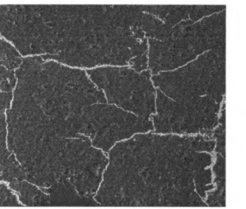

Original Image 125X

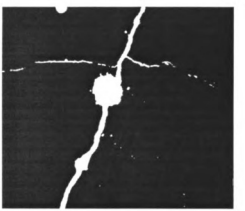

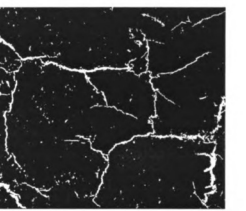

Binary Images

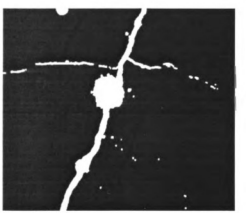

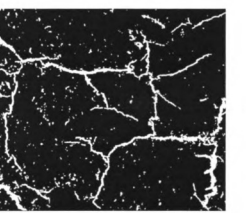

Dilated Images

(a) Fluorescent

(b) ESEM

Figure 5.8 Applying Dilation Function on Fluorescent and ESEM Concrete Micrographs

It can be shown in Figure 5.7 that applying erosion operation provides the opportunity to eliminate objects with a certain form; it has the disadvantage that all the remaining objects shrink in size. In order to overcome that problem erosion and dilation operations may be used together. This recovers most of the original feature size while producing a smooth shape. The sequence of erosion followed by dilation is called an opening. The initial erosion removes small features which may represent noise, and also sharp protuberances from the feature outline. The subsequent dilation does not restore the small features, which have permanently disappeared, but it does fill in any small indentations in the outlines. The overall result is that the feature size is restored to nearly the original value, while the shape is modified to become more rounded and smooth. The effect of opening operation is illustrated in Figure 5.9. In contrast to opening operation, closing is the combinations of dilation followed by erosion. Closing enlarges objects and closes small holes. Applying erosion operation after dilation is usually reverse the general enlargement of the object by the size of the mask. Effect of applying closing operation is illustrated in Figure 5.10.

In contrast to erosion, dilation enlarges objects and closes small holes and cracks. General enlargement of the object by the size of the mask can be reversed by follow-up erosion. This combination of operations is called a closing operation. The effect of closing operation is illustrated in Figure 5.10.

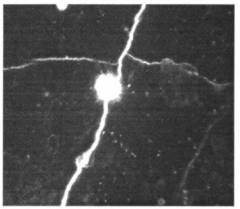

Original Image 250 X

Original Image 125X

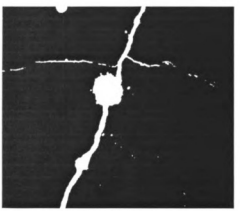

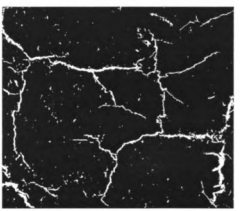

Binary Images

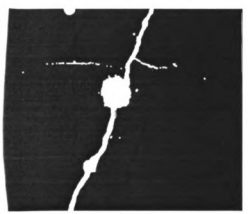

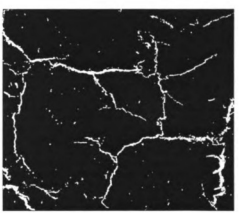

Images After Opening

(a) Fluorescent

(b) ESEM

Figure 5.9 Applying Opening Function on Fluorescent and ESEM Concrete Micrographs

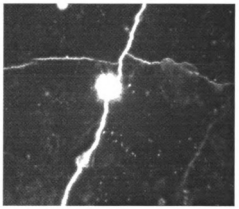

Original Image 250 X

Original Image 125X

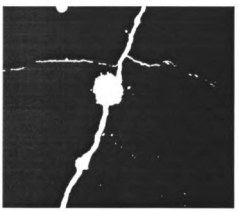

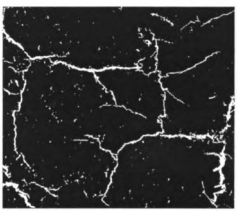

Binary Images

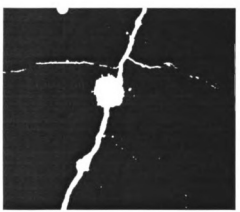

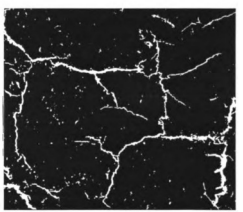

Images After Closing

(a) Fluorescent (b) ESEM

Figure 5.10 Applying Closing Function on Fluorescent and ESEM Concrete Micrographs

Both opening and closing operations are idem potent operations; i.e., a second application of a closing and opening with the same operator mask does not show any further effect. Figure 5.11 illustrates the difference between opening and closing functions.

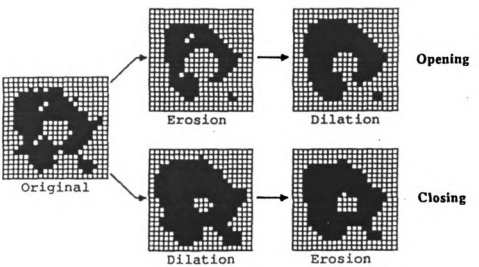

Figure 5.11 Opening and Closing Operations on Binary Pixels[77]

Although applying dilation operation can fill very small holes in the features of interest, it cannot fill big holes that may exist in some features. Dilation operation can't regain the missing part at low number of iterations. Increasing the number of dilation iterations to recover the missing hole can strictly damage the whole image by swelling the size of the other features. Thereby, applying hole-fill function is essential in that case. The hole-fill function recovers the missing holes within any feature (microcrack or void) without any

change to its size as shown in Figure 5.12. Application of the hole-fill function to microcracks or voids that do not have any holes does not produce any harmful effect on them or the rest of features in the image. Between auto-threshold and hole-fill functions, there are many scenarios can be proposed to achieve the goal of enhancing the features of interest (microcracks and voids); alternative scenarios combined in this work are shown in Figure 5.13.

As previously mentioned, concrete specimens were prepared by impregnation with Wood's metal for environmental scanning electron microscopy (ESEM) and with ink followed by epoxy for fluorescent microscope (section 4.2.4). Concrete micrographs were captured using either ESEM or fluorescent microscope, and the alternative image processing scenarios were applied to those images. The effect of applying the alternative scenarios on fluorescent and ESEM micrographs is shown in Figures 5.14 and 5.15 respectively.

Applying those scenarios on numerous images showed the best results were generally obtained when Scenario # 1 and # 7 were implemented. Scenario # 1 may be useful when images contain a noticeable number of noise where application of the opening operation first followed by the closing operation probably restore the image after removal of noise. Images containing missing parts of features of interest (microcracks and voids) can benefit from Scenario # 7 since the closing operation, when applied first, helps recover some missing parts of the features of interest while preventing further losses in original feature caused by the opening operation.

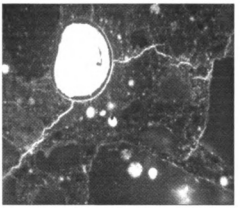

Original Image 250X

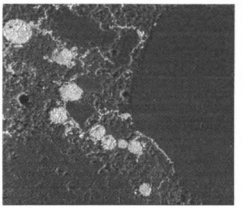

Original Image 125X

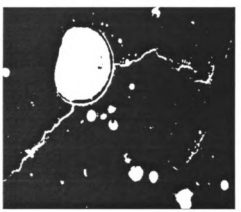

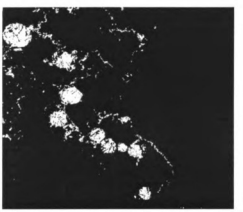

Binary Images

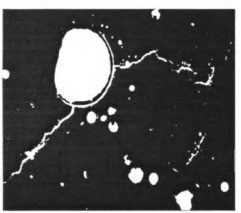

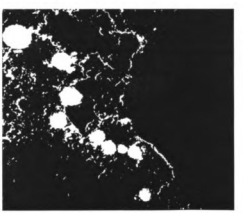

Images After Hole-Fill

(a) Fluorescent (b) ESEM

Figure 5.12 Applying Hole-Fill Function on Fluorescent and ESEM Concrete Micrographs

The quality of the original image decides the level of change brought about by any of these scenarios. For example, the generally better quality of environmental scanning electron micrographs, when compared with fluorescent micrographs, implies that ESEM images are less sensitive to the selection of particular image processing scenarios.

In order to determine the optimum number of iterations in different image processing operations, concrete microscopic images were processed with each scenario using different number of iterations (ranging from 1 to 10). The results suggested that a low number of iterations of the opening function could not efficiently remove the noise from images; a high number of iterations of the opening operation, on the other hand removes parts (pixels) of the feature of interest. In the case of closing operations, a low number of iterations may not effectively restore missing parts of interest, while a high number of iterations could cause noticeably swelling of features, yielding misleading measurements.

It was also noticed that using fixed number of closing and opening iterations may not be universally applicable to different image conditions; hence, a range was suggested for the number of iterations for different scenarios. These ranges were (0 – 2) for opening operation, and (0-3) for closing operation. The optimum number of iterations for certain image condition depends on the amount of noise and the size of noise relative to the size of the features of interest.

Figure 5.16 through Figure 5.19 show the effect of applying opening and closing operations at different number of iterations on fluorescent and ESEM concrete micrographs respectively.

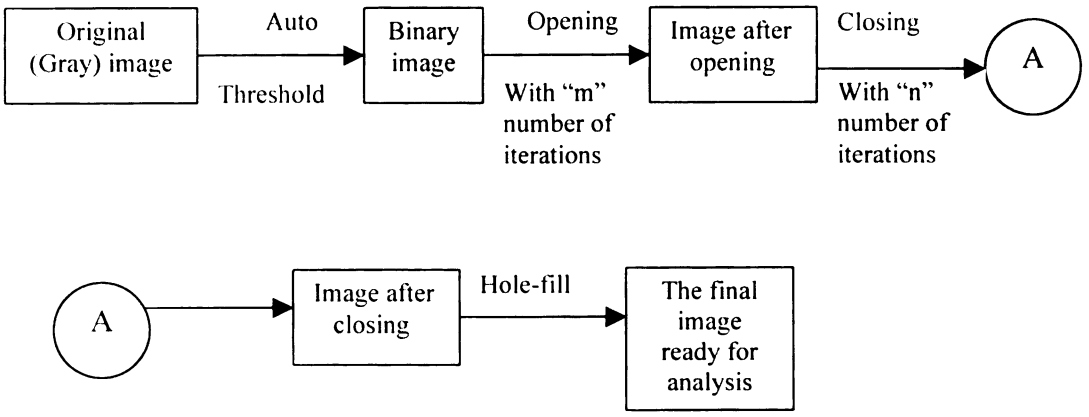

Scenario #1

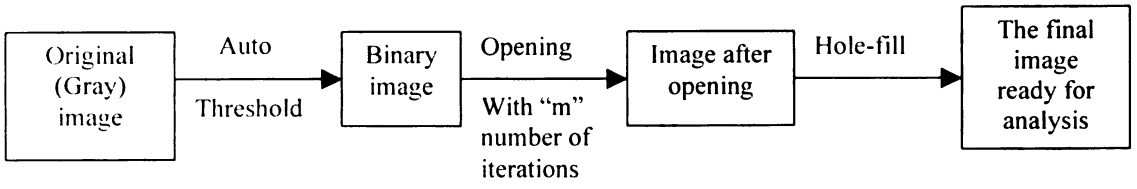

Scenario # 2

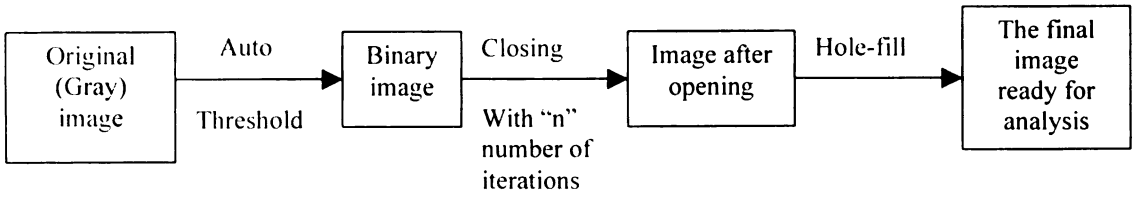

Scenario # 3

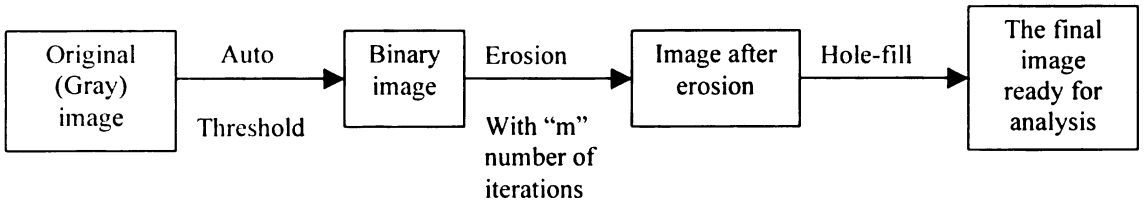

Scenario # 4

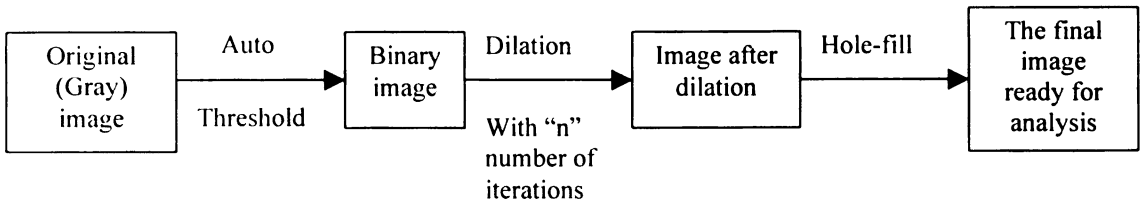

Scenario # 5

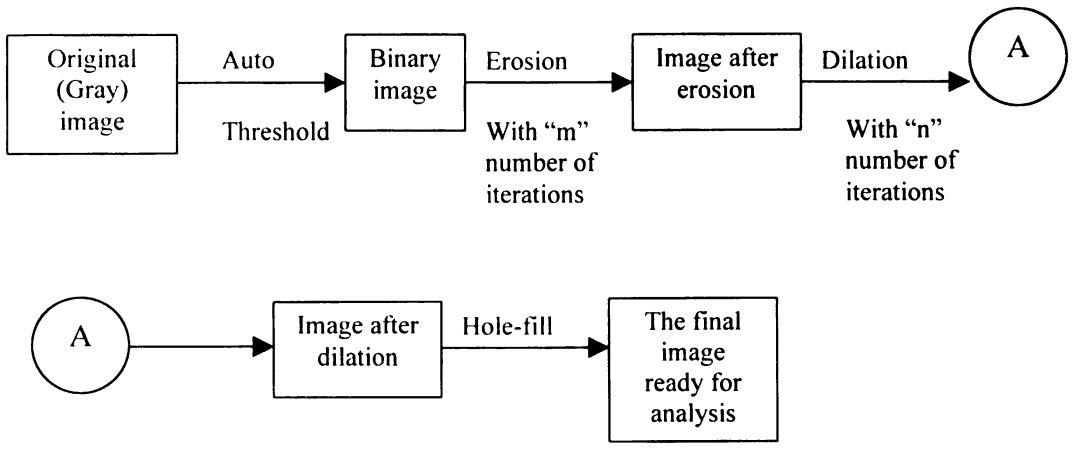

Scenario # 6

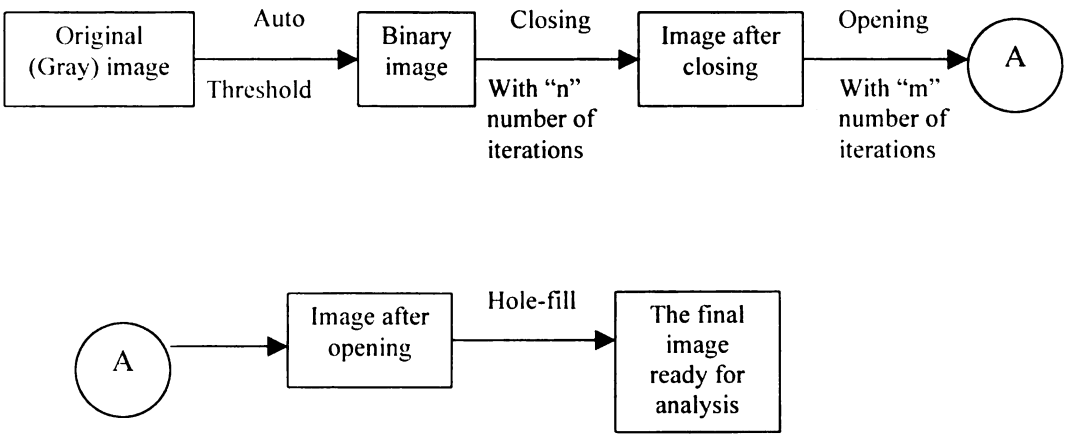

Scenario # 7

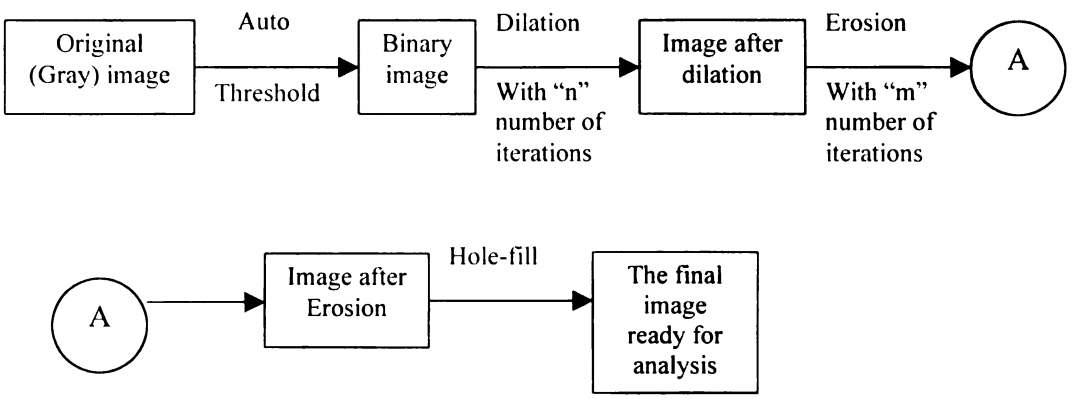

Scenario # 8

Figure 5.13 Proposed Image Processing Scenarios

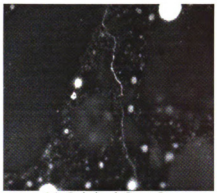

(a) Original Gray Image

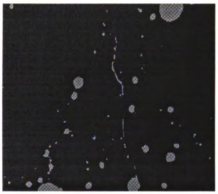

(b) Final Image (Scenario #1)

(c) Final Image (Scenario #2)

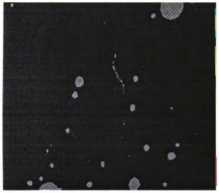

(d) Final Image (Scenario #3)

(e) Final Image (Scenario #4)

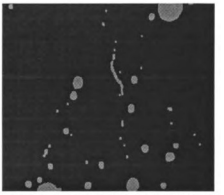

(f) Final Image (Scenario #5)

(g) Final Image (Scenario #6)

(h) Final Image (Scenario #7)

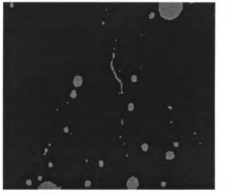

(i) Final Image (Scenario #8)

Figure 5.14 Effect of Applying Different Image Processing Scenarios on Fluorescent Gray Scale Concrete Micrograph at Magnification 125X

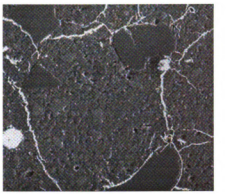

(a) Original Gray Image

(b) Final Image (Scenario #1)

(c) Final Image (Scenario #2)

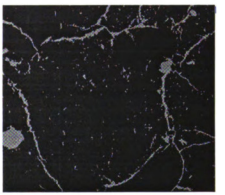

(c) Final Image (Scenario #3)

(d) Final Image (Scenario #4)

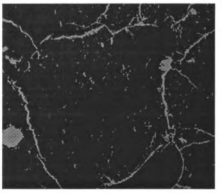

(f) Final Image (Scenario #5)

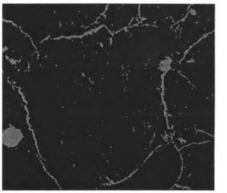

(g) Final Image (Scenario #6)

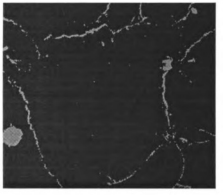

(h) Final Image (Scenario #7)

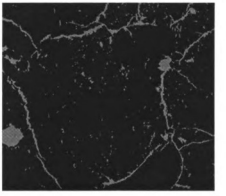

(i) Final Image (Scenario #8)

Figure 5.15 Effect of Applying Different Image Processing Scenarios on ESEM Gray Scale Concrete Micrograph at Magnification 250X

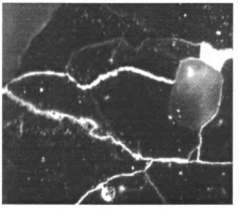

Original Image 250X

Binary Image

1 Number of Iterations

5 Number of Iterations

10 Number of Iterations

Figure 5.16 Applying Opening Operation on

Fluorescent Concrete Micrograph at Different Number of Iterations

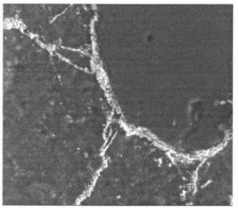

Original Image 500X

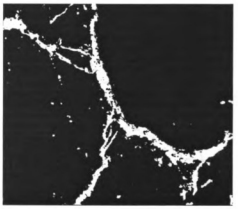

Binary Image

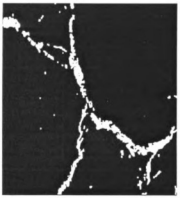

1 Number of Iterations

5 Number of Iterations

10 Number of Iterations

Figure 5.17 Applying Opening Operation on ESEM Concrete Micrograph at Different Number of Iterations

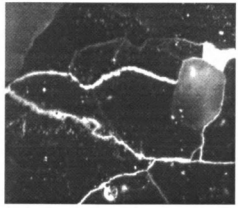

Original Image 250X

Binary Image

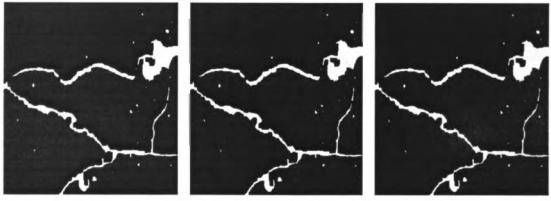

1 Number of Iterations 5 Number of Iterations 10 Number of Iterations

Figure 5.18 Applying Closing Operation on Fluorescent Concrete Micrograph at Different Number of Iterations

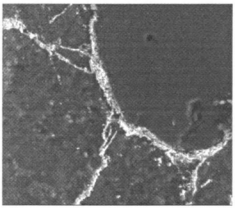

Original Image 500X

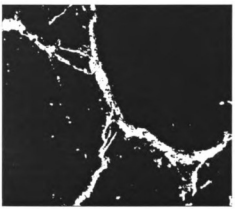

Binary Image

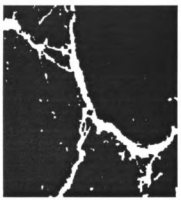

1 Number of Iterations

5 Number of Iterations

10 Number of Iterations

Figure 5.19 Applying Closing Operation on ESEM Concrete Micrograph at Different Number of Iterations

5.2.2 Detachment of Intersecting and/or Connected Microcracks and Voids

In few cases, some concrete microcracks and voids could intersect, and some concrete voids could also be attached. Measurements such as perimeter, crack width, and void diameter could be inaccurate if such connected features are not detached. An image processing scenario was developed to detach connected and intersecting features. This scenario begins with application of the "opening" operation on the original (gray) image (Figure 5.20a) with large number of iterations (about 10) in order to remove microcracks and produce an image with only voids (Figure 5.20b); the point operation function "arithmetic-subtract" was applied to create another image containing the removed microcracks (Figure 5.20c). The "opening" function may be applied on the microcrack image with small number of iterations (about 3) for the purpose of noise removal. The next step is to apply the "erosion" function on the voids image in order followed by the "thinning" operation by using "Ierode Kernel" with a relatively large number of iterations (about 8) (Figure 5.20d). The "thinning" operation is meant to remove some pixels, which connect cracks with voids, around voids without a noticeable loss of feature area. The point operation function "arithmetic–add" is then applied to reconstruct the original image again (Figure 5.20e), yielding an image very similar to the original image (gray) one where connected/intersecting features was detached. The "Auto-threshold" function can be applied on the resulting image in order to transform it to a binary scale image. Subsequently, the "closing" function may be applied in order to compensate for some of the removed pixels. Finally the "hole-fill" function can be applied to fill the empty holes created in voids by the "erosion operation" (Figure 5.20f). Figure 5.21 presents another application of the image processing scenario to detach connected microcracks and voids.

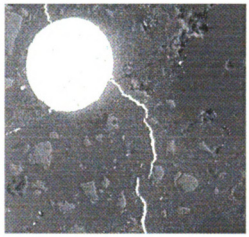

(a) Original "Gray" Image

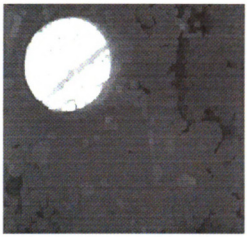

(b) Opening Operation

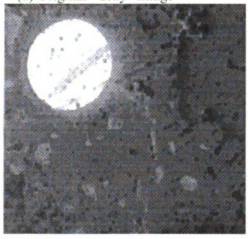

(c) Arithmetic-Subtract Operation

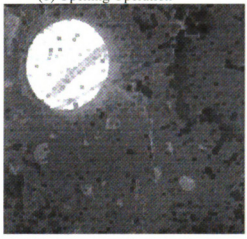

(d) Erosion and Thinning Operations

(e) Arithmetic-Add Operation

(f) Auto-Threshold and Hole-Fill Operations

Figure 5.20 Image Processing Scenario for Detachment of Intersecting Microcracks and Voids

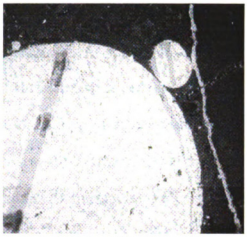

(a) Original "Gray" Image

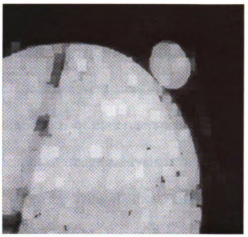

(b) Opening Operation

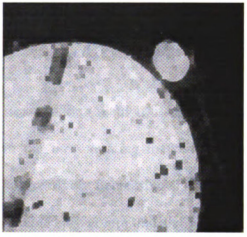

(c) Arithmetic-Subtract Operation

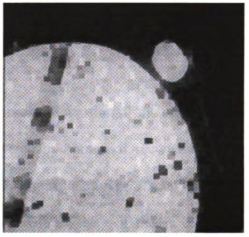

(d) Erosion and Thinning operations

(e) Arithmetic-Add Operation

(f) Auto-Threshold and Hole-Fill Operations

Figure 5.21 Image Processing Scenario for Detachment of Intersecting Microcracks and Voids as well as Connected Voids

5.3 IMAGE ANALYSIS

Image analysis is broadly defined as extracting a useful numerical data from an image.[75] Image analysis is generally implemented after image processing steps. Image analysis is used to determine quantitatively the different compounds of concrete specimens and to assess the characteristics of its components.[80] The aim of image analysis is to extract and produce the measurement results of each image. There are many methods and techniques can be used to perform image analysis. Selection of the suitable image analysis technique depends on the type and amount of the images to be analyzed and speed and precision of the required information.

Box counting method, is used to determine the fractal dimension of the cracks structure. In the box counting method, the image is covered by means of rectangular grids of progressively decreasing linear size as shown in Figure 5.22. The fractal dimension is obtained by computing the logarithmic density of the measure of theses coverings, as their linear size decreases.[81] It is obvious that box counting method is very limited to only one measurement and it is eligible only for cracks. Another method of image analysis for cracks is developed by mapping the cracks after imaging, as shown in Figure 5.23, and manually measure the length and the area of the cracks.[82] This method is tedious, time consuming and can't provide high precision. Moreover, it can't be applied on large number of images or on voids due to the difficulty of manual measuring.

(a) Original Image

(b) Threshold Image Patterns

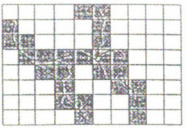

(c) Application of the Box Counting Method

Figure 5.22 Box Counting Method[81]

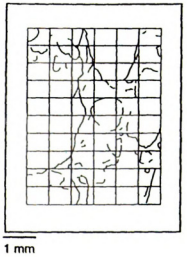

Figure 5.23 Microcrack Mapping for Manual Measuring[82]

Finite element and finite difference techniques are newly incorporated with image analysis in order to determine the properties or the strain distribution within the construction materials.[83] Finite element technique is applied to images obtained by the X-ray microtomography method to determine the transport properties of lime silica bricks. Throughout this approach, the circular noise ring pattern often inherent in X-ray microtomographic images as shown in Figure 5.24. Therefore, image processing operations include a special filter function to remove that kind of noise. The provided technique that showed too high of a resolution provides excellent individual pore delineation, but results in an overall volume which is too small to be representative. Low resolution provides a good representative elementary volume, but may result in pores which are difficult to isolate and whose 3-D connectivity is less than that of the pores in the actual material. As a result, for a material with a wide range of pore sizes (such as cement paste or mortar), it will be extremely difficult to balance these two concerns.[84]

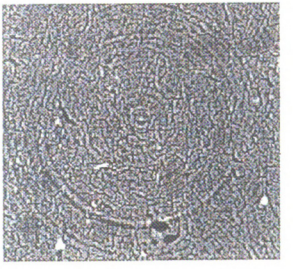

Figure 5.24 Original Microtomographic Image of The Lime Silica Brick[84]

Image analysis was also used for the quantitative evaluation of the main clinker phase namely, the alite C_3S, the belite C_2S, and the matrix, union of two aluminates C_3A and C_4AF.[85] Throughout this approach, a mathematical model "Logarithmic image processing model" which combines the automated thresholding algorithms and the use of contrast between the different phases of clinker is developed for that purpose. The original image (Figure 5.25) has been processed using the proposed approach to obtain alite, belite, and matrix. The proposed algorithms give satisfying results with clinker from different origins, nevertheless it can't be extended to any other material.

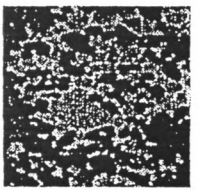

(a) Original Image

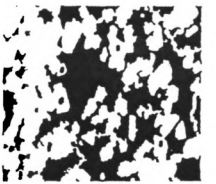

(b) Alite Binary Image

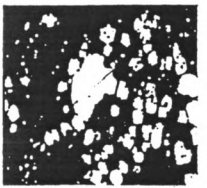

(c) Belite Binary Image

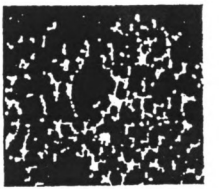

(d) Matrix Binary Image

Figure 5.25 Logarithmic Image Processing Approach[86]

5.3.1 Image Analysis Formulas (Models)

Throughout the current research, different formulas (models) were proposed and developed for the purpose of quantification. The main thrust of the proposed formulas is to determine the various measurements (characteristics) of the features of interest. Image analysis part is mainly concerned about the measurements in 2-D directions (planar measurements) of the features. The characteristic terms obtained from 2-D directions are transformed into parameters of 3-D directions using stereology interpretations. Image analysis formulas proposed herein covered wide range of microcracks, voids, aggregates and fibers characteristics. Selection of the proposed 2-D formulas was performed taking into account covering the measurements that might have physical meaning and might be related to the engineering properties of the concrete.

5.3.1.1 *Microcrack Planar (2-D) Measurements*

- Length Per Unit Area (L_{AC})

Crack length per unit area expresses "crack density"[20,86] in concrete specimens and provides an indication about crack characteristics in concrete. The crack length per unit area (are of the section of interest) can be expressed as follows:

$$L_{AC} = \frac{L_{ic}}{Area} \quad \text{.....(5.1)}$$

where, L_{ic} = length of each individual crack.

Area = area of the total images in the whole section.

- Perimeter Per Unit Area (P_{AC})

The perimeter measured in image analysis is the object perimeter measured form pixel

center to pixel center.[87] Perimeter of cracks provides an indication about the branching of cracks. In some cases it is possible that two cracks may have the same length but different perimeter, hence, crack length is not enough for crack characterizing as shown in Figure 5.26.

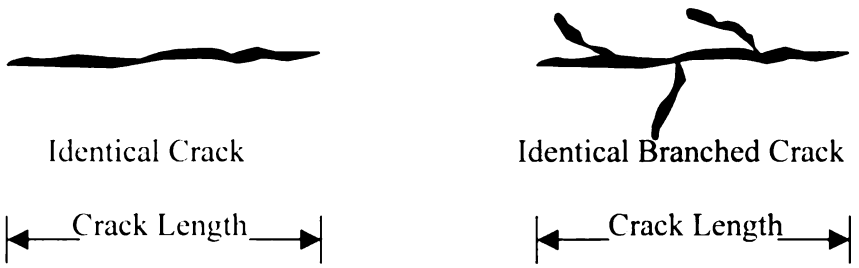

Figure 5.26 Two Cracks Have The Same Length and Different Perimeter

Crack perimeter per unit area can be expressed as follows:

$$P_{IC} = \frac{P_{IC}}{Area} \quad \text{.....(5.2)}$$

where, P_{IC} = perimeter of each individual crack

Area = area of the total images in the whole section

- Area Fraction (A_{AC})

Object area is determined as the number of pixels in the particle converted to square microns.[87] Cracks Area fraction can be considered one of the paramount parameters to characterize damage in concrete[20] since increasing crack area fraction in concrete gives an indication that the concrete has high degree of damage. Crack area fraction can be expressed as follows:

$$A_{AC} = \frac{A_{ic}}{Area} \quad \text{.....(5.3)}$$

where, A_{ic} = area of each individual crack.

Area = area of the total images in the whole section

- Width in Plane (W_{CP})

Crack width is an important parameter to characterize concrete properties and performance, since crack width can be related to the thermal properties of concrete and some of the transport properties. Crack width is difficult to be measured since most of image processing and analysis software programs determine the breadth of the feature rather than its width. Figure 5.27 illustrates the difference between the breadth and the width of cracks. Crack width per unit area can be expressed as follows:

$$W_{CP} = \frac{W_{ic}}{Area} \quad \text{.....(5.4)}$$

where, W_{iC} = width of each individual crack

Area = area of the total images in the whole section

Figure 5.27 The Difference between Crack Breadth and Width

If the used software provides crack breadth rather than crack width, an alternative equation may be used. Throughout the research study an empirical equation was developed to provide crack width measurement. The proposed equation is as follows:

$$W_{CP} = \frac{3.5 \times A_{tc}}{\pi \times L_{tc}} \quad \text{.....(5.5)}$$

In order to validate the applicability of the proposed equation, 100 different cracks vary in its shape and size were captured at different magnification factors and measured. The actual width of each individual crack was measured manually by using Visilog 5.3® and the proposed equation was also applied for the purpose of comparison. The error as a percentage in the calculations of crack width by the proposed equation is shown in Table5.3 and the comparison between calculated and measured crack width is shown in Figure 5.28. The 22.865 mean value of the error percent may be considered an acceptable since there is a large possibility that there is an error also in the manual measurement.

Table 5.3 Errors In Calculated Crack Width by The Proposed Equation

Statistics	Measured Crack Width	Calculated Crack Width	Error in Calculated Crack Width (%)
Minimum (Pixels)	6.833	5.1	10.219
Maximum (pixels)	262.33	235.526	41.285
Mean (pixels)	47.391	36.733	22.865
Std. Dev.	50.004	44.454	13.275

- Spacing in Plane (λ_{CP})

Spacing of cracks is considered an important parameter to characterize concrete properties and performance. Spacing of cracks provides an indication about the degree of damage and permeability in concrete. Throughout the research a mathematical expression is developed to calculate spacing of cracks in plane.

In the simplified model of Figure 5.29, it is assumed that each crack can be represented by a circle has the same area and positioned in the center of gravity of the crack. It is also assumed that cracks are uniformly and equally distributed in plane (2-D). The crack spacing expression can be derived as follows:

$$\lambda_{CPl} = \frac{L}{N_{Lc}} \qquad \text{.....(5.6)}$$

where, L = dimension of the section of the interest

N_{LC} = number of crack through length (L)

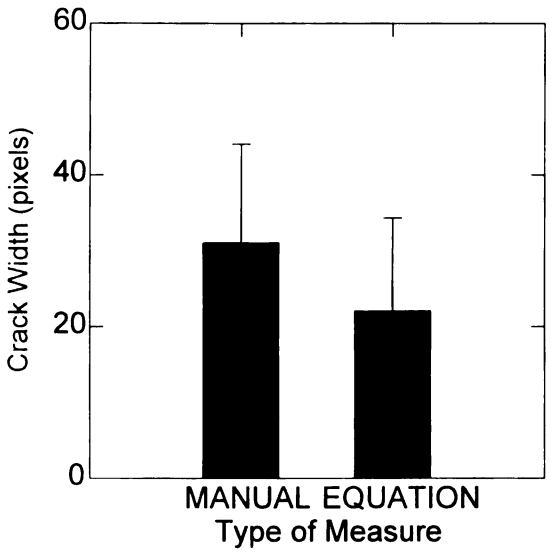

Figure 5.28 Comparison between Measured and Calculated Crack Width

The number of cracks along length L can be expressed as follows:

$N_{Lc} = \sqrt{N_{SC}}$ .....(5.7)

where, N_{SC} = total number of cracks in the section of interest

The total number of cracks in the section of interest is:

$N_{SC} = \frac{\sum A_{ic}}{A_{icm}}$ .....(5.8)

where, A_{icm} = mean of the area of each individual crack in the section of interest.

By substitution of equations (5.7 & 5.8) in equation (5.6), the following expression can be obtained:

$$\lambda_{CP1} = \frac{L}{\sqrt{\sum A_{AC} / Aicm}} \quad \text{.....(5.9)}$$

where λ_{CP1} = spacing in plane through length (L)

For the purpose of normalization (spacing per unit length), length (L) can be replaced by length per unit area, and the area of cracks can be replaced by area fraction. The crack spacing in plane thus can be expressed as follows:

$$\lambda_{CP} = \sqrt{\frac{A_{icm}}{\sum A_{AC}}} \quad \text{.....(5.10)}$$

where, A_{AC} = crack area fraction

The diagonal spacing can be obtained by using the following expression:

$$\lambda_{Cpdiagonal} = \sqrt{(\lambda_{cpx})^2 + (\lambda_{cpy})^2} \quad \text{.....(5.11)}$$

where, λ_{cpx} = spacing in X direction

λ_{cpy} = spacing in Y direction

Equations (5.10) and (5.11) yield the following expression for diagonal spacing:

$$\lambda_{Pcdiagonal} = \sqrt{2}\sqrt{\frac{A_{icm}}{\sum A_{AC}}} \quad \text{.....(5.12)}$$

where, $\lambda_{Pcdiagonal}$ = diagonal spacing

- Angle of Orientation in Plane (ω_C)

Direction of concrete cracks can be provided by the angle of orientation. Orientation of concrete cracks can be related to the direction of loading since each different direction of loading may lead to a certain crack orientation. Crack orientation can affect diffusion properties of concrete. Angle of orientation of each individual crack can be determined by measuring angle of crack length inclination on horizontal (X-X) or vertical (Y-Y). Throughout the study, angle of orientation of each individual crack was determined by measuring angle of crack length inclination on the horizontal axis as shown in Figure 5.29.

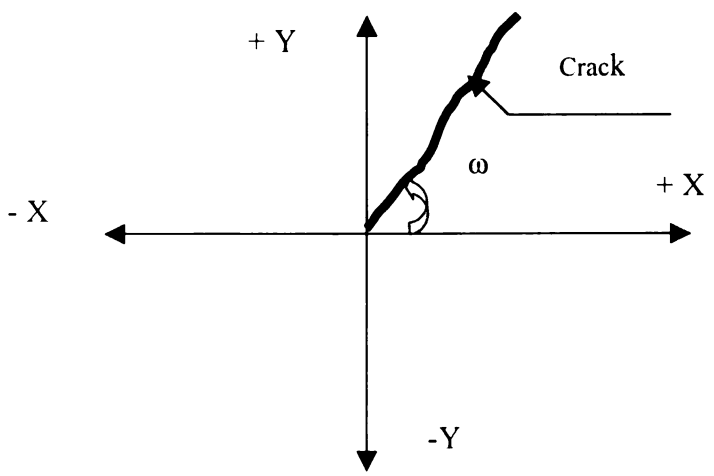

Figure 5.29 Schematic Presentation of Crack Angle of Orientation (ω_C)

- Tortuosity in Plane (T_{CP})

Crack tortuosity is a useful quantitative descriptor of the propagation characteristic of cracks in concrete. Propagation of cracks in concrete depends on the strength of mortar and aggregate. In normal strength concrete, cracking occur in mortar and most of cracks tortuous its path around the aggregate particles and as a result more aggregate particles in concrete leads to more tortuous cracks. Throughout the research study crack tortuosity is expressed as follows.

$$T_{CP} = \frac{Actual\ Crack\ Length}{\Pr ojected\ Crack\ Length} \quad \text{.....(5.13)}$$

Due to difficulty in measuring the actual crack length, the following expression was proposed

$$T_{CP} = \frac{P_{ic}}{2L_{ic}} \quad \text{.....(5.14)}$$

where, P_{ic} = perimeter of each individual crack.

L_{ic} = length of each individual crack.

- Crack Degree of Orientation in Plane (Ω_{CP})

While angle of orientation can provide an indication about orientation of each individual crack, degree of orientation provides an indication about the orientation of the overall cracks in the same section. If degree of orientation (Ω_p = 1), this means that the cracks system is completely planar orientated in a certain direction. If degree of orientation (Ω_p = 0.0), this means that the cracks system is completely planar random system.[88]

Depending on the value of the Ω_p (between zero and 1) the cracks system can be classified a partially planar oriented system. Assuming cracks as system of lines in the plane, crack degree of orientation in plane can be expressed as follows:[89]

$$\Omega_{(P)} = \frac{[(PL)t\perp - (PL)tII]}{[(PL)t\perp + 0.571(PL)tII]} \quad \text{.....(5.15)}$$

where $(PL)t\perp$ or $(PL)tII$ = number of point intersections per unit length of superimposed array of equally spaced parallel test lines oriented in a predetermined direction as shown in Figure 5.30. Subscripts "$\perp$"and "*II*" refer to test lines running perpendicular and parallel to the preferred orientation of cracks. Subscript "t" refers to the total point intersections in a certain direction. Subscripts "$\perp$"and "*II*" refer to test lines running perpendicular and parallel to the preferred orientation of cracks.

Subscript "t" refers to the total point intersections in a certain direction.

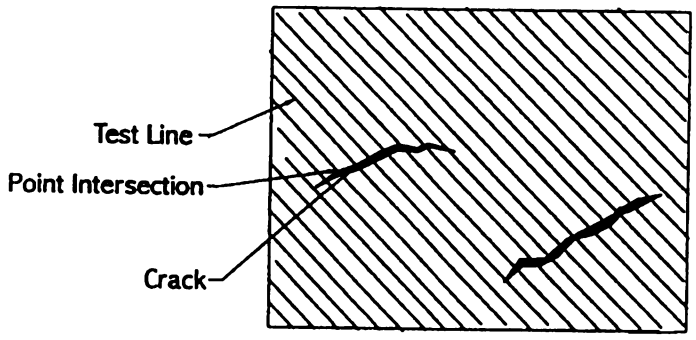

Figure 5.30 Schematic Presentation of Point Intersections

5.3.1.2 *Void Planar (2-D) Measurements*

- Equivalent Diameter ($d_{I,V}$)

The equivalent circular diameter is the diameter of a fictitious circular that has the same area as the void.[89] The equivalent diameter provides an easy way to estimate the diameter of the void; assuming that the void is spherical in shape. Once the area has been determined, it is often convenient to express it as an equivalent circular diameter and simply calculated from the following expression:

$$d_{EV} = \sqrt{\frac{4 \times A_{iv}}{\pi}} \qquad \text{.....(5.16)}$$

where A_{iv} = area of each individual void.

- Area Fraction (A_{AV})

Voids area fraction is important parameter. Area fraction of voids provides a measure about air content in concrete. Air content is an important factor for concrete subjected to freeze-thaw cycles. Area fraction of voids in concrete can be obtained using the same expression for cracks.

$$A_{AV} = \frac{A_{iv}}{Area} \qquad \text{.....(5.17)}$$

where A_{iv} = area of each individual void.

Area = area of the total images in the whole section.

- Perimeter Per Unit Area (P_{AV})

Void perimeter provides an indication about the nature of voids inside some special types of concretes such as aerated concrete. Perimeter per unit area can be obtained by the following:

$$P_{AV} = \frac{P_{iv}}{Area} \quad \text{.....(5.18)}$$

where, P_{iv} = the perimeter of each individual void.

Area = area of the total images in the whole section.

- Number Per Unit Area (N_{AV})

Number of voids in concrete is considered to be one of the most important parameters. The importance of the number of voids is owned to its effect on frost resistance and concrete durability and performance. Number of voids can also be used as an indication about the concrete strength, since large number of voids in concrete can lead to low concrete strength. Number of voids in concrete is also helpful in determination void size distribution[90] and some other additional parameters. Number of voids in concrete can be obtained by the following expression:

$$N_{AV} = \frac{\sum_{i=1}^{N} N_{iv}}{Area} \quad \text{.....(5.19)}$$

where, N_{iv} = total number of voids in the whole section.

Area = area of the total images in the whole section.

- Mean Diameter in Plane (d_{mvp})

Mean diameter introduces the average diameter of the voids found in a specified concrete section. The mean diameter can be obtained by the following equation:[77]

$$d_{mvp} = \sqrt{\frac{4 \times \sum A_{AV}}{\pi \times N_{AV}}} \quad \text{.....(5.20)}$$

where, ΣA_{AV} = the summation of the voids area fraction in the whole section.

N_{AV} = number per unit area for voids

- Void Spacing in Plane (λ_{VP})

The efficiency of the air-void system created by air-entrainment is governed by the spacing of the voids which determines the maximum distance that unstable water must travel to reach an escape boundary (the disruptive pressures are proportional to the cubic value of this distance).[91] Spacing of voids is of great importance since the spacing factor has a noticeable influence of concrete frost resistance. The proposed equation to calculate void spacing is based on the same assumptions proposed by ASTM C457 that voids are equal in size and are regularly spaced in a cubic arrangement as shown in Figure 5.31.

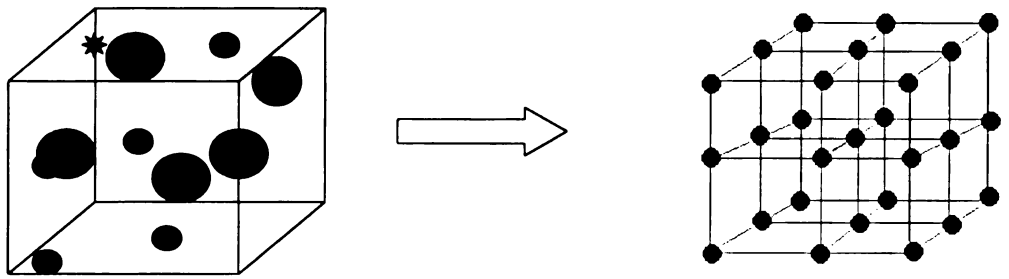

The Actual Status

Simplifying Assumptions

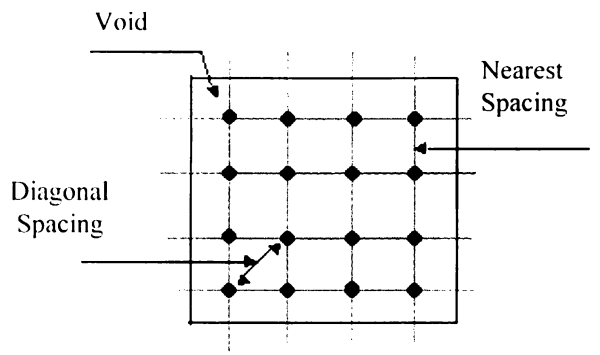

Voids Distribution in Plane

Figure 5.31 Schematic Presentation of the Assumptions Used in Spacing Computations

Following the same procedures for crack spacing, the following expression for void spacing can be obtained:

$$\lambda_{VP} = \sqrt{\frac{A_{ivm}}{\sum A_{AV}}} \quad \text{.....(5.21)}$$

where, A_{ivm} = mean of the area of each individual void.

$\sum A_{AV}$ = total area fraction of voids per unit area.

Most previous studies[90-92] characterized void spacing as the average distance between the outer boundaries of two adjacent air voids, a modification in the equation is proposed to obtain spacing between voids from the outer surface, therefore, the spacing from center to center is subtracted by the mean diameter of voids.

$$\lambda_{VP} = \left[\sqrt{\frac{A_{ivm}}{\sum A_{AV}}}\right] - d_{mvp} \quad \text{.....(5.22)}$$

where, d_m = mean diameter of voids in the section of interest.

The diagonal spacing can be obtained by using the following expression:

$$\lambda_{VPdiagonal} = \sqrt{(\lambda_{vpv})^2 + (\lambda_{vph})^2} \quad \text{.....(5.23)}$$

where, $\lambda_{Vpdiagonal}$ = void diagonal spacing

λ_{vpx} = spacing in X direction.

λ_{vpy} = spacing in Y direction.

Equations (5.22) and (5.23), yield the following equation.

$$\lambda_{VPdiagonal} = \sqrt{2}\sqrt{\frac{A_{ivm}}{\sum A_{iW}} - d_{mvp}} \quad \text{.....(5.24)}$$

Throughout the research study, the nearest spacing was taken into account. The spacing of voids obtained by the proposed equation provides spacing in plane. Stereological principles are applied in the next chapter to obtain spacing in space.

- Aspect Ratio (A_{Sv})

Aspect ratio is a shape index, used to distinguish the change in object elongation. Aspect ratio is close to 1 for spherical voids, and has larger values for elongated ones. Aspect ratio can be used also as a measure for pore size that gives and indication about any pore collapse may occur in the materials due to confining pressure.[93] Aspect ratio is proposed as follows:[77]

$$A_{sv} = \frac{L_{iv}}{W_{vc}} \quad \text{.....(5.25)}$$

where, L_{iv} = length (longest diameter) of each individual void.

W_{iv} = width (shortest diameter) of each individual void

- Form Factor (F_{Fv})

Form factor is often used to describe the shape of features. It is usually defined as:[94]

$$F_{Fv} = \frac{4 \times \pi \times A_{iv}}{(P_{iv})^2} \quad \text{.....(5.26)}$$

where, A_{iv} = area of each individual void

P_{iv} = perimeter of each individual void

The form factor is one of the most widely used shape indices. Form factor has a maximum value of 1 for a perfect circle, and has smaller values for shapes departing from circularity, or having rough edges and thus larger perimeter. (a square has a form factor of 0.785).

- Compactness (C_{Sv})

Compactness is used to measure the elongation of the features. The proposed expression for Compactness is as follows:

$$C_{sv} = \frac{(P_{iv})^2}{A_{iv}} \quad \text{.....(5.27)}$$

where, P_{iv} = perimeter of each individual void

A_{iv} = area of each individual void

The compactness has the lowest value for a circle, while its value is increased according to the elongation of the feature.

- Roundness (R_{Sv})

Roundness looks very much like the form factor. But instead of perimeter, roundness uses the length (longest chord) of the feature. This makes it more sensitive to how elongated the feature is, rather than how irregular its outline may be. It is very rare to find voids that vary independently in roundness and form factor. The roundness can be expressed as follows:[77]

$$R_{sv} = \frac{4 \times A_{iv}}{\pi \times (L_{iv})^2} \quad \text{.....(5.28)}$$

where, A_{iv} = area of each individual void

L_{iv}= length of each individual void.

5.3.1.3 *Aggregate Planar (2-D) Measurements*

Throughout the research study, mathematical expressions have been proposed for aggregates. The mathematical expressions for aggregates have not been applied on concrete specimens since most of the mathematical expressions used for voids can be applied for aggregates. While all voids mathematical expressions proposed for voids can be applied for aggregates, other additional expressions (shape indices) can be added and other shape indices have some differences in meanings for aggregates.

- Degree of Orientation in Plane (Ω_{gP})

Aggregate particles may take certain orientation in concrete due to pouring method and direction. Degree of orientation may provide an indication about aggregate orientation.

Degree of orientation can be expressed as follows:[88]

$$\Omega_{gp} = \frac{[(PL)t\perp - (PL)tII]}{[(PL)t\perp + 0.571(PL)tII]} \quad \text{.....(5.29)}$$

- Form Factor (F_{Fg})

The aggregate form factor can be defined in the same way as voids.

$$F_{fg} = \frac{4 \times \pi \times A_{ig}}{(p_{ig})^2} \quad \text{.....(5.30)}$$

where, A_{ig} = area of each individual aggregate.

P_{ig} = perimeter of each individual aggregate.

When formfactor is plotted against aggregate size, a trend of decreasing form factor with increasing size (e.g., equivalent spherical diameter) would suggest that large particles are more irregular than small ones, which could reflect the agglomeration of small particles to form large ones. Conversely, a trend of decreasing form factor with decreasing size could result if small irregular particles were produced by fragmentation of large smooth ones. Form factor is close to 1 for smooth, round natural sands, while manufactured sands with angular and rough edges have smaller form factors.[89]

- Nonequiaxiality Index (N_{Ig})

Nonequiaxiality index is similar to aspect ratio, a measure for particles shape and size. But it is higher precision.[92] Nonequiaxiality index is close to 1 for cubical or spherical

aggregates, and has larger values for elongated and flat aggregates. Nonequiaxiality index can be defined as follows:[88]

$$N_{lg} = \frac{(PL)i\perp}{(PL)i\amalg} \quad \text{.....(5.31)}$$

where, $(PL)i\perp$ or $(PL)i\amalg$ = number of point intersections per unit length of superimposed array of equally spaced parallel test lines oriented in a predetermined direction for each individual aggregate particle. Subscripts "$\perp$"and "II" refer to test lines running perpendicular and parallel to the preferred orientation of aggregates.

- Complexity index (C_I)

Complexity index is designed to reflect an increased jaggedness of the perimeter per area of the aggregate particle, it can be expressed as:[88]

$$C_I = \frac{\pi(PL)_{iav}}{2 \times A_{Ag}} \quad \text{.....(5.32)}$$

where, $(PL)_{iav}$ = average (PL) value for each individual aggregate

A_{Ag} = aggregate area fraction.

- Angularity (A_g)

The angularity index is believed to exclude the effect of aspect ratio and surface texture and is considered to be a vivid parameter for the second order of shape and roundness. The angularity for either a circle or ellipse is equal to 1.0. For angular aggregate

particles, their angularity will be larger than 1.0, therefore larger values of angularity indicates a higher degree of angularity. The angularity index is proposed as the following:[89]

$$\text{Angularity} = (\text{perimeter}_{convex} / \text{perimeter}_{ellipse})^2 \quad \text{.....(5.33)}$$

Where, $\text{Perimeter}_{convex}$ = perimeter of the bounding convex.

$\text{Perimeter}_{ellipse}$ = perimeter of an equivalent ellipse.

The terms of the proposed equation is not handy to be applied, therefore, a simplification is proposed as follows:

$$\text{Perimeter}_{convex} = 2(\text{bounding box } d_x + \text{bounding box } d_y) \quad \text{.....(5.34)}$$

$$\text{Perimeter}_{ellipse} = \sqrt{\frac{1 + A_{Sg}}{2 \times A_{Sg}}} \times \text{perimeter}_{circle} \quad \text{.....(5.35)}$$

where, A_{Sg} = aggregate particles aspect ratio.

By substituting equation 5.34 and 5.35 in equation 5.33, the angularity can be expressed as follows:

$$A_g = \frac{2}{\pi} \times \frac{(A_{sg}) \times (L_{ig} + W_{ig})}{[1 + (A_{sg})^2] \times (A_{ig})} \quad \text{.....(5.36)}$$

where, A_{sg} = Aspect ratio of each individual aggregate particle.

L_{ig} =length of each individual aggregate particle.

W_{ig} = width of each individual aggregate particle.

A_{ig} = area of each individual aggregate particle.

5.3.1.4 *Fibers Planar (2-D) Measurements*

Most of the fibers used in concrete are cylindrical in shape, with circular cross section. The in plane (2-D) equations used for voids or aggregates can be applied for fibers. In case of (3-D) special expressions should be used for fibers.

It should be emphasized that throughout the research study, all shape indices measurements have been applied on the objects not touching edges of the image. Since applying shape indices expressions on any feature touches image borders may produce misleading results due to changes in objects dimensions.

5.4 CONCLUSIONS

1- Automatic Threshold schemes best suiting automated identification of microcracks and voids in prepared concrete specimens were identified; these schemes greatly facilitate automation of concrete microstructural analysis.

2- Image processing scenarios were developed for detachment of intersecting microcracks and voids and also separation connected voids for accurate quantification of concrete microcrack and void system.

3- Thresholding, followed by opening, closing, and hole-fill operations provide the basis to process concrete micrographs with substantial noise. In the case of images with limited noise, thresholding followed by closing, opening, and hole-fill provided a better approach to remove noise and preserve features of interest (microcracks and voids). Opening operations in both causes generally require one to three iterations; closing operations require one to four.

4- Planar quantification of the microcrack system involved formulations of length per unit area, perimeter per unit area, width per unit area, area fraction, degree of orientation, spacing, and tortuosity were developed.

5- New formulations with higher precision were developed to determine crack width in plane and space and crack/void spacing in plane. New specific surface area formulation was adopted to determine crack specific surface area based on the preferred orientation of cracks in concrete.

6- Planar quantification of the void system involved formulation of equivalent diameter, number per unit area, aspect ratio, form factor, compactness, and roundness were developed.

7- Planar characteristics of microcracks on two perpendicular sections were used in stereological formulations to quantify microcrack volume fraction, spacing, width, degree of orientation and tortuosity in space. Different spatial formulations for biological applications were adopted to be used for microcrack system analyses.

8- Planar characteristics of voids on two perpendicular sections were used in stereological formulations to quantify the volume fraction, number per unit volume, specific surface area, spacing, and diameter of voids in space.

9-Limited quantification of planar aggregates characteristics covered angularity, complexity, and nonequiaxiality index were developed.

CHAPTER 6

STEREOLOGICAL INTERPRETATIONS & STATISTICAL ANALYSES

6.1 STEREOLOGY

6.1.1 Preface

Stereology can be defined as a body of mathematical methods relating three-dimensional parameters defining the structure to two-dimensional measurements obtainable on section of the structure.[95] Stereological principles can be used to quantify many spatial attributes of oriented features (such as degree of anisotropy, surface area of oriented cracks per unit volume, and void distribution) in terms of measurements conducted on two cross sections perpendicular to the orientation axis. Throughout the research study, stereological principles are used to relate the obtained planar (2-D) measurements from concrete sections to the true spatial (3-D) microstructure in order to interpret the actual (real) dimensions, measurements and orientations of the features of interest.

6.1.2 Basic Stereological Relationships

Basic stereological relationships embody expressions which relate points, lines, surfaces, and volumes in space to measurements make on 2-D sections through the space. Triangular matrix in Table 6.1 is arranged to present interrelationship of measured quantities on the section plane to the calculated spatial quantities.[96]

Table 6.1 Relationship of Measured (O) and Calculated (□) Quantities[96]

Microstructural Feature	Dimensions of Symbols (Arbitrarily expressed in terms of millimeters)			
	mm^0	mm^{-1}	mm^{-2}	mm^{-3}
Points	P_P	P_L	P_A	P_V
Lines	L_L	L_A	L_V	—
Surfaces	A_A	S_V	—	—
Volumes	V_V	—	—	—

The triangular array of symbols in Table 6.1 is arranged systematically to emphasize and compare the relationship of measured quantities in the two dimensional section to calculated quantities in three-dimensional space. The equations relating the quantities in Table 6.1 can be expressed as follows:[88]

$V_V = A_A = L_L = P_P$ mm^0 .....(6.1)

$S_V = (4/\pi)\, L_A = 2P_L$ mm^{-1} .....(6.2)

$L_V = 2\, P_A$ mm^{-2} .....(6.3)

$P_V = 0.5\, L_V S_V = 2\, P_A P_L$ mm^{-3} .....(6.4)

where, V_V = volume fraction, volume of features per unit volume.

A_A = area fraction, area of intercepted features per unit area.

L_L = lineal fraction, length of intercepts per unit length of test line.

P_P = point fraction, number of points per test point.

S_V = surface area per unit test volume.

L_A = length of lineal elements per unit test area.

P_L = number of point intersections per unit length of test line.

L_V = length of lineal elements per unit test volume.

P_A = number of points per unit test area.

P_V = number of points per unit test volume.

Equation 6.1 is always valid whatever the shape of the structure or the distribution of the features inside it. Equations (6.2, 6.3) can only be used in the case of isometric (non oriented) structures,[97] therefore, other complicated expressions are developed for oriented features. Equation 6.4 can be applied only in limited cases.[96] Figure 6.1 illustrates how the basic stereological expressions can relate the measurements in space (3-D) to the measurements in plane (2-D).

Basic stereological expressions relevant to three-dimensional features in space are illustrated in Table 6.2

where, N_L = number of interceptions of features per unit length of test line.

$\bar{L}_3$ = mean intercept length of three-dimensional bodies = $L_L / N_L = A_A/N_L = V_V/N_L$

$\bar{V}_\alpha$ = mean volume of α-objects = $(V_V)_\alpha/N_V$

$\bar{S}_\alpha$ = mean surface area of α-objects = $(S_V)_\alpha/N_V$

V = volume of individual object.

S = external surface area of individual object.

l = constant length of short test lines, thrown randomly on microstructure.

p = number of (end) points of l-lines that fall in phase of interest.

P = number of intersections with surfaces make by l-lines.

N_A = number of interceptions of features per unit test area.

N_V = Number of features per unit test volume.

6.1.3 Stereological Treatment of Oriented Features

Most of stereological relationships shown above are valid only under the condition that the cross-section planes are isotropic with respect to the structure space, i.e., that they may assume any orientation in space with equal likelihood. There are three different types of lines systems:[98] (1) isometric systems of lines, (2) systems that are completely oriented, and (3) systems that are partially oriented. Example of isometric systems of closed figures (circles) located at random throughout the structure is shown in Figure 6.2. The lines of an oriented system can be divided into elements which are very small and of equal length, and may be assumed to be straight. Some or all line elements will be found parallel to one or more definite directions, called the orientation axis, or axes, of the system. The greater the number of orientation axes in a system, the closer it is to an isometric system of lines. Examples of oriented systems with one-, two-, or three-orientation axes are presented in Figure 6.3.

Volume

V

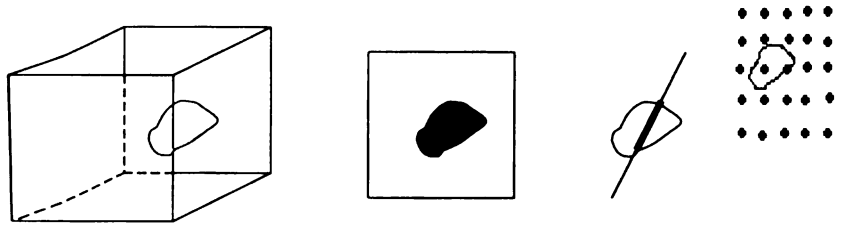

$V_V = A_A = L_L = P_P$

Surface

S

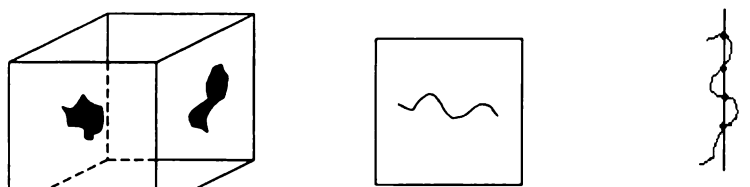

$S_V = (4/\pi)\, L_A = 2P_L$

Length

L

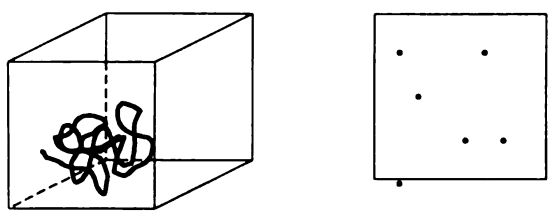

$L_V = 2P_A$

Number

N

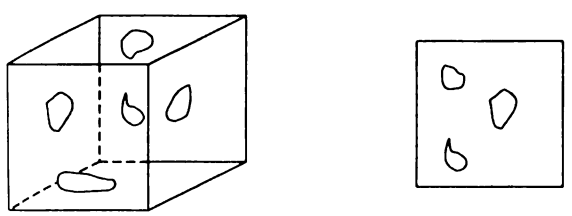

N_V N_A

Figure 6.1 Schematic Presentation of Basic Stereological Expressions

Table 6.2 Expressions Relevant to Three-Dimensional Features in Space[88]

Space-filling contiguous objects of one phase ($V_V = 1$)	Dispersed objects of α-phase [$(V_V)_\alpha < 1$]	Isolated single object (volume = V) not associated with a matrix
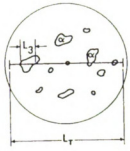	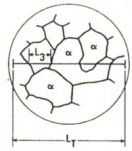	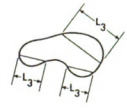
Two-dimensional internal surfaces* with sharing between contiguous cells. $N_L = 0.5+4+0.5 = 5$ $P_L = 5$ $P_L = N_L = 1/\bar{L}_3$	Two-dimensional interfaces† not shared with other α-objects. $N_L = 4$ $P_L = 8$ $P_L = 2N_L = 2(V_V)\alpha/\bar{L}_3$	Two-dimensional external object surface S.§ $N_L = 1,2,\ldots\ldots$ $P_L = 2,4,\ldots\ldots$ $P_L = 2N_L$
$S_V = 2P_L = 2N_L$	$(S_V)_\alpha = 2P_L = 4N_L$	$S/V = 2P_L / P_P$
$\bar{L}_3 = 2\bar{V} / \bar{S} = 2 / S_V$	$\bar{L}_3 = 4\bar{V}_\alpha / \bar{S}_\alpha = 4(V_V)_\alpha/(S_V)_\alpha$	$\bar{L}_3 = 4V/S$
$\bar{L}_3 = lp / 2P$	$\bar{L}_3 = lp/P = 4\bar{V}_\alpha / \bar{S}_\alpha$	$\bar{L}_3 = lp/P = 4V/S$
* Internal surface area referred to test volume (S_V) or to mean cell volume ($\bar{S}/\bar{V}$)	† Interface area of α-objects referred to test volume $(S_V)_\alpha$ or to mean particle volume ($\bar{S}_\alpha/\bar{V}_\alpha$)	§ External surface area referred to feature volume (S/V).

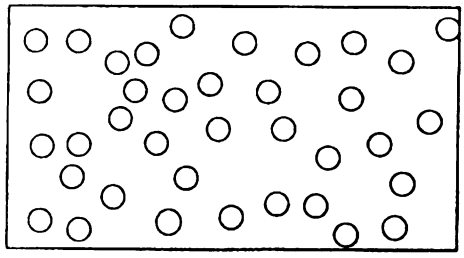

Figure 6.2 Example of an Isometric System of Lines[98]

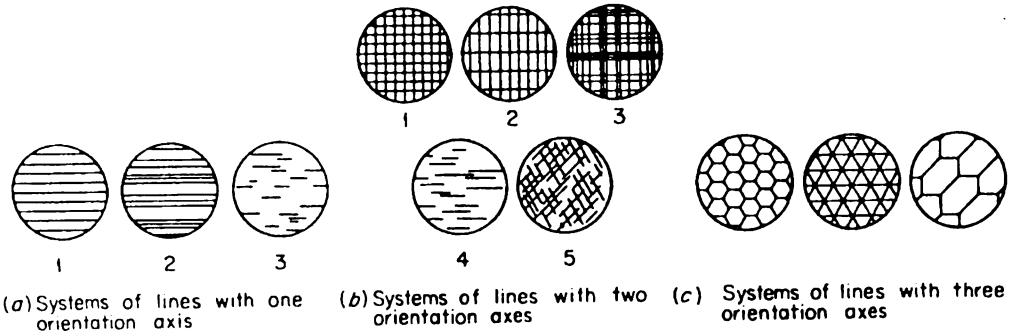

Figure 6.3 Examples of Completely Oriented System of Lines in a Plane[98]

In real structures the boundary lines of the systems appearing on the cross sections are either isometric or only partially oriented. Completely oriented systems of lines are relatively rare and occur only under exceptional circumstances. A partially oriented system of lines on a plane is defined as a system of lines in which only a part of the total length of lines is oriented in a definite direction. The remaining lines may either be

oriented in another preferred direction, or randomly and isometrically placed. Figure 6.4 gives a simple geometrical example of a partially oriented system of lines in which the long axes of randomly disposed ellipses are parallel.

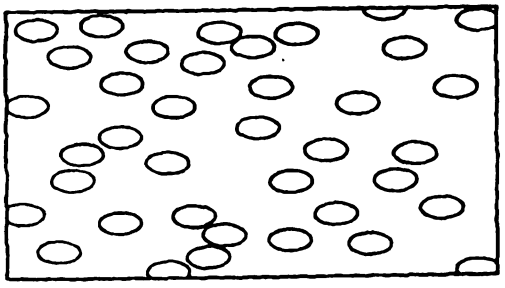

Figure 6.4 Example of Partially Oriented System of Lines[98]

Oriented damage phenomena (cracks, collapsed pores, etc.), however, occur quite often. Stereology treats such orientated structures at different lines, including systems of lines in a plane or in space, and system of surfaces in space.

6.1.3.1 *Systems of Lines in Plane*

As stated earlier, systems of lines in a plane can be completely or partially oriented. Figure 6.3 depicts lines that are equally or irregularly spaced, continuous, or discontinuous. When two or more orientation axes are present, as in Figures 6.3b and 6.3 c, the angle(s) formed by the axes must be specified. The grids in Figure 6.3c differ in

several respects. In grids c-1 and c-2, the line length along any orientation axis is the same; however, the lines are continuously straight only in c-2. Lengths of the lines in c-3 are greater in one direction than another.

Since the length of linear elements in a plane is proportional to the number of intersections made with a test line, for an oriented system of lines, the number of intersections with an array of straight parallel system of oriented (isometric) lines would vary markedly with the direction of the test array. This dependence of the number of intersections per unit length on the angle of the test array can be used to characterize the degree and types of orientation of a system of lines in a plane. A polar plot of P_L with respect to the orientation axis (axes), called the rose of lines of intersections,[98] provides convenient means of expressing the degree of orientation. The rose of an oriented system of lines can be obtained experimentally by applying a test array to the system of lines at equal angular increments with respect to the orientation axis, and determine P_L separately at each angle. By connecting the ends of the radius vectors by a smooth curve, giving the rose of orientation. As the number of orientation axes increases, the rose becomes more rounded, and for an isometric system of lines, the rose is a circular perimeter centered on the origin of coordinates.

The following relationship can be applied to completely oriented systems in plane with one axis of orientation.[88]

$$(L_A)_{or} = (P_L)_{\perp} \quad \text{.....(6.5)}$$

where, $(L_A)_{or}$ represents the length per unit area of the parallel (oriented) lines of the system, and $(P_L)_{\perp}$ is the number of intersections per unit length of the test array aligned in a direction perpendicular to the orientation axis. The relationship is equally valid for systems of equidistant, parallel straight lines and for arrays, linear segments with random lengths and locations.

In real structures the lines in a microsection are usually partially oriented. In a partially oriented system of lines in plane, part of the total lines is oriented in a definite direction (or directions). The remaining segments may have essentially a random orientation. The lines of a partially oriented system of lines in a plane can be divided into elementary straight segments that are very small and of equal length. Some or all segments will lie parallel to one or more definite directions (the orientation axes). The remaining segments are assumed to be oriented randomly, i.e., isometrically. From this point of view, a partially oriented system of lines may be regarded as consisting of two superimposed system of lines, i.e., and oriented portion and a random portion. To determine the specific lengths of the isometric and oriented portions of a partially oriented system of lines in a plane with one orientation axis requires only two measurements. These are $(P_L)_{\parallel}$ and $(P_L)_{\perp}$, where the subscripts indicate the directions of the test array with respect to the orientation axis. The length of the isometric and oriented segments of the system per unit area can be derived as follows:[88]

$$(L_A)_{is} = (\pi/2)\,(P_L)_{\parallel} \quad mm/mm^2 \qquad \text{.....(6.6)}$$

$$(L_A)_{or} = (P_L)_{\perp} - (P_L)_{\parallel} \text{ mm/mm}^2 \quad \text{.....(6.7)}$$

The total length of all lines per unit area in a partially oriented system of lines is the sum of the tow linear systems[88]

$$(L_A) = (L_A)_{is} + (L_A)_{or} \quad \text{.....(6.8)}$$

$$(L_A) = (P_L)_{\perp} + 0.571\ (P_L)_{\parallel} \quad \text{.....(6.9)}$$

Rose of intersections has been used to determine the preferred orientation of clasts in tillite deposit sample as shown in Figure 6.5. The rose of orientation has been constructed manually which is considered to be time and effort consuming.[99] Rose of orientation has been also used to detect the effect of casting direction on fiber orientation in concrete[100] as shown in Figure 6.6.

Constructing rose of orientation can be considered time and effort consuming and the preferred orientation provided by it may be considered not accurate enough,[99] for practical applications, the complete rose may not be too convenient. A simpler method is available for characterizing the degree of orientation of a system of partially oriented lines in a plane.

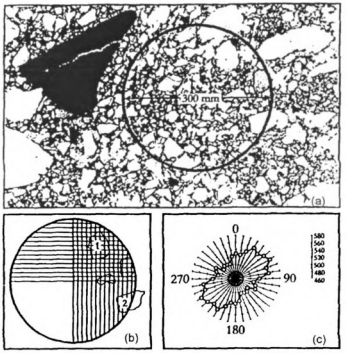

Figure 6.5 Applying Rose of Orientation Manually on Tillite Specimen[99]

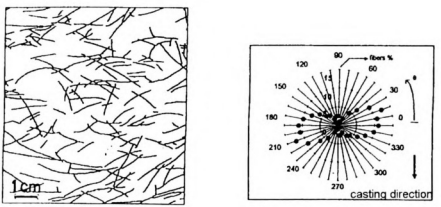

Figure 6.6 Using Rose of Orientation to Determine Fiber Orientation[100]

The length of oriented lines only per unit area is divided by the total length of all lines in the system per unit area. The resulting fraction gives and easily recognized, natural scale of anisotropy varying from 0 for no anisotropy to unity for a complete oriented system of lines. This ratio is called the degree of orientation Ω, and is defined as:[88]

$$\Omega_{12} = (L_A)_{or} / [(L_A)_{is} + (L_A)or] \quad \text{.....(6.10)}$$

$$\Omega_{12} = [(P_L)\perp - (P_L)\parallel] + [(P_L)\perp + 0.571\ (P_L)\parallel] \quad \text{.....(6.11)}$$

Table 6.3 summarizes the equations for systems of lines in a plane.

Table 6.3 Equations for System of Lines in Plane[88]

Type of system	Isometric lines $(L_A)_{is}$ =	Oriented lines $(L_A)_{or}$	Total specific line Length L_A =	Degree of orientation, Ω_{12}
Isometric	$1.571\ P_L$	—	$1.571\ P_L$	$\Omega_{12} = 0$
Oriented*	—	$(P_L)\perp\!\!\!\perp$	$1.571\ P_L$	$\Omega_{12} = 1.0$
Partially oriented†	$1.571\ (P_L)\parallel$	$(P_L)\perp - (P_L)\parallel$	$(P_L)\perp + 0.571(P_L)\parallel$	$\Omega_{12} = \frac{(P_L)_\perp - (P_L)_{//}}{(P_L)_\perp + 0.571(P_L)_{//}}$

* The subscript $\perp\!\!\!\perp$ symbol refers to measurements perpendicular to the orientation axis of an oriented system of (parallel) lines.
† Subscript $\perp$ and $\parallel$ symbols refer to direction of test array with respect to the orientation axis in partially oriented system of lines.

6.1.3.2 *Systems of Lines in Space*

The objects that will be presented in this section are not always true lines but features of the microstructure whose cross sections are significantly small compared with their longitudinal axis. Table 6.4 presents the equations relevant to systems of lines in space.[88]

Table 6.4 Equations for System of Lines in Space[88]

Type of System	Isometric Lines $(L_V)_{is}$ =	Oriented lines $(L_V)_{or}$ =	Total specific line length S_V =	Degree of orientation, Ω_{13}
Isometric	$2P_A$	—	$2P_A$	$\Omega_{13} = 0$
Oriented*	—	$(P_A)_{\perp\!\!\!\perp}$	$(P_A)_{\perp\!\!\!\perp}$	$\Omega_{13} = 1.0$
Partially oriented†	$2(P_A)_{\parallel}$	$(P_A)_{\perp} - (P_A)_{\parallel}$	$(P_A)_{\perp} + (P_A)_{\parallel}$	$\Omega_{13} = \frac{(P_A)_{\perp} - (P_A)_{//}}{(P_A)_{\perp} + (P_A)_{//}}$

6.1.3.3 *Systems of Surfaces in Space*

Even though sections through different planar structures appear to be identical, the spatial configuration may differ markedly. If just the total surface area of an oriented system of surfaces were desired, equations presented earlier still may be used for randomly oriented surfaces provided that a sufficient number of section planes were used in order to satisfy the requirement of randomness. In completely oriented systems of surfaces with one orientation axis, two important types are possible. In that case the systems have planar orientation if the planes are perpendicular to the orientation axis, and have linear

orientation if the planes are parallel to the orientation axis. In both cases, however, the analysis plane is parallel to the orientation axis. Table 6.5 presents equations for systems of isometric and completely oriented surfaces in space.[88]

Table 6.5 Equations for System of Surfaces in Space[88]

Type of System	Isometric Lines $(S_V)_{is}$ =	Oriented lines $(S_V)_{or}$ =	Total specific line length S_V =	Degree of orientation, Ω_{23}
Isometric	$2P_L$	—	$2P_L$	$\Omega_{23} = 0$
Oriented*	—	$(P_L)_{\perp}$†	$(P_L)_{\perp}$	$\Omega_{23} = 1.0$

*Applies to either completely planar or completely linear systems of surfaces under appropriate conditions.
† The subscript ⊥ symbol refers to direction of section planes perpendicular to oriented system of (parallel) planes.

For Partially oriented systems of surfaces in space, Figure 6.7 schematically presents possible classes of partial orientation (in addition to the isometric system), and designates the various orientation planes, orientation axes, and analysis planes.

In the linear system, the surfaces tend to lie parallel to the orientation axis and the orientation plane; in the planar system the surfaces tend to align themselves perpendicular to the orientation axis and parallel to the orientation plane; and in the planar-linear system, the surfaces have one orientation plane and an orientation axis parallel to the orientation plane in the direction of the longest unit dimension.[98]

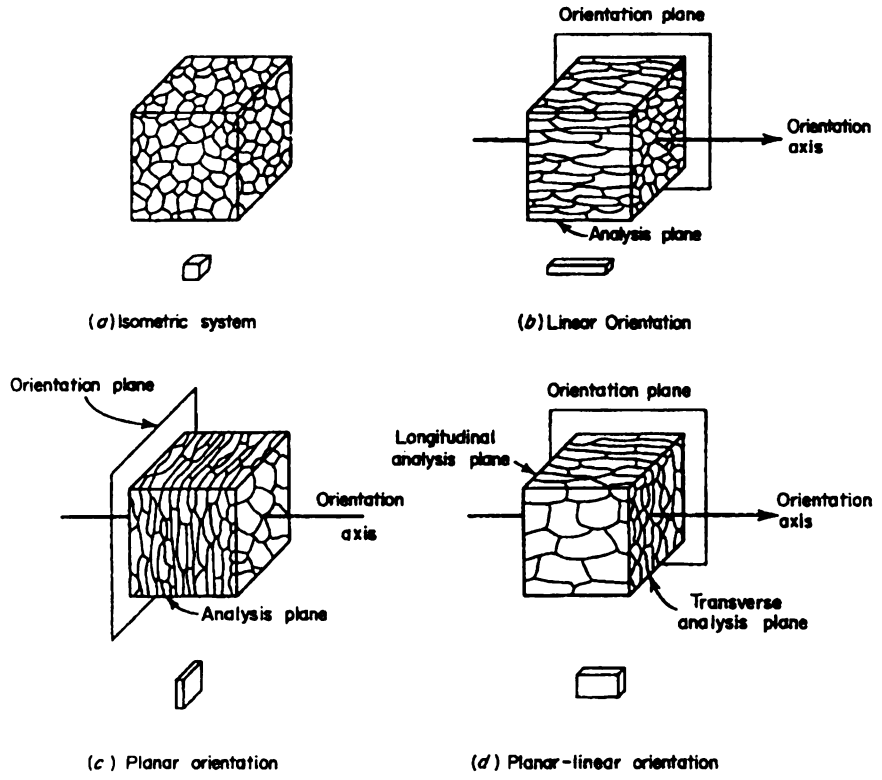

Figure 6.7 Classification of Partially Oriented Systems of Surfaces[98]

Table 6.6 presents equations for partially oriented systems of surfaces in space. In that table, the degree of orientation of partially oriented surfaces in space (Ω_{23}) is obtained by the following equation:[98]

$$\Omega_{23} = (S_V)_{or} / S_V \quad \text{.....(6.12)}$$

Table 6.6 Equations for Partially Oriented System of Surfaces in Space[88]

Type of orientation	Isometric surfaces $(S_V)_{is}$ =	Planar surfaces $(S_V)_{pl}$ =	Linear Surfaces $(S_V)_{lin}$ =	Total specific surface area S_V =
Planar†	$2(P_L)_{\parallel}$	$(P_L)_{\perp} - (P_L)_{\parallel}$	—	$(P_L)_{\perp} + (P_L)_{\parallel}$
Linear‡	$2(P_L)_{\parallel}$	—	$1.571[(P_L)_{\perp} - (P_L)_{\parallel}]$	$1.571(P_L)_{\perp} + 0.429(P_L)_{\parallel}$
Planar-linear§	$2(P_L)_{\parallel}$	$(P_L)_{\perp} - (P_L)_{\parallel}$	$1.571[(P_L)_{\mid} - (P_L)_{\parallel}]$	$(P_L)_{\perp} + {}_{0}.429(P_L)_{\parallel} + 0.571(P_L)_{\mid}$

All directions (perpendicular,⊥, and parallel,∥ and I)of test arrays are referred to orientation planes illustrated in Figure 6.7.

†‡ Subscripts ∥and ⊥ refer to direction of test array placed on the analysis plane.

§ Subscript∥ here refers to direction of test array placed on the longitudinal analysis plane.

Subscript I here refers to direction of test array placed ton the transverse analysis plane.

Subscript ∥ here refers to direction of test array placed on either the transverse or longitudinal analysis planes.

◊ The asterisks in Ω^{*}_{pl} and $\Omega^{*}_{l,m}$ specify planar and linear orientations in planar-linear orientations in the planar-linear system of surfaces.

6.1.4 Stereological Relationships

6.1.4.1 *Microcrack Spatial (3-D) Measurements*

- Specific Surface Area (S_{VC})

Specific surface area is the area of cracks per unit volume of concrete. It can be considered an indication about the percentage of cracks in the concrete volume and is expressed as follows:[95]

$$S_{VC} = \frac{4}{3\pi}(2L_{AC1} + L_{AC2}) \quad \text{.....(6.13)}$$

where, L_{AC1} = crack length per unit area of the first (horizontal) section (perpendicular to the direction of loading)

L_{AC2} = crack length per unit area of the second (vertical) section [perpendicular to the first (horizontal) section]

In the case of randomly oriented cracks, the above equation assumes the following form, with (2-D) measurement on one section sufficient to yield the specific surface area of cracks:[82,101]

$$S_{VC} = \frac{4}{\pi} L_{AC} \quad \text{.....(6.14)}$$

where, L_{AC} = length of cracks per unit test area.

Equation (6.13) is an easy and direct relationship but it is valid only for isometric structures, which is not the actual case in most of times. In order to determine specific surface area of cracks in case of the structures are not isometric, the cracks were assumed to be partially oriented planes in space, and as a result the specific surface area can be expressed as the following:

$$S_{VC} = (PL)_{TS} II + (PL)_{TS} \perp \quad \text{.....(6.14)}$$

- Volume Fraction (V_{VC})

Volume fraction is a parameter that gives an indication about how much concrete

specimen contains cracks which can affect most of concrete mechanical properties and it can be expressed as follows:

$$V_{VC} = \frac{A_{AC1} + A_{AC2}}{2} \quad \text{.....(6.15)}$$

where, A_{AC1}= crack area fraction of the first section (perpendicular to the direction of loading)

A_{AC2} = crack area fraction of the second section (perpendicular to the first section)

- Spacing in Space (λ_{CS})

Spacing of cracks in space can considerably affect the thermal properties of concrete such as thermal conductivity and thermal expansion which has a significant effect on concrete shrinkage. Crack spacing in space is considered as the mean free distance and expressed as the following:[102]

$$\lambda_{CS} = \frac{4(1 - V_{VC})}{S_{VC}} \quad \text{.....(6.16)}$$

where, V_{VC}= crack volume fraction

S_{VC} = crack specific surface area

- Crack Width in Space (W_{CS})

Cracks are manifested as lines of various thickness on (2-D) cross. The (2-D) crack widths are essentially of minimum crack width measured at non-perpendicular angles to plane of cracks. Figure 6.8 shows a schematic presentation of crack widths (W_{CP1} and

W_{CP2}) in plane due to cutting by the proposed two perpendicular sections, the actual crack width (W_{CS}) can be obtained as follows:

$$Sin\zeta = \frac{W_{CS}}{W_{CP1}} \quad \text{.....(6.17)}$$

$$Cos\zeta = \frac{W_{CS}}{W_{CP2}} \quad \text{.....(6.18)}$$

where, ζ = angle between crack width in the first section (perpendicular to the direction of loading) and horizontal axis.

W_{CP1}= crack width in the first section (perpendicular to the direction of loading)

W_{CP2}= crack width in the second section (perpendicular to the first section)

Since,

$$Sin^2\zeta + Cos^2\zeta = 1 \quad \text{.....(6.19)}$$

From equations (6.17), (6.18) and (6.19), the following equation can be derived,

$$(\frac{W_{CS}}{W_{CP1}})^2 + (\frac{W_{CS}}{W_{CP2}})^2 = 1 \quad \text{.....(6.20)}$$

which yields the following expression for (3-D) crack width:

$$W_{CS} = \frac{1}{\sqrt{\frac{1}{W_{CP1}^2} + \frac{1}{W_{CP2}^2}}} \quad \text{.....(6.21)}$$

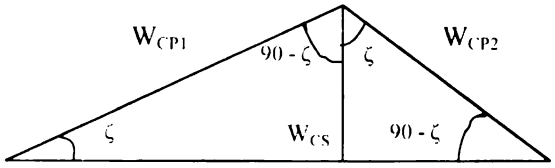

Figure 6.8 Schematic Presentation of The Relationship between Projected and Actual Crack Widths

- Degree of Orientation in Space (Ω_{CS})

Degree of orientation of cracks in space can be considered a useful quantitative descriptor of the direction and the attributes of cracks in concrete. Orientation of cracks can affect transport properties, permeability, and diffusion of chemical species in concrete. Throughout the research study, the cracks were assumed to be partially oriented planes in space, and the following expression was developed to determine its degree of orientation.

$$\Omega_{CS} = \frac{[(PL)ts\perp - (PL)tsII]}{[(PL)ts\perp + (PL)tsII]} \quad \text{.....(6.22)}$$

where, $(PL)ts\perp$ or $(PL)tsII$ = number of point intersections per unit length of superimposed array of equally spaced parallel test lines oriented in a predetermined direction. Subscripts "$\perp$"and "II" refer to test lines running perpendicular and parallel to the preferred orientation of cracks. Subscript "t" refers to the total point intersections in a certain direction. Subscript "s" refers to the point intersections in space.

- Tortuosity in Space (T_{CS})

Tortuosity of cracks in space is a shape index reflecting on the nature of concrete cracking at failure, and can be expressed as follows:

$$T_{CS} = \frac{T_{CP1} + T_{CP2}}{2} \quad \text{.....(6.23)}$$

where, T_{CP1} = crack tortuosity in plane for the first section (perpendicular to the direction of loading)

T_{CP2} = crack tortuosity in plane for the second section (perpendicular to the first section).

6.1.4.2 *Void Spatial (3-D) Measurements*

- Void Size Distribution

Generally, the analyses for void size distribution are based on the following assumptions: (a) the particle has spherical shapes and (b) the distribution of particle size can be represented by a discontinuous distribution. Analytical methods for calculating the size distribution of spheres may be classified into three major categories, according to the type of planar measurement performed; (1) Section diameters, (2) Section areas, and (3) section chords. Schwartz-Saltykov (diameter) analysis method[88] was employed throughout the study. The void sizes may be broken down into any number of groups up to 15, depending on the required precision. Saltykov introduced the symbol Δ, defined as the ratio of D_{max} to the total number of groups, K. The diameter of voids in the first group equals Δ, that of the second group equals 2Δ, etc., and the diameter of the larges voids, $D_{max} = k\Delta$.

Table 6.7 presents the nomenclature adopted for designating the sizes and numbers of voids and sections. The working equations can be expressed as the following:[88]

$$(N_{VV})_j = \frac{1}{\Delta}\sum_{i=j}^{k}\alpha_i (N_{AV})_i \qquad \text{.....(6.24)}$$

where, the numerical coefficient α_i was calculated and provided in tables by Saltykov.[92] The general equation for the number of voids of any size group per unit volume is

$$(N_{VV})_j = \frac{1}{\Delta}[\alpha_i (N_{AV})_i - \alpha_{i+1}(N_{AV})_{i+1} - \alpha_{i+2}(N_{AV})_{i+2} - \cdots\cdots - \alpha_k (N_{AV})_k] \qquad \text{.....(6.25)}$$

where, i and j assume integer values from 1 to k equals the total number of class intervals. The index j is constant in each size group, but i varies from i=j through i+1, i+2, etc. up to the k_{th} class interval.

Schwartz-Saltykov method is valid only for spherical features; hence, it can't be applied for ellipsoid voids. Ellipsoid voids may be formed in concrete as pore collapse due to projectile loads. Dehoff analysis method[108] is a modification of Schwartz-Saltykov method to determine the size distribution of ellipsoid voids. Dehoff proposed to divide the ellipsoid voids into k size classed, each class be Δ the same as Schwartz-Saltykov method, but Δ in that case can be expressed as:[103]

Table 6.7 Nomenclature Used in Schwartz-Saltykov Method

Group Number	Range of Section Diameters mm	Number of Sections per mm^2 $(N_A)_i$	Diameter of voids mm	Number of voids per mm^3 $(N_V)_j$	Distribution (%)
1	0 to Δ	$(N_{AV})_1$	Δ	$(N_{VV})_1$	$(D_{st})_1$
2	Δ to 2Δ	$(N_{AV})_2$	2Δ	$(N_{VV})_2$	$(D_{st})_2$
3	2Δ to 3Δ	$(N_{AV})_3$	3Δ	$(N_{VV})_3$	$(D_{st})_3$
.	.	.	.	.	.
.	.	.	.	.	.
.	.	.	.	.	.
j	(i-1)Δ to iΔ	$(N_{AV})_j$	jΔ	$(N_{VV})_j$	$(D_{st})_j$
.	.	.	.	.	.
.	.	.	.	.	.
.	.	.	.	.	.
k	(k-1)Δto kΔ	$(N_{AV})_k$	kΔ	$(N_{VV})_k$	$(D_{st})_k$

$$\Delta = \frac{(W_{cv})_{max}}{k} \qquad \text{.....(6.26)}$$

where, $(W_{cv})_{max}$ = the minor axis of the ellipsoid voids in the largest size class.

Dehoff proposed the following formulas for the number of voids of any size group per unit volume and working equation:

$$(N_{Vcv})_i = \frac{1}{k(q)\Delta}\sum_{i=j}^{k}\alpha_i (N_{Acv})_i \qquad \text{.....(6.27)}$$

$$(N_{Vcv})_i = \frac{1}{k(q)\Delta}[\alpha_i (N_{Acv})_i - \alpha_{i+1}(N_{Acv})_{i+1} - \alpha_{i+2}(N_{Acv})_{i+2} - \cdots - \alpha_k (N_{Acv})_k] \text{...(6.28)}$$

where, K(q) = shape factor for the ellipsoid voids, it is a function of the shape coefficient (q).

$$q = \frac{(W_{ev})_{av}}{(L_{ev})_{av}} \quad \text{.....(6.29)}$$

where, $(W_{ev})_{av}$ = the average minor axis for ellipsoid voids.

$(L_{ev})_{av}$ = the average major axis for the ellipsoid voids.

- Volume Fraction (V_{VV})

Voids volume fraction is a useful quantitative descriptor of the air content in concrete. The air content in concrete is a paramount importance for the mechanical properties of concrete and for free-thaw resistance. Volume fraction of voids can be determined using the same stereological principles used for cracks as follows:

$$V_{Vv} = \frac{A_{AV1} + A_{AV2}}{2} \quad \text{.....(6.30)}$$

where, A_{AV1}= void area fraction of the first section (perpendicular to the direction of loading)

A_{AV2}= void area fraction of the second section (perpendicular to the second section)

- Number per Unit Volume (N_{VV})

Number of voids per unit volume provides an indication about the distribution of the total voids volume fraction in concrete. Number of voids per unit volume can be expressed as

follows:[88]

$$N_{VV} = \frac{2 \times m \times N_{AV}}{\pi} \quad \text{.....(6.31)}$$

where, m = the mean value of the reciprocals of the circle diameters on the test section, which can be obtained by the following formula:[88]

$$m = \frac{\sum_{d_i=1}^{n} (1/d_{V1}) + (1/d_{V2}) + (1/d_{V3}) + \ldots\ldots\ldots + (1/d_{Vn})}{n_v} \quad \text{.....(6.32)}$$

where, d_{v1} = the diameter of the first void in the section of interest.

d_{v2} = the diameter of the second void in the section of interest.

d_{v3} = the diameter of the third void in the section of interest.

d_{vn} = the diameter of n voids in the section of interest.

n_v = number of voids in the section of interest.

Equation (6.31) is valid for spherical voids. In case of ellipsoid voids, the following equation may be used:[98]

$$N_{Vev} = \frac{1}{\beta_1} \times \frac{N_{Aev}^{1.5}}{V_{Vev}^{0.5}} \quad \text{.....(6.33)}$$

where, V_{Vev} = volume fraction of the ellipsoid voids.

β_1 = the dimensionless shape coefficient that relates the object volume and its mean cross-sectional area.

A mathematical expression was developed for the dimensionless shape coefficient and proposed as follows:

$$\beta_1 = 0.7683(A_{Sev})_{av}^{0.834} \quad \text{.....(6.34)}$$

where, $(A_{Sev})_{av}$ = mean value of the ellipsoid voids aspect ratio in the section of interest.

- Specific Surface Area (S_{VV})

Specific surface area of voids is the surface area of voids per unit volume of concrete. Simulating voids as partially oriented linear systems of surfaces in space yields the following expression for specific surface area:

$$S_{VV} = 1.571(PL)ts\perp + 0.429(PL)tsII \quad \text{.....(6.35)}$$

where, $(PL)ts\perp$ or $(PL)tsII$ = number of point intersections per unit length of superimposed array of equally spaced parallel test lines oriented in a predetermined direction. Subscripts "$\perp$"and "II" refer to test lines running perpendicular and parallel to the preferred orientation of voids. Subscript "t" refers to the total point intersections in a certain direction. Subscript "s" refers to the point intersections in space.

- Mean Diameter in Space (d_{mvs})

Mean diameter of voids provides a quantitative descriptor of the average size of voids in concrete. Mean diameter of voids can be derived as follows:

$$\text{Volume of sphere (V)} = \frac{4}{3}\times\pi\times(\frac{d_v}{2})^3 \quad \text{.....(6.36)}$$

which yields

$$d_v = \sqrt[3]{\frac{6}{\pi}\times V} \quad \text{.....(6.37)}$$

where, d_v = void diameter

In order to obtain the mean diameter of voids in space, volume of voids should be divided by the number of voids in the section of interest yielding the following expression:

$$d_{mvs} = \sqrt[3]{\frac{6 \times V_{VV}}{\pi \times N_{VV}}} \quad \text{.....(6.38)}$$

- Spacing in Space (λ_{VS})

Spacing voids in concrete is an important factor to evaluate air-entrained admixtures. Large spacing lead to inefficient influence of air-entrained in concrete and as a result, the probability of concrete deterioration due to freeze-thaw increases. Close spacing can adversely affect concrete mechanical properties. Voids spacing in space, can be determined using the same equation proposed for cracks.

$$\lambda_{VS} = \frac{4(1 - V_{VV})}{S_{VV}} \quad \text{..... (6.39)}$$

where, V_{VV} = void volume fraction

S_{VV} = void specific surface area

- Specific Surface (S_{SV})

Specific surface is the surface area of voids per unit volume of voids and quantifies the irregularity of void surfaces. Void surfaces irregularity is directly proportional to specific surface area value which could be expressed as follows:

$$S_{SV} = \frac{S_{VV}}{V_{VV}} \quad \text{.....(6.40)}$$

where, S_{VV} = void specific surface area

V_{VV} = void volume fraction

6.1.4.3 *Aggregate Spatial (3-D) Measurements*

Aggregate size distribution, volume fraction (V_{vg}), specific surface area (S_{vg}), mean diameter in space (d_{mgs}), spacing in space (λ_{vg}), and degree of orientation in space (Ω_{gs}) can be determined using the same equations for voids. Some measurements which are used particularly with aggregates are introduced below.

- Degree of Orientation in Space (Ω_{gS})

Degree of orientation of aggregate can be obtained assuming the aggregates are partially oriented linear systems of surfaces in space. The degree of orientation can be expressed as follows:

$$\Omega_{gS} = \frac{[(PL)_{ts}\perp - (PL)_{ts}II]}{[(PL)_{ts}\perp + 0.273(Pl)_{ts}II]} \quad \text{.....(6.41)}$$

where, $(PL)ts\perp$ or $(PL)tsII$ = number of point intersections per unit length of superimposed array of equally spaced parallel test lines oriented in a predetermined direction. Subscripts "$\perp$"and "II" refer to test lines running perpendicular and parallel to

the preferred orientation of aggregates. Subscript "t" refers to the total point intersections in a certain direction. Subscript "s" refers to the point intersections in space.

- Complexity index in space (CI_{gS})

Complexity index in space reflects on the shape of the aggregate particles, and can be expressed as follows:[88]

$$CI_{gs} = \frac{S_{Vg}}{V_{Vg}} \quad \text{.....(6.42)}$$

where, S_{vg} = specific surface area of aggregates

V_{Vg} = aggregate volume fraction

- Number per Unit Volume (N_{Vg})

Simulating aggregate shape as discs, number of aggregates per unit volume can be obtained using the following formula:[88]

$$N_{Vg} = \frac{8 \times E \times N_{Ag}}{\pi^2} \quad \text{.....(6.43)}$$

where, E = the mean value of the reciprocals of the disk lengths on the section plane.

N_{Ag} = number of aggregate particles per unit area of section of interest.

$$E = \frac{\sum_{L_g=1}^{n} (1/L_{g1}) + (1/L_{g2}) + (1/L_{g3}) + \cdots\cdots + (1/L_{gn})}{n_g} \quad \text{.....(6.44)}$$

where, L_{g1} = length of the first aggregate particle in the section of interest.

L_{g2} = length of the second aggregate particle in the section of interest.

L_{g3} = length of the third aggregate particle in the section of interest.

L_{gn} = length of "n" aggregate particles in the section of interest.

n_g = number of aggregate particles in the section of interest.

- Mean Thickness of Aggregates (t_{mg})

Simulating aggregate shape as discs, the mean thickness of aggregates can be obtained using the following formula:

$$t_{mg} = \frac{\pi \times G}{4 * E} \qquad \text{.....(6.45)}$$

where, G = the mean value of the width-to-length ratios of disc sections.

$$G = \frac{\sum_{\Gamma_g=1}^{n} (1/\Gamma_{g1}) + (1/\Gamma_{g2}) + (1/\Gamma_{g3}) + \cdots\cdots + (1/\Gamma_{gn})}{n_g} \qquad \text{.....(6.46)}$$

where, Γ_{g1} = width/length ratio of the first aggregate particle in the section of interest.

Γ_{g2} = width/length ratio of the second aggregate particle in the section of interest.

Γ_{g3} = width/length ratio of the third aggregate particle in the section of interest.

Γ_{gn} = width/length ratio of "n" aggregate particle in the section of interest.

n_g = number of aggregate particles in the section of interest.

6.1.4.4 *Fibers Spatial (3-D) Measurements*

The volume fraction (V_{Vf}), spacing in space (λ_{fs}), and specific surface area (S_{Vf}) of fibers can be expressed using the same formulas as voids, and their complexity index in space (CI_{fs}) can be determined using the same formula as aggregates. The following expressions are used particularly with fibers:

- Number per Unit Volume (V_{VF})

Number per unit volume of cylindrical fibers can be expressed as follows:[95]

$$N_{VF} = \frac{1}{\beta 2} \times \frac{N_{AF}^{1.5}}{V_{VF}^{0.5}} \quad \text{.....(6.47)}$$

where, N_{AF} = number of fibers per unit area.

V_{VF} = fibers volume fraction.

β_2 = the dimensionless shape coefficient that relates the object volume and its mean cross-sectional area.

A mathematical expression is developed for the dimension less shape coefficient.

$$\beta_2 = 0.3473(A_{SF})_{av} + 1.2251 \quad \text{.....(6.48)}$$

where, $(A_{SF})_{av}$ = mean value of fibers aspect ratio in the whole section of interest.

- Mean Diameter in Space (d_{mfs})

Mean diameter of fibers in space can be derived using the same procedures use to determine the mean diameter of voids in space taking into account that the fibers are

cylindrical in shape.

Volume of cylinder fiber

$$(V_{if}) = \frac{\pi \times d_{if}^{\,2}}{4} \times h_{if} \quad \text{.....(6.49)}$$

where, d_{if} = diameter of each individual fiber.

h_{if} = hHeight of each individual fiber.

$$V_{if} = \frac{V_{Vf}}{N_{Vf}} \quad \text{.....(6.50)}$$

where, V_{if} = volume of each individual cylindrical fiber

V_{VF} = fiber volume fraction in the section of interest.

N_{VF} = number of fibers in the section of interest.

From equations (6.49) and (6.50), the following expression can be obtained

$$d_{mfs} = 2 \times \sqrt{\frac{V_{Vf}}{\pi \times h_{mf} \times N_{Vf}}} \quad \text{.....(6.51)}$$

where, h_{mf} = average height of fibers in section of interest.

6.2 STATISTICAL ANALYSIS

6.2.1 Preface

Petrographic investigation and/or quantitative microscopic analysis of concrete require proper sampling of concrete system to represent the whole structure. Insufficient or biased selection of samples may lead to erroneous conclusions or misleading judgment about the structure under investigation; on the contrary, an excess number of samples could increase the level of effort and cost as well as time without viable gains in reliability of the end results. There are general guidelines to follow for sampling of concrete materials[104] or concrete specimens[105] for particular tests. There are also some guidelines relevant to petrographic investigation of concrete,[10,106,107] and to quantification of some of concrete features[108,109] (e.g., air voids or cement phases). Although there are some recommendation have been made for selection of a viable sample size for measurement of strength,[110,111] specific guides for selection of sample size in quantitative microscopic analysis of concrete systems are not available. The investigation reported herein developed data on variability of concrete microcrack systems based on which statistical criteria were developed for sampling of concrete systems for the purpose of quantitative microscopic analysis.

6.2.2 The Sampling Scheme

Given the nature and local variations of damage in a structure, an iterative approach would be undertaken when an initial sampling scheme is refined in light of the information generated. The steps involved in sampling and analysis of structures and verification of sample size are shown below.

6.2.2.1 *Preliminary sub-regioning*

This step divides the volume of concrete to regions with relatively uniform damage conditions as shown in Figure 6.9. This step can be implemented iteratively, with the sub-regioning scheme refined in light of the generated data. The sub-regions are not necessarily equal in size; they may be finer near severely damaged locations. Also, in the case of a structure with uniform damage condition; the whole structure may be treated as one sub-region. The initial decision on sub-regioning would be made based on an initial condition assessment which could simply involve surface observations. The data generated with this initial sub-regioning can then be used to develop more refined sub-regions scheme. Samples (cores) taken from each sub-region will be used to determine the means and variance of different microcracks and voids characteristics within each sub-region. This data can be used to determine the statistical significances of differences between sub-regions. These analyses provide the basis to refine sub-regioning by merging the sub-regions with statistical comparable conditions or by dividing sub-regions within which excess variations of quantified microstructural characteristics occur.

6.2.2.2 *Coring and sectioning*

Once the concrete system is sub-regioned, the next step involves extraction of statistically representative samples from each sub-region as shown in Figure 6.10. For the purpose of microstructural investigation of concrete, sampling involves:

- Coring from each sub-region (extraction of multiple cores from each sub-region)
- Cutting each core into two perpendicular (horizontal and vertical) sections.

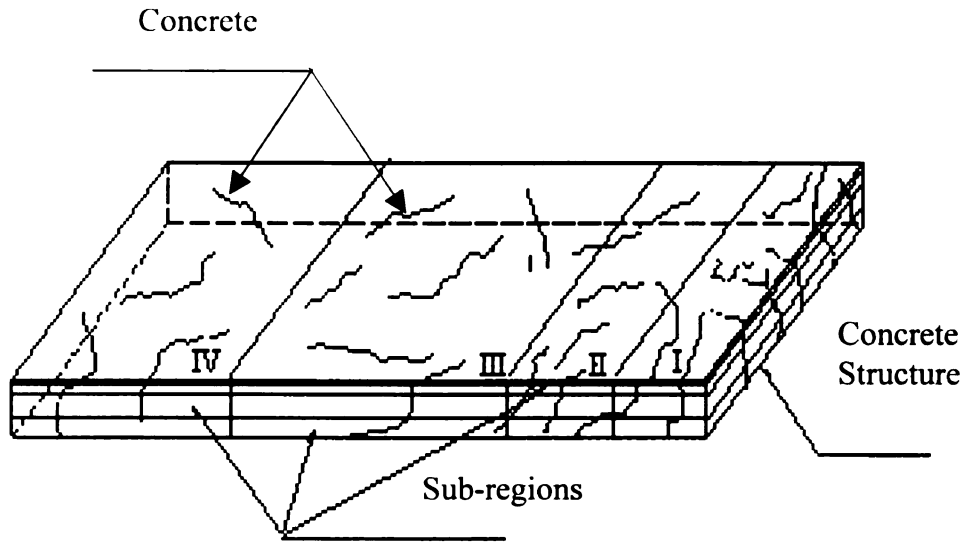

Figure 6.9 Example of Concrete System Divided into Sub-regions

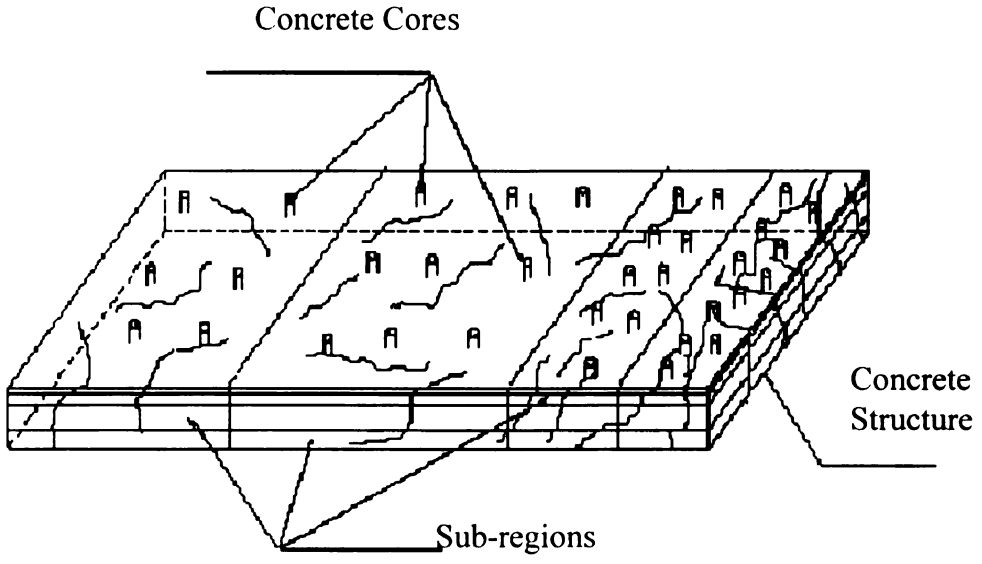

Figure 6.10 Example of Coring Concrete System

The variables involved in this sampling scheme include the diameter, length and number of cores. It is generally recommended that the diameter of drilled cores should not be less than three time the maximum aggregate size. [106] In order to reduce the damage to structure associated with coring, 100 mm (4 in) diameter cores may be used in most applications. The length of core depends partly on the thickness of sub-regions and the whole system.

It should be emphasized that the core should penetrate all sub-regions under investigation; (100 – 125 mm) (4 - 5 in) core length is recommended in case of one vertical sub-region for easy sectioning. Statistical criteria, to be reviewed later, determine the required number of cores obtained from each sub-region. Cores may be extracted from randomly selected locations within each sub-region. Water diamond-bit coring is the recommended method of sampling concrete when core diameters are 75 mm (3 in) or lesser, the core bits used should be designated by internal diameter as the loss of core diameter on a nominal 50 mm (2 in) diameter coring bit is considerable. For concrete of restricted dimensions, such as pavements and slabs or precast products, wet diamond sawing of samples is preferable to coring, as it is less likely to cause damage.

After cores are obtained, each core should be cut in two perpendicular sections [horizontal (XY) and vertical (YZ)] as shown in Figure 6.11. It is recommended to cut one section in the direction of applied load, and the second in perpendicular. Concrete should be cut with wet diamond-saws in order to prevent major damage. The aim of cutting two perpendicular sections is to generate sufficient in-plane (2-D) measurements for stereological analysis which yield viable data on (3-D) characteristics of microcrack and void system. After sectioning, depending on available facilities and tools, 75 × 75 ×

50 mm (3 × 3 × 2 in) square specimens should be cut from horizontal and vertical sections for preparation and analysis.

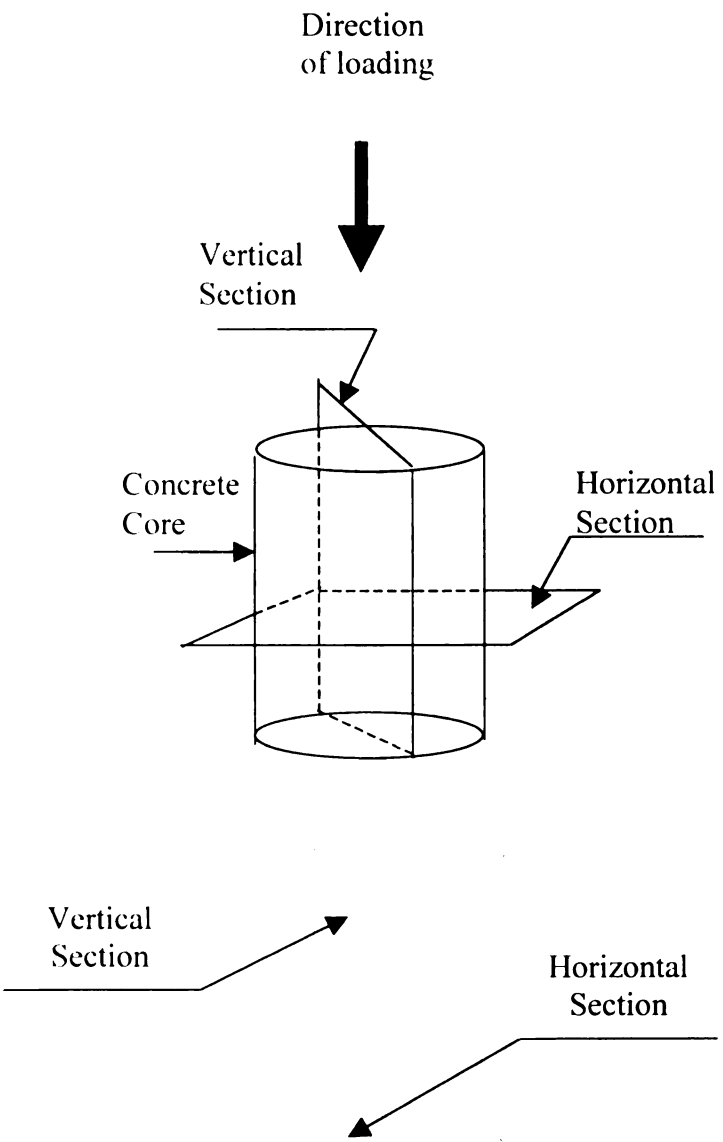

Figure 6.11 Sectioning of Concrete Cores

6.2.2.3 *Image acquisition and microstructural analysis*

Concrete specimens were prepared to produce (in the captured microscopic images) a reasonably sharp contrast between features of interest and the body of concrete. Specimen preparation was performed following the procedures illustrated in section 4.2.4 for ESEM and fluorescent microscopy investigations. Microcrack length per unit area was selected as the key probe for analysis of concrete microstructure system. Crack length has been selected because it tends to be affected in a more noticeable way by the load and damaging effects on concrete,[23] crack width may come after crack length. Crack length per unit area was determined using equation (5.1). The parameter in space corresponding to the crack length per unit area is the specific surface area of cracks. Specific surface area of cracks was determined using equation (6.13).

6.2.2.4 *Assessment of the required number of images, cores and sub-regions*

Statistically viable results can be obtained if a minimum number sample size is used in analysis; the sample size depends on the number of cores, and the scanned areas from each cross section. As far as capturing images for a cross section is concerned, a measurement such as crack length per unit area (L_{AC}) can be statistically compared when different percentages of area are scanned in order to determine condition which yield viable results without excess effort.

The required number of cores per sub-region may be determined assuming that each sub-region as a population of infinite number of cores. The specific surface area of cracks (S_{VC}) (the average of all specific surface areas from this infinite number of cores) can be used as the key measure in statistical analyses. For this purpose statistical distribution of

all specific surface areas can be assumed to have normal distribution with the calculated value of specific surface area as population mean with unknown finite variance. The sufficient number of cores for desired half-width (h), confidence coefficient (1-α), and planning value of standard deviation (σ) may be determined using the following equation:[112]

$$n = \frac{z^2 \sigma^2}{h^2} \quad \text{.....(6.52)}$$

where, z = z(1-α/2), the percentile of standard normal distribution with n-1 degree of freedom.

n = average number of cores required at the designated percent level of confidence.

σ = population standard deviation (for specific surface area of cracks within each sub-region).

h = acceptable error (precision) or half the maximum acceptable confidence interval.

α = the level at which the risk of making a Type I error is to be controlled.

The adequacy of the number of sub-regions may be checked through statistical/comparison of the variance of specific surface area of cracks between sub-regions. Planning sample sizes with power approach has been adapted for this purpose. The main procedure for implementing the power approach is to use the power tables[113] in a reverse way in order to check if the required power is reached. It should be emphasized that these tables (tables for determining sample size in analysis of variance-fixed factor level model) were established with noncentrality parameter when all factor levels are to

have equal sample sizes; hence, this approach can be used properly when equal number of cores are extracted from all sub-regions. These tables require a minimum range of factor level means for which it is important to detect differences between the means with high probability. The minimum range can be obtained using the following equation:[113]

$$\nabla = \max(\mu_i) - \min(\mu_i) \quad \text{.....(6.53)}$$

where, ∇ = the difference between maximum and minimum means of specific surface area between sub-regions.

$\max(\mu_i)$ = maximum mean of the specific surface area of cracks.

$\min(\mu_i)$ = minimum mean of the specific surface area of cracks.

By obtaining ∇, the ratio (∇ / σ) can be determined, (where σ is the standard deviation in probability distributions of the mean value of specific surface area of cracks in the structure - between sub-regions). Using the previous ratio, selected (α) level, and the preliminary number of sub-regions (r), the power of the test ($1-\beta$) can be obtained, where (β) is the risk of making a Type II error. Through comparison of the obtained power from tables $(1-\beta)_T$ against the required power $(1-\beta)_R$, the adequacy of the number of sub-regions can be checked. If $(1-\beta)_T \leq (1-\beta)_R$, the preliminary number of sub-regions is adequate and reliable. If $(1-\beta)_T > (1-\beta)_R$, the preliminary number of sub-regions need to be increased (or the results should be accepted at a lower designated test power).

If the damage levels at different locations within the structure are to be compared under investigation, one-way "ANOVA", and "F-test" followed by Tukey's procedure[114] may be used. Tukey's procedure involves the use of another probability distribution called the studentized range distribution. This distribution depends on two parameters: a numerator degree of freedom (m_n) and a denominator degree of freedom (υ). Values of ($Q_{\alpha,m,\upsilon}$)

"upper-tail α critical value of the studentized range distribution with (m_n) numerator degree of freedom and (υ) degree of freedom" are available in table form[114] [tables for critical values ($Q_{\alpha,m,\upsilon}$) for the studentized range distribution]. The values of [$Q_{\alpha,i,i(j-1)}$] can then be used to obtain simultaneous confidence intervals for all pairwise differences, where I is the total number of sub-regions in the whole structure, and J total number of cores per sub-region. Tukey's procedure can be used as follows:

$$\omega = Q_{\alpha,i,i(j-1)} \times \sqrt{\frac{MSE}{j}} \qquad \text{.....(6.54)}$$

where, ω = the numerical value used for comparison.

i = total number of sub-regions in the whole structure.

j = total number of cores per sub-region.

$Q_{\alpha,i,i(j-1)}$ = studentized range distribution (can be obtained from tables).

MSE = mean square error of specific surface area (can be obtained from ANOVA).

The comparison can then be carried out as follows. If $\delta\mu \leq \omega$, there is no significant difference between the two consecutive sub-regions under investigation. If $\delta\mu > \omega$, there is a significant difference between the two consecutive sub-regions under investigation. In this approach, δμ is the difference of means of specific surface areas for two sub-regions in the whole structure, $\delta\mu = \mu_k - \mu_{k+1}$ in which μ_k is the mean specific surface area for a certain sub-region, and μ_{K+1} is the mean of specific surface area of the successor sub-region.

ANOVA and F-test may be used to determine if there is a significant difference between the specific surface area of cracks between sub-regions; the Tukey's procedure may be

used to detect sub-regions which contain that difference. If the output of ANOVA shows that there is no significant difference between sub-regions, it may mean that the damage is uniformly distributed within the whole structure and it may also give an indication about the adequacy of the number of sub-regions.

6.2.3 Application of The Proposed Sampling Scheme

In order to assess the applicability of the proposed sampling scheme, it was applied to laboratory concrete specimens. Two concrete mixtures (normal-strength and relatively-high strength) were considered in the laboratory test program. Type I Portland cement and natural sand were used in both mixtures. Crushed limestone with maximum particle size of 19 mm (3/4 in) was used as coarse aggregate in mix I (normal-strength), with cement : fine aggregate : coarse aggregate : water mass ratios of 1 : 1.59 : 1.98 : 0.514, targeting 28-day compressive strength of 33 MPa (4750 psi) . This mix was air-entrained, and provided an air content of 3.5 percent with a slump of 190 mm (7.5 in). Mix II (relatively high-strength) incorporated natural granite with maximum particle size of 10 mm (3/8 in) as coarse aggregate; it also incorporated silica fume and superplasticizer, with cement: fine aggregate : coarse aggregate : water : silica fume mass ratios of 1 : 1.7 : 0.9: 0.42 : 0.2, targeting 28-day compressive strength 43 MPa (6120 psi). This mix provided 1.9 percent air content and a slump of 64 mm (2.5 in). Cylindrical specimens with 102 mm (4 in) diameter by 203 mm (8 in) height were prepared for compression testing, and 76 × 76 × 305 mm (3 × 3 × 12 in) prismatic specimens for microstructural analysis. Molded specimens were kept moist for 24 hours, after which they were demolded and moist cured at 100% relative humidity and 22°C (72°F) for 28 days, and

then conditioned at 50% relative humidity and 22°C (72°F) for 180 days prior to testing. Three cylinders from each mixture were tested to check the targeted compressive strength, and 8 prisms (4 undamaged prisms and 4 damaged prisms) from each mixture were used for microstructural analysis. Specimens were damaged by subjecting them to peak compressive stress (and then unloading them); this process left the specimens intact for subsequent cutting and preparation for the purpose of microstructural analysis. Undamaged and damaged prisms were cut into two perpendicular sections as described before yielding 16 sections with 75 x 75 x 50 mm (3 in x 3 in x 2 in). Both environmental scanning electron microscopy (ESEM) and fluorescent microscopy were used in the investigation. Half of the cut sections were prepared using Wood's metal impregnation for ESEM analysis and the other half were prepared using ink-fluorescent epoxy impregnation for fluorescence microscope. 125X, 250X, and 500X magnification factors were considered in this study according to 3.4. These magnifications suit the range of microcrack dimensions in concrete; the highest magnification (500 X) has not been used commonly with concrete; the current investigation was to assess the potential for detection of finer microcracks at higher magnification. Representative quantitative data on concrete microstructure would be produced if a sufficient fraction of concrete surface were analyzed. In order to establish such representative fraction, the following percentages of surface areas in both fluorescent microscopy and ESEM were scanned:

- 125X: 0.5%, 1%, 2%, 3%, and 4%
- 250X: 0.5%, 1%, and 2%
- 500X: 0.5%, 1%, and 2%

Each section (damaged or undamaged) was scanned three times for each combination of

magnification factors and percent scanned area (using each of the two microscopy techniques). Images were captured randomly from concrete surfaces suing a semi-automatic travel stage. Crack length per unit area (L_{AC}) for each section and Specific surface area (S_{VC}) of cracks for each two perpendicular sections were determined using the formulation presented earlier. Statistical analysis (equation 6.52) was also used to determine the adequate number of cores to be obtained from each sub-region.

6.2.4 Results and Discussion

Tables 6.8 and 6.9 show crack length per unit area (L_{AC}), mean values and standard deviation of 3 replicated measurements on the same section by ESEM and fluorescent microscopy for undamaged and damaged specimens at different magnification levels (125X, 250X, and 500X) of mix I (normal-strength) with different percentages of scanned areas for sections (X-Y) and (Y-Z) respectively. Tables 6.10 and 6.11 show the similar results for mix II (relatively high-strength). Statistical analyses (t-test at 5% level of significance, and paired comparison of means) were used to detect if there is any significant difference between measurements at different percentages.

Table 6.8 Crack Length Per Unit Area (1/mm) of Section (X-Y) for Mixture I

(3 Replicated Scans)

Magnification		125X					250X			500X		
Scanned Area		0.50%	1%	2%	3%	4%	0.50%	1%	2%	0.50%	1%	2%
Number of Images		16	36	64	100	144	64	144	256	256	512	1024
ESEM Undamaged	Mean (L_A)	0.031	0.05	0.06	0.09	0.09	0.034	0.08	0.07	0.19	0.255	0.29
	Sd. Dev.	0.042	0.06	0.03	0.06	0.06	0.074	0.06	0.09	0.151	0.033	0.02
ESEM Damaged	Mean (L_A)	0.118	0.16	0.27	0.27	0.3	0.211	0.33	0.4	0.439	0.487	0.52
	Sd. Dev.	0.011	0.02	0.04	0.07	0.04	0.067	0.06	0.07	0.06	0.101	0.12
Fluorescent Undamaged	Mean (L_A)	0.023	0.04	0.07	0.07	0.07	0.031	0.06	0.06	0.137	0.244	0.29
	Sd. Dev.	0.091	0.09	0.08	0.1	0.04	0.064	0.01	0.02	0.037	0.027	0.03
Fluorescent Damaged	Mean (L_A)	0.108	0.17	0.23	0.23	0.26	0.238	0.27	0.3	0.322	0.457	0.56
	Sd. Dev.	0.023	0.04	0.11	0.08	0.05	0.074	0.02	0.04	0.054	0.066	0.05

Sd. Dev. = Standard deviation

Table 6.9 Crack Length Per Unit Area (1/mm) of Section (Y-Z) For Mixture I

(3 Replicated Scans)

Magnification		125X					250X			500X		
Scanned Area		0.50%	1%	2%	3%	4%	0.50%	1%	2%	0.50%	1%	2%
Number of Images		16	36	64	100	144	64	144	256	256	512	1024
ESEM Undamaged	Mean (L_A)	0.026	0.04	0.06	0.09	0.1	0.046	0.13	0.13	0.103	0.205	0.26
	Sd. Dev.	0.034	0.04	0.03	0.07	0.11	0.088	0.05	0.07	0.026	0.035	0.03
ESEM Damaged	Mean (L_A)	0.154	0.11	0.19	0.2	0.22	0.167	0.31	0.28	0.482	0.587	0.54
	Sd. Dev.	0.021	0.02	0.02	0.07	0.05	0.031	0.06	0.07	0.122	0.114	0.1
Fluorescent Undamaged	Mean (L_A)	0.036	0.04	0.06	0.06	0.06	0.038	0.08	0.09	0.142	0.201	0.26
	Sd. Dev.	0.044	0.06	0.12	0.06	0.1	0.022	0.02	0.04	0.062	0.021	0.04
Fluorescent Damaged	Mean (L_A)	0.121	0.13	0.16	0.17	0.18	0.135	0.21	0.24	0.242	0.571	0.77
	Sd. Dev.	0.061	0.03	0.06	0.03	0.06	0.024	0.06	0.05	0.086	0.045	0.05

Sd. Dev. = Standard deviation

Table 6.10 Crack Length Per Unit Area (1/mm) of Section (X-Y) For Mixture II

(3 Replicated Scans)

Magnification		125X					250X			500X		
Scanned Area		0.50%	1%	2%	3%	4%	0.50%	1%	2%	0.50%	1%	2%
Number of Images		16	36	64	100	144	64	144	256	256	512	1024
ESEM Undamaged	Mean (L_A)	0.022	0.03	0.04	0.04	0.05	0.045	0.06	0.06	0.046	0.064	0.09
	Sd. Dev.	0.042	0.02	0.04	0.05	0.02	0.031	0.02	0.05	0.014	0.074	0.06
ESEM Damaged	Mean (L_A)	0.12	0.11	0.16	0.16	0.16	0.201	0.28	0.29	0.34	0.54	0.74
	Sd. Dev.	0.02	0.02	0.57	0.03	0.03	0.01	0.01	0.01	0.061	0.057	0.08
Fluorescent Undamaged	Mean (L_A)	0.044	0.05	0.08	0.09	0.09	0.047	0.07	0.07	0.095	0.112	0.09
	Sd. Dev.	0.015	0.03	0.05	0.06	0.06	0.012	0.07	0.09	0.09	0.081	0.13
Fluorescent Damaged	Mean (L_A)	0.148	0.11	0.16	0.16	0.17	0.131	0.2	0.25	0.371	0.389	0.41
	Sd. Dev.	0.024	0.06	0.05	0.06	0.05	0.034	0.05	0.11	0.087	0.111	0.07

Sd. Dev. = Standard deviation

Table 6.11 Crack Length Per Unit Area (1/mm) of Section (Y-Z) For Mixture II

(3 Replicated Scans)

Magnification		125X					250X			500X		
Scanned Area		0.50%	1%	2%	3%	4%	0.50%	1%	2%	0.50%	1%	2%
Number of Images		16	36	64	100	144	64	144	256	256	512	1024
ESEM Undamaged	Mean (L_A)	0.024	0.03	0.05	0.04	0.05	0.041	0.05	0.07	0.045	0.055	0.06
	Sd. Dev.	0.011	0.02	0.05	0.02	0.02	0.043	0.05	0.06	0.016	0.021	0.07
ESEM Damaged	Mean (L_A)	0.052	0.06	0.09	0.13	0.11	0.21	0.2	0.22	0.3	0.741	0.88
	Sd. Dev.	0.031	0.04	0.05	0.03	0.01	0.022	0.09	0.02	0.077	0.013	0.14
Fluorescent Undamaged	Mean (L_A)	0.037	0.06	0.06	0.06	0.07	0.044	0.06	0.06	0.118	0.047	0.08
	Sd. Dev.	0.04	0.02	0.03	0.03	0.05	0.047	0.03	0.07	0.113	0.112	0.08
Fluorescent Damaged	Mean (L_A)	0.069	0.09	0.13	0.13	143	0.157	0.21	0.24	0.232	0.254	0.21
	Sd. Dev.	0.011	0.04	0.05	0.01	0.02	0.088	0.06	0.08	0.034	0.078	0.1

Sd. Dev. = Standard deviation

Tables 6.12 and 6.13 show the results of the statistical analyses. The analyses showed that at 125X magnification in ESEM and fluorescent microscopy for undamaged and damaged specimens (considering both mixtures I and II), 3% of the surface should be scanned to produce reliable results at 5% level of significance. Scanning of 4% of the surface area would further improve the reliability of measurements. At 250X magnification in both ESEM and fluorescent microscopy of undamaged and damaged (considering both mixtures I and II), scanning 1% of surface area seems sufficient for producing representative results at 5% level of significance. The reliability of measurements would be further enhanced if 2% of the surface area was scanned. At 500X magnification in both ESEM and fluorescent microscopy of undamaged and damaged specimens (considering both mixtures I and II), for two conditions (ESEM of damaged specimens from mixture I and fluorescent microscopy of damaged specimens from mixture II), scanning of 0.5% of the surface area yielded representative results at 5% level of significance. For two other conditions (ESEM of undamaged specimens for mix I, and fluorescent microscopy undamaged specimens for mixture I), scanning of 1% of the surface area was needed to produce representative results at 5% level of significance. For the remaining 4 conditions at 500X magnification factor, 2% of the concrete surface area led to be scanned in order to produce representative results at 5% level of significance. However it is preferred to use 0.5% (256 images) since 1% (512 images) and 2% (1024 images) are time and const consuming. It should be noted that time and cost constrains may limit the percentage of area that is scanned at 500X magnification to 0.5%.

Table 6.12 Statistical Analysis of Crack Length Per Unit Area for Mixture I

Magnification		125X					250X			500X		
Scanned Area		0.50%	1%	2%	3%	4%	0.50%	1%	2%	0.50%	1%	2%
Number of Images		16	36	64	100	144	64	144	256	256	512	1024
ESEM Undamaged	0.50%	-	S	S			-	S		-	S	
	1%	S	-	S			S	-	I	S	-	I
	2%	S	S	-	S			I	-		I	-
	3%			S	-	I						
	4%				I	-						
ESEM Damaged	0.50%	-	I				-	S		-		
	1%	I	-	S			S	-	I	I	-	
	2%		S	-	I	I		I	-	I	I	-
	3%			I	-	I						
	4%			I	I	-						
Fluorescent Undamaged	0.50%	-	I				-	S		-	S	
	1%	I	-	S			S	-	I	S	-	I
	2%	S	S	-	I			I	-		I	-
	3%			I	-	I						
	4%			I	I	-						
Fluorescent Damaged	0.50%	-	S	S			-	I1, S2		-	S	
	1%	S	-	S			I1, S2	-	I	S	-	I1, S2
	2%	S	S	-	I	I		I	-		I1, S2	-
	3%			I	-	I						
	4%			I	I	-						

I = insignificant difference for both sections (X-Y) or (Y-Z), S = significant difference for both sections (X-Y) or (Y-Z), I1 = insignificant difference for section (X-Y), I2 = insignificant difference for section (Y-Z), S1 = significant difference for section (X-Y), and S2 = significant difference for section (Y-Z)

Table 6.13 Statistical Analysis of Crack Length Per Unit Area For Mixture II

Magnification		125X					250X			500X		
Scanned Area		0.50%	1%	2%	3%	4%	0.50%	1%	2%	0.50%	1%	2%
Number of Images		16	36	64	100	144	64	144	256	256	512	1024
ESEM Undamaged	0.50%	-	I				-	S		-	S	S
	1%	I	-	S			S	-	1	S	-	S1, I2
	2%		S	-	I			I	-	S	S1, I2	-
	3%			I	-	I						
	4%			I	I	-						
ESEM Damaged	0.50%	-	I				-	S1, I2	I2	-	S	
	1%	I	-	S			S1, I2	-	I	S	-	I
	2%		S	-	I1, S2		I2	I	-		I	-
	3%			I1, S2	-	I						
	4%			I	I	-						
Fluorescent Undamaged	0.50%	-	S							-	I1, S2	
	1%	S	-	S1, I2	I2	I2	-	S		I1, S2	-	S
	2%		S1, I2	-			S	-	1		S	-
	3%		I2	I	-			I	-			
	4%		I2	I	I	-						
Fluorescent Damaged	0.50%	-	I	I	I	I	-	S		-	I	I
	1%	I	-	S			S	-	1	I	-	I
	2%	I	S	-	I	I		I	-	I	I	-
	3%	I		I	-	I						
	4%	I		I	I	-						

I = insignificant difference for both sections (X-Y) or (Y-Z), S = significant difference for both sections (X-Y) or (Y-Z), I1 = insignificant difference for section (X-Y), I2 = insignificant difference for section (Y-Z), S1 = significant difference for section (X-Y) and S2 = significant difference for section (Y-Z)

The microcrack lengths per unit area were statistically comparable for horizontal (X-Y) and vertical (Y-Z) sections of undamaged specimens. In the case of damaged specimens, however, sections perpendicular to compressive load direction (X-Y) had a higher microcrack length per unit area than sections parallel to load direction (Y-Z). Microcrack length per unit area was higher (at 5% level of significance) in damaged sections when compared with undamaged sections. In the case of damaged specimens, the difference in specific surface and length per unit area was statistically significant at 5% level of significance for the two concrete mixtures.

Table 6.14 shows the measured value of specific surface area for damaged and undamaged specimens from mixtures I and II, which were scanned by ESEM and fluorescent microscopy at different magnifications, with different percentages of surface area scanned. The results were obtained through stereological analysis equation 6.13 of planar measurements. Table 6.14 compares the statistical significance of the difference between undamaged and damaged specimens (at 5% level of significance). The required number of cores was then determined using equation 6.52. Different precisions values (1%, 2%, 5%, 10% and 50%) were considered for comparison purposes. Figures 6.12 and 6.13 show the required number of cores for undamaged and damaged specimens from mixture I at the different magnification levels (average of ESEM and fluorescent microscopy). Figure 6.14 and 6.15 show the required number of cores for undamaged and damaged specimens from mixture II at the different magnification levels (average of ESEM and fluorescent microscopy). Comparisons between different precision levels suggest that 5% precision produces a reasonable balance as far as practical sampling of

concrete systems is concerned. The largest number of required cores at 5% precision is 26 (fluorescent microscopy, undamaged specimens, 500X magnification, mixture II), and the lowest number of cores is 1 (ESEM, undamaged specimens, 125X magnification, mixture II, and ESEM, damaged specimens, 250X magnification, mixture II).

Table 6.14 Microcrack Specific Surface Area (3 Replicated Scans)

Microscopy Type		ESEM			Fluorescent		
Magnification		125X	250X	500X	125X	250X	500X
Scanned Area		4%	2%	0.50%	4%	2%	0.50%
Undamaged Mix I	Mean	0.119	0.186	0.188	0.086	0.132	0.177
	Sd. Dev.	0.077	0.105	0.091	0.045	0.036	0.055
Damaged Mix I	Mean	0.349	0.456	0.51	0.199	0.184	0.363
	Sd. Dev.	0.044	0.074	0.069	0.063	0.056	0.054
Undamaged Mix II	Mean	0.058	0.082	0.059	0.102	0.088	0.131
	Sd. Dev.	0.023	0.087	0.022	0.056	0.063	0.128
Damaged Mix II	Mean	0.165	0.347	0.375	0.174	0.255	0.37
	Sd. Dev.	0.027	0.019	0.079	0.046	0.106	0.084

Sd. Dev. = Standard Deviation

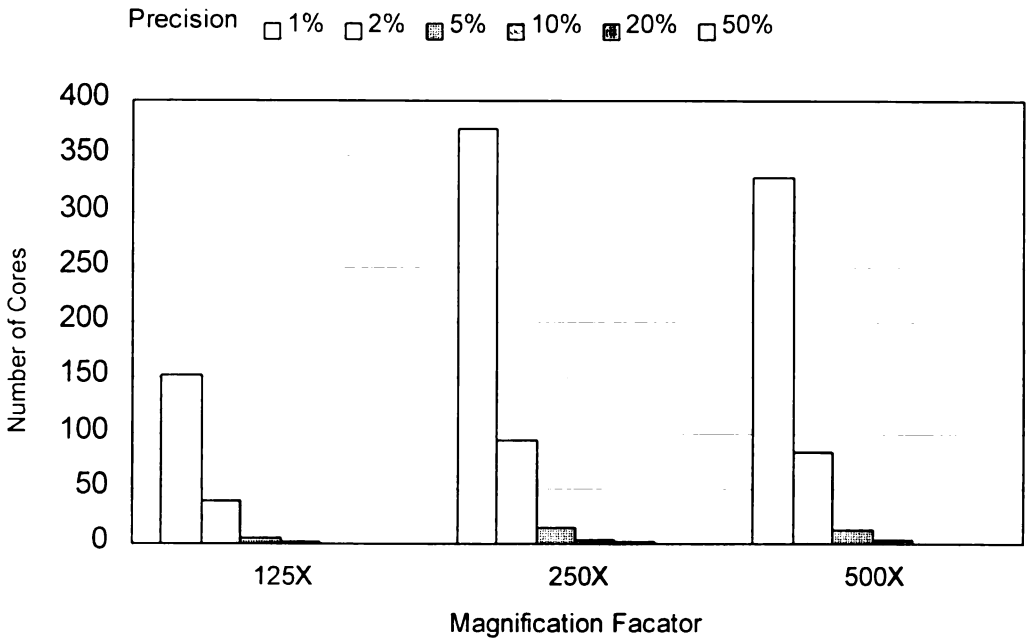

Figure 6.12 Required Number of Cores for Undamaged Specimens (Mix I) at Different Magnification Levels (Average of ESEM and Fluorescent Microscopy)

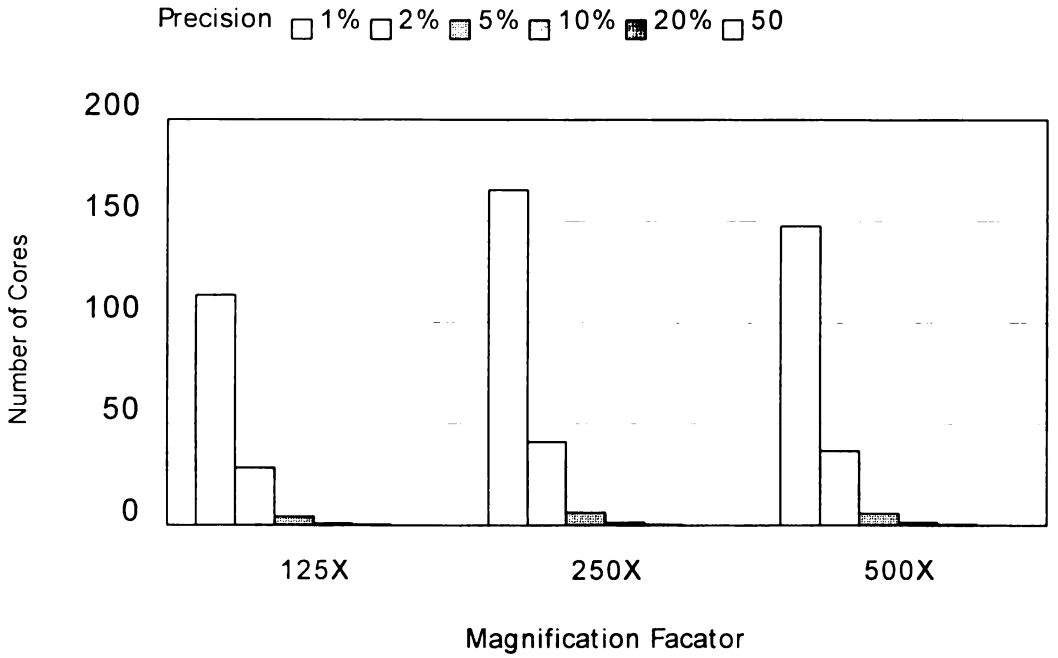

Figure 6.13 Required Number of Cores for Damaged Specimens (Mix I) at Different Magnification Levels (Average of ESEM and Fluorescent Microscopy)

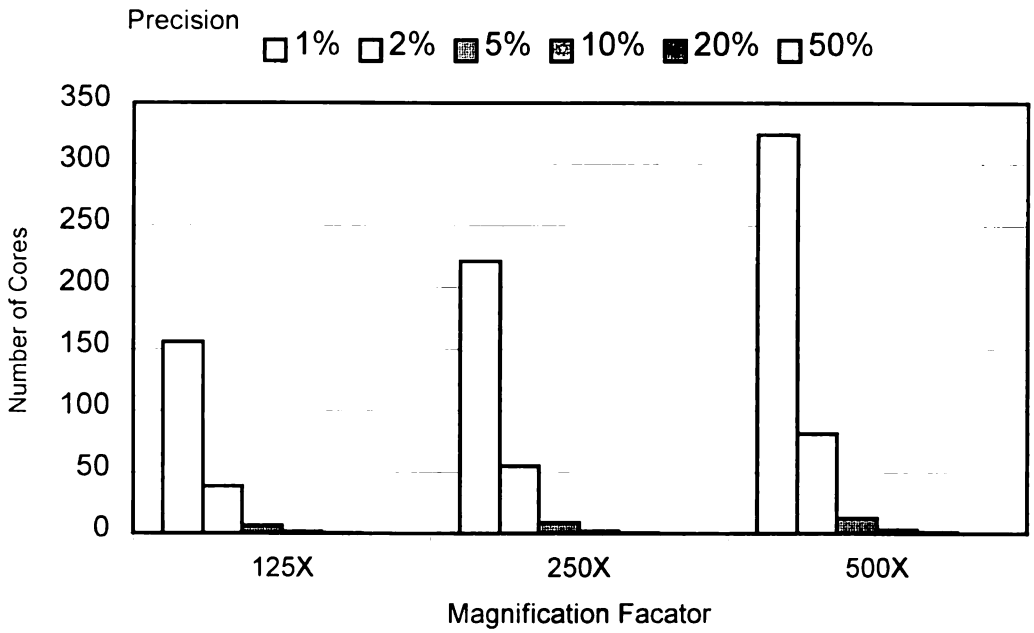

Figure 6.14 Required Number of Cores for Undamaged Specimens (Mix II) at Different Magnification Levels (Average of ESEM and Fluorescent Microscopy)

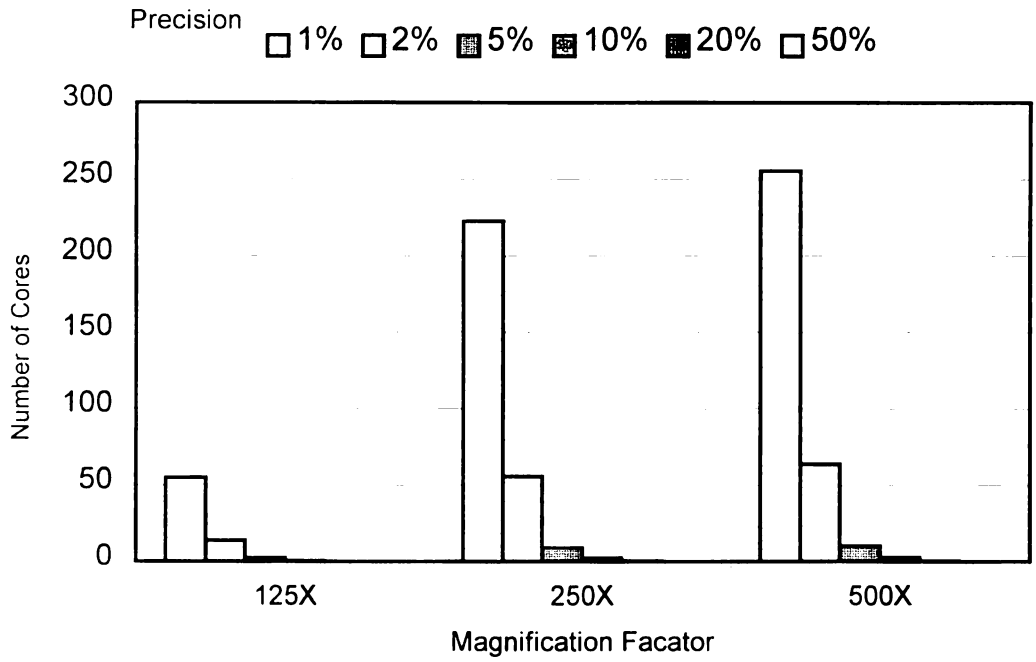

Figure 6.15 Required Number of Cores for Damaged Specimens (Mix II) at Different Magnification Levels (Average of ESEM and Fluorescent Microscopy)

6.3 CONCLUSIONS

1- Planar characteristics of microcracks on two perpendicular sections were used in stereological formulations to quantify microcrack volume fraction, spacing, width, degree of orientation and tortuosity in space.

2- Planar characteristics of voids on two perpendicular sections were used in stereological formulations to quantify the volume fraction, number per unit volume, specific surface area, spacing, and diameter of voids in space.

3- Limited application of stereological principals to planar measurement of aggregates, assuming disc geometry, yielded formulations for (3-D) complexity index, thickness and number per unit volume of aggregates. Limited application of stereological principals of fibers, assuming cylindrical shape, yielded formulations for number per unit volume and diameter of fibers.

4- A comprehensive statistically-based methodology was developed for sampling of concrete systems for the purpose of quantification microstructural analysis of concrete. The approach starts with dividing the concrete system into a preliminary number of sub-regions within which damage level is relatively uniform. A representative number of cores should then be taken from each sub-region; the microscopic investigation should also cover a representative fraction of sectioned concrete surface (two perpendicular sections are cut for each specimen for stereological analyses). Statistical criteria together with data generated for different concrete mixtures and different damage conditions at various magnification levels in order to select the required fraction of area to be scanned and the required number of cores to be taken from each sub-region to yield representative results.

5- At 125X and 250X magnification levels, scanned areas should cover 0.5% and 2% of concrete surface area, respectively, to yield representative results. At 500X magnification, scanning of 0.5% surface area would be generally sufficient, noting that higher fractions of scanned surface area imply major time and cost expenditures. As far as the required number of cores per sub-region is concerned, a precision level of 5% seemed to provide a reasonable balance between applicability and reliability of the approach.

6- the type of damage considered (load to peak compressive stress followed by immediate unloading) produce a statistically significant increase in the length per unit area (and specific surface area) of concrete microcrack, for damaged specimens, the crack length per unit area was greater on sections normal to the direction of compressive loading (when compared to those parallel to the direction of loading). Concrete mixture composition also influences the microcrack length per unit area (and specific surface area) of damaged specimens.

MICHIGAN STATE UNIVERSITY LIBRARIES
3 1293 02551 6844

5
2004

V.2
56954764

LIBRARY
Michigan State
University

PLACE IN RETURN BOX to remove this checkout from your record.
TO AVOID FINES return on or before date due.
MAY BE RECALLED with earlier due date if requested.

DATE DUE	DATE DUE	DATE DUE

6/01 c:/CIRC/DateDue.p65-p.15

QUANTITATIVE MICROSTRUCTURAL INVESTIGATION OF DAMAGED CONCRETE

VOLUME II

By

Mohamed Farouk Elzafraney

A DISSERTATION

Submitted to
Michigan State University
in partial fulfillment of the requirements
for the degree of

DOCTOR OF PHILOSOPHY

Department of Civil and Environmental Engineering

2004

CHAPTER 7

QUALITATIVE MICROSTRUCTURAL INVESTIGATION OF CONCRETE

7.1 PREFACE

When concrete is subjected to externally imposed structural loads or damaging environmental effects, concentrations of tensile stresses occurs at interfaces due to differences in elastic modulus and also because of the pre-existing of interfacial microcracks.[2,3,20] As a result, concrete macrocracks will occur and develop first in the interface zones (and then into the paste) under load and environmental effects. Concrete materials of different strengths and reinforcement conditions behave differently under load and environmental effects. If the stiffness of aggregate particles is distinctively higher than that of the paste (in normal-strength concrete case), microcracks tend to propagate through the matrix/aggregate interfaces around aggregate particles, which constitutes the path of least resistance.[19] In case of the stiffness of aggregate particles is slightly higher than or equal to the stiffness of the paste (in high–strength concrete), microcracks tend to propagate through aggregate particles, creating shorter fracture surfaces.[6] Compared to normal-strength concrete, high-strength concrete behaves more like a homogeneous material, with its stress-strain curve remaining closer to linearity at higher stress/strength ratios.[22,23] The reduced amount of microcracking in interfacial transition zones of high–strength concrete a more brittle mode of fracture and less volumetric dilation.[4,16] Adding mineral admixtures such as silica fume or fly ash to increase strength of concrete in case of high-strength concrete increases the extent of microcracking,[21,42] with most of microcracks propagating through the interfaces between

fly ash particles and paste. Fiber reinforcement in concrete can arrest the propagation of microcracks created in concrete. Fibers with high elastic modulus, bond strength, count per unit volume and surface area are particularly effective in the suppression and stabilization of the microcrack system.[5,43] The main thrust of this chapter is qualitatively investigate concrete microstructure under damage effects and weathering conditions and to qualitatively compare between microstructure of normal-strength and relatively high-strength concrete under these damage effects.

7.2 EXPERIMENTAL PROGRAM

7.2.1 Concrete Mixtures and Specimens

Three concrete mixtures were considered in the experimental program: (1) normal-strength; (2) relatively high-strength, and (3) fiber reinforced. Type I Portland cement and natural sand were used in all mixtures. Crushed limestone with maximum particle size of 19 mm (3/4 in) was used as coarse aggregate in the normal-strength mix and fibrous mix comprised cement : fine aggregate : coarse aggregate : water at 1 : 1.59 : 1.98 : 0.514 mass ratios, targeting 28-day compressive strength 33 MPa (4750 psi) . This mix was air-entrained, and provided an air content of 3.5 percent with a slump of 190 mm (7.5 in). The high-strength mix incorporated natural granite with maximum particle size of 10 mm (3/8 in) as coarse aggregate; it also incorporated silica fume and superplasticizer comprised cement: fine aggregate : coarse aggregate : water : silica fume at 1 : 1.7 : 0.9: 0.42 : 0.2 mass ratios, targeting 28-day compressive strength 43 MPa (6120 psi). This mix provided 1.9 percent air content and a slump of 64 mm (2.5 in). The fibrous mix incorporated 0.35% by volume of 10 mm long crimped steel fibers with 0.58 mm

diameter (Ribtec Alloy 017-30). The following specimens were molded and consolidated with these concrete mixtures: 102 mm (4 in) diameter by 203 mm (8 in) height cylindrical specimens for compression testing; 152 mm (6 in) diameter by 304 mm (12 in) cylindrical specimens for splitting tension testing; 76 × 76 × 305 mm (3 × 3 × 12 in); prismatic specimens for flexural, fatigue, compression, freeze-thaw and fire endurance testing; 152 mm (6 in) diameter × 63.5 mm (2.5 in) cylindrical specimens for impact resistance; 102 mm (4 in) diameter × 51 mm (2 in) cylindrical specimens for permeability; and 102 × 76 × 406 mm (4 × 3 × 16 in) prismatic specimens for restrained shrinkage and weathering testing. All 102 × 76 × 406 mm (4 × 3 × 16 in) prismatic molds incorporated two 38 mm (1.5 in) long threaded steel bars of 6.35 mm (0.25 in) at two ends, which were embedded within concrete to restrain longitudinal shrinkage of concrete. Molded specimens were kept moist for 24 hours, after which they were demolded (except for restrained specimens) and moist cured at 100% relative humidity and 22°C (72°F) for 28 days, and then conditioned at 50% relative humidity at 22°C (72°F) for 180 days prior to compression, flexural, splitting tension, freeze – thaw, fire endurance and impact testing. This relatively long period of conditioning allows for development of shrinkage microcracks which occurs within concrete largely due to the restraint of cement paste shrinkage measurements by aggregates. Restrained normal–strength concrete specimens were kept moist for 24 hours, after which they stored (without demolding) for 28 days at 55°C (130°F) for hot weather exposure or at –3.5°C (-25°F) for cold exposure, and then demolded and conditioned at 50% relative humidity and 22°C (72°F) for 180 days. The restraint against shrinkage was effective as far as the specimen was not demolded.

7.2.2 Testing Plan

Engineering properties and microcracking characteristics of concrete were assessed prior to and after exposure to different damaging phenomena. Two categories of tests were performed on concrete specimens: (1) control tests prior to any damaging effects; and (2) post damage tests after concrete specimens were exposed to various damaging phenomena. The control and post damage conducted in this investigation included compression (ASTM C39), splitting tension on cylinders (ASTM C96), flexure on prisms with a span of 228 mm (9 in) under 4-point loading (ASTM C78), flexural fatigue between 15% to 85% of ultimate flexural strength at 450 cycles per minute (ACI Com. 225), and drop weight impact (ACI Com. 215), and permeability (ASTM C1202).

The control tests performed on different concrete mixtures were as follows:

- Normal-strength concrete: compression, splitting tension, flexure, fatigue, impact, and permeability.
- Relatively high-strength concrete: compression, splitting tension, flexure, impact, and permeability.
- Fiber reinforced concrete: compression and flexure.

The following damaging phenomena were considered in this investigation: (1) compression loading to peak compressive stress with immediate unloading; (2) impact to 85% of the number of blows causing failure; (3) fatigue loading to 85% of the number of cycles causing failure; (4) 300 cycles (75 days) of freeze-thaw in water (ASTM C666); and (5) compression loading to peak compressive stress followed by immediate unloading and then exposure to 300 freeze-thaw cycles in water; (6) exposure to fire endurance of 425°C (800°F) within an electrical furnace for 3 hours, followed by cooling

at room temperature; and (7) restraint against longitudinal (drying and thermal) shrinkage movements in normal 22°C (72°F), hot 55°C (130°F), and cold –3.5°C (-25°F) temperatures. These damaging phenomena left the specimens intact for the purpose of post-damage evaluation. The test program is summarized in Table 7.1.

7.3 MICROSTRUCTURAL INVESTIGATION SCHEME

In order to assess the microstructural manifestations of damaging effects, two sections were cut perpendicular and parallel to loading direction in case of compression and flexure test specimen or perpendicular and parallel to the longer dimension in the case of freeze-thaw, exposure to fire endurance, and restrained shrinkage test specimens as shown in Figure 7.1. One section was investigated through environmental scanning electron microscopy (ESEM) by means of backscattered technique, and the other was examined using fluorescent microscopy. Twenty-five images were captured from each section at 125X magnification value. The contrast between microcracks/voids and the body of concrete was enhanced using specimen preparation method described in section 3.4. Fibrous mixture, however, was investigated using ESEM without any prior specimen preparation in order to avoid any interference of fibers with the process of specimen preparation (both steel fibers and Wood's metal appear in white "silver" color on black background under the microscopy and thus can not be distinguished easily), fibrous specimens surfaces were simply lapped and then observed under ESEM.

Table 7.1 The Post-Damage Test Program For Concrete Mixtures

Damaging Effect	Post-Damage Tests	Specimens	Number of Specimens
Normal–Strength Concrete			
Compression	Flexure	Prism (76×76×305 mm)	4
	Splitting Tension	Cylinder (300×150 mm)	5
	Impact	Cylinder (152×63.5 mm)	5
	Permeability	Cylinder (102×51 mm)	5
Impact	Permeability	Cylinder (102×51 mm)	5
Freeze-Thaw	Compression	Prism (76×76×305 mm)	3
	Flexure	Prism (76×76×305 mm)	3
	Permeability	Cylinder (102×51 mm)	3
Compression + Freeze-Thaw	Flexure	Prism (76×76×305 mm)	2
Fatigue	Flexure	Prism (76×76×305 mm)	6
Fire Endurance	Flexure	Prism (76×76×305 mm)	3
Shrinkage Restraint in Room Temperature	Flexure	Prism (102×76×405 mm)	2
Shrinkage Restraint in Hot Temperature	Flexure	Prism (102×76×405 mm)	2
Shrinkage Restraint in Cold temperature	Flexure	Prism (102×76×406 mm)	2
High–Strength Concrete			
Compression	Flexure	Prism (76×76×305 mm)	3
	Splitting Tension	Cylinder (300×150 mm)	5
	Impact	Cylinder (152×63.5 mm)	3
	Permeability	Cylinder (102×51 mm)	5
Impact	Permeability	Cylinder (102×51 mm)	5
Fiber Reinforced Concrete			
Shrinkage Restraint in Room Temperature	Flexure	Prism (102×76×406 mm)	3

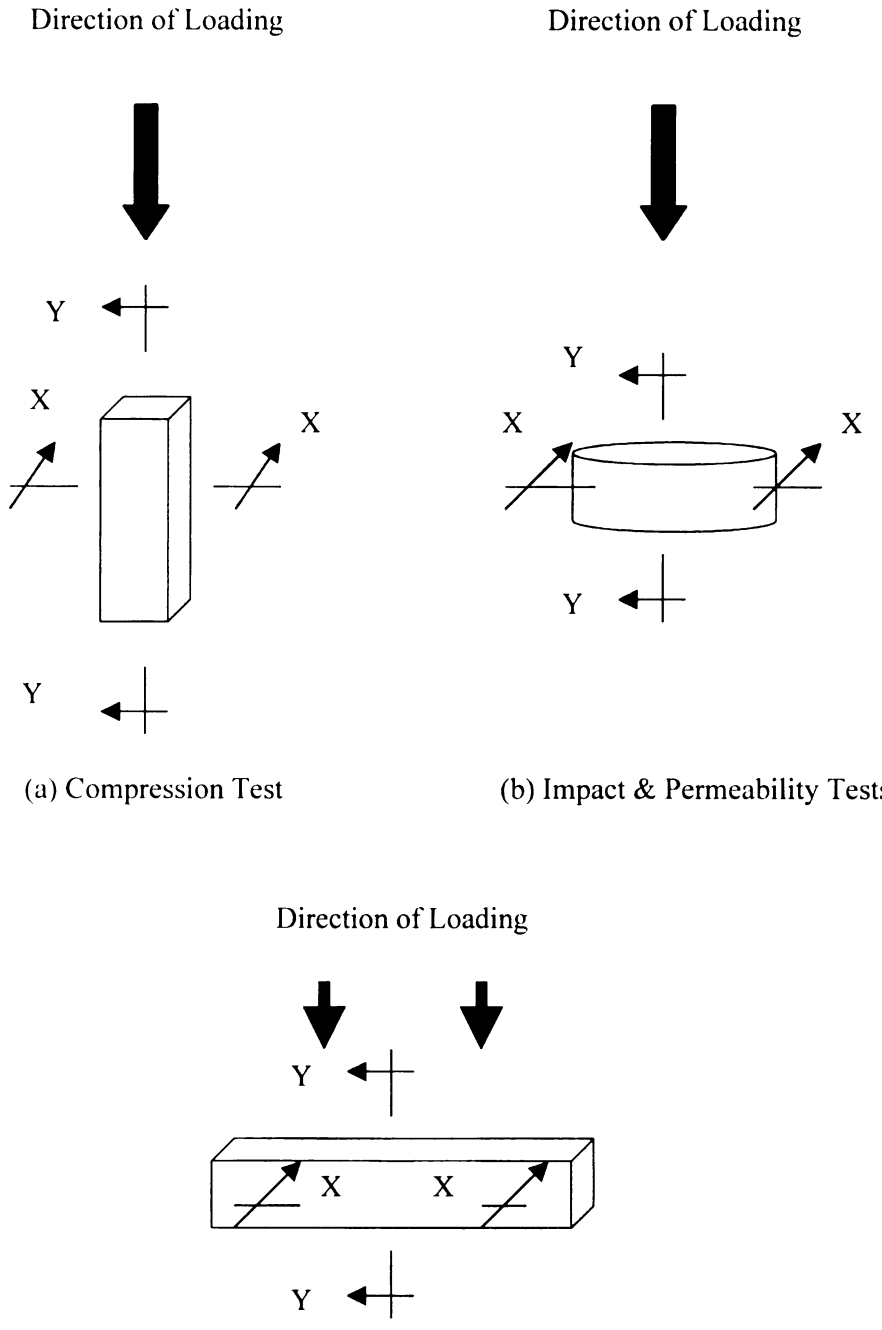

(a) Compression Test

(b) Impact & Permeability Tests

(c) Flexure, Fatigue, Freeze-Thaw, and Different Environmental Exposure

Figure 7.1 Sectioning Directions for Microscopic Investigations

7.4 PERFORMANCE TEST RESULTS

The effect of compression, freeze-thaw, compression+freeze-thaw, fatigue, and fire endurance on flexural strength of normal-strength concrete are presented in Figure 7.2. Reductions in flexure strength under different damaging effects range from 15% to 43%. Statistical analysis of variance "ANOVA" followed by pairwise comparison of results indicated that there were statistically significant effects of freeze-thaw, and compression+freeze-thaw at 10% level of significance and compression and fire endurance at 5% level of significance.

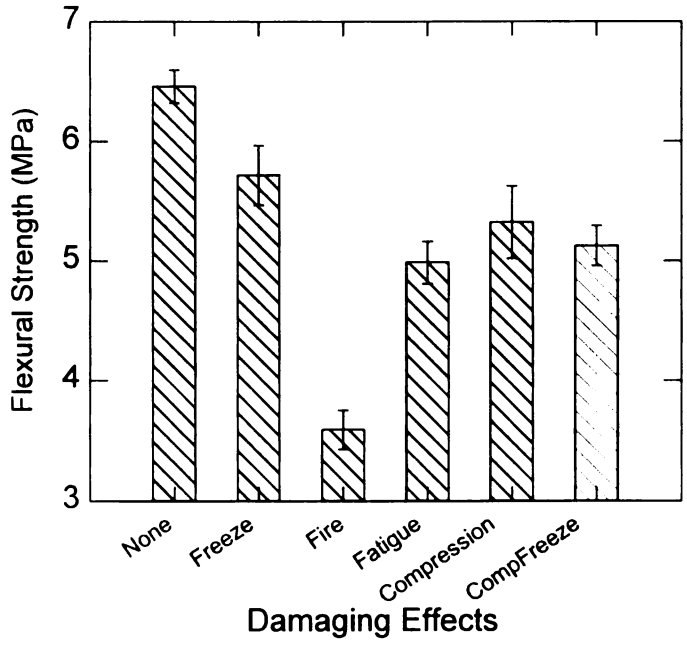

Figure 7.2 Damaging Effects on Flexural Strength of Normal-Strength Concrete

Exposure to fire endurance caused spalling of concrete surface as shown in Figure 7.3 which may be attributed to the build up of steam pressure within concrete. There was no statistically significant difference between different damaging effects (except for fire endurance) on flexural strength of normal-strength concrete.

Figure 7.3 Damage Normal–Strength Concrete Specimen after Exposure to Elevated Temperature

In case of high-strength concrete (Figure 7.4), analysis of variance of test results indicated that the damaging effect of compression on flexural strength was statistically significant at 5% level of significance. There was no statistically significant difference between the damaging effects of compression on flexure strength of normal-strength versus high-strength concrete (which suffered 20% and 21% loss of mean flexural strength, respectively, after compression loading).

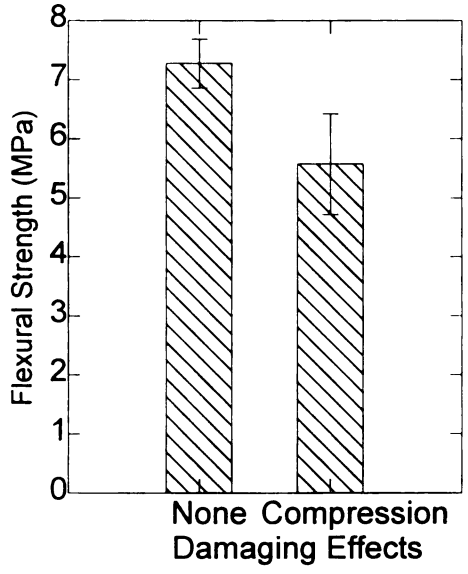

Figure 7.4 Damaging Effects of Compression on Flexural Strength of High-Strength Concrete

Figure 7.5 presents the damaging effects of compression on splitting tensile strength of normal-strength and high-strength concrete, which suffered 12% and 24% loss of splitting tensile strength, respectively, after compression loading. These effects were statistically significant at 5% level of significance. Statistical analysis also indicated that there is a significant difference at 5% level of significance between the effects of compression on the splitting tensile strength of normal-strength versus high-strength concrete.

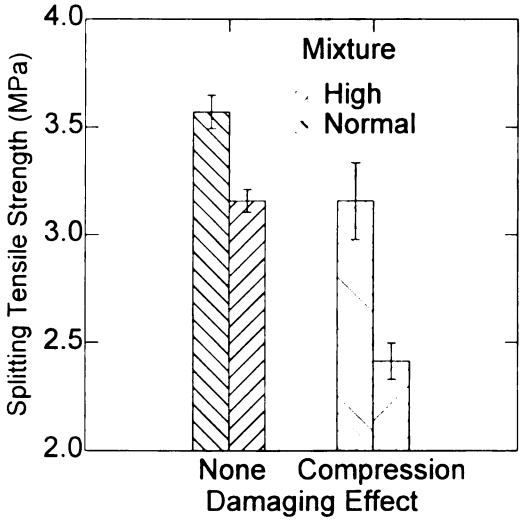

Figure 7.5 Splitting Tensile Strength Test Results Prior to and After Exposure to Peak Compressive Stress

Figure 7.6 presents the damaging effects of compression on impact resistance of normal-strength and high-strength concrete. Analysis of variance of the test data indicated that the damaging effects of compression on impact resistance of normal-strength and high-strength concrete were statistically significant at 5% level of significance. Normal-strength seemed to suffer a greater loss of impact resistance than high-strength concrete after compression loading.

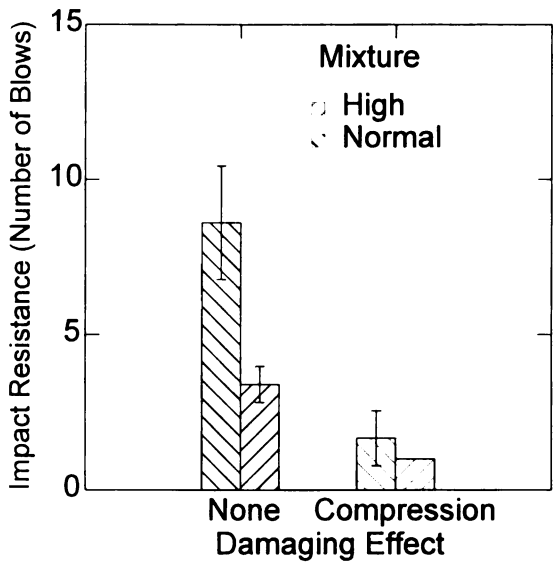

Figure 7.6 Damaging Effects of Compression on Impact Resistance

The influence of freeze-thaw cycles on compressive strength of normal-strength concrete is shown in Figure 7.7. The average compressive strength dropped by 22% of the freeze-thaw cycles. Statistical analysis of results indicated that the effect of freeze-thaw cycles on compressive strength was significant at 10% level of significance.

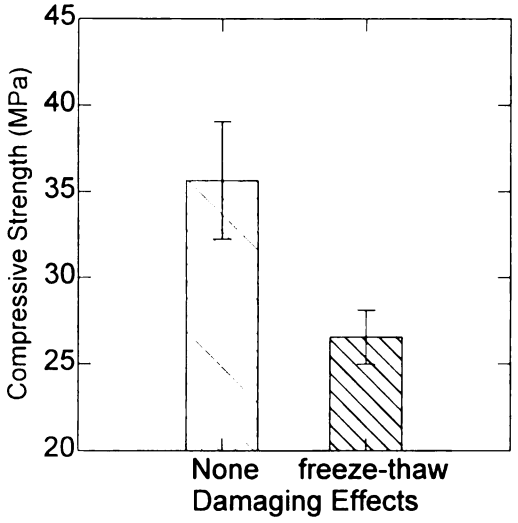

Figure 7.7 Effect of Repeated Freeze–Thaw Cycles on Compressive Strength of Normal–Strength Concrete

As shown in Figure 7.8, except for impact, other damaging effects seem to significantly increase the chloride permeability of both normal-strength and high-strength concrete. The variability of chloride permeability test results, however, such that statistical analysis of results indicated that only compression has statistically significant effects (at 5% level of significance) on chloride permeability of normal-strength and high-strength concrete.

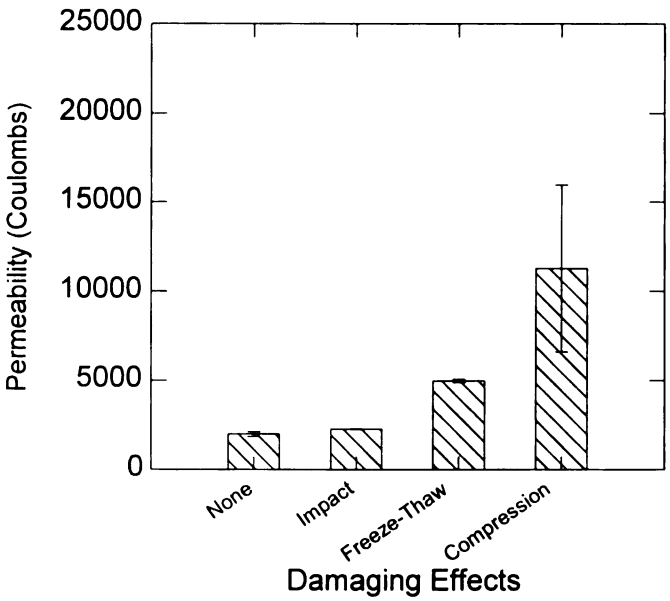

(a) Normal-Strength Concrete

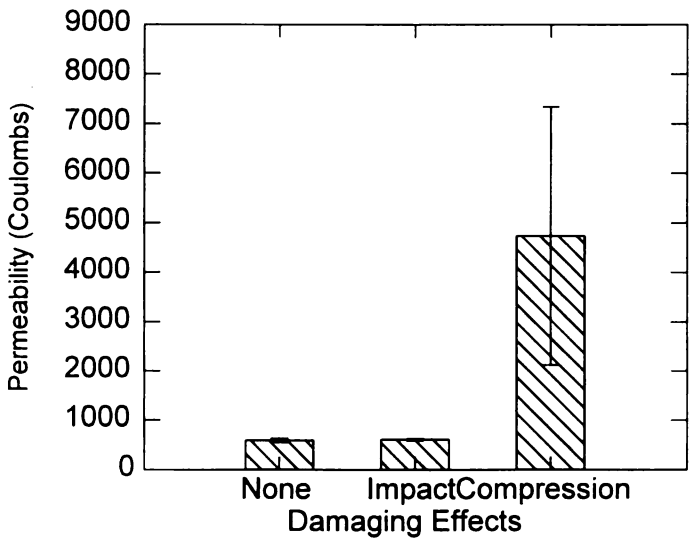

(b) High-Strength Concrete

Figure 7.8 Damaging Effects on Chloride Permeability

Figure 7.9 illustrates the effects of shrinkage restraint in hot weather and cold weather compared to non–restrained and restrained concrete specimens in room temperature. Reduction in flexural strength due to shrinkage restraint in hot weather compared to non–restrained and restrained specimens cured in room temperature is 55% and 54% respectively. It was also found that there is no statistical significance difference between flexural strength of restrained and non-restrained concrete specimens cured in room temperature. Analysis of variance showed that there is significant effect of restrained shrinkage in hot weather at 5 % level of significance on flexural strength of non–restrained and restrained specimens cured in room temperature. Non–restrained and restrained specimens cured in room temperature suffered 47% and 46% loss of flexural strength due to shrinkage restraint in cold weather. Analysis of variance of test data indicated that the damaging effect of shrinkage restraint in cold weather is statistically significance at 5% level of significance for non–restrained and restrained specimens in room temperature respectively.

In case of fiber reinforced mixture (Figure 7.10), analysis of variance indicated that there is no statistical significance effect of shrinkage restraint on flexural strength.

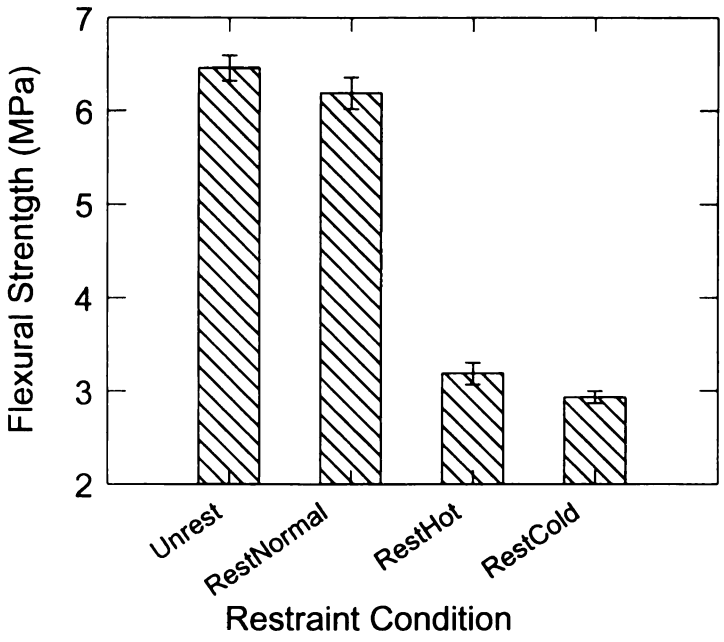

Figure 7.9 Effects of Restraint Condition and Exposure Temperature on Flexural Strength of Normal-Strength Concrete

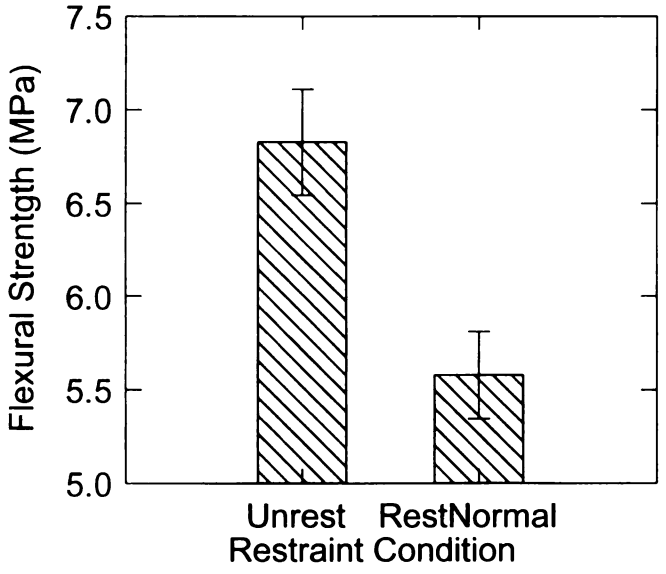

Figure 7.10 Effects of Restraint Condition on Compressive Strength of Fiber Reinforced Concrete

7.5 RESULTS OF MICROSTRUCTURAL INVESTIGATION

Microstructural investigations were conducted using both ESEM and fluorescent microscopy in order to detect any variations in results related to microscopy technique or to specimen preparation method. The following observations could be made on microscopic images:

Microcracks already exist in normal-strength, high-strength, and fibrous concretes prior to any damaging effects. Most of these microcracks occur at interfaces between cement paste and coarse aggregates as shown in Figures 7.11a, 7.12a and 7.13a. Fiber reinforced concrete seems to exhibit less microcracking (noting that the lack of specimen preparation for fibrous specimens made detection of microcracks, to some extent, difficult). All damaging effects considered in the investigation increased the intensity of concrete microcracking. Freeze-thaw effects on undamaged specimens yielded less tortuous microcrack growth paths when compared with other damaging effects as shown in Figure 7.11b. Freeze-thaw effects on concrete specimens which were already subjected to compression did not substantially change the nature and extent of microcracking as shown in Figure 7.11c. Fire endurance (Figure 7.11d) seems to produce a more distributed network of microcracks inducing significant damage to cement paste and produce a more tortuous path of microcrack growth. Fatigue loading seems to introduce more new microcracks as shown in Figure 7.11e, when compared with other damaging effects which largely cause propagation of existing microcracks. It means that the energy required to create more new microcracks due to fatigue loading is less than the energy required to propagate existing microcracks. In concrete specimens subjected to impact, microcracks seem to be still limited to interfacial transition zones but their local widths

seem to have grown when compared with undamaged specimens as shown in Figures 7.11f and 7.12b. Loading to peak compression stress led to substantial growth and interconnection of the microcrack system in both normal-strength and high-strength concrete as shown in Figures 7.11g and 7.12c. In case of normal-strength concrete (Figure 7.11g), compression damage effect seems to produce a more distributed network of microcracks than in high-strength concrete (Figure 7.12c). The extent of microcracking and the tortuosity of microcracks were less pronounced in high-strength concrete when compared with normal-strength concrete both prior to and after different damaging effects. Arresting and shifting of microcracks by voids and aggregates are occasionally observed in both normal-strength and high-strength concrete. A comparison of figures 7.11h and 7.13b may suggest that fiber reinforced concrete suffers to some extent less restrained shrinkage microcrack growth. The combined effects of inadequate curing (i.e. early exposure to hot or cold weather) and restraint of shrinkage (Figures 7.11i and 7.11j) produced, in addition to increased interface microcracking, a highly microcracked/porous cement paste.

Generally, It was noticed that there is no distinct difference in microcrack density in parallel or perpendicular sections of undamaged specimens; after different damaging effects; however, differences appeared in microcrack intensity of the two perpendicular sections. In the case of compression and impact loading, sections perpendicular to the loading direction showed more intense microcracking than sections parallel to the loading direction.

Comparison between concrete micrographs captured by ESEM or fluorescent microscopy showed that neither microscopy type or specimen preparation technique has an effect on

the judgment of concrete microcrack behavior. Concrete microstructure microcracks trend and observations were the same in both types.

7.6 DISCUSSION

Various damaging effects produce different levels and types of microcrack propagation in concrete. There seem to be differences in tortuosity and number of microcracks (as well as the extent of microcracking) after different damaging effects. Post-damage properties of concrete reflect on these microstructural changes. For instance, the less tortuous nature of microcracks under freeze-thaw effect yields a relatively more significant effect on permeability than flexural strength. Quasi-static compression of concrete (to peak load) followed by immediate unloading produced extensive growth and interconnection of microcracks, thereby lowering the post-damage mechanical properties and transport properties of concrete. High-strength concrete exhibited less extensive interfacial microcracking in undamaged condition when compared with normal-strength concrete; this could be attributed to differences in aggregate texture, water/cement ratio and interfacial bond strength. Increased microcracking associated with damaging effects (e.g., compression) generally reduced the difference between properties of normal-strength and high-strength concrete. Microstructural investigations indicated that compression produces more intense microcrack growth than impact loading. Permeability measurements suggested that compression is far more damaging to transport properties of concrete than impact; this points at the correlation between the intensity of microcracking of the changes in key engineering properties after damaging effects. Microcrack analysis could thus be a valuable tool in condition assessment of deteriorated concrete structures.

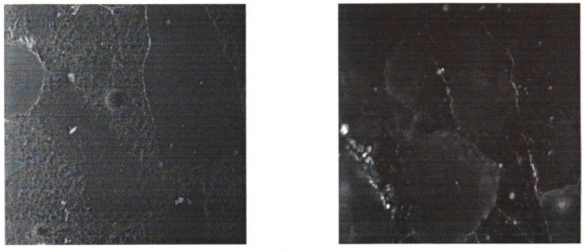

(a) No Damage

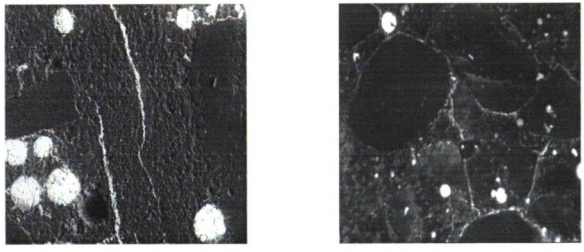

(b) Freeze-Thaw Damage

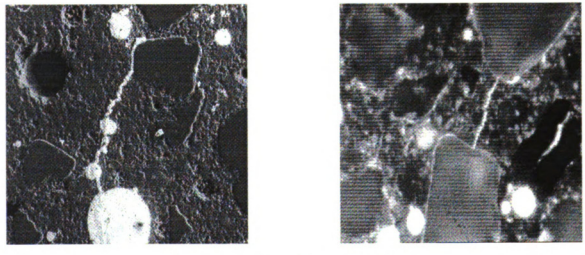

(c) Compression + Freeze-Thaw Damage

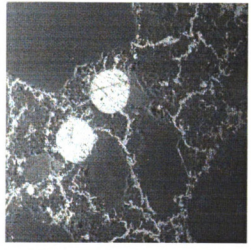
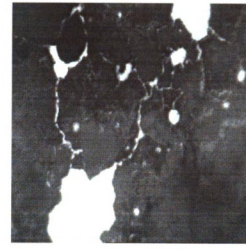

(d) Fire Endurance Damage

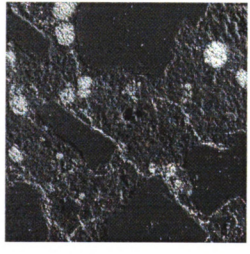
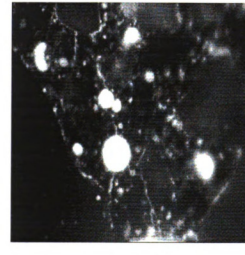

(e) Fatigue Damage

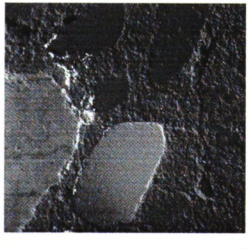
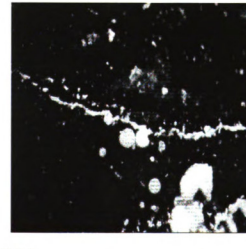

(f) Impact Damage

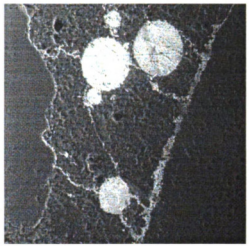
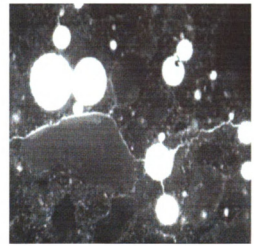

(g) Compression Damage

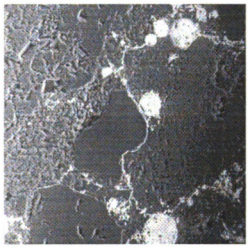
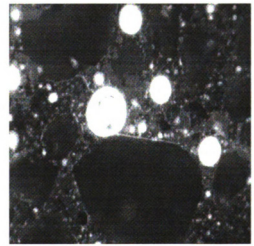

(h) Restrained Shrinkage "Room Temperature" Damage

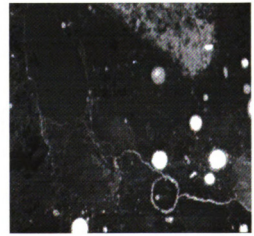

(i) Restrained Shrinkage "Hot Weather" Damage

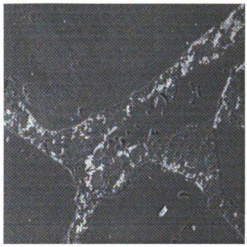

ESEM

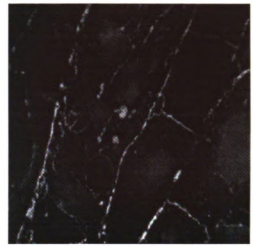

Fluorescent

(j) Restrained Shrinkage "Cold Weather" Damage

Figure 7.11 Micrographs for Normal-Strength Concrete

Compression loading to peak stress caused more damage to splitting tensile strength of high-strength concrete than normal-strength concrete, which could result from the less distributed nature of microcrack growth and the larger microcrack widths in high-strength concrete when compared with normal-strength concrete. Damaging effects which caused not only growth and interconnection of interface microcracks but also introduced low damage in cement paste (e.g., fire endurance or restraint shrinkage under early-age exposure to extreme climates) had particularly damaging effects on concrete performance.

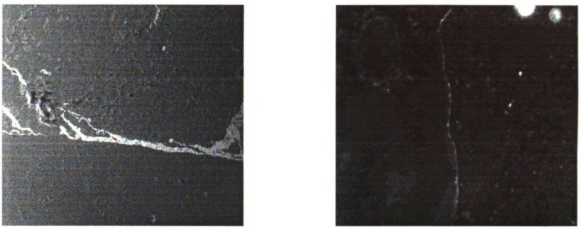

(a) No Damage

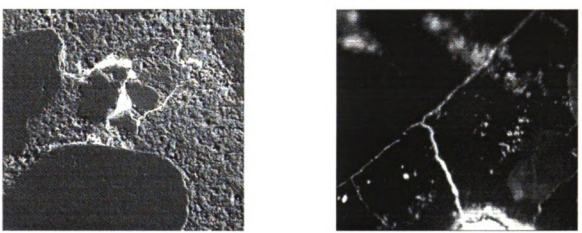

(b) Impact Damage

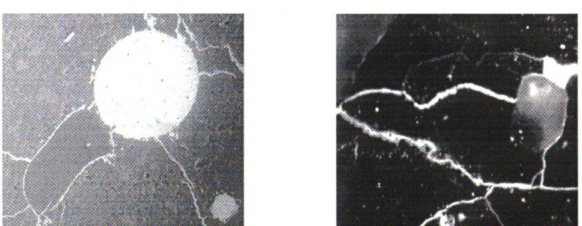

ESEM Fluorescent

(c) Compression Damage

Figure 7.12 Micrographs for High-Strength Concrete

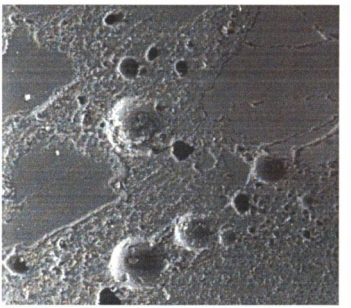

(a) No Damage

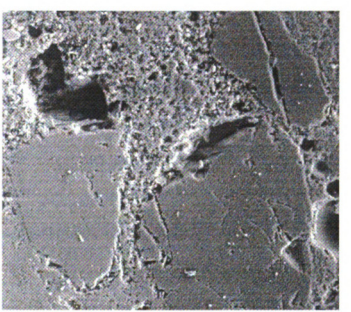

(b) Restrained Shrinkage "Room Temperature" Damage

Figure 7.13 Scanning Electron Micrographs for Fiber Reinforced Concrete

7. 7 CONCLUSIONS

Changes in concrete properties associated with various damaging effects were qualitatively investigated. Observations were also made on microcrack attributes of concrete prior to and after such damaging effects. The results indicated that:

1- Different damaging effects (compression, impact, freeze-thaw, fatigue, freeze-thaw+compression, fire endurance) produced different changes in the extent and nature of microcrack propagation within concrete. Compression increased the length, width and area fraction of microcracks; fatigue increased the number of microcracks, freeze-thaw produced a less tortuous microcrack growth, and impact increased the width of microcrack density increased noticeably in sections perpendicular to the loading direction when compared to the parallel with sections loading direction.

2- Consecutive damaging processes do not always have adverse effects on concrete strength; for example, freeze-thaw damage effect and compression + freeze-thaw damage effect almost has the same influence on concrete flexural strength.

3- Differences in the extent and pattern of microcrack propagation reflected on the deterioration of different properties (flexural strength, impact resistance and permeability) of concrete after damaging effects.

4- Damaging phenomena do not have similar effects on different properties of concrete. Compression damage sharply increases permeability of concrete which impact damage has only slight effects on permeability. Compression damage also noticeably lowers the impact resistance of concrete. Fatigue loading was more damaging to flexural strength. Compression loading to peak followed by immediate unloading proved to be particularly

damaging to concrete when compared with the other damaging phenomena considered in this investigation.

5- Microcrack propagation under compression damage seems to reduce the differences in properties of high-strength versus normal-strength concrete.

6- Variations in the extent and pattern of microcrack propagation and networking (and initiation of new microcracks) reflect on the corresponding changes in different properties (compressive, flexural, and splitting tensile strength) of concrete.

7- Damaging effects (e.g., exposure to fire endurance) cause not only growth and interconnection of microcracks but also introduce new cement paste microcracks yield particularly severe damage to engineering properties of concrete.

8- Under compression loading to peak compressive stress, a more distributed system of finer microcracks in normal-strength concrete yields less damage to performance than a less distributed system of microcracks with larger widths.

CHAPTER 8

QUANTITATIVE MICROSTRUCTURAL ANALYSIS OF CONCRETE

8.1 PREFACE

Qualitative analysis of concrete microcracks has been used to investigate concrete quality and deterioration mechanisms.[47,115-117] Such qualitative studies could involve visual inspection,[10] microscopy,[1] acoustic,[40,61,62] neutron radiography[24,48] and x-ray techniques.[10] Qualitative analysis approaches, however, lack the rigor and statistical viability of quantitative analysis approaches, therefore it is difficult to assess consistency and reliability in qualitative analysis of concrete microcrack systems. The experience of investigator and the sampling scheme would strongly influence the outcomes of qualitative analyses.[10] Quantification of the microcrack system can provide thorough and reliable basis for investigation the effects of different damaging phenomena on concrete. As Lord Kelvin[92] said "when you can measure what you are speaking about and express it in numbers, you know something about it; but when you cannot express it in numbers, your knowledge is of a meager and unsatisfactory kind; it may be the beginning of knowledge, but you have scarcely in you thoughts advanced to the state of science, whatever the matter may be". Erick Ringot[118] tried to systematically quantify the concrete microcrack system, but his approach faced the limitation of computer technology at that time. Recent developments in computer-based image processing and analysis and microscopy techniques provide powerful tools for quantitative microstructural investigation of concrete; and allowed to quantify microcrack density in mortar and cement paste.[119] Application of the proposed comprehensive approach towards

investigation of microcrack characteristics in normal-strength, relatively high-strength, and normal-restrained concrete specimens under different damaging load and weathering phenomena are reported herein.

8.2 EXPERIMENTAL PROGRAM

Two concrete mixtures were considered in the experimental program: (1) normal-strength (unrestrained and restrained specimens) and (2) relatively high-strength. Type I Portland cement and natural sand were used in both mixtures. Crushed limestone with maximum particle size of 19 mm (3/4 in) was used as coarse aggregate in the normal-strength mix, with cement : fine aggregate : coarse aggregate : water mass ratios of 1 : 1.59 : 1.98 : 0.514, targeting 28-day compressive strength of 33 MPa (4750 psi). This mix was air-entrained, and provided an air content of 3.5 percent with a slump of 190 mm (7.5 in). The relatively high-strength mix incorporated natural granite with maximum particle size of 10 mm (3/8 in) as coarse aggregate; it also incorporated silica fume and superplasticizer, with cement: fine aggregate : coarse aggregate : water : silica fume mass ratios of 1 : 1.7 : 0.9: 0.42 : 0.2, targeting 28-day compressive strength 43 MPa (6120 psi). This mix provided 1.9 percent air content and a slump of 64 mm (2.5 in).

The following specimens were molded and consolidated: 76 × 76 × 305 mm (3 × 3 × 12 in) prismatic specimens for compression, fatigue, freeze-thaw, compression + freeze-thaw, and fire tests; 152 mm (6 in) diameter by 63.5 mm (2.5 in) height cylindrical specimens for drop weight impact testing; 102 × 76 × 406 mm (4 × 3 × 16 in) prismatic specimens for restrained shrinkage tests under different exposure conditions incorporated two 38 mm (1.5 in) long threaded steel bars of 6.35 mm (0.25 in) at two ends, which were

embedded within concrete to restrain longitudinal drying shrinkage of concrete during curing and 102 × 76 × 406 mm (4 × 3 × 16 in) prismatic specimens reinforced with four #3 Grade 60 steel or four #3 glass fiber composite bars having 12.5 mm (0.5 in) cover on all sides for exposure to corrosive environment (steel and composite reinforcement) and hot water (composite reinforcement).

The following damaging effects were investigated: compressive loading (ASTM C39) to peak stress with immediate unloading, drop weight impact loading (ACI com.215) to 85% of the ultimate capacity, four point flexural fatigue loading (ACI com. 225) up to 85% of the number of cycles causing flexure failure, 300 cycles (75 days) of freeze-thaw in water (ASTM C666), compressive loading to peak compressive stress followed by immediate unloading and then exposure to 300 freeze-thaw cycles in water, exposure to fire at 425°C (800°F) for 3 hours, exposure to relatively hot, 55°C (130°F), environment, and exposure to relatively cold, -3.5°C (-25°F), environment, and exposure to 3.5% corrosive solution of sodium chloride at 40°C (105°F) for 7 days followed by air-drying at 50% relative humidity and 22°C (72°F) for 7 days with a total test period 4 months (for specimens reinforced with steel or composite rebars), and 4 months of continuous immersion of in 60°C (140°F) water (for specimens reinforced with composite rebars to assess the consequence of alkali attack on glass fiber composites). These damaging phenomena left the specimens intact for the purpose of microstructural analysis. Tables 8.1 and 8.2 summarize types, dimensions, number of specimens, and damaging effects considered in the experimental program.

Table 8.1 Summary of Specimens and Damaging Effects of Normal-Strength Concrete in The Experimental Program

Damaging Effect	Specimen Type and Geometry	Number of Specimens	Number of Sections	Number of Images
Unreinforced-Unrestrained Specimens				
No Damaging Effect	Unreinforced prisms 76 × 76 × 305 mm	4	16	10496
Compression	Prisms 76 × 76 × 305 mm	7	28	18368
Impact	Cylinders 152 mm diameter by 63.5 mm height	4	16	10496
Fatigue	Prisms 76 × 76 × 305 mm	2	8	5248
Freeze-Thaw	Prisms 76 × 76 × 305 mm	4	8	5248
Comp. + Freeze-Thaw	Prisms 76 × 76 × 305 mm	2	8	5248
Fire	Prisms 76 × 76 × 305 mm	3	12	7872
Reinforced-Unrestrained Specimens				
No Damaging Effect	Steel reinforced prisms 102 × 76 × 406 mm	2	8	5248
	Composite reinforced prisms 102 × 76 × 406 mm	2	8	5248
Corrosive Environment (Salt Water)	Steel reinforced prisms 102 × 76 × 406 mm	2	8	5248
	Composite reinforced prisms 102 × 76 × 406 mm	2	8	5248
Hot Water	Composite reinforced prisms 102 × 76 × 406 mm	2	8	5248
Unreinforced-Restrained Specimens				
No Damaging Effect	Prisms 102 × 76 × 406 mm	2	8	5248
Exposure to Hot Environment	Prisms 102 × 76 × 406 mm	2	8	5248
Exposure to Cold Environment	Prisms 102 × 76 × 406 mm	2	8	5248

Table 8.2 Summary of Damaging Effects and Specimens of High-Strength Concrete in The Experimental Program

Damaging Effect	Specimen Type and Geometry	Number of Specimens	Number of Sections	Number of Images
Unreinforced-Unrestrained Specimens				
No Damaging Effect	Prisms 76 × 76 × 305 mm	4	16	10496
Compression	Prisms 76 × 76 × 305 mm	3	12	7872
Impact	Cylinders 152 mm diameter by 63.5 mm height	4	16	10496

Control specimens were tested in compression (to check the targeted compressive strength and to determine the ultimate peak stress), four-point flexure (to determine ultimate flexural strength), and flexural fatigue at 450 cycles per minute with repeated flexural loads ranging from 15% to 85% of ultimate flexural strength (to determine the number of cycles causing failure), and impact testing. Quantitative investigation of the microcrack effects system in undamaged concrete provided the basis to assess the effects of different damaging phenomena on microcrack growth.

Molded specimens were kept moist for 24 hours, after which they were demolded (except for restrained specimens) and moist cured at 100% relative humidity and 22°C (72°F) for 28 days, and then conditioned at 50% relative humidity at 22°C (72°F) for 180 days prior to compression and impact testing. Restrained normal–strength concrete specimens were kept moist for 24 hours, after which they were stored (without demolding) for 28 days at 55°C (130°F) for hot weather exposure or at –3.5°C (-25°F) for cold exposure, and then

demolded and conditioned at 50% relative humidity and 22°C (72°F) for 180 days. The restraint against shrinkage was effective as far as the specimens were not demolded. This relatively long period of conditioning allows for development of shrinkage microcracks which occur within concrete largely due to the restraint of cement paste shrinkage measurements by aggregates.

8.3 MICROSTRUCTURAL ANALYSIS SCHEME

For the purpose of specimen preparation, two pairs of two perpendicular sections were cut out of each specimen. One pair was cut in the direction of loading and the other parallel to the direction of loading or in the longer and shorter directions of concrete specimens when no mechanical loads were applied. One pair of sections was used for fluorescent microscopy and the other for the environmental scanning electron microscopy "ESEM" (backscattered technique). Specimen preparation methods described in section 4.2.4 were used to generate a sharp contrast between features of interest (microcracks and voids) and the body of concrete. Each section was investigated 3 times at different magnifications (125X, 250X, 500X) using each microscopy technique. A total of 144 images were captured from each section at 125X, and 256 images were captured from each section at 250X and 500X magnifications; these selections were chosen to yield representative data based on statistical criteria. The number of sections and total number of images captured from each specimen are shown in Tables 8.1 and 8.2. Images were captured randomly using a programmed travel stage to move randomly in different positions and capture images from a scanned 75 mm × 75 mm (3 in × 3 in) area. Image processing scenarios selected in section 5.2.1.3 were employed to enhance the contrast

between microcracks versus the body of concrete and also to eliminate noise and provide crisp images. Mathematical expressions provided in section 5.3.1.1 were used to produce microcrack planar measurements while stereological relationships provided in section 6.1.4.1 were used to produce microcrack spatial measurements.

8.4 MICROSTRUCTURAL ANALYSES RESULTS

8.4.1 Analogy Between Unreinforced (Unrestrained) and Reinforced (Unrestrained) Normal-Strength Concrete Specimens

8.4.1.1 *Planar (2-D) Measurements*

Figures 8.1 and 8.2 present results (means and standard errors) of planar (2-D) microcrack measurements in horizontal sections (perpendicular to the loading direction) for unreinforced (unrestrained) and reinforced (unrestrained) concrete specimens, respectively. It should be emphasized that since images were captured from random locations on sections, the quantified microcrack characteristics for reinforced concrete sections reflect on conditions both in the vicinity and away from reinforcement. The data presented herein combine the results of fluorescent and scanning electron microscopy. There were minor differences between results of the two microscopy techniques, which can be largely attributed to the associated differences in sample preparation techniques and the precision of each microscope. Generally, higher magnification levels seem to provide far detection of finer microcracks. One-way analysis of variance "ANOVA" (t-test) at 10% level of significance was used to detect any statistically significant differences between measurements made on concrete specimens in undamaged condition and after different damaging effects.

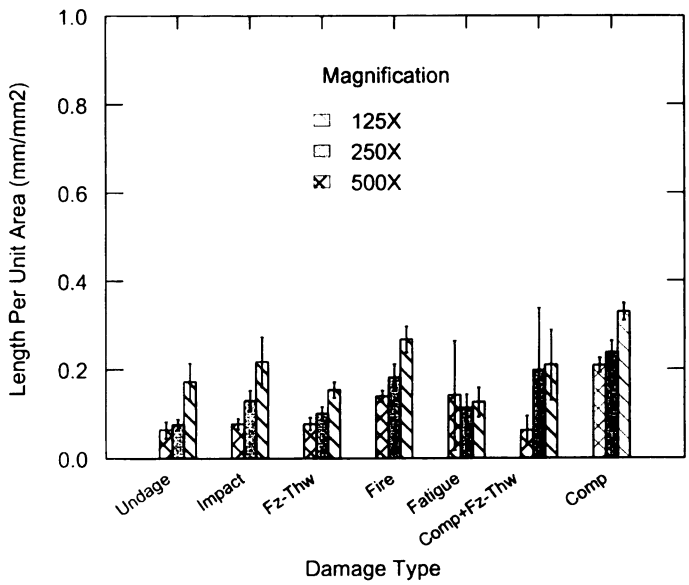

(a) Length Per Unit Area

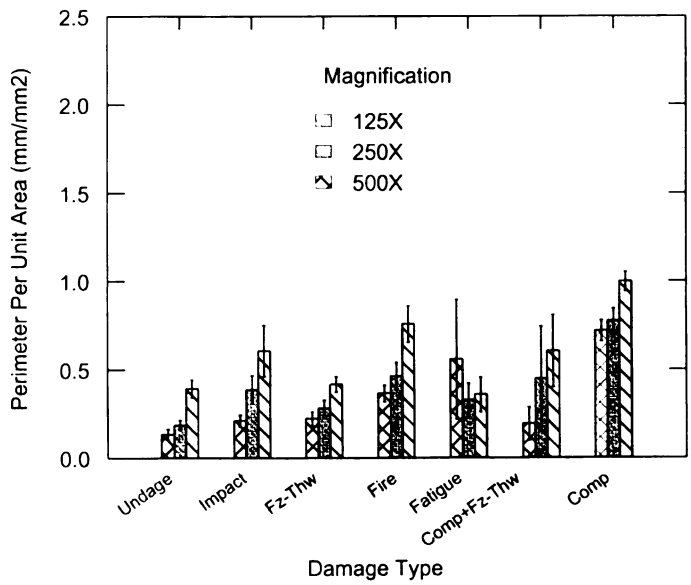

(b) Perimeter Per Unit Area

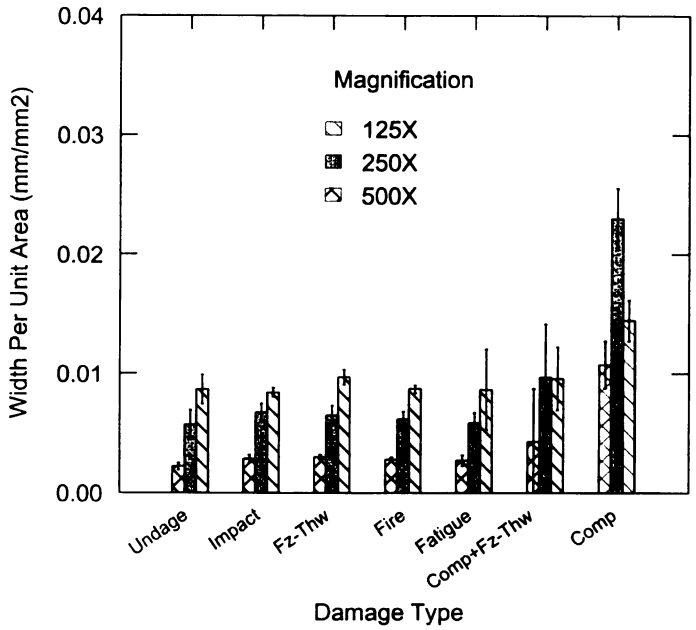

(c) Width Per Unit Area

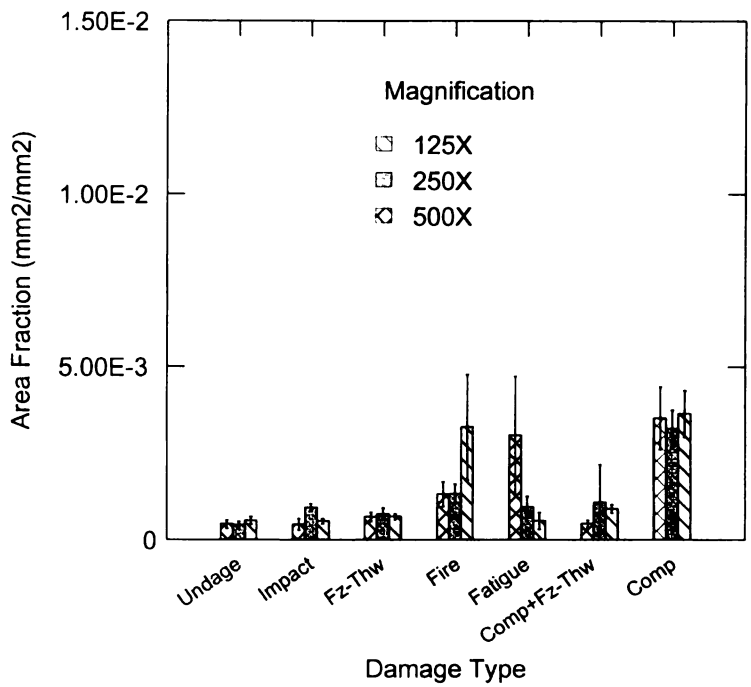

(d) Area Fraction

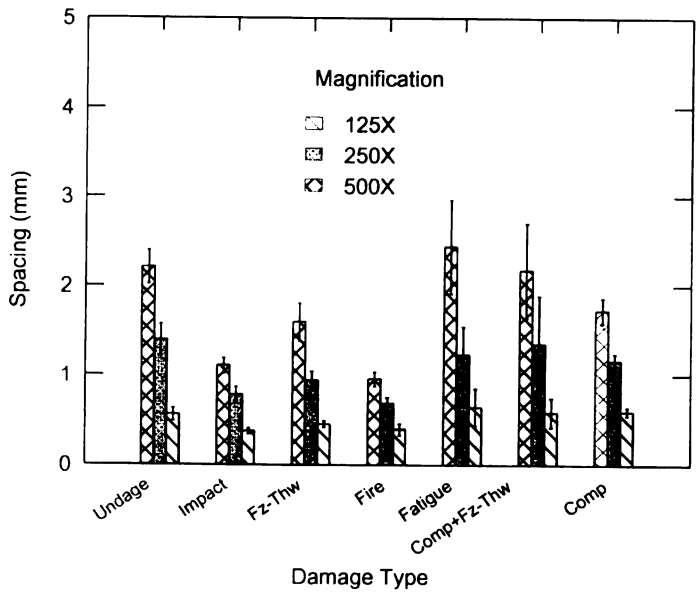

(e) Spacing

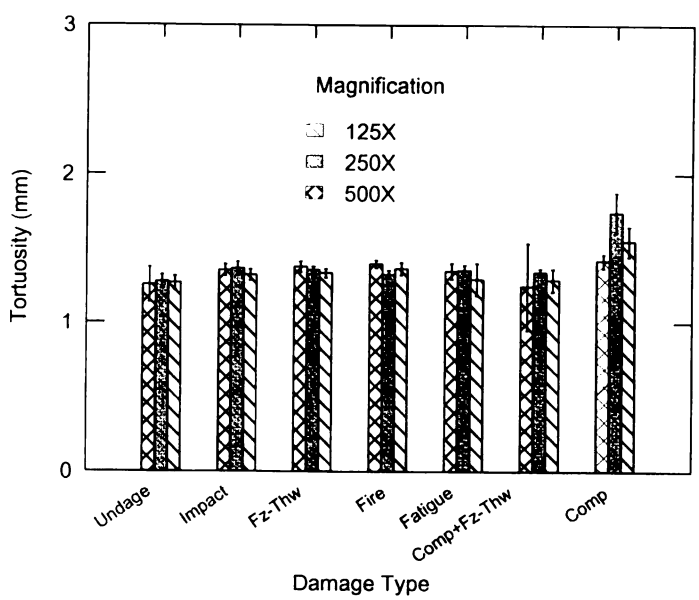

(f) Tortuosity

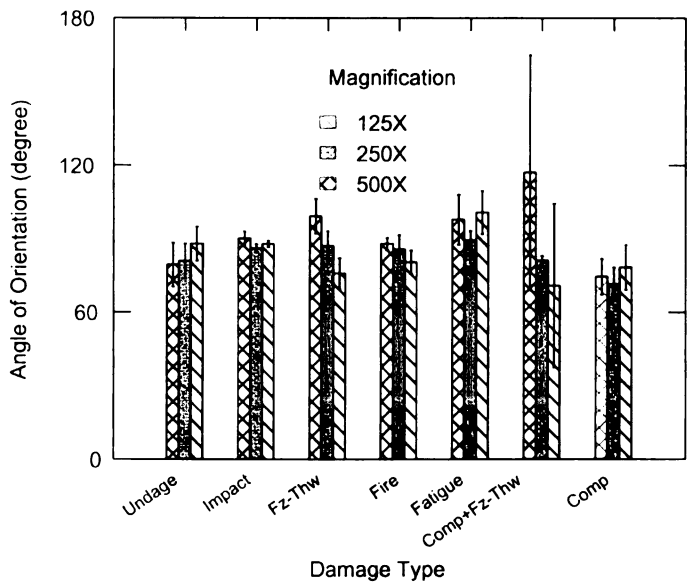

(g) Angle of Orientation

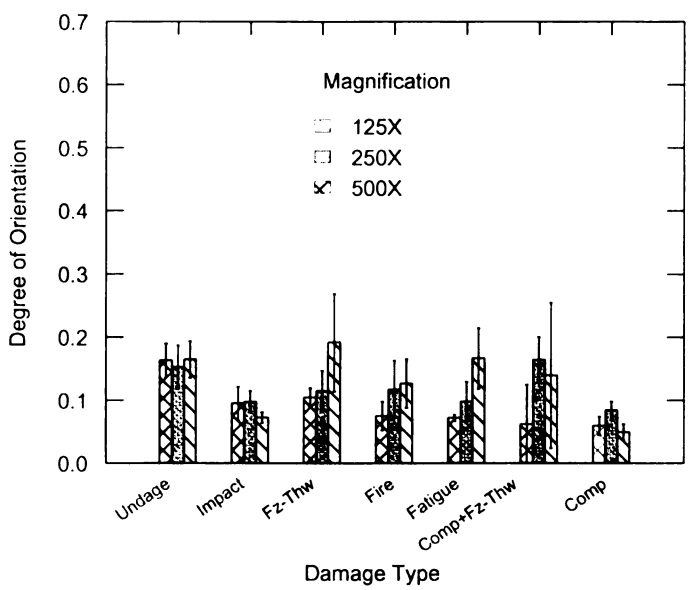

(h) Degree of Orientation

Figure 8.1 Planar (2-D) Measurements for Unreinforced (Unrestrained) Normal-Strength Specimens in Horizontal Section (X-Y)

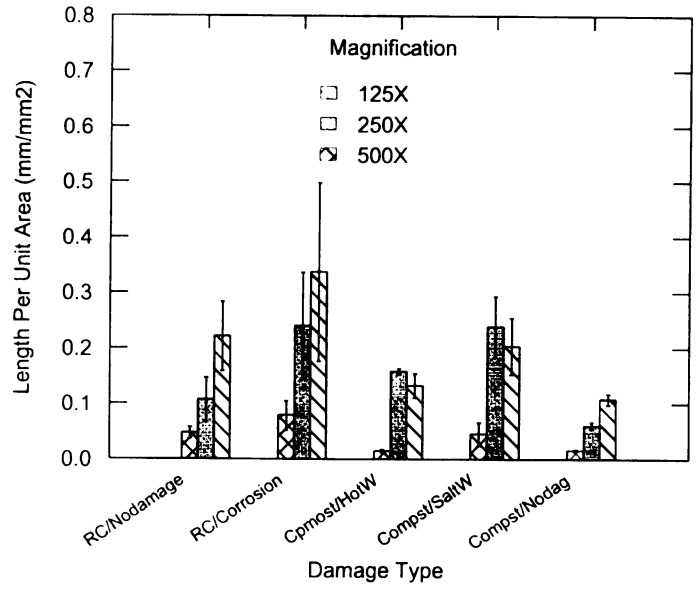

(a) Length Per Unit Area

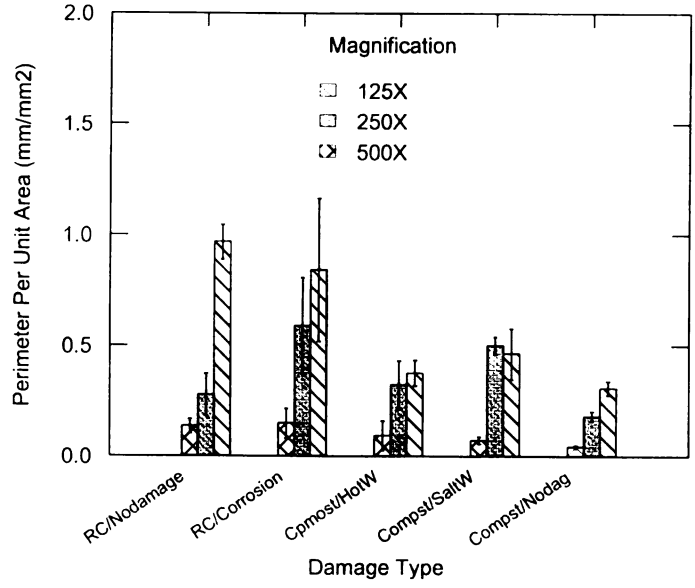

(b) Perimeter Per Unit Area

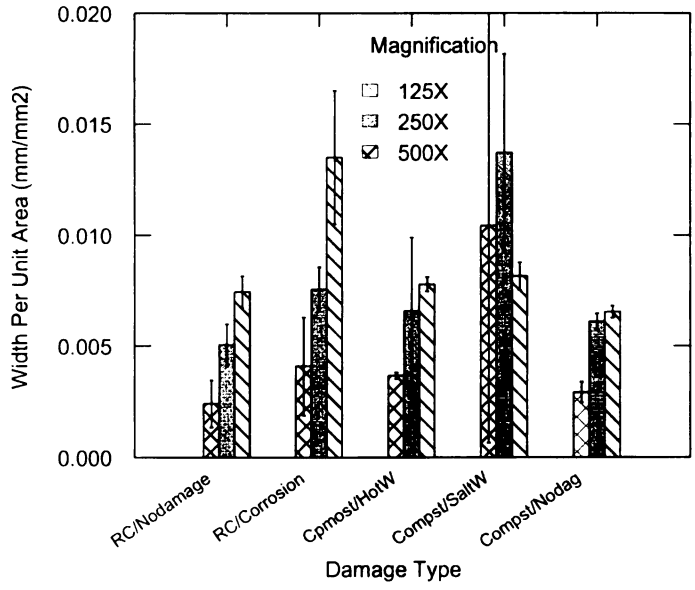

(c) Width Per Unit Area

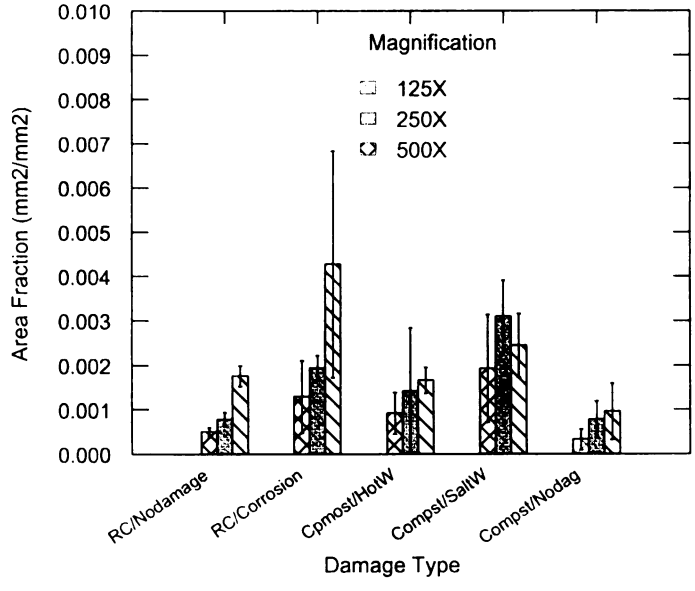

(d) Area Fraction

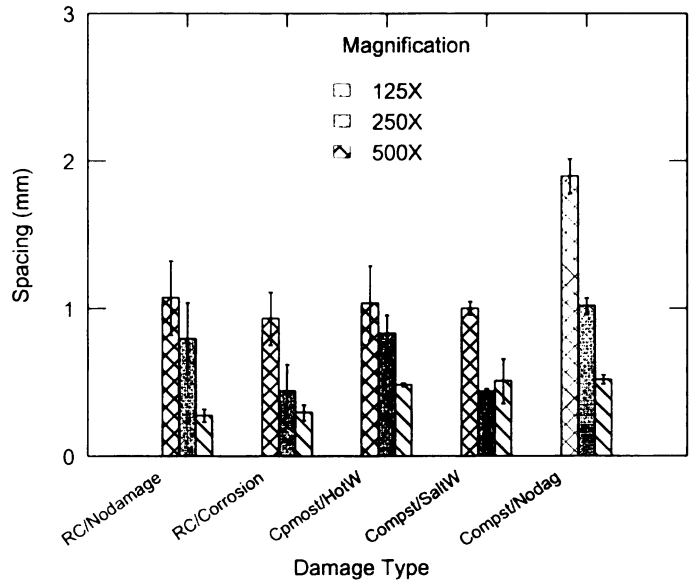

(e) Spacing

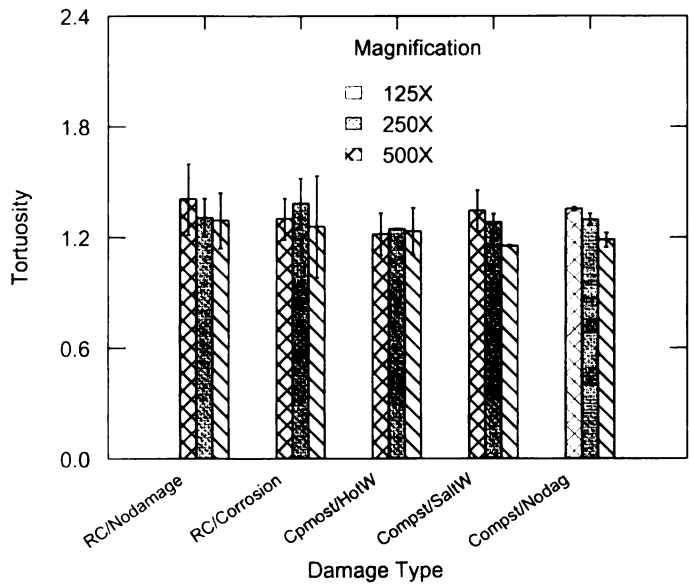

(f) Tortuosity

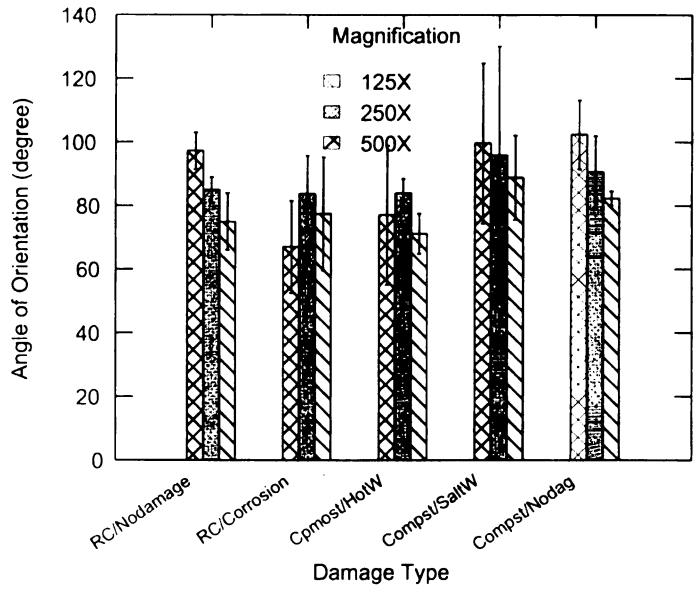

(g) Angle of Orientation

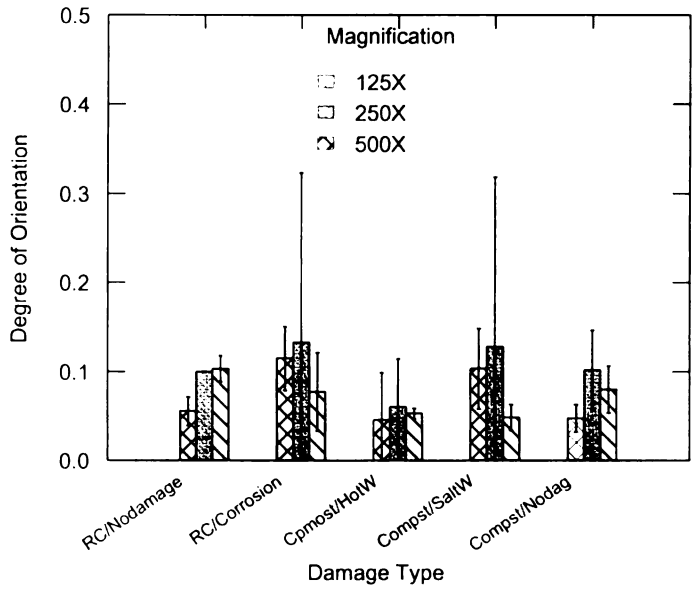

(h) Degree of Orientation

Figure 8.2 Planar (2-D) Measurements for Reinforced (Unrestrained) Normal-Strength Specimens in Horizontal Section (X-Y)

This statistical analysis covered the combined results of fluorescent and scanning electron microscopy at all magnifications considered in this investigation. The results of statistical analysis for unreinforced and reinforced concrete specimens (changes from undamaged conditions) are presented in Tables 8.3 and 8.4, respectively.

In the case of unreinforced specimens (Table 8.3), compression seems to be the most severe damaging effect considered in this investigation; it tends to markedly change the microcracks characteristics measured on cross sections perpendicular to load direction. This simply confirms the fact that microcrack growth planes tend to be parallel to the direction of loading under compression. Damaging effects of fire and freeze-thaw on microcrack characteristics are also significant; unlike compression, however, fire and freeze-thaw do not seem to yield any preferred orientation of microcracks. Impact damage moderately alters various microcrack characteristics; its effect on crack width per unit area was somewhat pronounced, which may be attributed to the nature of the sudden failure due to the internal pressure produced by the impact force. Fatigue damage increased the length per unit area and reduced the spacing of microcracks, but did not significantly alter the width per unit area of microcracks. Combined effects of compression followed by freeze-thaw did not yield the expected level of damage to microcrack system; this may be attributed to the different influence of compression and freeze-thaw on microcrack characteristics, however, more studies are needed to make conclusive remarks.

Table 8.3 Results of Statistical Analysis for Unreinforced (Unrestrained) Normal-Strength Specimens (Planar Measurements) (Changes from Undamaged Condition in Percent)

Measurements	Section	Comp.	Impact	Freeze-Thaw	Comp. + Freeze-Thaw	Fatigue	Fire
Length per Unit Area	XY	S	I	I	S	I	S
		81.1	14.2	1.2	40.2	3.21	69.6
	YZ	I	I	I	I	S	S
		11.5	7.6	4.71	14.6	50.5	41.4
Perimeter per Unit Area	XY	S	S	I	S	S	S
		92.4	63.4	11.4	73.3	59.8	77.7
	YZ	I	I	S	I	I	S
		22.2	21.7	38.9	12.8	14.5	45.6
Width per Unit Area	XY	S	I	I	I	I	I
		191.2	5.32	1.01	6.48	2.04	1.12
	YZ	I	S	S	I	I	S
		41.5	35.4	34.2	11.5	14.5	31.3
Area Fraction	XY	S	I	I	S	I	S
		214	10.5	11.3	53.5	14.6	113
	YZ	I	S	S	S	S	S
		31.8	43.2	66.8	48.6	74.3	88.6
Spacing	XY	I	S	S	I	I	S
		-22.2	-64.9	-47.4	-8.65	-2.04	-67
	YZ	S	I	S	S	S	I
		-15.5	-8.4	-31.2	-44.5	-31.5	-18
Tortuosity	XY	S	I	I	I	I	I
		25.1	6.34	5.48	2.47	3.01	9.44
	YZ	I	I	I	I	I	S
		6.4	8.45	1.1	4.45	8.71	35.5
Angle of Orientation	XY	I	I	I	S	I	I
		-13.4	6.25	2.01	17.8	14.3	5.87
	YZ	S	I	I	I	S	I
		61.7	11.7	-4.57	13.68	58.6	-6.6
Degree of Orientation	XY	S	S	I	I	I	I
		-238	-66.5	-16.6	-22.6	-33.4	-28
	YZ	I	S	S	S	I	I
		-15	81.8	75.5	44.8	-11.4	14.6

Table 8.4 Results of Statistical Analysis for Reinforced (Unrestrained) Normal-Strength Specimens (Planar Measurements) (Changes from Undamaged Condition in Percent)

Measurements	Section	Corrosive Environment (Salt water)		Hot water Composite Reinforced Specimens
		Steel Reinforced Specimens	Composite Reinforced Specimens	
Length per Unit Area	XY	S 75.6	S 112	S 70.0
	YZ	I 33.3	I 13.7	S 48.5
Perimeter per Unit Area	XY	S 31.1	I 37.6	I 18.5
	YZ	I 5.67	I 4.51	I 9.89
Width per Unit Area	XY	S 64.3	S 108	I 16.1
	YZ	I 7.58	I 23.7	I 4.36
Area Fraction	XY	S 98.4	S 184.7	S 54.5
	YZ	I 31.1	I 28.9	I 15.5
Spacing	XY	S -21.6	S -33.3	I -18.4
	YZ	I -5.5	I -3.6	I -7.71
Tortuosity	XY	I -1.64	I -0.57	I -1.5
	YZ	I 2.21	I 1.58	I -0.88
Angle of Orientation	XY	I -19.5	I -3.1	I -10.7
	YZ	S 48.7	I -25.1	I -3.5
Degree of Orientation	XY	S 61.5	S 25	I -18.7
	YZ	I 11.6	I 5.7	I -6.86

S = Significant effect
I = Insignificant effect

In the case of reinforced concrete specimens (Table 8.4), cyclic exposure to corrosive (salt soluble) environment altered the microcrack characteristics with both steel and polymer composite reinforcement. These points at the damaging effects of the wet–dry exposure conditions on the body of concrete (irrespective of the type of reinforcement type). Hot water immersion increased microcrack length per unit area; its overall effect on microcrack characteristics, however, were relatively small.

8.4.1.2 Spatial *(3-D) Measurements*

Figures 8.3 and 8.4 present the results (means and standard errors) of spatial (3-D) microcrack measurements for unreinforced (unrestrained) and reinforced (restrained) concrete specimens, respectively. One-way analysis of variance "ANOVA" (t-test) at 10% level of significance was used to detect any statistically significant difference between measurements made on concrete specimens in undamaged condition and after different damaging effects. The results of statistical analysis for unrienforced and reinforced concrete specimens (changes from undamaged conditions) are shown in Tables 8.5 and 8.6, respectively.

In the case of unreinforced specimens (Table 8.5), compression and fire damage yield the most pronounced (3-D) propagation of microcracks. Freeze-thaw and impact damage seem to increase the width and thus the volume fraction of existing microcracks, without greatly altering their surface area and spacing of microcracks. Again the combined effects of compression followed by freeze-thaw produce less damaging effect on microcrack characteristics than expected. More thorough investigations are needed to make conclusive remarks in this regard.

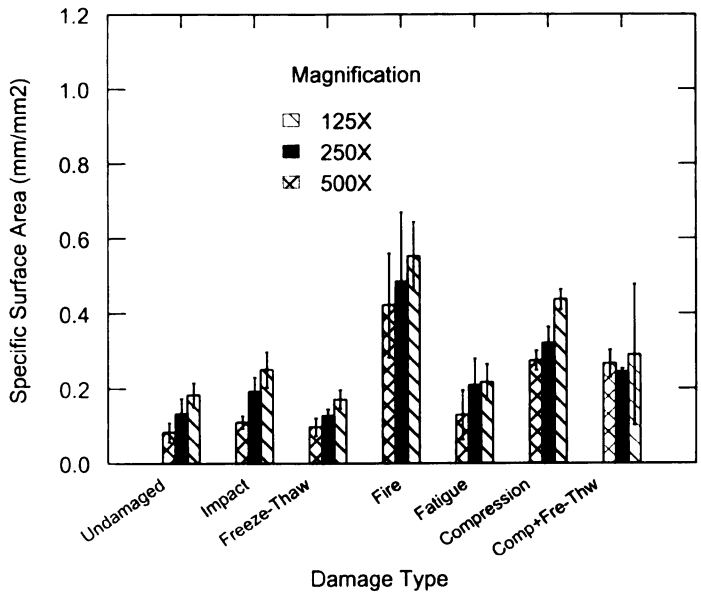

(a) Specific Surface Area

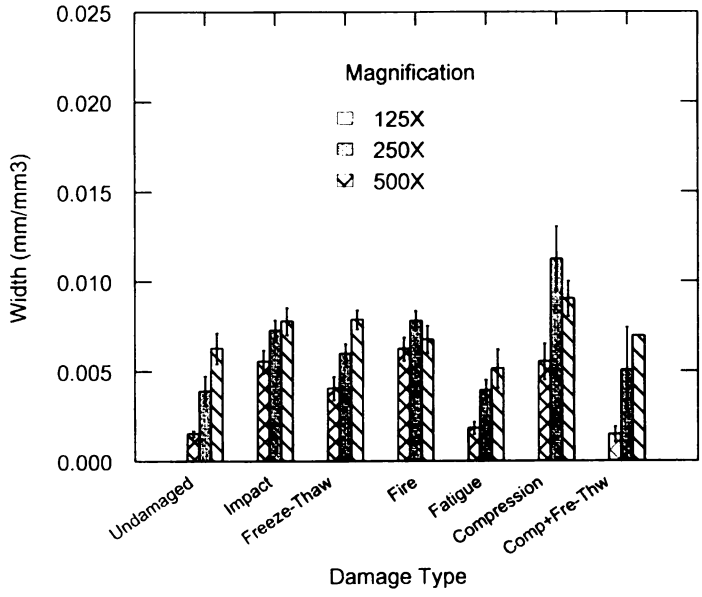

(b) Width

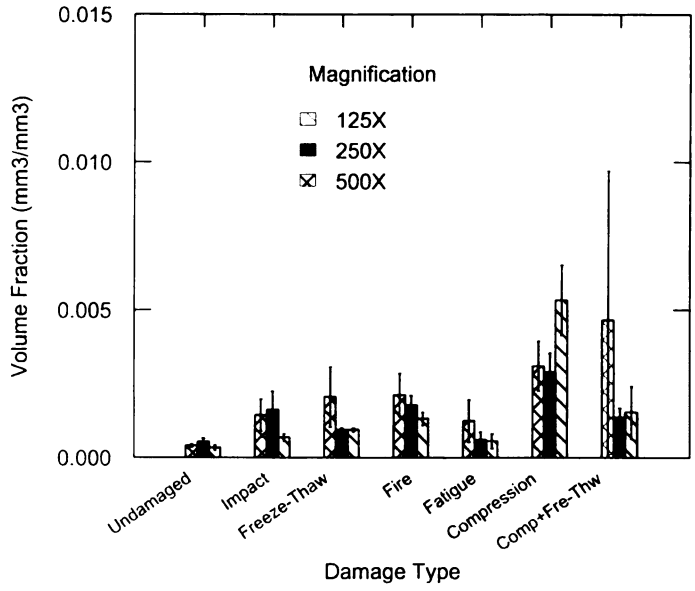

(c) Volume Fraction

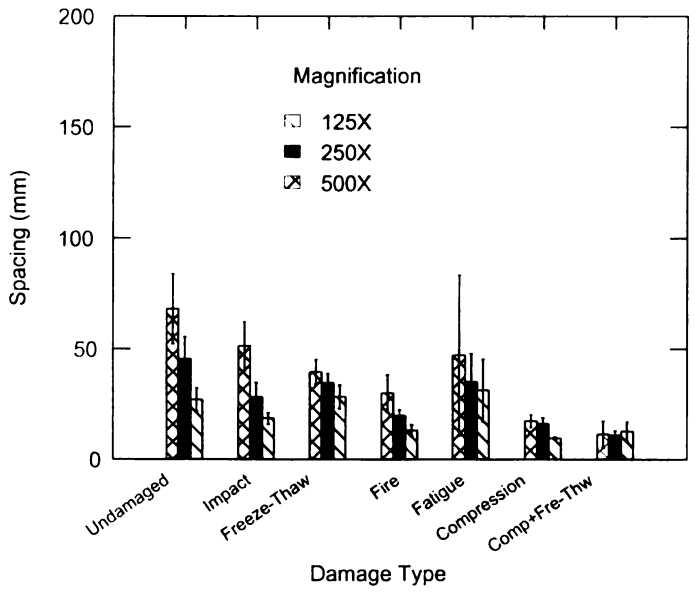

(d) Spacing

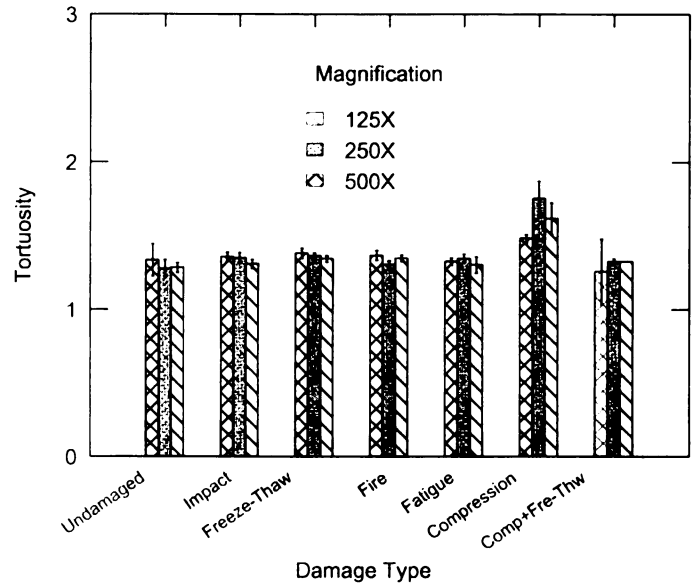

(e) Tortuosity

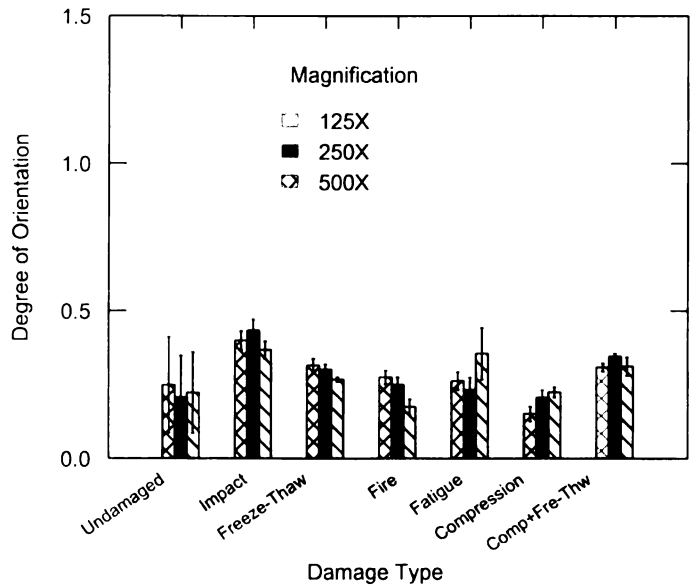

(f) Degree of Orientation

Figure 8.3 Spatial (3-D) Measurements for Unreinforced (Unrestrained) Normal-Strength Specimens

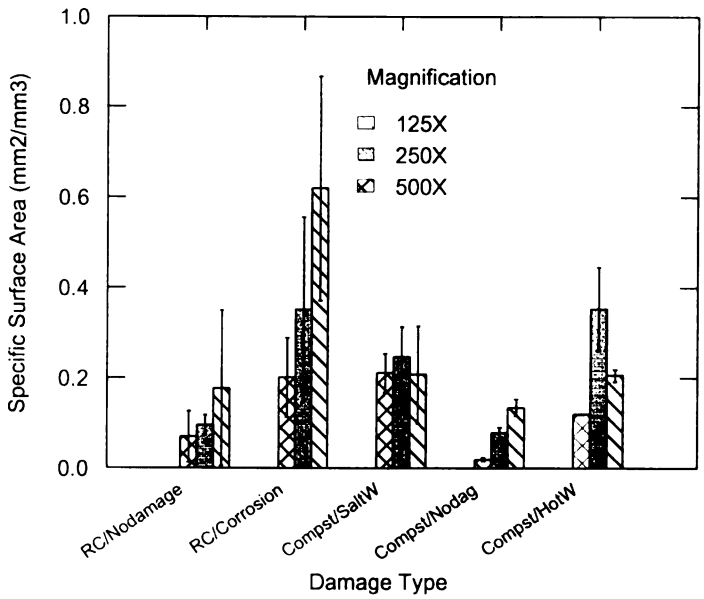

(a) Specific Surface Area

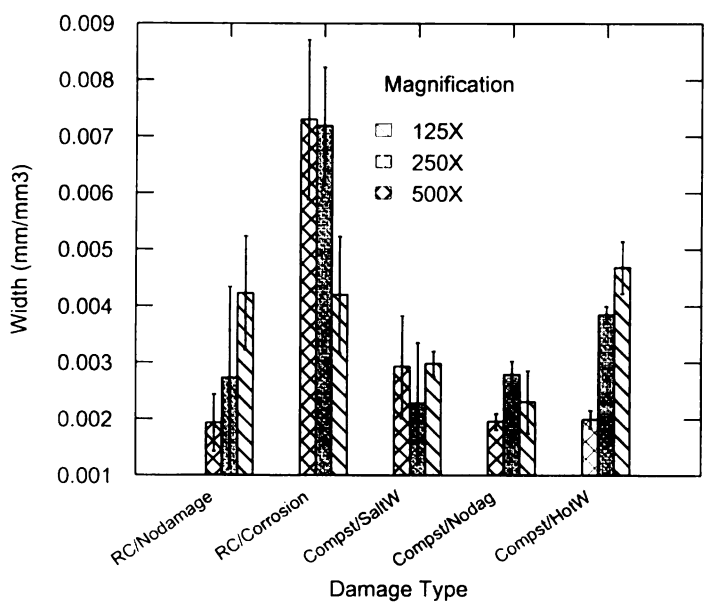

(b) Width

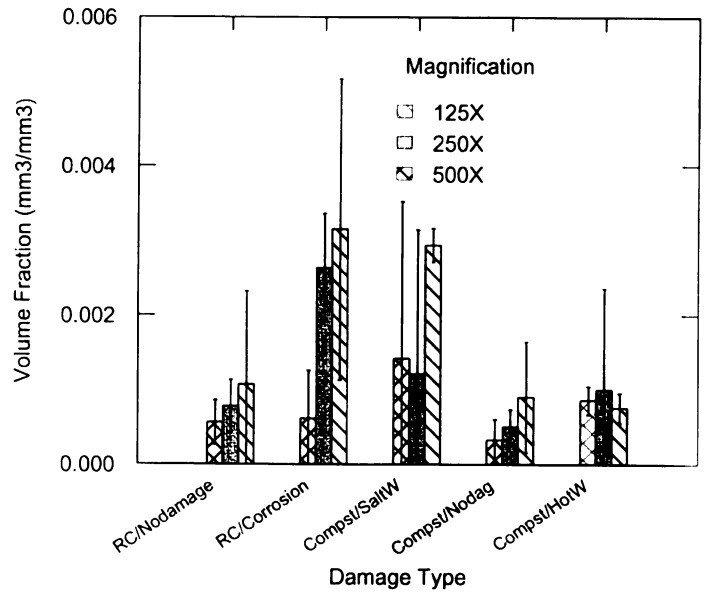

(c) Volume Fraction

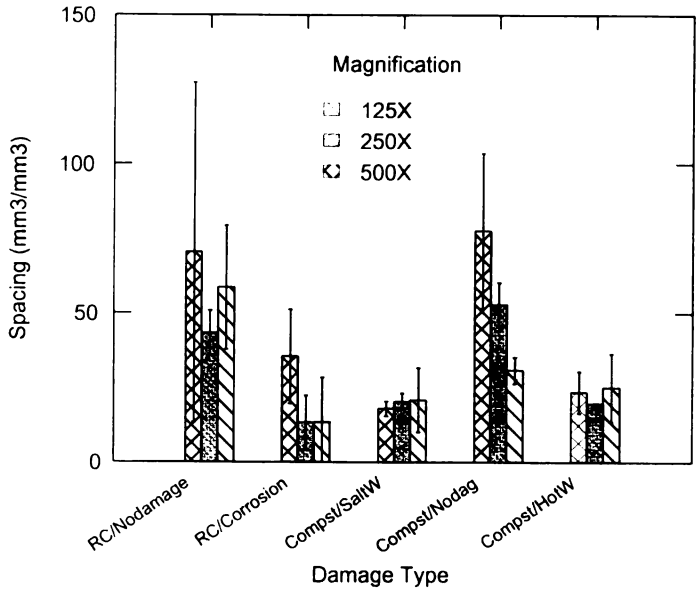

(d) Spacing

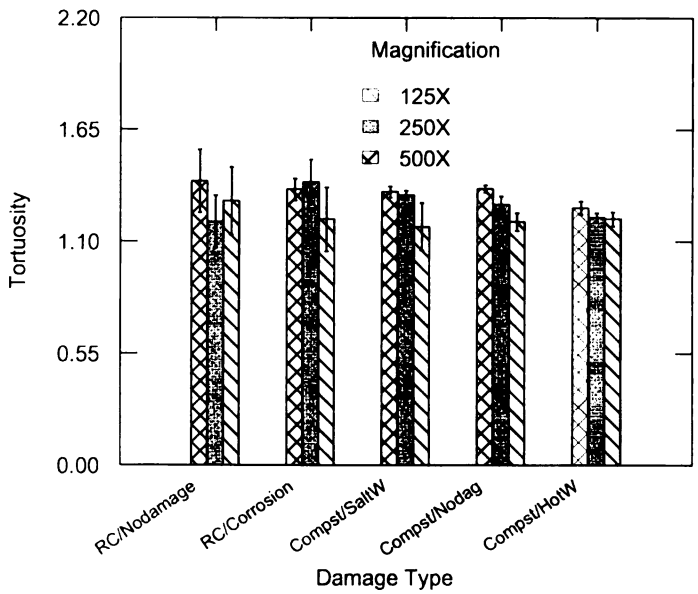

(e) Tortuosity

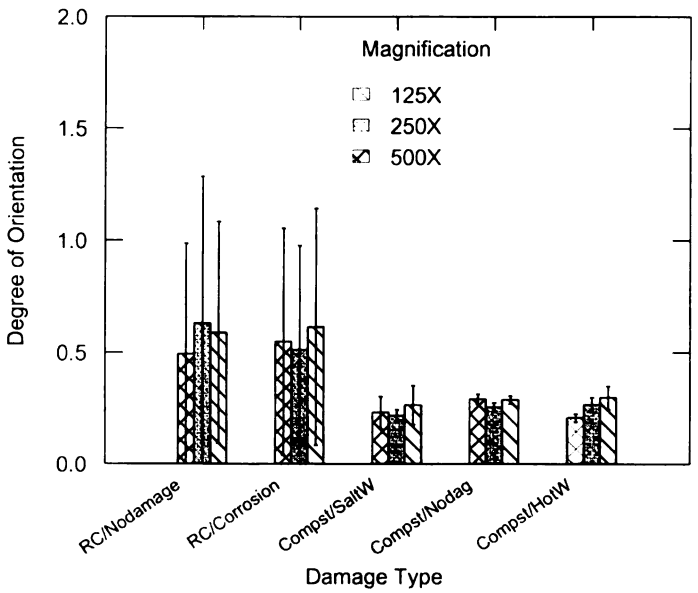

(f) Degree of Orientation

Figure 8.4 Spatial (3-D) Measurements for Reinforced (Unrestrained) Normal-Strength Specimens

Table 8.5 Results of Statistical Analysis for Unreinforced (Unrestrained) Normal-Strength Specimens (Spatial Measurements) (Changes From Undamaged Condition in Percent)

Measurements	Compression	Impact	Freeze-Thaw	Compression +Freeze-Thaw	Fatigue	Fire
Specific Surface Area	S	I	I	S	S	S
	80.2	7.65	3.54	51.5	35.4	147
Width per Unit Volume	S	S	S	I	I	S
	98.5	68.5	51.4	21.4	-11.4	88.4
Volume Fraction	S	S	S	S	I	S
	214	96.4	76.5	81.4	23.3	133
Spacing	S	I	I	S	I	S
	-48.3	-15.6	-21.4	-55.4	-13.8	-41
Tortuosity	S	I	I	I	I	I
	84.6	5.41	5.74	1.23	2.21	8.47
Degree of Orientation	I	S	I	S	I	I
	-11.5	77.8	18.4	38.3	16.5	8.74

S – Significant effect
I – Insignificant effect

Table 8.6 Results of Statistical Analysis for Reinforced (Unrestrained) Normal-Strength Specimens (Spatial Measurements) (Changes from Undamaged Condition in Percent)

Measurements	Corrosive Environment (Salt Water)		Hot water
	Steel Reinforced Specimens	Composite Reinforced Specimens	Composite Reinforced Specimens
Specific Surface Area	S	S	S
	136	108	151
Width per Unit Volume	S	I	S
	98.8	13.8	48.7
Volume Fraction	S	S	I
	113	81.4	36.7
Spacing	S	S	S
	-47.7	-51.5	-53.7
Tortuosity	I	I	I
	-0.87	4.64	-3.47
Degree of Orientation	I	I	I
	-8.78	-5.48	4.87

S = Significant effect
I = Insignificant effect

In the case of reinforced concrete specimens (Table 8.6) the spatial (3-D) data suggest that steel reinforced concrete suffered somewhat more damage than composite reinforced concrete under cyclic (wet-dry) exposure to salt solution. The (3-D) data also highlighted the damaging effects of hot water immersion on the microcrack system in composite reinforced concrete.

8.4.2 Analogy Between Unrestrained (Unreinforced) and Restrained (Unreinforced) Normal-Strength Concrete Specimens

8.4.2.1 *Planar (2-D) Measurements*

Figure 8.5 presents the results (means and standard errors) of all measurements in plane (2-D) on horizontal sections (XY - perpendicular to loading direction) for unrestrained (unreinforced) and restrained (unreinforced) normal-strength concrete specimens. The horizontal sections showed more extensive microcracking than the vertical sections (parallel to the direction of loading). The data presented herein combine the results of fluorescent and ESEM at the three used magnifications. There were minor differences between results of the two microscopy techniques, which could result from the differences in sample preparation and the precision of each microscope. Generally, higher magnification levels seem to allow far detection of finer microcracks. One-way analysis of variance "ANOVA" (t-test) at 10% level of significance was used to detect any significant effects of different damage phenomena and restraint condition (unrestrained vs. restrained) on microcrack characteristics. Results of statistical analysis and comparisons between unrestrained and restrained normal-strength specimens are presented in Table 8.7.

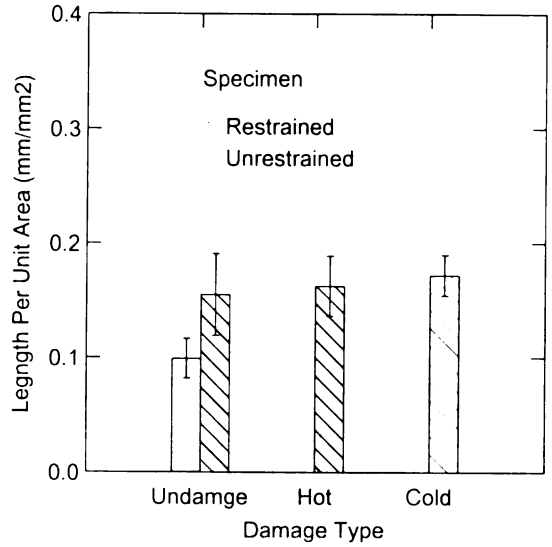

(a) Length Per Unit Area

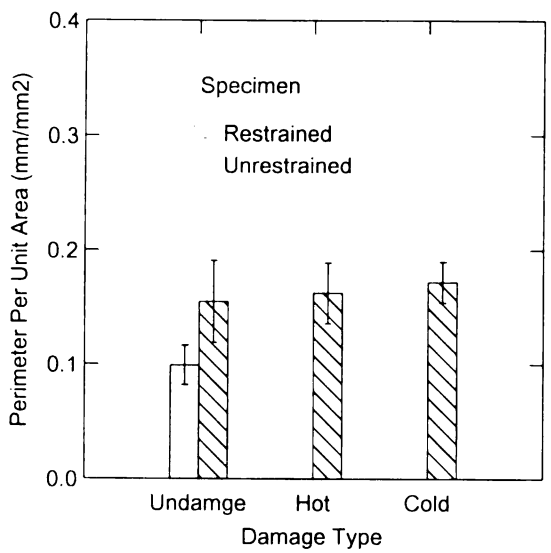

(b) Perimeter Per Unit Area

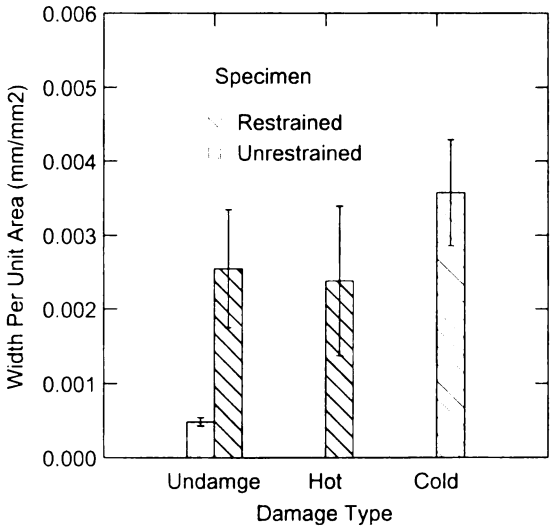

(c) Width

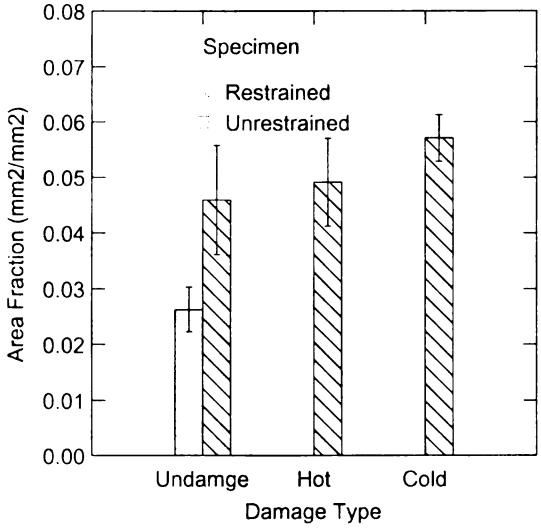

(d) Area Fraction

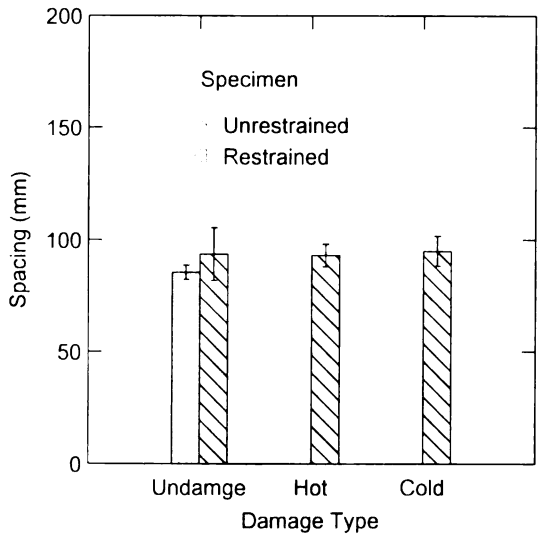

(e) Spacing

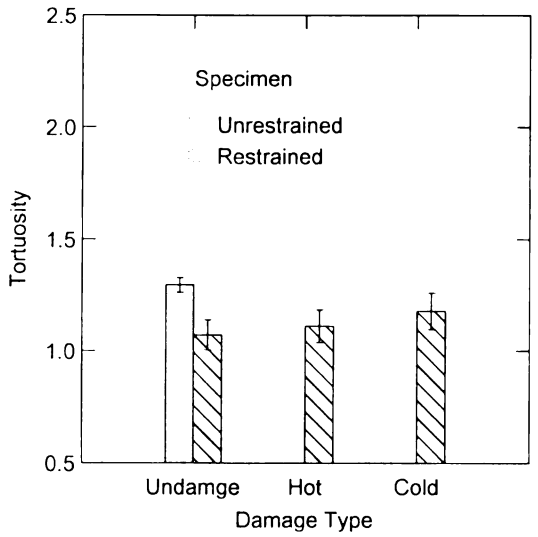

(f) Tortuosity

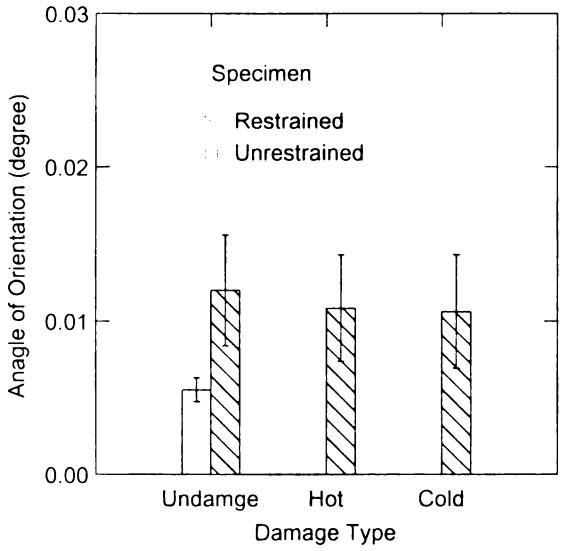

(g) Angle of Orientation

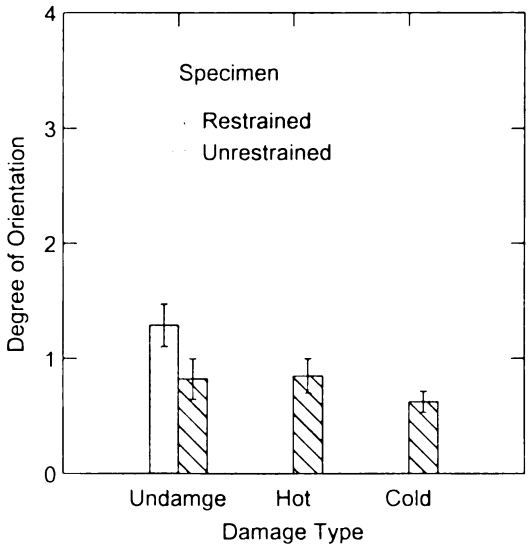

(h) Degree of Orientation

Figure 8.5 Planar (2-D) Measurements for Unrestrained (Unreinforced) and Restrained (Unreinforced) Normal-Strength Specimens in Horizontal Section (X-Y) (Average of Three Magnification Levels)

Table 8.7 Results of Statistical Analysis For Unrestrained (Unreinforced) and Restrained (Unreinforced) Normal-Strength Specimens (Planar Measurements) (Percent Changes Vs. Undamaged Condition)

Measurements	Section	Environmental Effects on Restrained Specimens		Comparison Between Unrestrained and Restrained Specimens
		Hot Weather	Cold Weather	No Damage
Length per Unit Area	XY	I +2.12	I +2.42	S +54.2
	YZ	I +4.85	I +3.50	S +48.3
Perimeter per Unit Area	XY	I +0.85	I +1.75	S +48.3
	YZ	I +2.34	I -3.34	S +38.8
Width per Unit Area	XY	I -7.40	S +49.4	S +343
	YZ	I +12.6	S +41.6	S +301
Area Fraction	XY	I +4.10	S +22.8	S +87.8
	YZ	S -51.6	S +44.5	S +475
Spacing	XY	I -5.26	I -1.10	I +8.21
	YZ	I -4.40	I -6.56	S -49.6
Tortuosity	XY	I +11.4	I +13.1	I -11.5
	YZ	I -16.6	I -24.8	I +9.55
Angle of Orientation	XY	I -7.33	I -13.5	S +128
	YZ	I +15.4	S -42.6	I -33.1
Degree of Orientation	XY	I +2.50	I -21.1	I -26.1
	YZ	S +25.4	I -5.47	S -88.8

S = Significant effect
I = Insignificant effect

Before application of any damaging effect, there were significant differences in crack length per unit area, perimeter per unit area, width per unit area and area fraction in both sections (XY and YZ), and in spacing, angle of orientation and degree of orientation in vertical section (YZ) between restrained and unrestrained specimens (restraint of shrinkage movements increased the extent of microcracking, and reduced the spacing of microcracks). Exposure to hot environment did not cover any significant effect on microcrack characteristics of the restrained specimens except for area fraction and degree of orientation in vertical section (YZ). Exposure to cold environment showed significant effects on width per unit area and area fraction in both (XY and YZ) sections and on angle of orientation in vertical (YZ) section.

8.4.2.2 *Spatial (3-D) Measurements*

Figure 8.6 presents the results (mean values and standard errors) for all measurements in space (3-D) for unrestrained and restrained normal-strength concrete specimens. One-way analysis of variance "ANOVA" (t-test) at 10% level of significance was used to detect any significant effects of different damage phenomena and restraint condition on microcrack characteristics. The results of statistical analysis and the comparison between unrestrained and restrained normal-strength concrete specimens are presented in Table 8.8. Before application of any damaging effect, significant differences exist between unrestrained and restrained specimens in terms of crack specific surface area, width, volume fraction, spacing and degree of orientation. Restraint of shrinkage movements increased the extent of microcracking and reduced microcrack spacing.

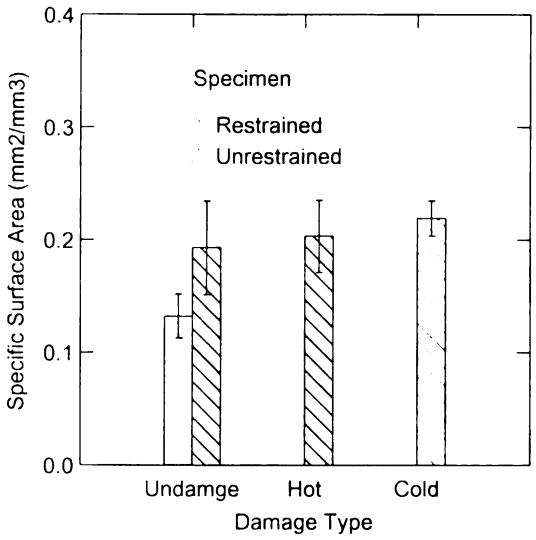

(a) Specific Surface Area

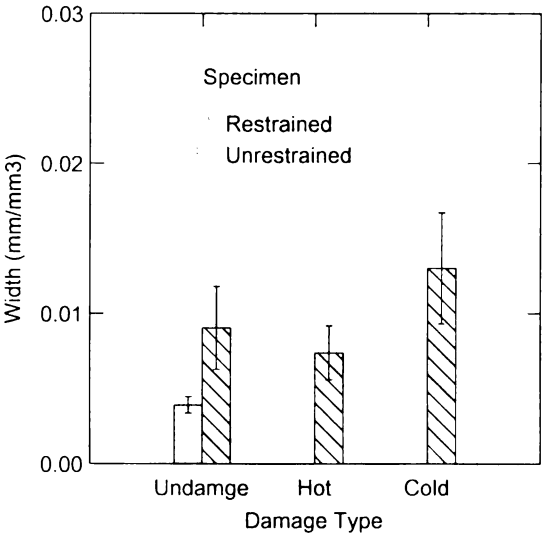

(b) Width

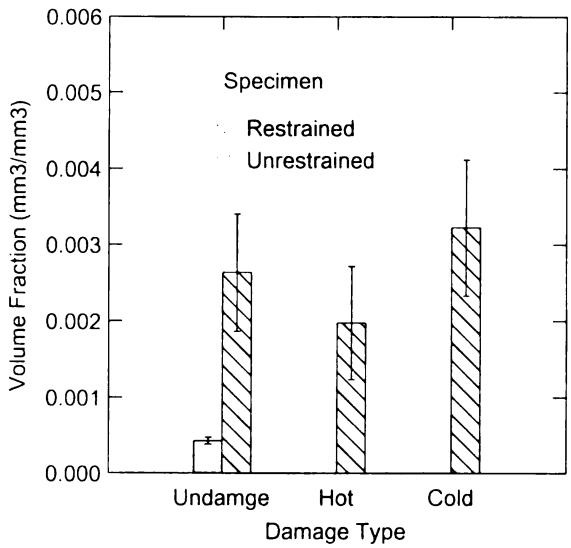

(c) Volume Fraction

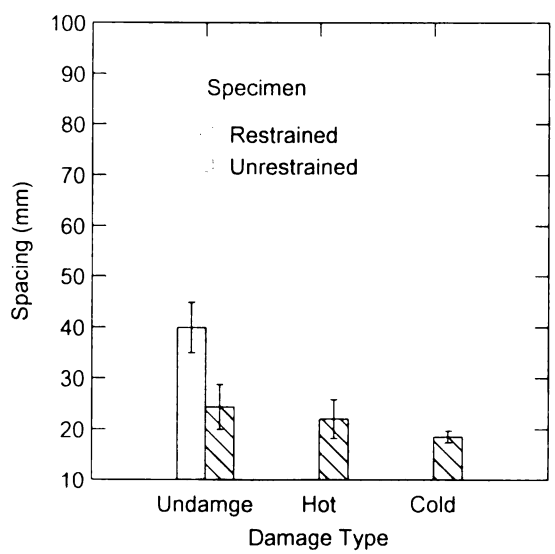

(d) Spacing

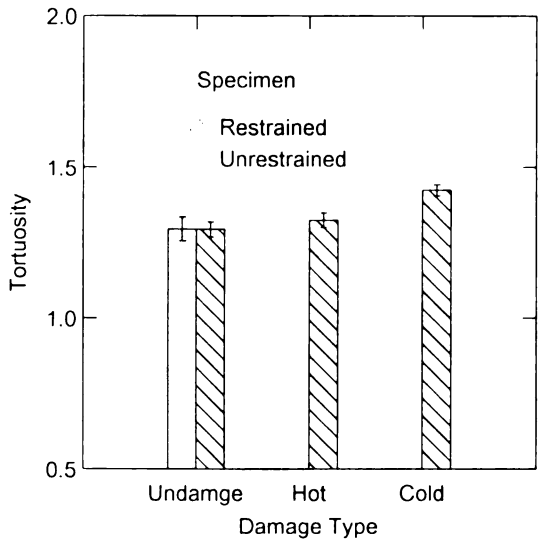

(e) Tortuosity

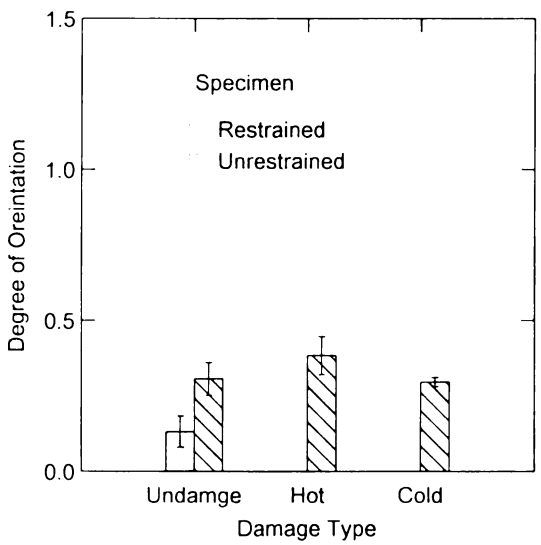

(f) Degree of Orientation

Figure 8.6 Spatial (3-D) Measurements for Unrestrained and Restrained (Unreinforced) Normal-Strength Specimens (Average of Three Magnification Values)

Table 8.8 Results of Statistical Analysis for Unrestrained (Unreinforced) and Restrained (Unreinforced) Normal-Strength Specimens (Spatial Measurements) (Percent Changes Vs. Undamaged Condition)

Measurements	Environmental Effects on Restrained Specimens		Comparison Between Unrestrained and Restrained Specimens
	Hot Weather	Cold Weather	No Damage
Specific Surface Area	I +6.79	I +14.7	S +58.3
Width per Unit Volume	I -15.0	S +38.8	S +77.2
Volume Fraction	S -38.7	S +30.1	S +324
Spacing	I -12.5	I -21.5	S -35.2
Tortuosity	I +1.53	I +7.69	I -0.92
Degree of Orientation	I +29.1	I -13.3	S +65.5

S = Significant effect
I = Insignificant effect

Exposure to hot environment did not generally cause any significant change in microcrack characteristics of restrained normal-strength specimens. Exposure to cold environment increased the width and reduced the spacing of microcracks.

8.4.3 Analogy Between Normal-Strength and Relatively High-Strength Concrete Specimens

8.4.3.1 *Planar (2-D) Measurements*

Figure 8.7 presents the results (means and standard errors) of all planar (2-D) measurements on horizontal (XY) sections perpendicular to the direction of loading for (unreinforced-unrestrained) normal-strength and relatively high-strength concrete specimens. The trends in microcrack growth under different damage phenomena are depicted in Figure 8.7. Results are presented here for horizontal sections, which exhibited more severe cracking than vertical sections (parallel to the direction of loading). The data presented herein are the average values obtained in fluorescent and ESEM at three different magnifications. There were minor differences between results of the two microscopy techniques, which can be largely attributed to the associated differences in sample preparation procedures and the precision of each microscope. Generally, higher magnification levels seem to provide far detection of more microcracks. One-way analysis of variance "ANOVA" (t-test) at 10% level of significance was used to detect any significant effects of different damage phenomena and concrete strength on microcrack characteristics. Results of the statistical analysis and the comparison between normal-strength and relatively high-strength concrete specimens are summarized in Table 8.9. No statistically significant difference was found between normal-strength and relatively high-strength concrete in undamaged condition for all measurements except the degree of orientation that was higher for normal-strength concrete.

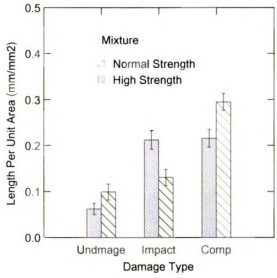

(a) Length Per Unit Area

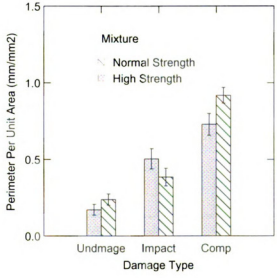

(b) Perimeter Per Unit Area

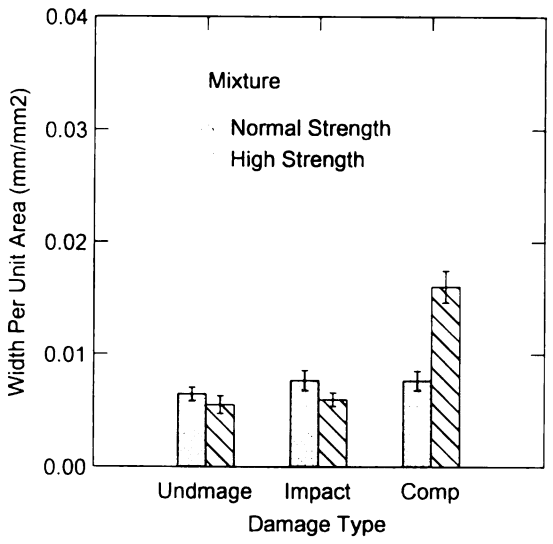

(c) Width Per Unit Area

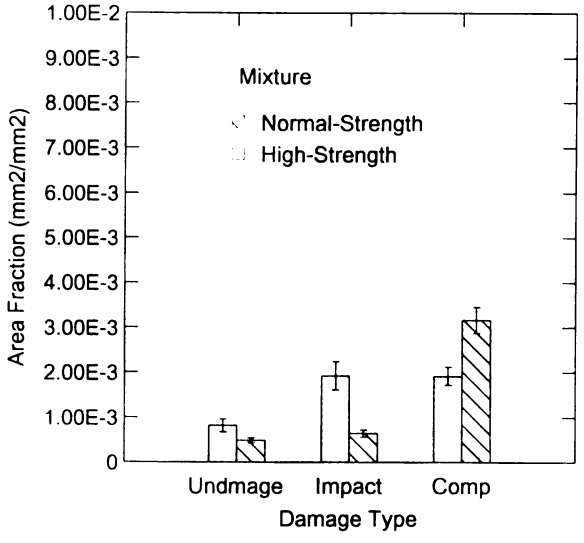

(d) Area Fraction

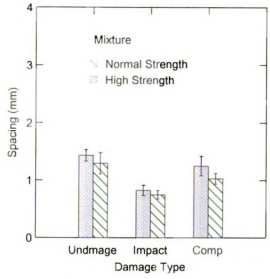

(e) Spacing

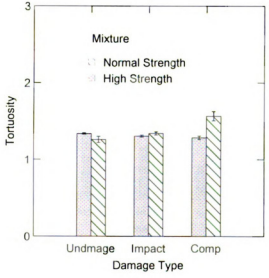

(f) Tortuosity

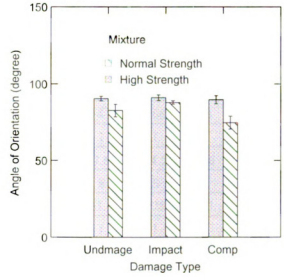

(g) Angle of Orientation

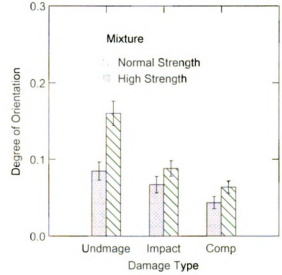

(h) Degree of Orientation

Figure 8.7 Planar (2-D) Measurements for Normal-Strength (Unreinforced-Unrestrained) and Relatively High-Strength Concrete Specimens in Horizontal Section (X-Y) (Average of Three Magnification Levels)

Table 8.9 Results of Normal-Strength and Relatively High-Strength Specimens

Measurements	Section	Comp.	Impact	Comp.	Impact	Comparison between Normal-Strength and Relatively High-Strength Concrete		
		Normal-Strength		High-Strength		No Damage	Comp.	Impact
Length per Unit Area	XY	S	I	S	S	I	S	S
		81.1	14.2	166	151	15.5	48.7	-37.7
	YZ	I	I	I	I	I	I	I
		11.5	7.6	14.5	34.6	22.4	15.4	-5.87
Perimeter per Unit Area	XY	S	S	S	S	I	I	I
		92.4	63.4	128	143	28.6	-23.3	-18.4
	YZ	I	I	I	S	I	I	I
		22.2	21.7	26.5	66.7	21.6	1.21	-12.4
Width per Unit Area	XY	S	I	I	I	I	S	I
		191.2	5.32	18	18.5	13.6	97.4	-6.25
	YZ	I	S	S	S	I	I	I
		41.5	35.4	47.7	98.7	-8.54	23.2	5.41
Area Fraction	XY	S	I	S	S	I	S	S
		214	10.5	95.6	100	19.9	52.1	-68.9
	YZ	I	S	S	S	I	I	I
		31.8	43.2	58.6	51.8	32.5	21.3	-11.6
Spacing	XY	I	S	I	I	I	I	I
		-22.2	-64.9	-11.3	-28.5	-16.5	-19.8	-2.5
	YZ	S	I	S	S	I	I	S
		-15.5	-8.4	-44.6	-64.5	1.5	-17.3	-1.5
Tortuosity	XY	S	I	I	I	I	S	I
		25.1	6.34	-17.2	-4	6.54	25	1.6
	YZ	I	I	I	I	I	I	I
		6.4	8.45	-5.6	-12.8	2.57	18.7	6.6
Angle of Orientation	XY	I	I	I	I	I	I	I
		-13.4	6.25	-2.2	-1.2	-26.8	-12.3	-3.75
	YZ	S	I	I	I	I	I	I
		61.7	11.7	-14.6	2.6	16.7	14.6	-7.84
Degree of Orientation	XY	S	S	S	I	S	S	I
		-238	-66.5	-44.2	-21.1	61.9	-62.5	21.8
	YZ	I	S	I	I	I	S	S
		-15	81.8	-9.41	6.54	-14	45.7	41.8

Compression damage significantly affected length per unit area, perimeter per unit area, width per unit area, area fraction, and degree of orientation for both normal-strength and relatively high-strength concrete, crack tortuosity in normal-strength concrete, and crack spacing in relatively high-strength concrete. Horizontal (XY) (perpendicular to loading direction) showed more severe crack growth after compression damage. The crack width per unit area was higher in normal-strength concrete than in relatively high-strength concrete, and the degree of orientation was higher in normal strength-concrete when compared with relatively-high strength concrete; other microcrack measurements were statistically comparable in normal-strength vs. relatively high-strength concrete after compression damage. Impact loading had statistically significant effect on perimeter per unit area, width per unit area and area fraction for both normal-strength and relatively high-strength concrete and length per unit area of relatively high-strength concrete. Statistically significant differences were found between normal-strength and relatively high-strength concrete, in terms of length per unit area, area fraction (XY) and spacing (YZ) after impact damage.

8.4.3.2 Spatial *(3-D) Measurements*

Figure 8.8 presents the results (means and standard errors) of all measurements in space (3-D) for (unreinforced-unrestrained) normal-strength and relatively high-strength concrete specimens. One-way analysis of variance "ANOVA" (t-test), at 10% level of significance, was used to detect any statistically significant effects of different damage phenomena and concrete strength on microcrack growth under any damaging effects. The

results of statistical analysis and the comparison between normal-strength and relatively high-strength concrete specimens are presented in Table 8.10.

In undamaged condition, there was no statistically significant difference between normal-strength and relatively high-strength concrete (except that the degree of orientation was higher in normal-strength concrete). Application of compression damage effect had significant effects on crack specific surface area, width, volume fraction and spacing for both normal-strength and relatively high-strength concrete (spacing was reduced, and all other measurements were increased). Compression load also had a significant effect on microcrack tortuosity in case of normal-strength concrete (but not high-strength concrete). After compression damage, there were significant differences between normal-strength and relatively high-strength concrete in terms of the specific surface area, width, volume fraction and tortuosity of microcracks. Impact damage treatment had significant effects on crack width, volume fraction and degree of orientation for normal-strength concrete (all measurements were increased), and also on the crack specific surface area of relatively high-strength concrete. It also had significant effects on crack width of relatively high-strength concrete. After application of impact damage, there were statistically significant differences between normal-strength and relatively high-strength concretes in terms of the microcrack specific surface area and volume fraction.

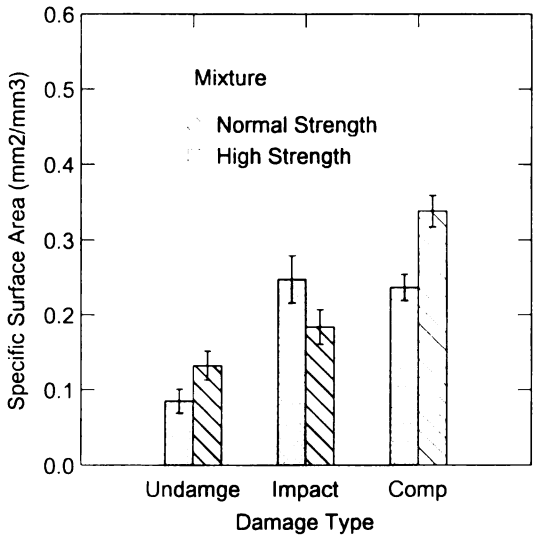

(a) Specific Surface Area

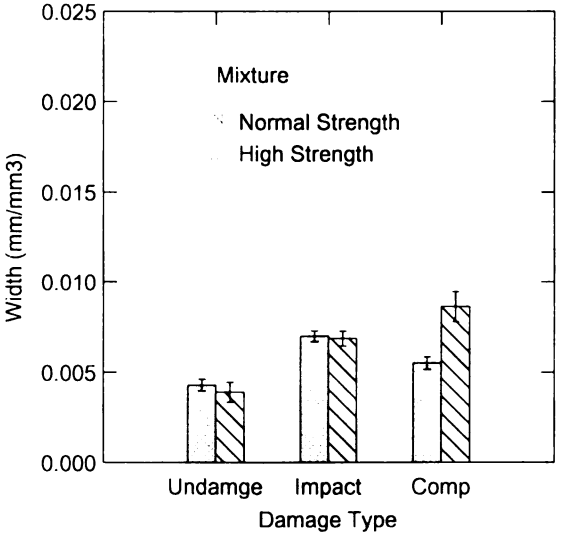

(b) Width

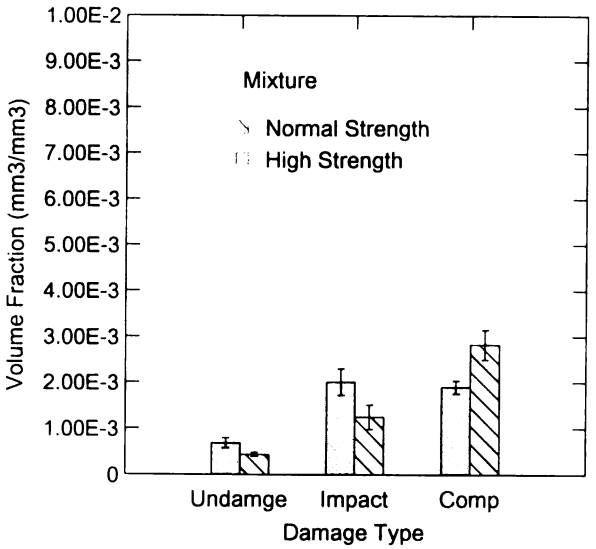

(c) Volume Fraction

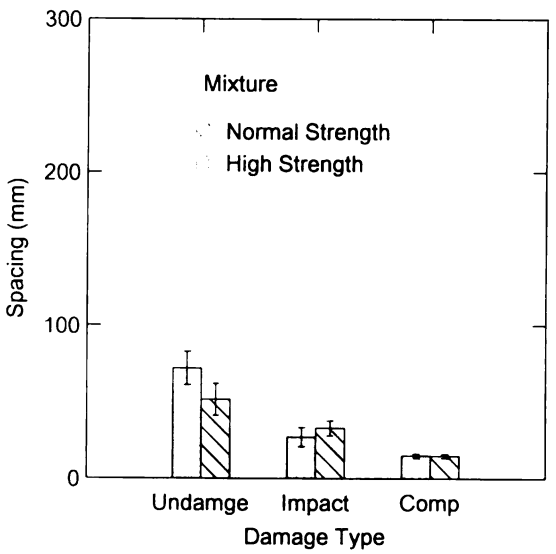

(d) Spacing

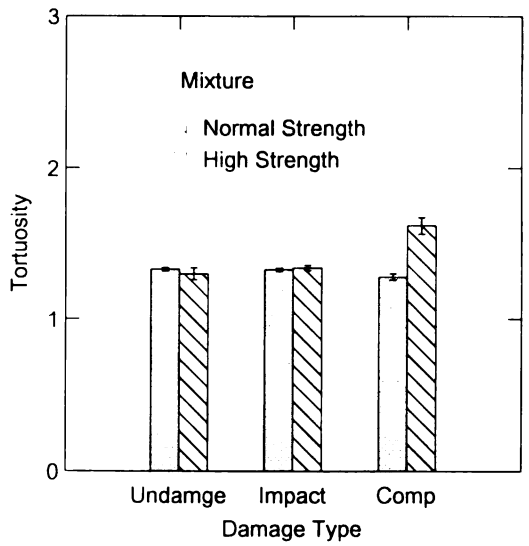

(e) Tortuosity

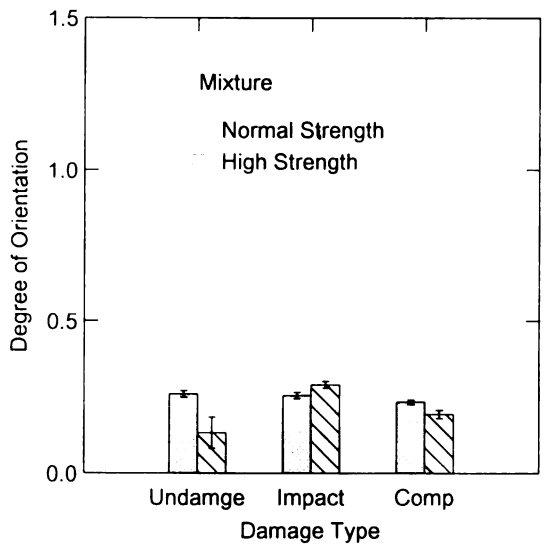

(f) Degree of Orientation

Figure 8.8 Spatial (3-D) Measurements for Normal-Strength (Unreinforced-Unrestrained) and Relatively High-Strength Concrete Specimens (Average of Three Magnification Levels)

Table 8.10 Results of Statistical Analysis for Normal-Strength (Unreinforced/ Unrestrained) and Relatively-High Strength Concrete (Spatial Measurements) (Percent Changes Vs. Undamaged Condition)

Measurements	Comp.	Impact	Comp.	Impact	Comparison between Normal-Strength and Relatively High-Strength		
	Normal-Strength		High-Strength		No Damage	Comp.	Impact
Specific Surface Area	S	I	S	S	I	S	S
	80.2	7.65	125	128	16.6	42.5	-28.4
Width per Unit Volume	S	S	S	S	I	S	I
	98.5	68.5	27.6	41.9	7.85	41.6	-2.3
Volume Fraction	S	S	S	S	I	S	S
	214	96.4	122	131	16	47.2	-31.6
Spacing	S	I	S	S	I	I	I
	-48.3	-15.6	-65.1	-55.2	-13.3	8.3	-0.5
Tortuosity	S	I	I	I	I	S	I
	84.6	5.41	-2.3	0.77	5.78	36.4	1.27
Degree of Orientation	I	S	I	I	S	I	I
	-11.5	77.8	-8.2	-4	58.7	-3.1	3.2

S = Significant effect
I = Insignificant effect

8.5 DISCUSSION

Quantitative analysis and comparison between normal-strength and relatively high-strength concrete showed that microcrack systems have comparable characteristics in undamaged specimens of different strength levels (after similar curing and air drying conditions). Compression load (up to peak stress level followed by immediate unloading) noticeably increased the extent of microcracking in both normal-strength and high-strength concretes. Compression load led to microcrack propagation (i.e., increased

length and surface area) and widening and coalescence (i.e. increased width). The normal-strength concrete considered in this investigation (which had higher) air content exhibited more extensive microcrack growth (vs. relatively high-strength concrete) under compression damage; this could be attributed to the concentrations of stresses around air voids. The relatively high-strength concrete experienced more microcrack growth under impact damage, which could be attributed to its more brittle nature when compared with normal-strength concrete.

Restraint of shrinkage movements led to pronounced microcracking of (otherwise) undamaged concrete, which can be attributed to development of restraint shrinkage tensile stresses. Short-term exposure to cold climate caused more microcrack propagation than short term exposure to hot climates. This could result from development of tensile stresses in cement paste due to restraint of its thermal shrinkage movements by aggregates in cold climates; noting the differences in coefficients of thermal expansion of cement paste and aggregates.

Under damaging effects involving application of (static or dynamic) compression loads, horizontal sections perpendicular to the loading direction exhibited more extensive microcracking than vertical directions. This can be attributed to development of tensile stresses (due to Poisson's effects in planes perpendicular to compressive loading direction).

8.6 CONCLUSIONS

The effects of different load and environmental damaging effects on normal-strength and relatively high-strength concrete microcrack system were assessed based on quantitative evaluation of the microcrack system in plane and in space. Statistical analyses of the quantified microcrack system in damaged and undamaged normal-strength concrete specimens (with and without steel or composite reinforced- restrained and unrestrained) yielded the following conclusions:

1- Compression loading and fire endurance effects have the most significant effect on normal-strength concrete microcracks measurements. Compression increased crack length per unit area, width, volume fraction, tortuosity, and crack specific surface area, and decreased spacing in plane and spacing in space, while fire increased crack length per unit area, perimeter per unit area, area fraction, and specific surface area, width, volume fraction and decreased spacing in plane and spacing in space.

2- Fatigue loading has the least significant effect on normal-strength concrete microcrack measurements. Fatigue damage significantly increased crack specific surface area in space.

3- Drop-weight impact loading significantly increased the microcrack width; crack width may thus be considered an index for assessing the effects of impact loading on concrete.

4- Corrosive environments (salt water) have more profound effect on concrete microcrack system more than immersion in hot water. Salt water significantly increased crack specific surface area, width, and volume fraction but reduced spacing.

5- Combined damaging effects (compression + freeze-thaw) did not provide the expected severe changes in concrete microcrack characteristics; this may give an indication that compression and freeze-thaw damage effects imposed as biaxial loading on concrete specimens which reduced the severity of individual damaging effects. More studies are needed to investigate the behavior of concrete microcrack system under combined damaging phenomena.

6- Composite rebars reinforced concrete specimens did not show severe changes in microcrack characteristics compared to steel reinforced concrete specimens when exposed to salt water. Crack width did not increase in composite reinforced concrete specimens compared to steel reinforced concrete specimens.

7- Restraint of shrinkage movements significantly increased the extent of microcracking in an otherwise undamaged normal-strength concrete.

8- Concrete experiences more microcrack growth after a short period of exposure to cold climate than hot climate; microcrack widths and area fractions were especially higher after exposure to cold weather versus hot weather. This observation could be a function of the relative thermal movements of the cement paste versus aggregates.

9- Undamaged concrete specimens of normal-strength and relatively high-strength concrete exhibited similar microcrack characteristics after similar curing and air drying conditions (prior to application of any damage effects).

10- Compression load led to substantial microcrack growth in relatively high-strength concrete. Compression damage increased microcrack length, width and area fraction in plane, and specific surface area, width and volume fraction in space.

11- Planar and spatial microcrack characteristics are significantly different in normal-strength vs. relatively high-strength concrete under application of compression damage effect.

12- Relatively high-strength concrete experienced more extensive microcrack growth under impact lading than normal-strength concrete; the microcrack volume fraction and specific surface area were significantly higher for the high-strength mixture.

13- Tortuosity, angle of orientation and degree of orientation are the lowest measurements that have been affected by damaging effects while length per unit area (specific surface area) and area fraction (volume fraction) are the highest measurements that have been affected by damaging effects. This provides an indication that these measurements could be excluded from efforts to relate concrete performance to microcrack attributes.

CHAPTER 9

FIELD APPLICATIONS

9.1 RIGID PAVEMENT APPLICATION

9.1.1 Preface

Rigid pavements are prone to distress and cracking under traffic loads and weathering effects. These damage mechanisms can significantly undermine the serviceability and durability of pavement systems, with adverse effects on their life-cycle economy.[120-122] Freeze-thaw attack, alkali-silica reactivity, fatigue and shrinkage are among factors contributing to microcrack development in rigid pavements.[123-126] Quantitative analysis of the microcrack system would provide substantial insight into health condition of existing pavement systems, and may emerge as an effective tool in management of the transportation infrastructure. Such quantitative microstructural data can complement visual inspection which can not yield explicit details of concrete condition.[117,127] While visual inspection rely heavily on the investigator's experience and judgment, quantitative microstructural data can through statistical analysis yield reliable and consistent outcomes. Throughout the first part of this chapter, the quantitative proposed approach was applied on rigid pavement slab for the purpose of microstructural analysis and to verify the applicability of the proposed approach.

9.1.2 Pavement Description

The rigid pavement that was subject of this investigation is part of I 496 freeway near Shepard Street in East Lansing, Michigan. The road has four lanes, two in each direction

and a ditch in the middle. The width of each lane is 3.6 m (12 ft). The investigation was focused on one lane (the outer westbound lane) of the highway; this selection based on the available free areas (not occupied by construction machines) taking into consideration not to interrupt work progress in the situ. The pavement segment integrated is 21.3 m (70 ft) in length and 3.6 m (12 ft) in width. The pavement thickness is 20 cm (8 inches), and two contraction joints were included in this investigation. The pavement shows crack formation largely attributed to restraint of concrete shrinkage. This phenomenon constitutes a very common damage to the pavements and other slabs-on-grade; the restrained shrinkage cracks accelerate deterioration of concrete under environmental and traffic load effects. Although the pavement was in moderately damaged condition, visual inspection identified two major cracks across the whole width and through the whole depth of the slab, with average width of about 12.5 mm (0.5 inch). Edges of the expansion joints were also deteriorated under weathering and traffic effects. Figure 9.1a shows one of the restrained shrinkage cracks in and Figure 9.1b shows a partial-depth patch placed at highly damaged areas of the crack. Figure 9.1c presents deterioration at the edge of an expansion joint. Such joint fraying could be attributed to many reasons, such as snow plow damage, load transfer across the joints (and cracks) under traffic loading effects, local intrusion of incompressible or damage during joint sawing/forming at the time of construction.

(a) First Major Crack

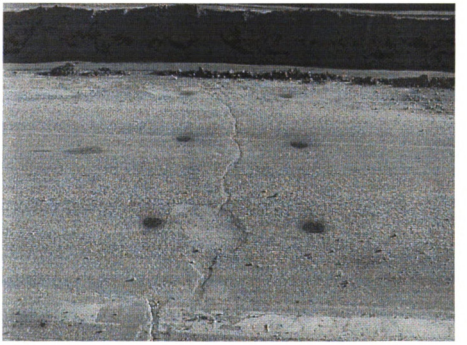

(b) Second Major Crack

(c) Deterioration at Contraction Joint

Figure 9.1 Different Views of The Concrete Damage Conditions

9.1.3 Pavement Sub-Regioning and Coring

The pavement slab was divided into seven (preliminary number) horizontal and two vertical (top and bottom) sub-regions based on the visual evaluation of damage conditions and targeting power of test $(1-\beta) = 0.8$ where β is the risk of making type II error[113]. Horizontal sub-regions III and V which contains the two major cracks are considered to have suffered severe level of damage. Horizontal sub-regions II, IV and VI were considered to have suffered moderate levels of damage due to their vicinity to major restrained shrinkage cracks and their location far from the two visual cracks. Horizontal sub-regions I, and VII, on the other hand, were located far from the two major cracks and thus considered to have suffered relatively low levels of damage as shown in Figure 9.2. The horizontal sub-regions were divided vertically into two vertical sub-regions.

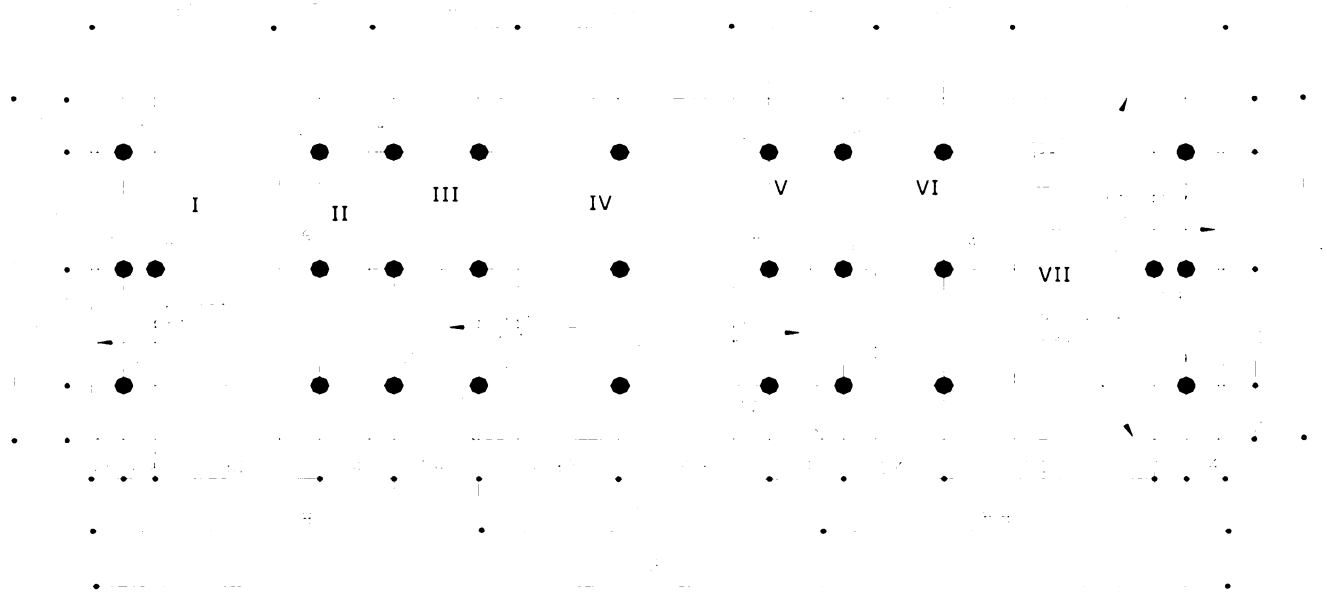

Dimensions in Meters (Distorted Scale)

Figure 9.2 Sub-Regioning and Coring Configuration of The Concrete Pavement

Twenty-nine cores were extracted from the pavement slab (targeting a precision ± 5%). Figure 9.2 also depicts the location of cores extracted from different sub-regions. Four cores were extracted from horizontal sub-regions I and VII (with low level of damage), three from horizontal sub-regions II, IV, and VI (with moderate level of damage), and six cores from horizontal sub-regions III and V (with severe level of damage). Core diameters were selected to be either 15 cm (6 inches) (cores 3, 7, 10, 13, 16, 19, 22, 25 and 29) or 10 cm (4 inches) (the remaining cores) to suit different types of tests (mechanical characterizations and microstructural investigations); all cores were extracted in full depth. The extracted cores were stored at 50% relative humidity and 20°C (68°F) for 3 months. Concrete cores did not exhibit any obvious signs of deterioration or steel corrosion.

9.1.4 Experimental Methodology

Concrete cores were subjected to the following engineering tests: compression test (ASTM C39), splitting tension test (ASTM C96) and permeability (ASTM C1202). Compression and splitting tension tests were performed on the whole length of the cores, neglecting the vertical sub-regioning scheme. Permeability tests, on the other hand, were performed on 5 cm (2 inch) height specimens cut (using wet diamond concrete saw) from top and bottom of cores representing the two vertical sub-regions. Grinding process of some specimens was necessary to obtain flat surfaces for the purpose of capping and performance of compression tests. Splitting tension test was applied on the cores as extracted without special preparation. During permeability test sodium chloride (NaCl) and Sodium Hydroxide (NaOH) solutions were poured at the same time in the specimen

mold to avoid instantaneous flow before connecting the molds to the instrument due to existence of cracks in cores extracted from sub-regions III and V. Table 9.1 summarizes the test plan for concrete cores. Compression and splitting tension tests were selected to reflect concrete performance under traffic loads and permeability test was selected to concrete resistance to weathering conditions.

Table 9.1 Tests Performed on Pavement Sub-Regions

Sub-Region #	Tests			
	Compression	Splitting Tension	Permeability	Microstructural Investigation
Sub-Regions # I and VII	Core # 29	Core # 3	Cores # 2 and 27	Cores # 1, 4, 26 and 28
Sub-Regions # II, IV, and VI	Core # 7	Cores # 16 and 25	Cores # 14 and 24	Cores # 5, 6, 15 and 23
Sub-Regions # III and V	Core # 13	Cores # 10, 19 and 22	Cores # 9 and 17	Cores # 8, 11, 12, 18, 20 and 21

9.1.5 Microstructural Investigation

Concrete cores were cut using wet diamond concrete saw in two halves (representing the two vertical sub-regions), and each half was cut into two perpendicular sections [horizontal (XY) and vertical (YZ)] as shown in Figure 6.11. A total of 56 sections were

prepared from 14 cores. Sections were cut, parallel and perpendicular to the direction of traffic loading. The two perpendicular sections allow acquisition of planar (2-D) measurements which through stereological interpretation, yield information on the spatial (3-D) microcrack system in concrete. The sections used in the microstructural investigation were 75 mm (3 in) square with 50 mm (2 in) thickness. Fluorescent microscopy was used for acquisition of microscopic images. The sections were prepared for fluorescent microscopy using ink/epoxy impregnation following the procedures described in section 4.2.4.2. Planar (2-D) and spatial (3-D) characteristics of microcracks were determined using the equations presented earlier in parts 5.3.1.1 and 6.1.4.1 respectively. The correlations between engineering properties of concrete and the quantified measurements of microcracks were considered. Statistical analyses were used to detect any significance differences amongst different sub-regions. Cores subjected to engineering microstructural analysis test are introduced in Table 9.1.

9.1.6 Mechanical Test Results and Discussion

Compression, splitting tension and permeability test results for concrete cores obtained from different sub-regions are presented in Table 9.2. Correction factors were applied to compression strength test data when length-to-diameter ratio deviated from 2.0 (ASTM C39). Horizontal sub-regions III and V contain the two major cracks and were thus assumed to have suffered severe level of damage. The permeability test data, which are particularly sensitive to the extent of concrete microcracking, confirmed the more extensive level of damage in sub-regions III and V. the compressive and splitting strength test data were in conclusive as far as the differences in damage conditions of different

sub-regions are concerned. Specimens obtained from top sub-regions showed higher permeability levels than those from bottom sub-regions. This could be attributed to the more severe impact of load and environmental effects on top (exposed) sub-regions. Statistical analysis of data did not confirm, however at 10% level of significance, the statistical significance of permeability differences between the top and bottom sub-regions.

Table 9.2 Mechanical and Transport Properties of Concrete Cores

Sub-Region #		Tests			
		Compression (MPa)	Splitting Tension (MPa)	Permeability (Coulombs)	
				Top Sub-region	Bottom Sub-region
Sub-regions # I and VII	Mean	37.8	3.38	441	243
	Std. Dev.	NA	NA	44.3	18.5
Sub-regions # II, IV, and VI	Mean	24.6	4.08	522	441
	Std. Dev.	NA	0.19	39.1	14.14
Sub-regions # III and V	Mean	43.5	4.14	2241	1187
	Std. Dev.	NA	0.38	87.1	24.6

NA = Not applicable

9.1.7 Microstructural Data and Discussion

The Qmac™ software system was used to obtain planar (2-D) of microcrack system; quantitative data were then derived through stereological analysis of (2-D) data generated for two perpendicular sections.

9.1.7.1 *Planar (2-D) Measurements*

Tables 9.3 and 9.4 show the planar measurements of microcracks; length per unit area, perimeter per unit area, width per unit area, area fraction, angle of orientation, tortuosity, spacing and degree of orientation for top and bottom sub-regions respectively. One-way analysis of variance "ANOVA" (T-test) at 10% level of significance showed that there are no statistically significant differences between top and bottom sub-regions in terms of microcrack characteristics in horizontal (XY) sections. For vertical (YZ) sections, however, top sub-regions exhibited higher levels of microcrack length and perimeter per unit area, width and area fraction. This corroborates permeability test data, and can be attributed to direction exposure of top sub-regions to load and weathering effects. It also found that there is no significance difference of microcrack length per unit area between sub-region III (severe level of damage) and sub-regions I and II (low and moderate levels of damage, respectively) for both top and bottom vertical sub-regions in spite of core # 8 in sub-region III showed much higher values than cores in sub-region I or II. Statistical analyses at 10% level of significance indicated significant differences in microcrack length per unit area between sub-region V (severe level of damage) versus sub-regions VI and VII (moderate and low level of damage, respectively); there was no statistically significant difference between sub-regions IV and V (both of which were rated of moderate level of damage). These microcrack measurements corroborated the original sub-regions scheme and also the relative permeability values. Measurements of microcrack orientation on horizontal and vertical sections indicate that microcracks propagated dominantly perpendicular to the direction of traffic flow.

Table 9.3 Planar (2-D) Measurements for Top Sub-Region

Sub-region #	Core #	Section	Length per Unit Area (mm/mm2)	Perimeter per Unit Area (mm/mm2)	Area Fraction (mm2/mm2)	Width per Unit Area (mm/mm2)	Angle of Orientation (degree)
		XY	0.0102	0.0293	0.000108	0.01	79.5
	1	YZ	0.0514	0.145	0.001399	0.0144	81.8
		XY	0.0461	0.1406	0.000371	0.0081	85.2
I	4	YZ	0.0362	0.1188	0.000288	0.0079	95.6
		XY	0.031	0.0877	0.00034	0.0096	109.1
	5	YZ	0.0141	0.0394	0.00019	0.0092	112.8
		XY	0.0371	0.1022	0.000654	0.0092	110.1
II	6	YZ	0.0528	0.1405	0.000976	0.0113	88.6
		XY	0.0861	0.2375	0.000853	0.008	90.7
	8	YZ	0.0887	0.2604	0.001128	0.0094	87.3
		XY	0.0363	0.0986	0.000588	0.0104	85.3
	11	YZ	0.0297	0.0795	0.000272	0.0081	79.6
		XY	0.0385	0.1122	0.000505	0.0096	101.6
III	12	YZ	0.0622	0.1869	0.000761	0.0098	79.4
		XY	0.044	0.1196	0.00076	0.0131	61.2
IV	15	YZ	0.0376	0.1067	0.00076	0.0128	80.3
		XY	0.0554	0.164	0.000588	0.0083	89
	18	YZ	0.0752	0.2115	0.000736	0.0076	98.6
		XY	0.0548	0.1637	0.000737	0.0086	102
	20	YZ	0.0807	0.2259	0.00069	0.0071	74.5
		XY	0.0455	0.1333	0.000416	0.0075	97.7
V	21	YZ	0.0293	0.0828	0.000278	0.0091	94.3
		XY	0.0225	0.0613	0.000189	0.0077	75.6
VI	23	YZ	0.0562	0.1582	0.000761	0.0092	91.6
		XY	0.0493	0.1435	0.000637	0.0097	88.7
	26	YZ	0.0686	0.1924	0.000593	0.0074	99.9
		XY	0.0295	0.0822	0.00028	0.0082	112.6
VII	28	YZ	0.0208	0.0624	0.000369	0.0118	97

Table 9.3 Planar (2-D) Measurements for Top Sub-Region (Cont.)

Sub-region #	Core #	Section	Tortuosity	Spacing (mm)	Degree of Orientation	Number of microcracks
I	1	XY	1.38	2.90	0.058	10
		YZ	1.37	1.58	0.052	34
	4	XY	1.36	1.47	0.080	40
		YZ	1.36	1.57	0.061	35
II	5	XY	1.36	1.77	0.137	27
		YZ	1.34	2.55	0.063	13
	6	XY	1.30	1.53	0.144	36
		YZ	1.28	1.51	0.137	37
III	8	XY	1.32	1.03	0.079	79
		YZ	1.36	1.07	0.024	73
	11	XY	1.33	1.58	0.130	34
		YZ	1.31	1.65	0.110	31
	12	XY	1.38	1.45	0.045	40
		YZ	1.43	1.18	0.007	61
IV	15	XY	1.31	1.62	0.018	32
		YZ	1.36	1.65	0.028	31
V	18	XY	1.37	1.31	0.068	49
		YZ	1.34	1.02	0.090	81
	20	XY	1.36	1.33	0.103	48
		YZ	1.33	1.00	0.039	84
	21	XY	1.37	1.26	0.093	53
		YZ	1.39	1.68	0.048	30
VI	23	XY	1.32	1.71	0.013	29
		YZ	1.36	1.24	0.091	55
VII	26	XY	1.37	1.38	0.155	44
		YZ	1.35	1.10	0.097	70
	28	XY	1.34	1.55	0.126	35
		YZ	1.37	2.16	0.027	18

Table 9.4 Planar (2-D) Measurements for Bottom Sub-Region

Sub-region #	Core #	Section	Length per Unit Area (mm/mm^2)	Perimeter per Unit Area (mm/mm^2)	Area Fraction ($mm^2/mm2$)	Width per Unit Area (mm/mm^2)	Angle of Orientation (degree)
		XY	0.0297	0.0783	0.000323	0.0091	85.2
	1	YZ	0.0393	0.1125	0.000466	0.0094	80.9
		XY	0.0222	0.0702	0.000186	0.0083	80.1
I	4	YZ	0.0194	0.069	0.001451	0.0062	95.5
		XY	0.0216	0.0575	0.000213	0.0082	92.6
	5	YZ	0.0239	0.0677	0.00029	0.0089	98.4
		XY	0.0239	0.0828	0.000382	0.0077	85.6
II	6	YZ	0.0393	0.1187	0.000453	0.0081	73.5
		XY	0.0784	0.227	0.000946	0.0083	98
	8	YZ	0.0549	0.1518	0.000604	0.0089	83.7
		XY	0.0369	0.1047	0.000604	0.0098	88.1
	11	YZ	0.0146	0.0388	0.000176	0.0077	86
		XY	0.0335	0.093	0.000331	0.009	99
III	12	YZ	0.04	0.1201	0.000563	0.0095	103.8
		XY	0.0198	0.0524	0.000267	0.0096	113.2
IV	15	YZ	0.0136	0.0362	0.000105	0.0077	86.2
		XY	0.0546	0.1504	0.000482	0.0073	85.3
	18	YZ	0.0556	0.1528	0.000439	0.0065	97.1
		XY	0.0431	0.1234	0.000496	0.0087	65.5
	20	YZ	0.0933	0.2605	0.00148	0.0079	85.5
		XY	0.0308	0.0908	0.000425	0.0089	83.7
V	21	YZ	0.0214	0.0616	0.000187	0.0078	87.1
		XY	0.0178	0.0533	0.000253	0.01	79.8
VI	23	YZ	0.0199	0.0663	0.000425	0.0112	67.8
		XY	0.0263	0.0774	0.000436	0.0098	96.2
	26	YZ	0.0189	0.0563	0.000147	0.0069	106.4
		XY	0.0365	0.104	0.000456	0.0095	86
VII	28	YZ	0.0233	0.0726	0.000572	0.0143	74.1

Table 9.4 Planar (2-D) Measurements for Bottom Sub-Region (Cont.)

Sub-region #	Core #	Section	Tortuosity	Spacing (mm)	Degree of Orientation	Number of microcracks
I	1	XY	1.28	1.71	0.072	29
		YZ	1.37	1.43	0.104	41
	4	XY	1.26	1.86	0.086	22
		YZ	1.37	1.71	0.093	30
II	5	XY	1.30	1.77	0.058	27
		YZ	1.36	1.80	0.106	26
	6	XY	1.34	1.80	0.044	26
		YZ	1.38	1.38	0.095	44
III	8	XY	1.35	1.05	0.121	76
		YZ	1.33	1.24	0.088	55
	11	XY	1.37	1.65	0.160	31
		YZ	1.32	2.11	0.195	19
	12	XY	1.34	1.60	0.113	33
		YZ	1.39	1.42	0.102	42
IV	15	XY	1.28	2.00	0.034	21
		YZ	1.31	2.23	0.238	17
V	18	XY	1.34	1.25	0.010	54
		YZ	1.32	1.14	0.085	65
	20	XY	1.36	1.42	0.106	42
		YZ	1.32	1.02	0.031	81
	21	XY	1.38	1.71	0.028	29
		YZ	1.35	1.84	0.130	25
VI	23	XY	1.39	2.16	0.102	18
		YZ	1.50	2.16	0.113	18
VII	26	XY	1.37	1.80	0.000	26
		YZ	1.42	1.96	0.074	22
	28	XY	1.36	1.62	0.087	32
		YZ	1.37	2.30	0.132	16

9.1.7.2 *Spatial (3-D) Measurements*

Figure 9.3 shows the spatial (3-D) microcrack characteristics for horizontal and vertical sub-regions; the following microcrack characteristics are presented: specific surface area, width, volume fraction, spacing, tortuosity, and degree of orientation. One-way analysis of variance "ANOVA" (F-Test) followed by Tukey's statistical procedure[114] indicated significant difference in specific surface area between sub-region III (severe level of damage) and sub-regions I, II and IV (low and moderate level of damage, respectively); sub-region III showed higher values of microcrack specific surface area, while measurements for other sub-regions were statistically comparable. Statistical analyses of microcrack spacing test data also indicated that in sub-regions V (severe level of damage), microcracks were more closely spaced than in other sub-regions (IV, VI and VII) which exhibited statistically comparable levels of microcrack spacing.

These (3-D) microcrack data further validate the (2-D) microcrack data and permeability measurements which all indicate higher damage levels near visible crack systems. Figure 9.4 illustrates the correlation between changes in permeability measurements and specific surface area. More extensive microcracking is observed to raise concrete permeability, which supports practical value of quantitative microcrack studies to condition assessment of concrete systems.

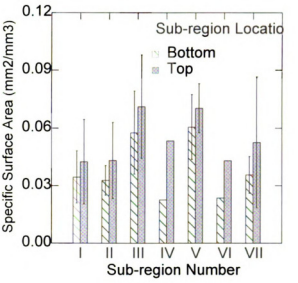

(a) Specific Surface Area

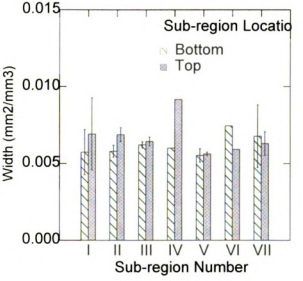

(b) Width

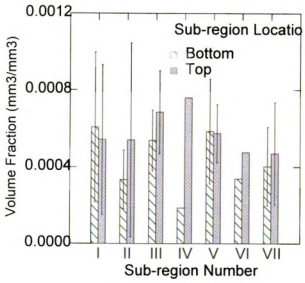

(c) Volume Fraction

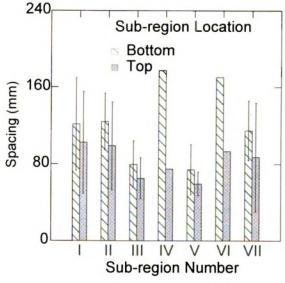

(d) Spacing

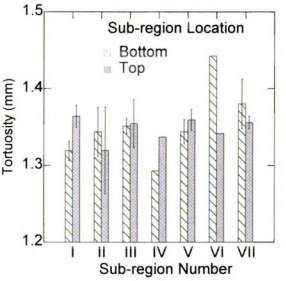

(e) Tortuosity

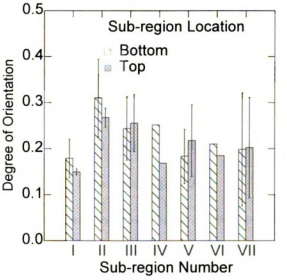

(f) Degree of Orientation

Figure 9.3 Spatial (3-D) Measurements for Horizontal and Vertical Sub-regions

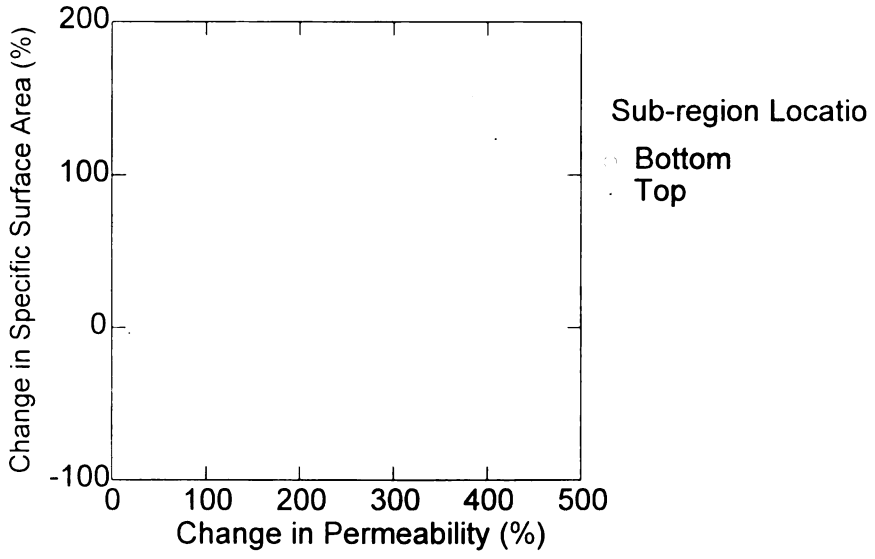

Figure 9.4 Changes in Specific Surface Area Versus Changes in Permeability

9.1.8 Assessment of the Adequacy of the Number of Cores and Sub-regions

A sub-region may be assumed to comprise a population of infinite number of cores. Sufficient number of cores should be extracted from each sub-region to provide a statistically viable representation of the whole population.

The microcrack specific surface area (S_{VC}) was used as the key measure to establish the required number of samples. A normal distribution was assumed for microcrack specific surface area, with unknown finite variance. The representative average number of cores (n) at desired level of confidence for each sub-region can then be expressed in terms of the targeted confidence coefficient ($1-\alpha/2$), half-width (h) and planning value of population standard deviation using equation 6.52. In the current study, a 95% level of confidence and ± 2.5% precision were considered reasonable in this investigation.

Therefore, 1- α is equal to 0.95, (i.e., α = 0.05, and 1- $\alpha/2$ = 0.975). Hence z = 1.96 and h = 0.025.[112] Standard deviation of specific surface area within each sub-region was calculated, and then the required number of cores per each sub-region was determined using the above equation 6.52 (Table 9.5).

The required number of cores to meet the targeted levels of confidence and precision depending on the standard deviation for each sub-region, generally below 4. The number of cores actually extracted from different sub-regions is thus generally sufficient to achieve the targeted levels of confidence and precision.

Adequacy of the number of sub-regions used in the study may be assessed using the variance of microcrack specific surface area between different sub-regions. Analysis of variance "ANOVA" is the primary statistical method employed for comparative evaluation of different sub-regions (see section 6.2.2.4). The minimum range was obtained using equation 6.53. In the current study, the power of the test (1- β) is selected to be 0.8, with α = 0.05 (noting that the differences between sub-regions are expected to be more than those between cores), with 6 degrees of freedom (r-1). For top sub-regions ∇ = 0.028123 and σ = 0.012463, and thus the ratio ∇/σ is 2.25. From the tables for determining sample size for analysis of variance (fixed factor level mode),[113] at ∇/σ = 2.0, the required number of sub-regions is 8 and at ∇/σ = 2.50 it is 6. By interpretation, the required number of sub-regions to achieve the required power of the experiment is 7 which is the same of the preliminary number of sub-regions. For bottom sub-regions ∇ = 0.036971 and σ = 0.015184, and thus the ratio ∇/σ = 2.43. From the tables and by interpretation, the required number of sub-regions is 6.2. Hence the preliminary number of sub-regions satisfies the targeted power of experiments (0.8).

Table 9.5 Required Number of Cores Per Sub-Region for Microstructural Investigation

Top Sub-region			Bottom Sub-region		
Sub-region #	Standard Deviation of Specific Surface Area	Required Number of Cores	Sub-region #	Standard Deviation of Specific Surface Area	Required Number of Cores
I	0.017	1.78	I	0.0105	0.68
II	0.015	1.44	II	0.0059	0.22
III	0.035	7.64	III	0.028	4.9
IV	NA	NA	IV	NA	NA
V	0.017	1.27	V	0.022	2.98
VI	NA	NA	VI	NA	NA
VII	0.026	4.24	VII	0.0074	0.34

NA = Not applicable

9.2 REINFORCED CONCRETE BRIDGE DECK

9.2.1 Preface

A large number of concrete bridge decks suffer from premature deterioration and cracking.[128,129] Steel corrosion is considered to be the main cause of damage to concrete bridges.[130,131] Besides steel corrosion, alkali-silica reactivity, drying and thermal shrinkage, and freeze-thaw attack are the major factors contributing to deterioration of concrete bridges.[132-134] Keeping concrete bridges in reliable condition for service requires frequent inspection and maintenance. Visual or non-destructive inspection of concrete structures may not provide sufficient information thorough assessment of the health condition of major infrastructure systems. Internal microcracking is the primary physical manifestation of most damage and deterioration phenomena in concrete; statistically viable quantitative investigation of the microcrack system could thus provide valuable information for judging the health condition of concrete and making critical decisions on costly maintenance and repair practices.[135,136] A reinforced concrete bridge deck located in Albion, Michigan was subjected to quantitative microcrack analysis for assessment of its health condition using the proposed approach in section 6.2.

9.2.2 Description of the Bridge

The bridge under investigation is located in Albion, Michigan over I-94 at Exit 121; it was built in 1980. The bridge has four lanes (two in each direction), and has two main internal supports and two abutments. One of these directions was closed to traffic while the other was opened. The closed direction was the subject of the current study. Each support in the bridge contains 2 frames; one for each direction, and each frame has 3

columns. The bridge deck slab rested on 12 main girders (6 in each direction). The two lanes considered in this investigation are 68.3 m (205 ft) long with total width of 8 m (24 ft). The bridge deck is 22.5 cm (9 inches) thick, and has one expansion joint. Figure 9.5 shows a general view for the bridge. The bridge deck shows crack configurations largely attributed to corrosion of reinforcing steel (attributed to deicer salt application in winter). Visual inspections identified close to 50 visible cracks on the bridge deck.

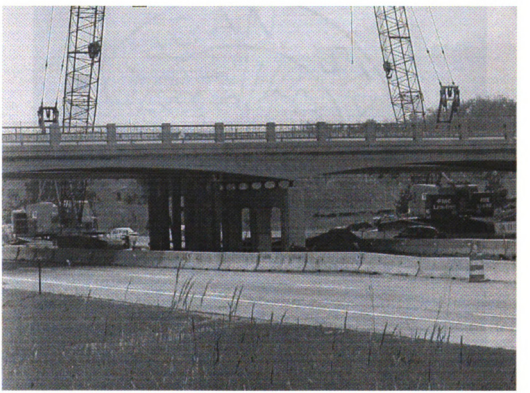

Figure 9.5 General View of The Bridge

The crack widths generally ranged from 10 to 20 mm (3/8 to 3/4 inches), with a wide range of crack lengths. Figures 9.6a through 9.6c present typical surface cracks which seem to be caused largely by the expansive forces associated with corrosion of the reinforcing steel; restraint of bridge deck. Shrinkage movement could also contribute to formation of these cracks.

(a) Random Cracks Partially Parallel to Traffic Direction

(b) Transverse Crack Partially Perpendicular to Traffic Direction

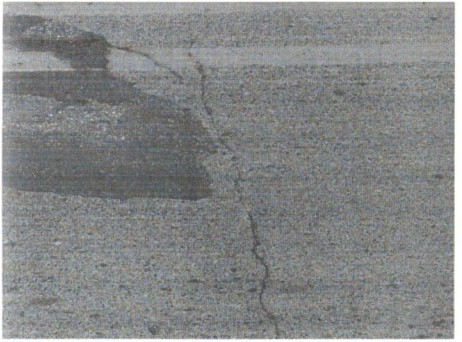

(c) Transverse Cracks Across the Bridge Deck "Perpendicular to Traffic Direction"

Figure 9.6 Typical Surface Cracks of the Bridge Deck

9.2.3 Sub-Regioning and Coring of The Bridge Deck

The bridge deck was divided into three preliminary sub-regions based on the degree of damage: sub-region I (severe level of damage); sub-region II (moderate level of damage); and sub-region III (low level of damage). The targeted power of statistical analyses in this investigation (1-β) was selected to be 0.8, where β is the risk of making type II error.[14] Sub-regions I, II and III are 8 × 23.3 m (24 × 70 ft), 8 × 18.3 m (24 × 55 ft), and 8 × 26.7 m (24 × 80 ft), respectively. The total number of visible cracks in sub-regions I, II and III are 25, 12 and 6, respectively. A total of 32 cores of 10 cm (4 in) diameter were extracted from the bridge deck: 14 from sub-region I (with severe level damage); 11 from sub-region II (with moderate damage); and 7 from sub-region III (with low level of damage). Some core locations were chosen over or near the visible surface cracks, while others were extracted far from cracks, as shown in Figure 9.7. About half of the cores were extracted from locations over or near visible cracks. The I-94 freeway underneath the bridge remained open to traffic during the coring process. Therefore, in order to avoid any risk of cores falling through onto the traffic, cores were not extracted no full depth. The cores extracted from the deck were typically 12.5 cm (5 in) high, which limited the analysis to one vertical sub-region. Cores were stored at 50% relative humidity and 20°C (68°F) for 3 months. During extraction of cores it was observed that steel reinforcement has suffered severe corrosion and noticeable loss of cross-sectional area. During the coring process, some cores (especially those from sub-region I) were broken into two pieces because accumulated rust layers caused full separation between concrete and steel reinforcement. These cores were eliminated from the investigation due to difficulties in cutting and sample preparation. Some cracks at aggregate-paste interfaces were visibly

observed in some cores especially those that were extracted over/near visual cracks.

9.2.4 Experimental Methodology

In order to evaluate damage conditions of the bridge deck, cores from each sub-region were subjected to the following tests: compression (ASTM C39), splitting tension (ASTM C96) and permeability (ASTM C1202). The cores were cut into 5 cm (2 in) height cylinders, using wet diamond concrete saw, for the performance of permeability tests. Some specimens were ground in order to obtain flat surfaces for capping and performance of compression tests. Splitting tension tests were performed on the cores as extracted without special preparation. During permeability tests, both sodium chloride (NaCl) and sodium hydroxide (NaOH) solutions were poured at the same time before connecting the molds to the instrument. The two solutions were poured in the same time to avoid any instantaneous flows due to the presence of major cracks in the specimens. Compression and splitting tension tests provided measure of the mechanical performance of deteriorated concrete. Permeability tests provided indications for the durability aspects of concrete performance. Cores extracted over/near and far from cracks were subjected to the same tests for the purpose of comparisons. Table 9.6 summarizes the test plan for concrete cores extracted from the bridge deck.

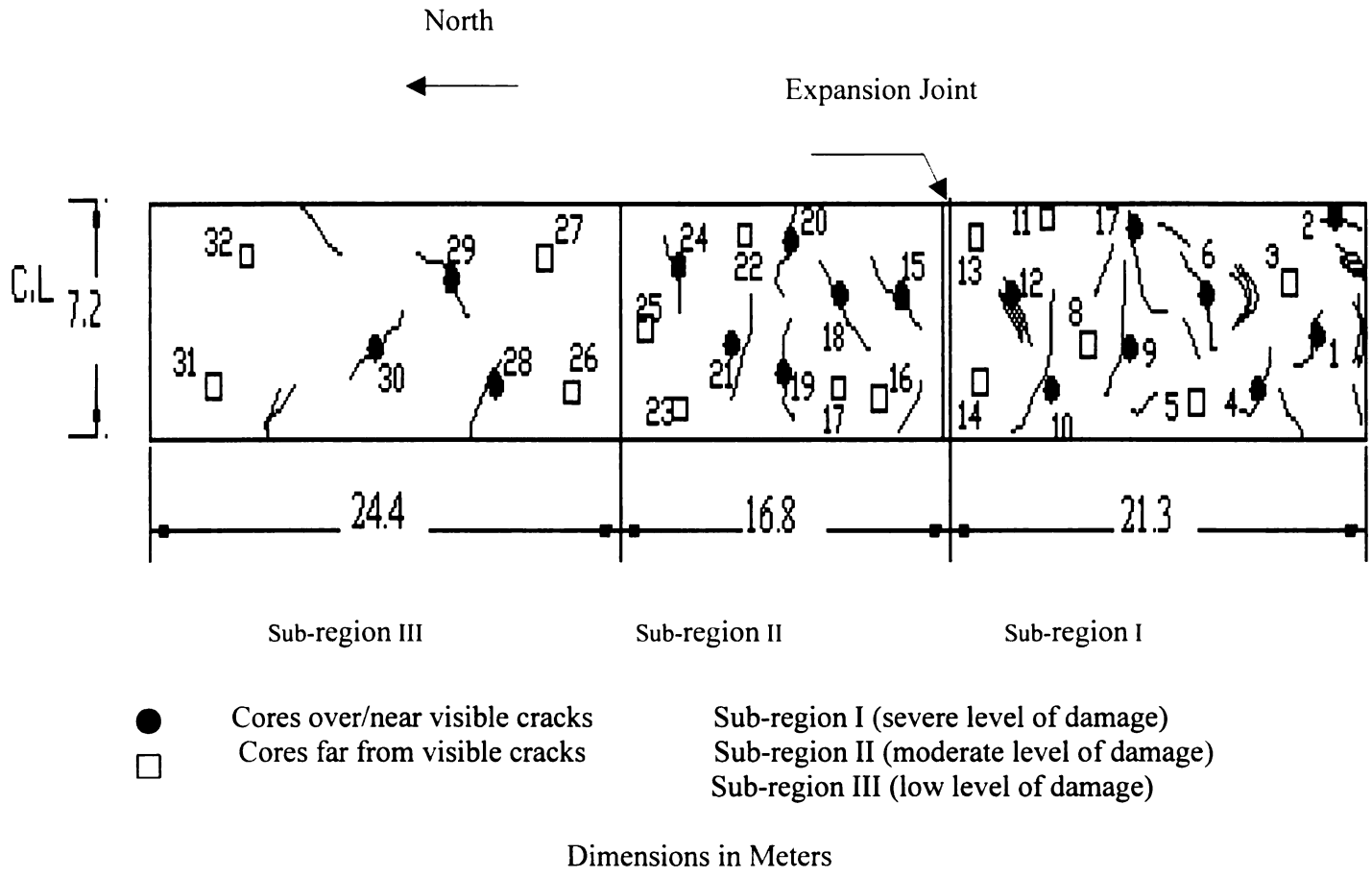

Figure 9.7 Plan of the Bridge Deck Under Investigation

Table 9.6 Details of Test Plan

Sub-Region #	Tests			
	Compression	Splitting Tension	Permeability	Microstructural Investigation
Sub-Region # I	Cores # 5^{+} and 12^{*}	Cores # 3^{+} and 7^{*}	Cores # 2^{*}, 10^{*} and 11^{+}	Cores # 1^{*},4^{*},6^{*}, 8^{+},9^{*},13^{+} and 14^{+}
Sub-Region # II	Cores # 20^{*} and 25^{+}	Cores # 17^{+} and 19^{*}	Cores # 21^{*} and 23^{+}	Cores # 15^{*}, 16^{+}, 18^{*}, 22^{+} and 24^{+}
Sub-Region # III	Core # 30^{*}	Core # 31^{+}	Cores # 27^{+}, and 29^{*}	Cores # 26^{+}, 28^{*} and 32^{+}

* Cores over/near visible cracks
\+ Cores far from visible cracks

9.2.5 Microstructural Investigation Scheme

For the purpose of microstructural analysis, concrete cores were cut using a wet diamond concrete saw into two perpendicular sections [horizontal (XY) and vertical (YZ)] as shown in Figure 6.11. Sections were cut; one in the direction of the applied traffic loads, and the second is perpendicular to the direction of traffic loading. The aim of cutting two perpendicular sections is to obtain planar (2-D) measurements which were incorporated into stereological analyses for quantification of the (3-D) microcrack system. After sectioning, 75 mm × 75 mm × 50mm (3 in × 3 in × 2 in) specimens were cut from horizontal and vertical sections.

Environmental scanning electron microscopy (ESEM) was used for acquisition of microscopic image acquisition. The cut sections were prepared using Wood's metal impregnation following the procedures presented in section 4.2.4.1. The magnification used in this investigation is 125X, with 144 images captured from each section to cover

4% of section area; the total number of images captured in the investigation is 4320. Planar (2-D) and spatial (3-D) characteristics of microcracks were determined using equations presented in parts 5.3.1.1 and 6.1.4.1 respectively. Cores which were subjected to microstructural analysis are presented in Table 9.6.

9.2.6 Mechanical Test Results and Discussion

The compression, splitting tension and permeability test results for different concrete cores are presented in Table 9.7. Correction factors were applied to compressive strength test data when length-to-diameter ratio deviated from 2.0 (ASTM C39). Generally, it can be noted that compressive and splitting tensile strengths of concrete cores were not significantly different in various sub-regions. Permeability, however, was higher for sub-region I (severe level of damage) and lower for sub-region II (moderate level of damage) and III (low level of damage). The high permeability of sub-region I is reflected on the severe microcracking in this sub-region. Cores extracted over/near cracks were lower in compressive strength and higher in permeability when compared with cores extracted far from cracks. However, due to the limitation of the number of cores designated for physical and transport properties, the obtained results of the physical properties may not be representative but are only an approximation of the physical properties of the concrete in the bridge deck.

Table 9.7 Mechanical and Transport Properties of Concrete Cores

Sub-Region #		Compressive Strength (MPa)	Splitting Tensile Strength (MPa)	Permeability (Coulombs)
Sub-Region I	Mean	32.4	2.49	4582
	Sd. Dev.	6	0.12	1308.15
Sub-Region II	Mean	26.3	2.04	2823.67
	Sd.Dev.	14.7	0	1799.09
Sub-Region III	Mean	30	2.23	2009.5
	Sd. Dev.	NA	NA	533.86
Over / near Cracks	Mean	28.3	2.22	3993
	Sd. Dev	12.4	0.26	1724.52
Far from Cracks	Mean	36.7	2.28	2127.3
	Sd. Dev.	0.09	0.27	1181.1

NA = Not applicable
Sd. Dev. = Standard deviation

9.2.7 Microstructural Data and Discussion

9.2.7.1Planar (2-D) Measurements

Table 9.8 presents the planar microcrack characteristics. One-way analysis of variance "ANOVA" (T-test) at 90% level of confidence revealed no statistically significant difference between horizontal (XY) and vertical (YZ) sections from all sub-regions in terms of the quantified features of the microcrack system. This is consistent with the hypothesis that corrosion of steel is the main source of damage to bridge decks; with reinforcing steel running in perpendicular directions, major differences in microcrack intensity on horizontal versus vertical sections would not be expected.

Table 9.8 Planar (2-D) Measurements

Sub-region #	Core #	Section	Length per Unit Area (mm/mm2)	Perimeter per Unit Area (mm/mm2)	Area Fraction (mm2/mm2)	Width per Unit Area (mm/mm2)	Angle of Orientation (degree)
I	1*	XY	0.136	0.403	0.005	0.012	61.941
		YZ	0.095	0.352	0.004	0.01	77.946
	4*	XY	0.229	0.687	0.008	0.011	84.616
		YZ	0.189	0.701	0.01	0.015	85.646
	6*	XY	0.246	0.934	0.018	0.015	91.632
		YZ	0.179	0.413	0.004	0.009	101.549
	8^{+}	XY	0.106	0.256	0.002	0.006	44.674
		YZ	0.056	0.146	0.001	0.008	56.875
	9*	XY	0.168	0.659	0.006	0.009	90.981
		YZ	0.257	0.779	0.013	0.014	91.676
	13^{+}	XY	0.166	0.615	0.004	0.007	23.875
		YZ	0.203	0.719	0.004	0.005	75.574
	14^{+}	XY	0.203	0.658	0.007	0.008	74.659
		YZ	0.255	0.688	0.009	0.013	84.697
II	15*	XY	0.213	0.789	0.015	0.013	66.874
		YZ	0.143	0.555	0.006	0.009	95.874
	16^{+}	XY	0.062	0.18	0.002	0.01	93.645
		YZ	0.045	0.103	0.001	0.009	71.543
	18*	XY	0.166	0.558	0.005	0.008	113.684
		YZ	0.223	0.603	0.009	0.013	96.645
	22^{+}	XY	0.098	0.287	0.002	0.006	79.649
		YZ	0.089	0.198	0.001	0.005	65.641
	24^{+}	XY	0.123	0.336	0.003	0.007	85.674
		YZ	0.056	0.149	0.002	0.01	81.547
III	26^{+}	XY	0.046	0.103	0	0.005	92.713
		YZ	0.036	0.888	0.005	0.006	87.655
	28*	XY	0.069	0.198	0.002	0.009	34.647
		YZ	0.114	0.306	0.003	0.007	74.235
	32^{+}	XY	0.046	0.123	0.001	0.005	71.65
		YZ	0.036	0.095	0	0.005	100.06

Table 9.8 Planar (2-D) Measurements (Cont.)

Sub-region #	Core #	Section	Tortuosity	Spacing (mm)	Degree of Orientation	Number of Cracks
I	1*	XY	1.31	1.10	0.060	80
		YZ	1.36	1.16	0.012	64
	4*	XY	1.25	0.86	0.080	101
		YZ	1.37	0.96	0.026	88
	6*	XY	1.31	0.83	0.231	112
		YZ	1.24	1.03	0.008	79
	8+	XY	1.40	1.13	0.010	67
		YZ	1.32	1.38	0.006	44
	9*	XY	1.33	1.06	0.016	75
		YZ	1.36	0.74	0.011	125
	13+	XY	1.35	1.06	0.113	75
		YZ	1.37	0.87	0.014	100
	14+	XY	1.22	1.00	0.065	84
		YZ	1.27	0.80	0.130	115
II	15*	XY	1.34	0.92	0.065	91
		YZ	1.37	1.10	0.008	71
	16+	XY	1.34	1.26	0.132	51
		YZ	1.36	1.53	0.157	36
	18*	XY	1.39	1.07	0.031	74
		YZ	1.41	0.88	0.011	98
	22+	XY	1.28	1.13	0.001	67
		YZ	1.34	1.29	0.046	59
	24+	XY	1.35	1.16	0.005	64
		YZ	1.30	1.42	0.024	42
III	26+	XY	1.31	1.60	0.002	33
		YZ	1.28	1.71	0.187	30
	28*	XY	1.37	1.31	0.136	49
		YZ	1.36	1.05	0.006	76
	32+	XY	1.34	1.62	0.013	32
		YZ	1.31	1.71	0.063	29

* Cores over/near visible cracks
\+ Cores far from visible cracks

Statistically significant differences were found between sub-region I (severe level of damage) and sub-region III (low level of damage) in terms of microcrack length per unit area, perimeter per unit area, width per unit area, area fraction, spacing and number of cracks. Sub-regions I (severe level of damage) and III (low level of damage) were statistically similar in terms of the angle of orientation, tortuosity, and degree of orientation of microcrack on both horizontal and vertical sections. No statistically significant differences were found between sub-region I (severe level of damage) and II (moderate level of damage), and also between II and sub-region III (low level of damage) in terms of all microcrack on horizontal or vertical sections. This may give an indication that most of the deterioration in the bridge deck is concentrated in sub-region I. Statistically significant differences were also found between cores extracted over/near visible cracks and cores extracted far from visible cracks (for all sub-regions) in terms of microcrack length per unit area and area fraction. This may lead to the conclusion that coalescence of microcracks has led to formation of macrocracks near visible cracks. There is no distinct trend of microcracks angle of orientation was observed; this may be attributed to that combination of steel corrosion, traffic loads and drying shrinkage are the main cause of microcracks.

9.2.7.2 *Spatial (3-D) Measurements*

Figure 9.8 presents the quantified in space microcrack characteristics in different sub-regions. One-way analysis of variance "ANOVA" (F-Test), followed by Tukey's procedure[114] indicated that there are statistically significant differences in microcrack specific surface area, width, volume fraction, and spacing between sub-region I (severe

level of damage) and sub-region III (low level of damage); there were, however, no significant differences in tortuosity and degree of orientation. Statistical analysis also indicated no statistically significant difference between microcrack characteristics of sub-region I (severe level of damage) and sub-region II (moderate level of damage). Statistically significant differences were found between sub-region II (moderate level of damage) and sub-region III (low level of damage) in terms of microcrack width while but no other microcrack characteristics. The spatial results are in general agreement with the planar measurements leading to the conclusion that there is a direct relationship between visible surface damage (cracks) and internal damage (microcracks); most internal damage occurs in sub-region I which also exhibits severe visible surface cracks; on the other hand, the internal damage in sub-region III was limited where visible surface damage was also limited. Figure 9.9 compares the quantified features of microcracks for cores obtained over/near visible cracks versus those obtained far from visible cracks. Again, vicinity to visible surface cracks implies severe internal microcracking. The more severe microcracking in sub-region I versus sub-region III can be used to explain the higher permeability values measured in sub-region I versus sub-region III.

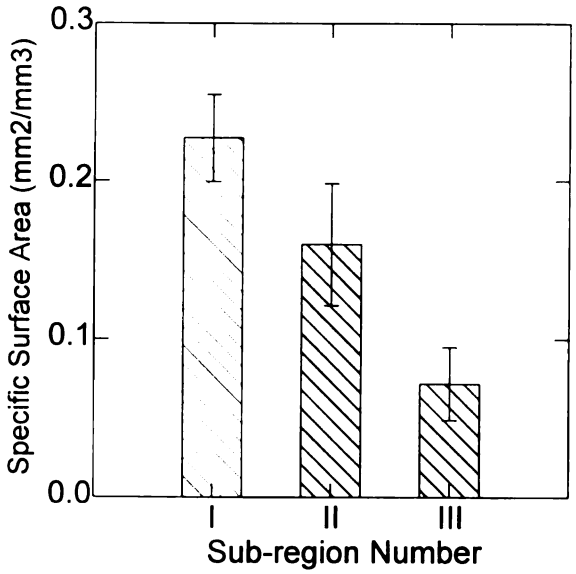

(a) Specific Surface Area

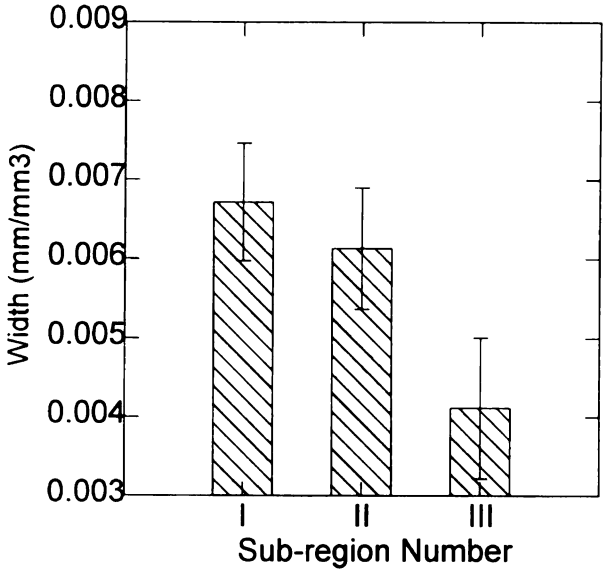

(b) Width

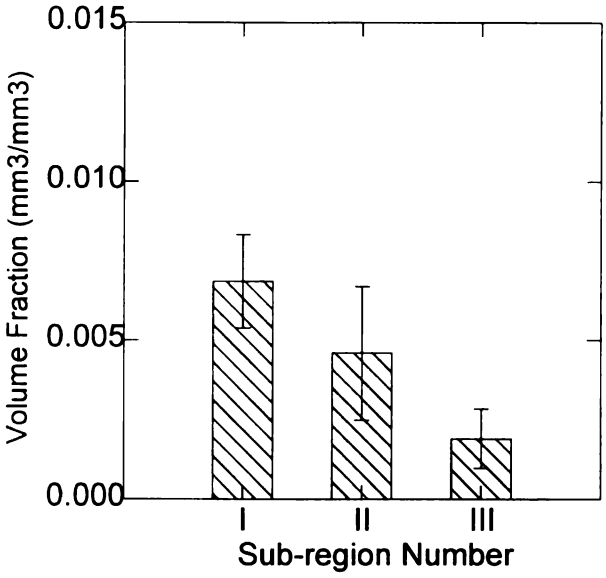

(c) Volume Fraction

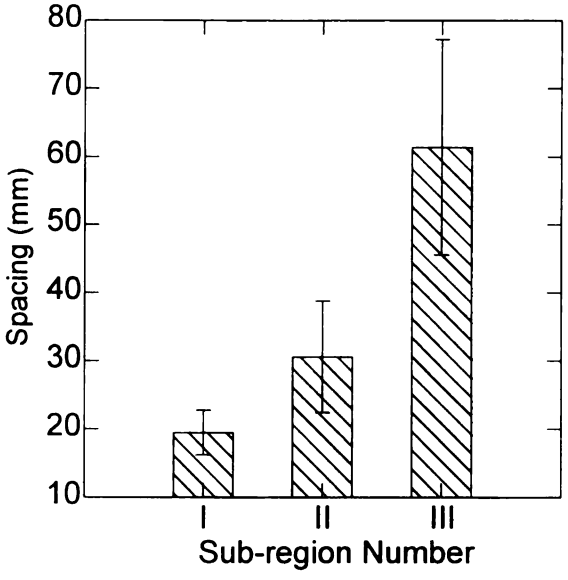

(d) Spacing

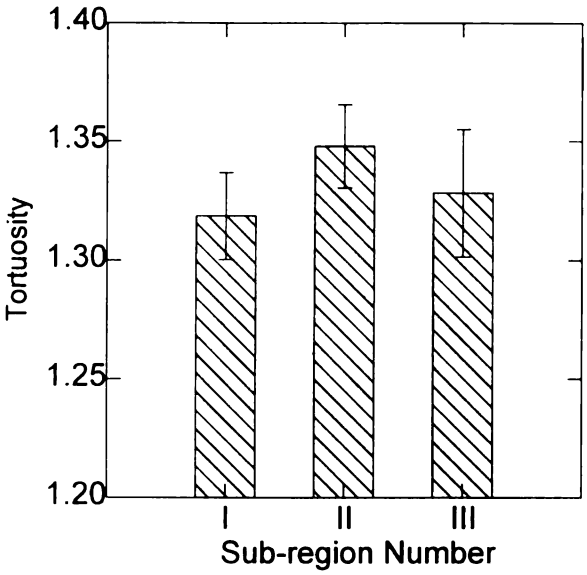

(e) Tortuosity

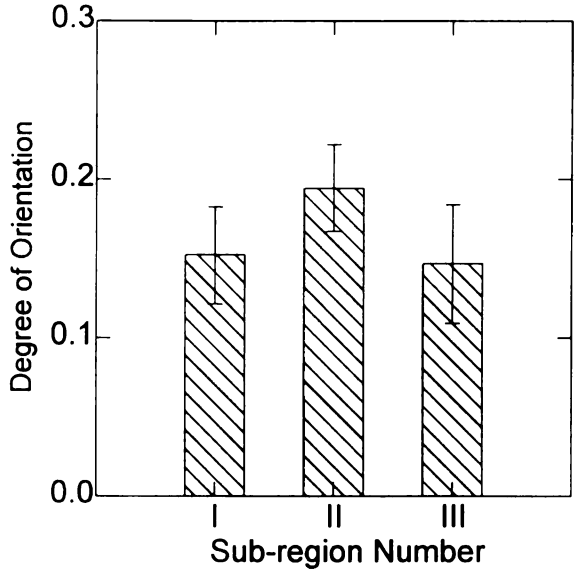

(f) Degree of Orientation

Figure 9.8 Spatial (3-D) Measurements for All Sub-regions

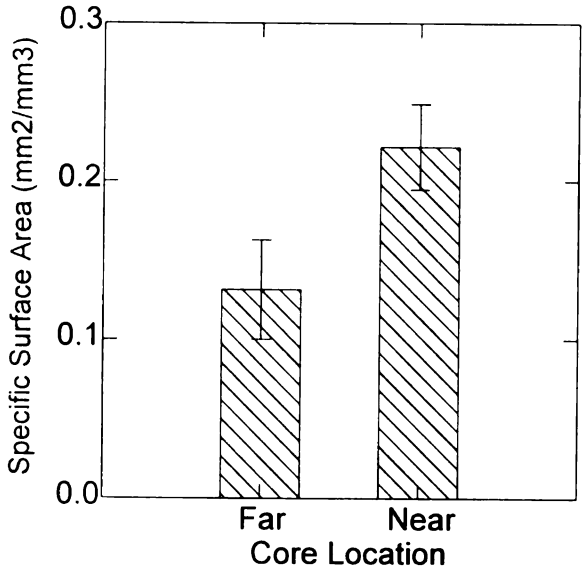

(a) Specific Surface Area

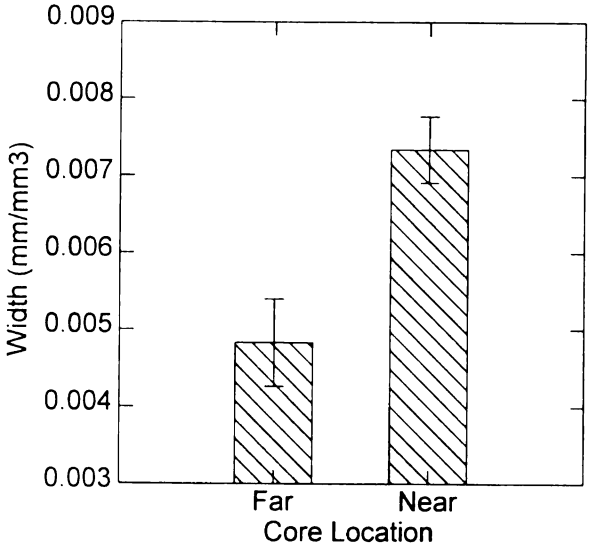

(b) Width

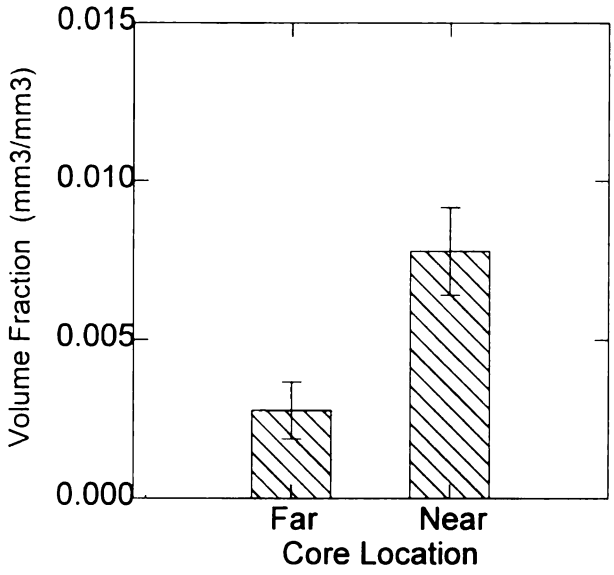

(c) Volume Fraction

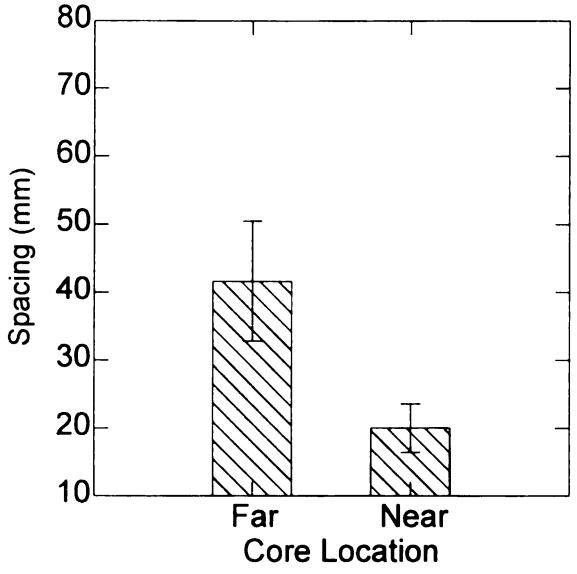

(d) Spacing

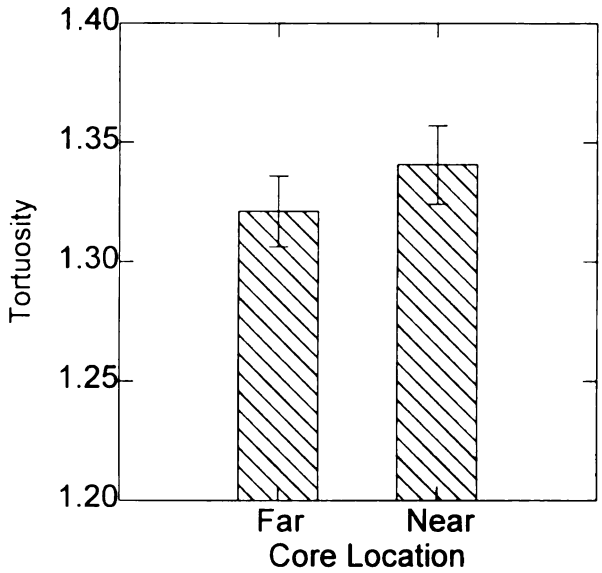

(e) Tortuosity

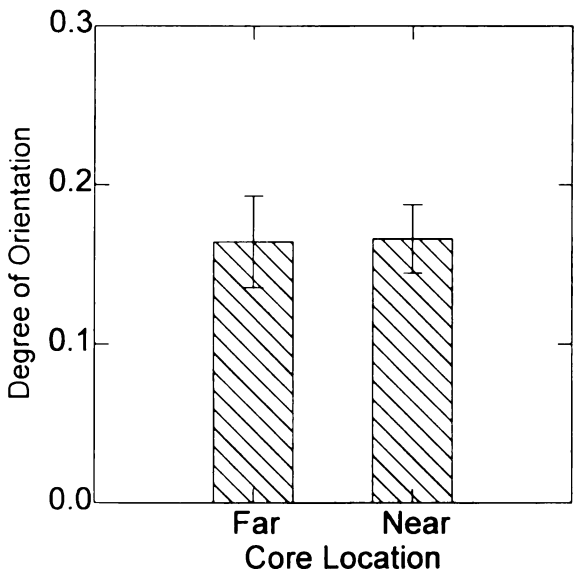

(f) Degree of Orientation

Figure 9.9 Spatial (3-D) Measurements for Cores Extracted Over/Near and Far from Cracks

9.2.8 Assessment the Adequacy of the Number of Cores and Sub-Regions

A sub-region may be assumed to comprise a population of infinite number of cores. Sufficient number of cores should be extracted from each sub-region to provide a statistically viable representation of the whole population.

The microcrack specific surface area (S_{VC}) was used as the key measure to establish the required number of samples. A normal distribution was assumed for microcrack specific surface area, with unknown finite variance. The representative average number of cores (n) at desired level of confidence for each sub-region can then be expressed in terms of the targeted confidence coefficient ($1-\alpha/2$), half-width (h) and planning value of population standard deviation using equation 6.52. In this investigation, a 10% level of significance and ± 5% precision were considered reasonable for this investigation, therefore, $1-\alpha$ is equal to 0.90 (i.e., $\alpha = 0.1$ and $1-\alpha/2 = 0.95$). Hence, $z = 1.645$ and $h = 0.05$.[112] Standard deviation of specific surface area within each sub-region was calculated, and then the required number of cores per each sub-region was determined using Equation 6.52.

The required number of cores to meet the targeted levels of confidence and precision depend on the standard deviation for each sub-region are 5.4, 6.1, and 2.7 cores for sub-regions I, II and III, respectively. These results indicate that the actual extracted number of cores is satisfactory for sub-regions I and III, but one more core is needed for sub-region II. Comparisons between the required and the actual number of cores per sub-region are illustrated in Table 9.9.

Adequacy of the number of sub-regions used in the study may be assessed using the variance of microcrack specific surface area between different sub-regions. Analysis of

variance "ANOVA" is the primary statistical method employed for comparative evaluation of different sub-regions (see section 6.2.2.4). The minimum range was obtained using equation 6.53. In the current study, the power of the test (1- β) is selected to be 0.8, with $\alpha = 0.05$ (noting that the differences between sub-regions are expected to be more than those between cores), with 2 degrees of freedom (r-1). For the data generated in this investigation, it was found $\nabla = 0.1553$ and $\sigma = 0.077881$, and thus the ratio $\nabla / \sigma = 1.99$. From the tables for determining sample size for analysis of variance (fixed factor level mode),[113] at $\nabla / \sigma \approx 2.0$, the required number of sub-regions is equal to 4 which means that the preliminary number of sub-regions needs to be increased by one, or alternatively the power of the experiment may need to be re-evaluated (decreased).

Table 9.9 Comparison of The Required and Actual Number of Cores Per Sub-region for Microcrack Analysis

Sub-region Number	Extracted Number of Cores	Required Number of Cores	Comment
Sub-region I	7	5.4	Satisfactory
Sub-region II	5	6.1	Needs one more core
Sub-region III	3	2.7	Satisfactory

9.3 CONCLUSIONS

Rigid pavement slab and reinforced concrete bridge deck were subjected to the proposed approach to quantify microcrack characteristics. The pavement slab was divided into seven horizontal and two vertical sub-regions and the bride deck was divided into 3 horizontal sub-regions targeting a power of 0.8 for statistical analyses of quantified microcrack data. A number of concrete cores were obtained from each sub-region, targeting a precision level of ±2.5% and ±5% for pavement slab and bride deck respectively in quantitative analyses of microcrack systems. Cores were cut into two perpendicular sections, which were prepared for the automated acquisition of microscopic images through fluorescent microscopy. Quantitative microstructural analyses were conducted for planar and spatial microcrack measurements. Mechanical and transport properties (compressive and splitting strength, and permeability) of concrete cores were also determined. Statistical procedures were employed to determine the adequacy of the number of cores and sub-regions for achieving the targeted power and precision levels. The following conclusions were drawn:

1- During pavement investigation, as far as vertical (top and bottom) sub-regions are concerned, the differences in permeability and quantified microcrack attributes were not statistically significant, but generally pointed of higher damage levels to top (exposed) sub-regions.

2- During bridge deck investigation, statistically significant differences were found between sub-region I (severe level of damage) versus sub-region III (low level of damage) in terms of microcrack length per unit area, perimeter per unit area, width per

unit area, area fraction and spacing (planar measurements) and microcrack specific surface area, width, volume fraction and spacing. The quantified microcrack characteristics also indicated statistically significant rise in microcrack area fraction (planar) and volume fraction (spatial) for cores extracted over/near visible cracks

3- Permeability test data correlated well with quantified microcrack data. There were statistically significant differences between permeability and microcrack measurements between sub-regions rated differently in terms of visible manifestations of damage. Sub-regions with higher microcrack specific surface area and closer microcrack spacing exhibited higher permeability levels.

4- The increase in microcrack intensity correlated well with the increase in permeability compared to mechanical properties. This may suggest that permeability is more sensitive than mechanical performance of concrete to certain levels of damage and microcracking; permeability tests thus provide more insights into concrete quality and health condition than is possible by only mechanical tests. Given the significant impact of permeability on durability under weathering effects, this finding indicates that mechanical test results alone may not truly reflect on durability and remaining service life of concrete pavements, and quantitative microcrack data can provide reliable insight into health conditions and durability of concrete.

5- Spatial (3-D) microcrack measurements are more preferred than planar (2-D) measurements to investigate the degree of damage distribution along concrete structures. Microcrack specific surface area is the most reliable measurement to be used as the viable probe of condition assessment of concrete. Spatial (3-D) data provide a more thorough assessment of concrete damage conditions than planar (2-D) data.

6- The proposed statistical approach to determine the sufficient number of sub-regions and number of cores per sub-region was successfully applied to achieve the targeted power of experiment and precision of the results. However, statistical analyses, using microcrack specific surface area indicated that the selected number of cores and sub-regions are reasonable (with some minor compromise) to meet the targeted levels of confidence, precision and power.

CHAPTER 10

DEVELOPMENT OF CONCRETE MICROCRACK-PROPERTY RELATIONSHIPS

10.1 PREFACE

At some level, the behavior of concrete may be related to its microstructure. Concrete microstructure encompasses a wide range of structural scales, and it is generally assumed that behavior at one level can be explained in terms of concrete structure observed at a lower level. The microstructure of concrete is too complex and random to allow for development of exact analytical formulas (at this time) that describe relationships between engineering properties and microstructure.[137,138] Most previous studies have focused on relationships between concrete behavior and qualitative changes in its microstructure during hydration of cement paste, but have not able to express these relationships in numerical (quantitative) format. Although concrete performance (permeability, durability, and strength) depends to a large extent on the amount and distribution of the microcracks that are initiated by internal restraint of shrinkage and grown under load and environmental effects, quantitative relationships between concrete performance and microcrack characteristics have not been developed yet. Few investigators have tried to correlate concrete performance to its damage condition and microstructure. Gettu et al.[139] reported that concrete tensile strength decreased significantly after compression loading in a perpendicular direction. The drop in dynamic modulus of elasticity of concrete under freeze-thaw cycles is well known.[140] Concrete permeability often increases under repeated freeze-thaw cycles.[140,141] Zhang[142] detected an increase in pore specific surface area under flexural fatigue. Dienes et al[143,144]

developed a model that related the permeability of crystalline rocks to crack shape factor, average crack radius and spacing, and fraction of interconnected cracks. The relative lack of information on concrete microstructure-property relationships may be attributed to the difficulty in quantifying concrete microstructure. Throughout the current study, the relationships between concrete properties (permeability and flexural strength) and microcrack measurements (planar and spatial) were developed using image processing and analysis techniques in conjunction with fluorescent microscopy. Theoretical principles were employed to justify the empirical structure-property relationships.

10.2 EXPERIMENTAL AND MICROSTRUCTURAL ANALYSIS PROGRAM

Two concrete mixtures (normal-strength and relatively high-strength) with different ingredients and proportions were considered in the experimental program. Type I Portland cement, natural sand and crushed limestone with maximum particle size of 19 mm (3/4 in) as coarse aggregate were used in both mixtures. Mixture I (normal-strength concrete) comprised cement : fine aggregate : coarse aggregate : water at 1 : 1.59 : 1.98 : 0.485 mass ratios, targeting 28-day compressive strength of 39 MPa (5650 psi). This mix was air-entrained, and provided an air content of 3.5 percent with a slump of 190 mm (7.5 in). Mixture II (relatively high-strength concrete) comprised cement: fine aggregate: coarse aggregate : water at of 1 : 1.7 : 1.9: 0.404 mass ratios, targeting 28-day compressive strength of 44 MPa (6374 psi). This mix provided 1.9 percent air content and a slump of 64 mm (2.5 in) cylinder specimens. 102 mm (4 in) diameter by 203 mm (8 in) height were prepared for compression tests, and prismatic specimens of 76 × 76 × 305 mm (3 × 3 × 12 in) dimensions were made for microstructural investigations. Molded

specimens were kept moist for 24 hours, after which they were demolded and moist cured at 100% relative humidity and 22°C (72°F) for 28 days, and then conditioned at 50% relative humidity at 22°C (72°F) for another 28 days prior to testing. Three 100 mm diameter × 200 mm height cylinder (4 × 8 in) from each mixture were tested for compressive strength, while twenty four 102 × 76 × 406 mm (4 × 2 × 16 in) prisms and twenty four 100 mm diameter × 200 mm height cylinder (4 × 8 in) from each mixture were used for application of different damaging effects and subsequent investigation of microcrack characteristics and engineering performance. Three prisms and cylinders were reserved to be used as control (undamaged) specimens for comparison purposes; prismatic specimens were subjected to 4 point flexural loading (ASTM C78), while cylindrical specimens were subjected to chloride permeability (ASTM C1202) tests. The damaging effects considered in the study are:

1- Compression loading to peak stress with immediate unloading (ASTM C39)

2- Exposure to fire at 425°C (800°F) for 3 hours

3- Compression loading to 80% of ultimate strength followed by immediate unloading and exposure to fire at 425°C (800°F) for 3 hours

4- 300 cycles (75 days) of freeze-thaw in water (ASTM C666)

5- Compression loading to 80% of ultimate strength followed by immediate unloading and exposure to 300 cycles (75 days) of freeze- thaw in water

After application of damaging effects, prismatic specimens were subjected to the 4-point flexural strength test (ASTM C78), and cylindrical specimens were subjected to the chloride permeability test (ASTM C1202). Some specimens were cut into two perpendicular sections for the purpose of microstructural investigations; the schematic of

horizontal and vertical sections cut into prismatic and cylindrical concrete specimens are previously presented in Figure 7.1.

For the purpose of microscopic investigation, cut sections were prepared using the method described in section 4.2.4.2 for fluorescent microscopy. Each section was investigated at 250X magnification; a total of 256 images were captured from each section. Planar and spatial microcrack measurements were obtained using equations provided in sections 5.3.1.1 and 6.1.4.1, respectively.

10.3 EXPERIMENTAL RESULTS

Changes in flexural strength and permeability caused by different damaging effects for both Mixtures I and II are summarized in Table 10.1. From Table 10.1 it can be noticed that all damage phenomena decreased flexural strength and increased permeability, Mix II (with higher strength) showed less reduction in flexural strength and also less increase in permeability under damaging effects when compared with Mix I of lower strength. It is also observed that exposure to elevated temperature has the most severe effect on both flexural strength and permeability. At 10% level of significance, exposure to 80% of compressive strength and then elevated temperature (80% compression + fire) caused the severe level of damage to flexural strength and permeability as exposure to fire alone. The damaging effects comprising 80% of compression strength then freeze-thaw cycles (80% compression + freeze-thaw) caused (statistically significant at 10% level of significance) more damaging effects than freeze-thaw above for Mix I (but not Mix II). Figures 10.1 through 10.4 present the effects of different damage phenomena on the flexural strength and permeability of Mix I and Mix II.

Table 10.1 Changes (%) in Flexural Strength and Permeability Caused by Different Damaging Effects

Damage Type	Mix I (Normal-Strength)		Mix II (Relatively High-Strength)	
	Flexural Strength (MPa) (Prismatic Specimens)	Permeability (Coulombs) (Cylindrical Specimens)	Flexural Strength (MPa) (Prismatic Specimens)	Permeability (Coulombs) (Cylindrical Specimens)
Undamaged	-	-	-	-
100 % Compression	-42.3	84.2	-25.1	16.7
Fire	-92.3	84.5	-83.3	76.8
80% Comp. + Fire	-76.9	65.6	-85.7	78.4
Freeze-Thaw	-32.7	34.7	-23.8	26.2
80% Comp. + Freeze-Thaw	-50	39.9	-28.6	30.2

10.4 RESULTS OF MICROSTRUCTURAL ANALYSIS

Tables 10.2 and 10.3 show changes (%) in planar microcrack measurements due to different damaging effects for Mix I and Mix II, respectively. These results indicate that length, width, perimeter per unit area and area fraction of microcracks are increased after exposure to different damaging effects for both Mix I and Mix II. Spacing has been decreased after applying damaging effects for Mix I and II (negative sign in table values means measurements decreased after applying damaging effects). Tortuosity and degree of orientation did not show a constant trend after applying damaging effects; they

fluctuated between increases and decreases. Some specimens showed different trends in tortuosity and degree of orientation between horizontal (XY) and vertical (YZ) sections.

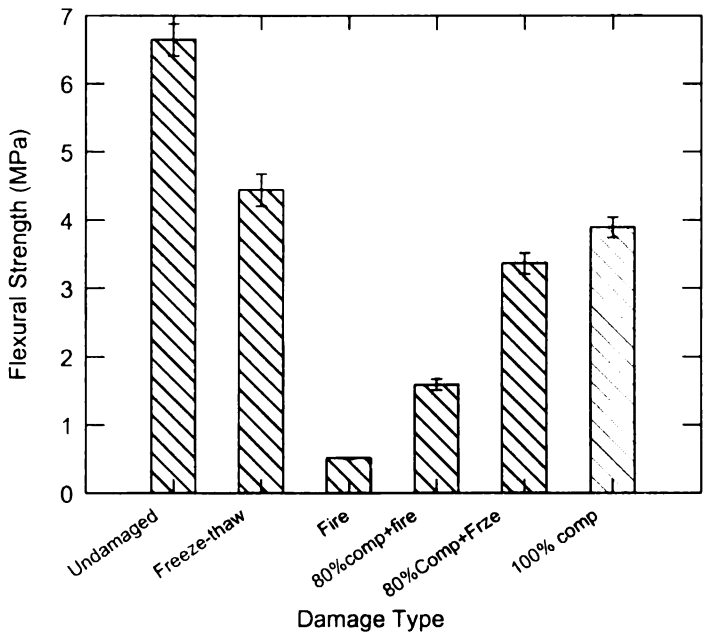

Figure 10.1 Flexural Strength of Mix I (Normal-Strength) After Different Damaging Effects

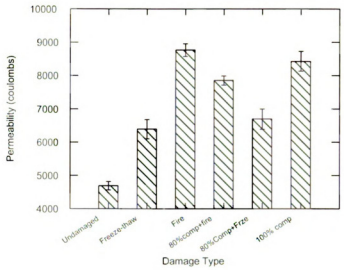

Figure 10.2 Permeability of Mix I (Normal-Strength) After Different Damaging Effects

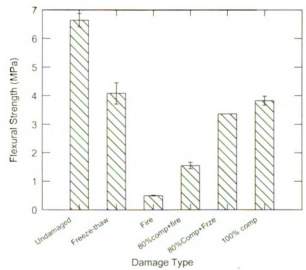

Figure 10.3 Flexural Strength of Mix II (Relatively High-Strength) After Different Damaging Effects

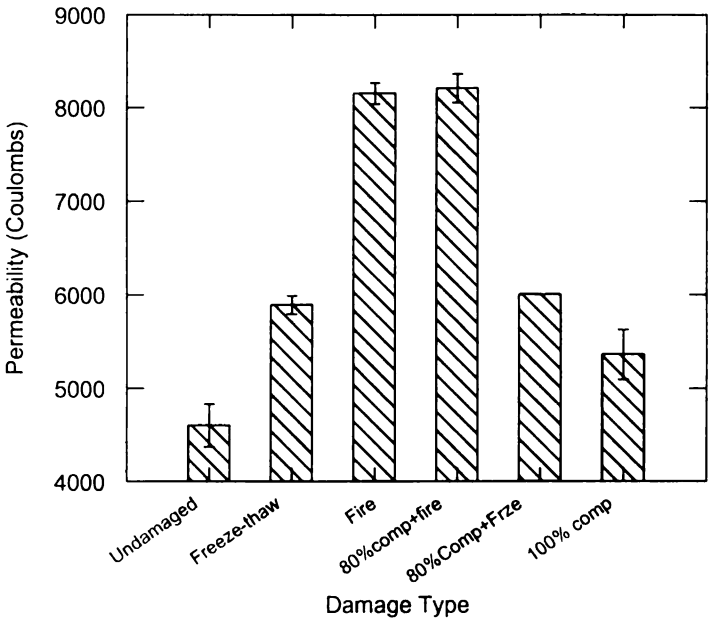

Figure 10.4 Permeability of Mix II (Relatively High-Strength) After Different Damaging Effects

Table 10.2 Changes (%) in Planar Measurements for Mix I

Damage Effects	Section	L_{AC} (mm/mm^2)	P_{AC} (mm/mm^2)	A_{AC} (mm^2/mm^2)	W_{CP} (mm/mm^2)	λ_{CP} (mm)	T_{CP}	Ω_{CP}
		Prismatic Specimens						
100% Comp	XY	68.0	19 .0	137.6	16.8	-13.90	0.20	61.9
	YZ	13.7 0	9.30	14.7	4.2	-11.3	-1.10	64.7
Fire	XY	83.1	52.0	313	30.2	- 46.8	3.60	21.0
	YZ	46.2	27.70	118.9	13.0	-60.7	4.90	-17.1
80% Comp + Fire	XY	146.2	55.8	513	30.8	-6.50	3.00	-42.3
	YZ	15.90	4.30	13.1	3.5	-49.3	-0.60	27.2
Freeze-Thaw	XY	28.6	8.90	37.9	6.50	3.10	-1.70	-12.0
	YZ	21.8	27.8	29.3	21.9	-38.7	-5.50	-58.2
80% Comp + Freeze-Thaw	XY	61.3	59.2	184.7	24.2	-2.80	4.10	-42.2
	YZ	81.0	82.7	107.1	18.3	-39.6	6.50	146.9
		Cylindrical Specimens						
100% Comp	XY	84.9	82.1	83.5	5	-15.4	-2.1	21.1
	YZ	41.3	71.6	60.2	7.3	-5.01	1.3	15.5
Fire	XY	194.8	214.9	353.7	23.3	-28.2	2.92	255.9
	YZ	128.7	366	1371	6.1	-31.5	4.6	-14
80% Comp + Fire	XY	70.2	83.1	57.5	4.9	-17.5	-6	-30.7
	YZ	44.4	151	453	5.74	-20.6	5.3	-30.3
Freeze-Thaw	XY	54.5	62.2	50	3.5	-15.7	-2.6	11.6
	YZ	30	82.6	301	0.76	-6.03	1.51	77.3
80% Comp + Freeze-Thaw	XY	14.5	16.8	37.5	4.6	-5.5	1.06	-3
	YZ	85.2	227	910	14.2	-21.7	-3.4	-87.4

Table 10.3 Changes (%) in Planar Measurements for Mix II

Damage Effects	Section	L_{AC} (mm/mm^2)	P_{AC} (mm/mm^2)	A_{AC} (mm^2/mm^2)	W_{CP} (mm/mm^2)	λ_{CP} (mm)	T_{CP}	Ω_{CP}
		Prismatic Specimens						
100% Comp	XY	84.3	26.5	65.5	6.1	-15.5	0.89	23.2
	YZ	11.6	6.6	3.5	1.2	-3.4	1.2	-45.7
Fire	XY	67.5	115	188	12.4	-33.4	2.2	13.3
	YZ	107.4	212	150	11.7	-55.1	1.5	-17.4
80% Comp + Fire	XY	116.6	77.3	78.8	18.8	-26.4	-1.2	11.4
	YZ	51.4	52.2	64.3	10.5	-14.8	-2.2	55.6
Freeze-Thaw	XY	31.7	3.4	30	5.5	-6.4	2.5	-45.8
	YZ	41	13.5	41.1	6.3	-7.7	-4.6	-14.7
80% Comp + Freeze-Thaw	XY	57.8	33.1	88.4	13.9	-26.6	4.7	115.6
	YZ	31.5	15.4	55.1	10.1	-21.1	-1.6	-22.6
		Cylindrical Specimens						
100% Comp	XY	65.8	44.2	80.4	10	-23.3	1.7	112.5
	YZ	23.2	29.4	25.7	5.4	-9.8	2.5	45.8
Fire	XY	82.2	66.5	124	7.1	-35.6	-9.7	-31.5
	YZ	14.5	6.8	16.3	11.4	-2.7	-6.3	78.3
80% Comp + Fire	XY	71.1	55.5	98.7	8.2	-15.3	3.3	22.6
	YZ	35.5	44.6	36.4	6.4	-11.8	-6.4	-17.8
Freeze-Thaw	XY	59.7	37	100.6	11	-32.3	-12.3	-15
	YZ	22.5	12	47.7	14.1	10.5	-5.8	223.3
80% Comp + Freeze-Thaw	XY	12.9	1.5	14	6.7	-19.6	-12.4	26.7
	YZ	23.8	17.7	114	46.1	-4.8	-8.8	-118

Generally changes in length, width, perimeter per unit area, area fraction and spacing in Mix I were larger than the corresponding changes in Mix II (with higher strength). Sections perpendicular to load direction (XY) under the effect of 100% compression, 80% compression + fire, and 80% compression + freeze-thaw exhibited greater increases in crack length and perimeter per unit area and area fraction when compared with sections parallel to load direction (YZ) for both Mixtures I and II. Exposure to 80% compression + fire damaging effect had the most severe effect on concrete microcracking, while 80% compression + freeze-thaw had the least severe effect. Under 80% compression + freeze-thaw, the microcrack system was not as severely damaged (in both Mixture I and II – cylindrical specimens) compared with under freeze-thaw exposure alone.

Tables 10.4 and 10.5 show present changes (%) in spatial measurements due to different damaging effects for Mix I and Mix II, respectively. These results indicate that microcrack specific surface area, width, and volume fraction were increased after application of damaging effects for both Mixtures I and II. Microcrack spacing in space was decreased after application of different damaging effects for both Mixtures I and II. No consistent damaging effects on tortuosity and orientation of microcrack were detected. Changes in microcrack surface area, with, volume fraction, and spacing were larger in Mix I than in Mix II. As with the in-plane measurements, 80% compression + fire showed the most severe damaging effect on the (3-D) microcrack system, while 80% compression + freeze-thaw produced the least damaging effects. The effect of 80% compression + freeze-thaw on the microcrack system for (in both Mixture I and II) were comparable to the damaging effect of freeze-thaw exposure alone. This may give an

indication that the combination of compression and freeze-thaw damage treatments imposed biaxial effects on concrete specimens which reduced the severity of individual damage treatment; this finding is, however, needs additional study. Fire caused greater damage to concrete mixtures than exposure to freeze-thaw because fire tends to exhibit internal pressure and thus damage to concrete structure, which air entrainment of concrete controls the stress and thus the damage caused by freeze-thaw treatments. Longer-term exposure to freeze-thaw cycles could also pronounce the damage to concrete.

Table 10.4 Changes (%) in Spatial Measurements for Mix I

Damage Effects	S_{VC} (mm^2/mm^3)	W_{CS} (mm/mm^3)	V_{VC} (mm^3/mm^3)	λ_{CS} (mm)	T_{CS}	Ω_{CS}
	Prismatic Specimens					
100% Comp	15.1	10	16.9	-11.6	-1.44	14.6
Fire	37.1	18.3	29.7	-59.6	4.3	10.8
80% Comp + Fire	23.9	18.9	50.7	-19.4	1.19	-6.67
Freeze-Thaw	9.12	6.75	10.8	-10.1	-3.6	-11.7
80% Comp + Freeze-Thaw	15.25	33.2	13.8	-8.56	1.28	29.9
	Cylindrical Specimens					
100% Comp	39.8	11.3	33.7	-18.5	-1.1	11.5
Fire	84.6	14.8	74.9	-43.6	3.75	31.9
80% Comp + Fire	62.4	5.28	51.4	-38.4	-1.65	-7.62
Freeze-Thaw	37.1	1.69	30.1	-27	2.08	8.4
80% Comp + Freeze-Thaw	36	4.95	64.5	-26.5	-1.91	-13.2

Table 10.5 Changes (%) in Spatial Measurements for Mix II

Damage Effects	S_{VC} (mm^2/mm^3)	W_{CS} (mm/mm^3)	V_{VC} (mm^3/mm^3)	λ_{CS} (mm)	T_{CS} (mm/mm)	Ω_{CS}
	Prismatic Specimens					
100% Comp	18.4	5.54	13.6	-11.6	2.44	-22.6
Fire	44.8	9.7	35.6	-28.1	1.41	8.08
80% Comp + Fire	20.5	8.11	37.7	-13.5	-1.22	26.7
Freeze-Thaw	5.84	4.68	8.42	-4.61	-2.45	-31.8
80% Comp + Freeze-Thaw	13.74	7.17	6.5	-9.87	1.88	38.6
	Cylindrical Specimens					
100% Comp	28.8	8.70	21.3	-8.80	1.3	23.8
Fire	50.3	14.6	28.8	-33.5	-7.05	7.18
80% Comp + Fire	44.8	8.60	33.4	-10.5	-2.7	4.50
Freeze-Thaw	26.1	24.2	10.0	-20.7	-7.84	31.57
80% Comp + Freeze-Thaw	12.97	19.0	11.37	-1.91	-9.34	-21.8

10.5 MICROCRACK-PROPERTY RELATIONSHIPS

Changes in spatial microcrack measurements and the corresponding changes in concrete permeability and flexural strength under different damaging effects were used to develop the microstructure-property relationships. Statistical analyses were used to reduce the number of variables (specific surface area, width, volume fraction, spacing, tortuosity, and degree of orientation) that did not have significant effect on concrete permeability or flexural strength. Correlations between the changes in each of microcrack characteristics and the corresponding changes in permeability/flexural strength were investigated; analysis of variance "ANOVA" was then performed to detect whether these variables have any statistically significant effects on concrete permeability or flexural strength. The results of correlation analysis (coefficients of correlation) are shown in Table 10.6.

Coefficients of correlation between changes in tortuosity and degree of orientations showed the least values for Mix II in the case of flexural strength and permeability, changes in tortuosity showed the least value for Mix I in case of permeability and changes in degree of orientation showed the least coefficient of correlation for Mix I in case of flexural strength. Examples of good and poor correlations for Mixture I and II are shown in Figure 10.5 and 10.6. Analysis of variance "ANOVA" (T-test) at 5% level of significance also confirmed that there are no statistically significant effects of changes in tortuosity and degree of orientation on concrete permeability or flexural strength for Mix II, and that there are no significant effects of changes in microcrack tortuosity on the corresponding changes in permeability or changes in the microcrack degree of orientation

on the corresponding changes in flexural strength for Mix I. Hence, tortuosity and degree of orientation were eliminated from trials to correlate damage to engineering properties

Table 10.6 Correlation Coefficients between Changes in Spatial Microcrack Characteristics and the Corresponding Changes in Flexural Strength and Permeability

Measurements	Mix I (Normal-Strength)		Mix II (Relatively High-Strength)	
	Flexural Strength	Permeability	Flexural Strength	Permeability
Specific Surface Area	-0.97	0.63	-0.72	0.84
Width	-0.31	0.91	-0.87	0.35
Volume Fraction	-0.75	0.23	-0.96	0.82
Spacing	0.85	-0.25	0.73	-0.48
Tortuosity	-0.91	0.16	0.15	-0.09
Degree of Orientation	-0.02	0.6	-0.48	-0.24

with the corresponding changes in microcrack attributes. Nonlinear regression models were employed to develop the relationships between engineering properties and microcrack system in concrete. Scatter plots for different changes in microcrack characteristics versus corresponding changes in permeability and flexural strength for mix I and II (Figures 10.7 and 10.8) were produced to help in providing the type of the nonlinear regression models.

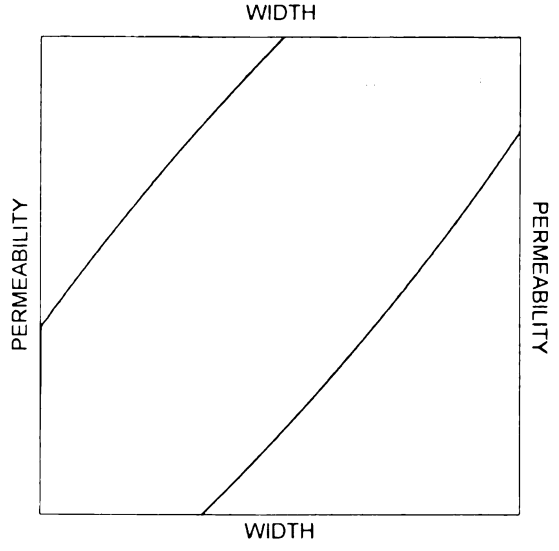

(a) Good Correlation

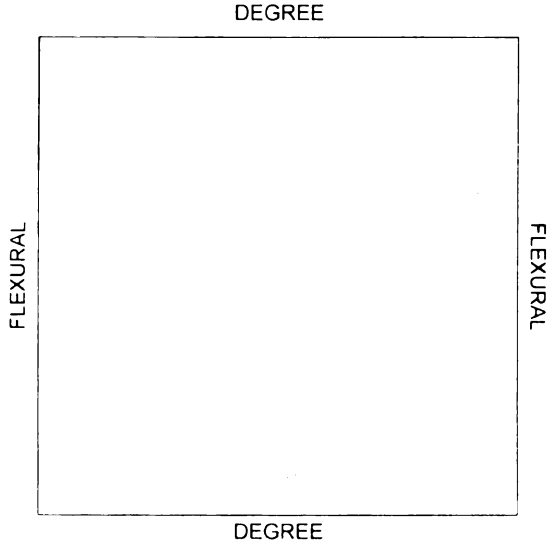

(b) Poor Correlation

Figure 10.5 Examples of Good and Poor Correlations between Changes in Flexural Strength/Permeability and Microcrack Characteristics for Mix I (Normal-Strength)

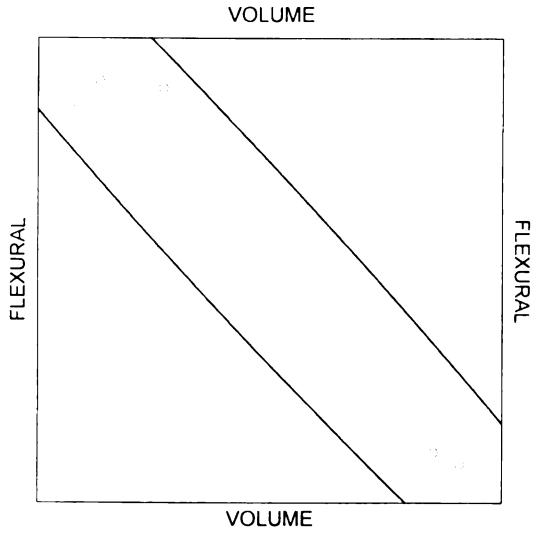

(a) Good Correlation

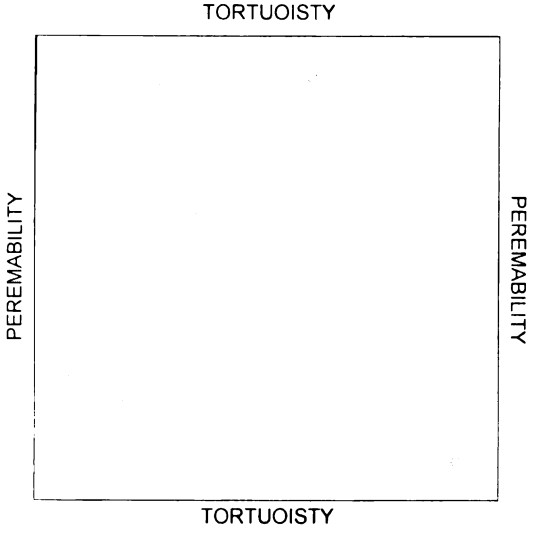

(b) Poor Correlation

Figure 10.6 Examples of Good and Poor Correlations between Changes in Flexural Strength/Permeability and Microcrack Characteristics for Mix II (Relatively High-Strength)

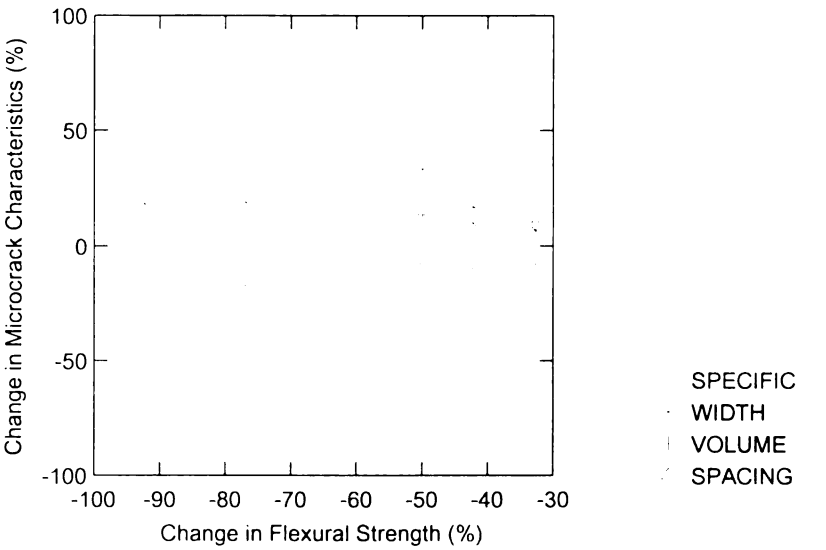

(a) Flexural Strength

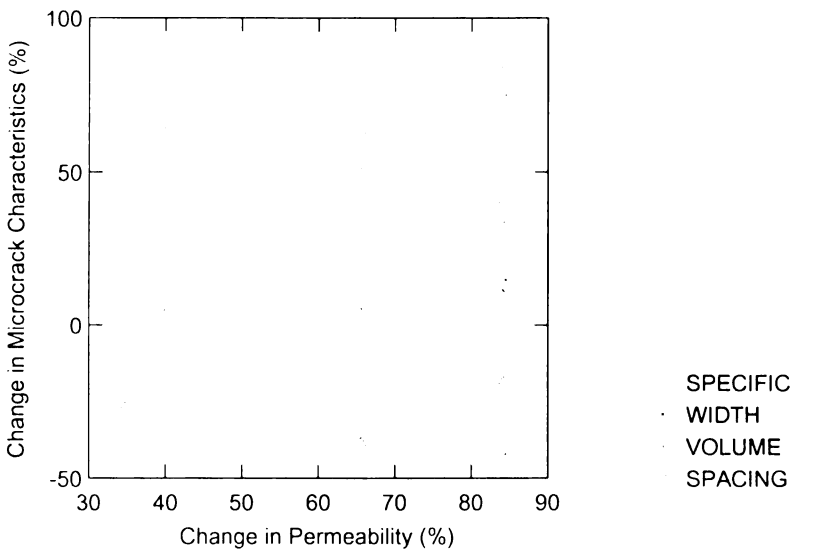

(b) Permeability

Figure 10.7 Trends between Changes in Flexural Strength/Permeability and Microcrack Characteristics for Mix I (Normal-Strength)

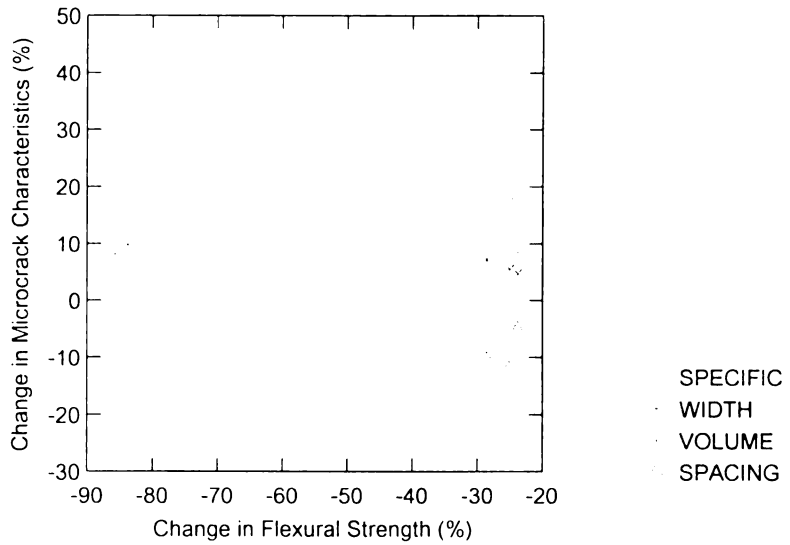

(a) Flexural Strength

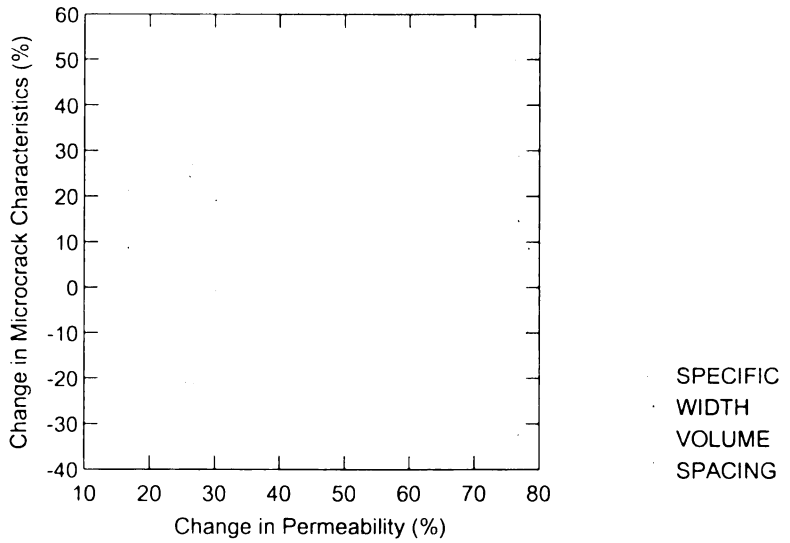

(b) Permeability

Figure10.8 Trends between Changes in Flexural Strength/Permeability and Microcrack Characteristics for Mix II (Relatively High-Strength)

Figures 10.7 and 10.8 indicated that the relationships of changes in volume fraction and spacing versus corresponding changes in flexural strength and permeability may be assumed linear for Mix I and Mix II, while relationships between changes in specific surface area and width versus corresponding changes in flexural strength and permeability may be assumed nonlinear, the best assumption (fitting curve) for these relationships were log or square functions. However, several functions and combinations were assumed while statistics software was used to determine the different variable and the least error. The following relationships were developed:

Mix I (normal-strength concrete)

$$\partial F = -2.97\log(\partial S_{IC}) - 4.63(\partial W_{CS})^2 - 0.66\,\partial V_{IC} + 0.71\,\partial \lambda_{CS} \quad \text{.....(10.1)}$$

$$\partial \rho = 0.84\,\partial S_{IC} + 55.7(Ln\partial W_{CS})^2 - 0.68\,\partial V_{IC} + 0.56\,\partial \lambda_{CS} \quad \text{.....(10.2)}$$

Mix II (relatively high-strength concrete)

$$\partial F = 4(\partial S_{IC})^2 - 35.1\,Log(\partial W_{CS}) - 1.5\,\partial V_{IC} + 0.325\,\partial \lambda_{CS} \quad \text{.....(10.3)}$$

$$\partial \rho = -123\,Log(\partial S_{IC}) + 23.8(\partial W_{CS})^2 + 5.89\,\partial V_{IC} - 0.95\,\partial \lambda_{CS} \quad \text{.....(10.4)}$$

where, ∂F = change (%) in concrete flexural strength

$\partial \rho$ = change (%) in concrete permeability

∂S_{IC} = change (%) in microcrack specific surface area

∂W_{CS} = change (%) in microcrack width

∂V_{IC} = change (%) in microcrack volume faction

$\partial \lambda_{CS}$ = change (%) in microcrack spacing in space

Errors in prediction of above produced nonlinear models (versus test data) are summarized in Table 10.7.

Table 10.7 Errors in Predication of The Developed Models for Mixtures I and II

Changes in Flexural Strength (%) (Experimental)	Changes in Flexural Strength (%) (Model)	Errors (%)	Changes in Permeability (Experimental) (%)	Changes in Permeability (%) (Model)	Errors (%)
Mix I (Normal-Strength)					
-42.3	-37.5	-11.2	84.2	87.2	3.6
-92.3	-86.2	-6.6	84.5	87.9	4
-76.9	-71.6	-6.94	65.6	68.3	4.16
-32.7	-29.1	-10.7	34.7	36.2	4.41
-50	-45.4	-9.21	39.9	42.5	6.41
Mix II (Relatively High-Strength)					
-25.1	-33.1	31.9	16.7	24.5	46.7
-83.8	-70.4	-15.9	76.8	83.1	8.2
-85.7	-74.7	-12.7	78.4	9.4	-6.39
-23.8	-28	17.7	26.2	21.4	-18.3
-28.6	-28.1	-1.45	30.2	35.6	17.9

10.6 VERIFICATION OF THE DEVELOPED MODELS

A theoretical model developed by Gueguen and Dienes[143,144] to describe the fluid flow in rocks was used in the current study to evaluate and verify the developed experimental model. The theoretical model was, however, developed basically to determine permeability assuming that fluids flow through pipes (continuous pores) inside rocks, and then the model was modified for cracks in which case the relationships between the permeability and porosity in rocks was as follows:[143,144]

$$\rho = 7.5\, f\, \overline{w}^2\, \phi \quad \ldots\ldots (10.5)$$

where, ρ = permeability

f = the fraction of the connected pipes: $0 \leq f \leq 1$

$\overline{w}$ = average half-crack aperture

ϕ = porosity

In order to evaluate the developed empirical model, the ratio between permeability of undamaged to damaged specimens was investigated based on the theoretical model (Eq. 10.5). The following relation was used:

$$\frac{\rho_{un}}{\rho_d} = \frac{f_{un}\, \overline{w_{un}}^2\, \phi_{un}}{f_d\, \overline{w_d}^2\, \phi_d} \quad \ldots\ldots (10.6)$$

where, the subscript "un" refers to undamaged specimens and "d" refers to damaged specimens.

In light of percolation theory, the fraction of connected pipes can be expressed in terms of crack volume fraction and average half-crack aperture as average crack width. The porosity of concrete depends mainly on the specific surface area and spacing of features; therefore, porosity in the model may be expressed as crack specific surface area / crack spacing. Equation 10.6 can be rewritten in the following form:

$$\frac{\rho_{un}}{\rho_d} = \frac{S_{VCun}\, \overline{W}^2_{CSun}\, \lambda_{CSun}}{S_{VCd}\, \overline{W}^2_{CSd}\, \lambda_{CSd}} \quad \ldots\ldots (10.7)$$

where, S_{VC} = crack specific surface area

λ = crack spacing

The ratio of permeability of undamaged to damaged concrete obtained from the modified theoretical model (Eq. 10.7) was calculated for different damaging treatments with the two concrete mixtures considered in this study. These values were compared with the ratio obtained from the developed experimental models (Eq. 10.2 and 10.4). Figure 10.9 presents the comparison between the two models for normal and high-strength concrete mixtures. There is good agreement between the modified theoretical and the developed experimental models. The best agreement between two models was observed in the case of 100% compression damage, while the least agreement was in the case of compression + freeze-thaw damage. Some of the difference between the two models may be attributed to the fact that the theoretical model was mainly developed for rocks which are significantly less porous than concrete and have far less connected voids and cracks which compared with the heterogeneous and multiphase structure of concrete.

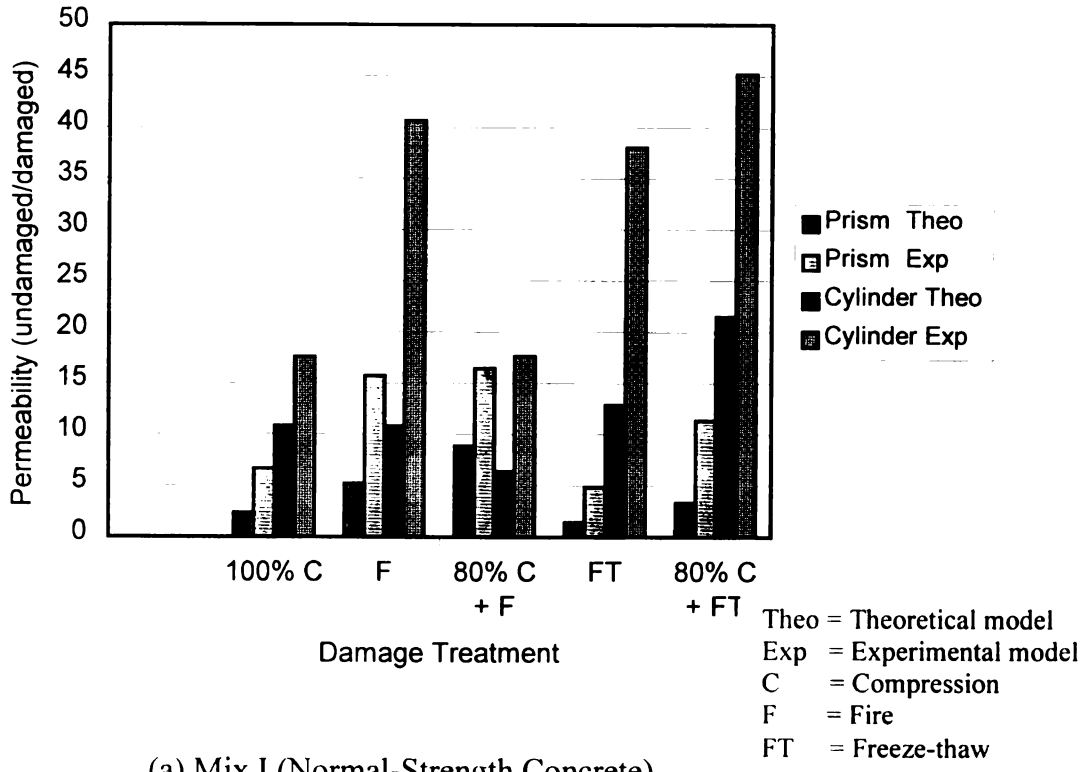

(a) Mix I (Normal-Strength Concrete)

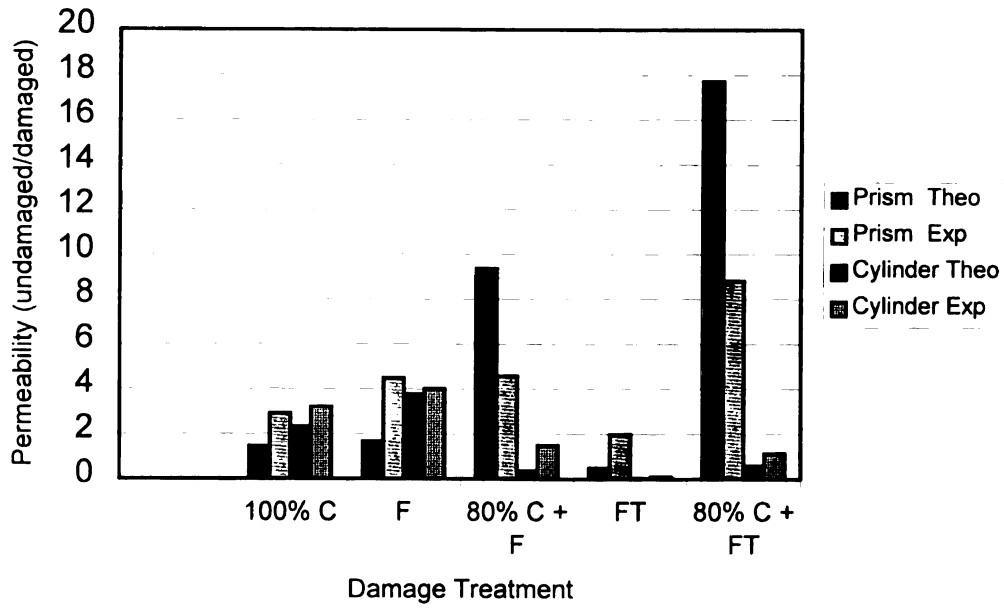

(b) Mix II (High-Strength Concrete)

Figure 10.9 Comparison between Modified Theoretical and Developed Experimental Models

10.7 CONCLUSIONS

Concrete specimens from two concrete mixtures were subjected to different damaging effects; damaged specimens were tested to assess the effects of damaging phenomena on concrete engineering properties and quantified microcrack attributes. The following conclusions were drawn:

1- Different damaging effects reduced concrete flexural strength and increased its permeability; these effects were more pronounced for the concrete mix with lower compressive strength.

2- Fire treatment and exposure to 80% compressive stress followed by fire caused the most severe damage to concrete microcrack system. Fire increased the microcrack specific surface area of normal-strength prismatic and cylindrical concrete specimens by 37% and 85%, respectively, and increased microcrack volume fraction by 50% and 75%, respectively. Fire also increased the microcrack specific surface area of prismatic and cylindrical high-strength concrete specimens by 45% and 50%, respectively, and increased microcrack volume fraction by 35% and 28%, respectively.

3- Exposure to freeze-thaw cycles caused the least severe changes in microcrack attributes when compared with other damage phenomena considered in this study. Freeze-thaw increased the microcrack specific surface area of normal-strength prismatic and cylindrical concrete specimens by 9% and 37%, respectively, and increased microcrack volume fraction by 10% and 30%, respectively. Freeze-thaw also increased microcrack specific surface area of the high-strength prismatic and cylindrical concrete specimens by 5% and 26%, respectively, and increased microcrack volume fraction by 8% and 10%, respectively.

4- Exposure of concrete to 80% of its compressive strength prior to exposure to freeze-thaw cycles caused similar damage to microcrack system as the case where freeze-thaw cycles were applied alone; this may give an indication that the combination of compression and freeze-thaw damage treatments imposed a biaxial loading on concrete specimens which reduced the severity of individual damaging effects.

5- Changes in microcrack tortuosity and degree of orientation in space under different damage treatments were least correlated with the corresponding changes in concrete flexural strength and permeability. This provides an indication that these measurements could be excluded form efforts to relate concrete performance to microcrack attributes.

6- Nonlinear regression analyses were used to develop empirical models between changes in flexural strength and permeability of concrete versus the corresponding changes (under damaging phenomena) in microcrack characteristics; specific surface area, width, volume fraction and spacing. Further work in this area can provide deep insight into microstructure-property relationships of concrete.

7- A theoretical model developed to predict permeability in rocks was modified and used to evaluate the developed experimental model. There was a good agreement between the two models. The two models can be satisfactorily used separately or together to relate concrete microstructure to its performance.

CHAPTER 11

SUMMARY AND CONCLUSIONS

Throughout the research study a comprehensive quantitative approach to quantify concrete microcracks was developed. The developed approach includes statistical basis for concrete sampling, specimen preparation methods for automated microcrack detection, image processing and analysis for ESEM and fluorescent micrographs, stereological relationships to interpret microcrack characteristics in space. The proposed approach was successfully applied on concrete mixtures in the laboratory and on filed structures. Concrete microcrack-property relationships were also developed in the study. The proposed approach and the developed relationships can provide deep insight into fundamental of concrete performance under load and environmental effects. Microcrack-property relationships also enable practical microstructural investigations towards assessment of infrastructure health conditions. Throughout the study, the following conclusions were drawn:

I – Specimen Preparation and Image Processing & Analysis

Automated quantitative microstructural analysis of concrete microcracks and voids systems requires proper selection of image processing operations complemented with appropriate sample preparation techniques which highlight microcracks and voids against the body of the concrete. The accomplishments and conclusions of this aspect of the study are summarized below:

I.1- A refined specimen preparation technique was developed to prepare concrete

specimens for ESEM investigation by Wood's metal impregnation. A new two-stage specimen preparation method was developed to prepare concrete specimens for fluorescent microscopy investigation. This two-stage approach first impregnates concrete with ink, which is cured to fill capillary pores; subsequently, microcracks and voids are impregnated with fluorescent epoxy dye.

I.2- Automatic threshold schemes best suiting automated identification of microcracks and voids in prepared concrete specimens were identified; these schemes greatly facilitate automation of concrete microstructural analysis.

Image processing scenarios were developed for detachment of intersecting microcracks and voids and also separation of connected voids for accurate quantification of concrete microcrack and void system.

I.3- Image analysis schemes were developed to distinguish between microcracks and voids and to identify noise in concrete microscopy images. Formfactor (length–width ratio) of "3.5" was found to distinguish microcracks from voids at magnifications 125X, 250X, and 500X. Recognizing and filtering out noise (produced due to poor specimen preparation and/or setting of instrumentation) from concrete micrographs were carried out by comparing the length of features of interest with noise and addressing the critical length of the noise. The critical length ranged from 25 pixels to 35 pixels based upon the used magnification factor.

II- Morphological Operations and Mathematical Formulations

An image processing methodology was developed for automated microstructural investigation of concrete, emphasizing microcrack and void systems. A range of (2-D)

mathematical formulations was used to quantify planar microstructural features of concrete. Stereological principles were used to derive quantitative information on the (3-D) microstructure of concrete based on planar measurements. The proposed formulations provide a solid basis for software development towards a quantitative microstructural investigation of concrete microcracks and void systems. The key issues involved in the proposed approach to processing and analysis of concrete microscopic images are summarized below:

II.1- Thresholding, followed by opening, closing, and hole-fill operations provide the basis to process concrete micrographs with substantial noise. In the case of images with limited noise, thresholding followed by closing, opening, and hole-fill provided a better approach to remove noise and preserve features of interest (microcracks and voids). Opening operations in both causes generally require one to three iterations; closing operations require one to four.

II.2- Planar quantification of the microcrack system involved formulations of length per unit area, perimeter per unit area, width per unit area, area fraction, degree of orientation, spacing, and tortuosity.

II.3- Planar quantification of the void system involved formulation of equivalent diameter, number per unit area, aspect ratio, form factor, compactness, and roundness.

II.4- Limited quantification of planar aggregates characteristics covered angularity, complexity, and nonequiaxiality index.

II.5- Planar characteristics of microcracks on two perpendicular sections were used in stereological formulations to quantify microcrack volume fraction, spacing, width, degree of orientation and tortuosity in space.

II.6- Planar characteristics of voids on two perpendicular sections were used in stereological formulations to quantify the volume fraction, number per unit volume, specific surface area, spacing, and diameter of voids in space.

II.7- Limited application of stereological principals to planar measurement of aggregates, assuming disc geometry, yielded formulations for (3-D) complexity index, thickness and number per unit volume of aggregates. Limited application of stereological principals of fibers, assuming cylindrical shape, yielded formulations for number per unit volume and diameter of fibers.

III- Statistical Sampling for Quantitative Microscopic Investigation

A comprehensive statistically-based methodology was developed for sampling of concrete systems for the purpose of quantification microstructural analysis of concrete. The accomplishments of this aspect of the study are summarized below:

III.1- The proposed approach starts with dividing the concrete system into a preliminary number of sub-regions within which damage level is relatively uniform. A representative number of cores should then be taken from each sub-region; the microscopic investigation should also cover a representative fraction of sectioned concrete surface (two perpendicular section are cut for each specimen for stereological analyses). Statistical criteria together with data generated for different concrete mixtures and different damage conditions at various magnification levels in order to select the required fraction of area to be scanned and the required number of cores to be taken from each sub-region to yield representative results.

III.2- At 125X and 250X magnification levels, scanned areas should cover 0.5% and 2%

of concrete surface area, respectively, to yield representative results. At 500X magnification, scanning of 0.5% surface area would be generally sufficient, noting that higher fractions of scanned surface area imply major time and cost expenditures. As far as the required number of cores per sub-region is concerned, a precision level of 5% seemed to provide a reasonable balance between applicability and reliability of the approach.

III.3- the type of damage considered (load to peak compressive stress followed by immediate unloading) produce a statistically significant increase in the length per unit area (and specific surface area) of concrete microcrack, for damaged specimens, the crack length per unit area was greater on sections normal to the direction of compressive loading (when compared to those parallel to the direction of loading). Concrete mixture composition also influences the microcrack length per unit area (and specific surface area) of damaged specimens.

IV- Qualitative Investigation of Concrete

Changes in concrete properties associated with various damaging effects were quantified. Observations were also made on microcrack attributes of concrete prior to and after such damaging effects. The results indicated that:

VI.1- Different damaging effects (compression, impact, freeze-thaw, fatigue, freeze-thaw+compression) produced different changes in the extent and nature of microcrack propagation within concrete. Compression increased the length, width and area fraction of microcracks; fatigue increased the number of microcracks, freeze-thaw produced a less tortuous microcrack growth, and impact increased the width of microcrack density

increased noticeably in sections perpendicular to the loading direction when compared to the parallel with sections loading direction.

IV.2- Combined damage processes do not always have the expected adverse effects on concrete strength; for example, freeze-thaw damage effect and compression + freeze-thaw damage effect almost has the same influence on concrete flexural strength.

IV.3- Differences in the extent and pattern of microcrack propagation reflected on the deterioration of different properties (flexural strength, impact resistance and permeability) of concrete after damaging effects.

Damaging phenomena do not have similar effects on different properties of concrete. Compression damage sharply increases permeability of concrete which impact damage has only slight effects on permeability. Compression damage also noticeably lowers the impact resistance of concrete. Fatigue loading was more damaging to flexural strength. Compression loading to peak followed by immediate unloading proved to be particularly damaging to concrete when compared with the other damaging phenomena considered in this investigation.

IV.4- Microcrack propagation under compression damage seems to reduce the differences in properties of high-strength versus normal-strength concrete.

IV.5- Undamaged concrete (after normal curing and air drying) incorporates microcracks, which largely occur of interfaces of cement paste and coarse aggregates. Various damaging effects (freeze-thaw, elevated temperature, restrained shrinkage in normal, hot and cold temperature, and compression) produced marked changes in the nature, and extent of concrete microcracking

IV.6- Variations in the extent and pattern of microcrack propagation and networking (and initiation of new microcracks) reflect on the corresponding changes in different properties (compressive, flexural, and splitting tensile strength) of concrete.

IV.7- Damaging effects (e.g., fire endurance) cause not only growth and interconnection of microcracks but also introduce new cement paste microcracks yield particularly severe damage to engineering properties of concrete.

IV.8- Under compression loading to peak compressive stress, a more distributed system of finer microcracks in normal-strength concrete yields less damage to performance than a less distributed system of microcracks with larger widths.

V- Quantitative Analysis of Concrete

The effects of different load and environmental damaging effects on normal-strength and relatively high-strength concrete microcrack system were assessed based on quantitative evaluation of the microcrack system in plane and in space. Statistical analyses of the quantified microcrack system in damaged and undamaged normal-strength concrete specimens (with and without steel or composite reinforced- restrained and unrestrained) yielded the following conclusions:

V.1- Compression loading and fire endurance have the most significant effect on normal-strength concrete microcracks measurements. Compression increased crack length per unit area, width, volume fraction, tortuosity, and crack specific surface area, width, volume fraction, tortuosity and decreased spacing in plane and spacing in space, while fire increased crack length per unit area, perimeter per unit area, area fraction, and

specific surface area, width, volume fraction and decreased spacing in plane and spacing in space.

V.2- Fatigue loading has the least significant damaging effect on normal-strength concrete microcrack measurements. Fatigue damage significantly increased crack specific surface area in space.

V.3- Impact loading does not have the same severe effect on normal-strength concrete microcracks as compression or fire endurance; impact loading mainly increased microcrack width in plane and in space.

V.4- corrosive environment (salt water) has profound effect on normal-strength concrete microcracks; it increased crack length per unit area, perimeter per unit area, width per unit area, area fraction, and crack specific surface area, width, volume fraction and decreased spacing in plane and spacing in space, while it does not have significant effect on tortuosity or degree of orientation in space.

V.5- Hot water immersion has significant effect on length per unit area, spacing in plane, crack specific surface area, width and spacing in space of normal-strength concrete.

V.6- Combined damaging effects (compression + freeze-thaw) does not provide sever damaging effect compared to compression damage or freeze-thaw damage (each alone) for normal-strength concrete, however, more studies are needed to reach conclusive remarks.

V.7- Composite rebars reinforced concrete specimens did not show severe changes in normal-strength concrete microstructure (specific surface area or volume fraction) compared to steel reinforced concrete specimens.

V.8- Restraint of shrinkage movements significantly increased the extent of microcracking in an otherwise undamaged normal-strength concrete.

V.9- Normal-strength concrete experiences more microcrack growth after a short period of exposure to cold climate than hot climate. This observation could be a function of the relative thermal movements of the cement paste versus aggregates.

V.10- Undamaged concrete specimens of normal-strength and relatively high-strength concrete exhibited similar microcrack characteristics after similar curing and air drying conditions (prior to application of any damage effects).

V.11- Compression load led to substantial microcrack growth in relatively high-strength concrete. Compression damage increased microcrack length, width and area fraction in plane, and specific surface area, width and volume fraction in space.

V.12- Planar and spatial microcrack characteristics are significantly different in normal-strength vs. relatively high-strength concrete under application of compression damage effect.

V.13- Relatively high-strength concrete experienced more extensive microcrack growth under impact lading than normal-strength concrete.

V.14- Tortuosity, angle of orientation and degree of orientation are the lowest measurements that have been affected by damaging effects while length per unit area (specific surface area) and area fraction (volume fraction) are the highest measurements that have been affected by damaging effects. Therefore they may be used as indices to evaluate concrete condition rather than number of cracks.

VI- Filed Application of the Developed Approach

Rigid pavement slab and reinforced concrete bridge deck were subjected to the proposed approach to quantify microcrack characteristics. The pavement slab was divided into seven horizontal and two vertical sub-regions and the bride deck was divided into 3 horizontal sub-regions targeting a power of 0.8 for statistical analyses of quantified microcrack data. A number of concrete cores were obtained from each sub-region, targeting a precision level of ±2.5% and ±5% for pavement slab and bride deck respectively in quantitative analyses of microcrack systems. Cores were cut into two perpendicular sections, which were prepared for the automated acquisition of microscopic images through fluorescent microscopy. Quantitative microstructural analyses were conducted for planar and spatial microcrack measurements. Mechanical and transport properties (compressive and splitting strength, and permeability) of concrete cores were also determined. Statistical procedures were employed to determine the adequacy of the number of cores and sub-regions for achieving the targeted power and precision levels. The following conclusions were drawn:

VI.1- During pavement investigation, as far as vertical (top and bottom) sub-regions are concerned, the differences in permeability and quantified microcrack attributes were not statistically significant, but generally pointed of higher damage levels to top (exposed) sub-regions.

VI.2- During bridge deck investigation, statistically significant differences were found between sub-region I (severe level of damage) versus sub-region III (low level of damage) in terms of microcrack length per unit area, perimeter per unit area, width per unit area, area fraction and spacing (planar measurements) and microcrack specific

surface area, width, volume fraction and spacing. The quantified microcrack characteristics also indicated statistically significant rise in microcrack area fraction (planar) and volume fraction (spatial) for cores extracted over/near visible cracks

VI.3- Permeability test data correlated well with quantified microcrack data. There were statistically significant differences between permeability and microcrack measurements between sub-regions rated differently in terms of visible manifestations of damage. Sub-regions with higher microcrack specific surface area and closer microcrack spacing exhibited higher permeability levels.

VI.4- The increase in microcrack intensity correlated well with the increase in permeability compared to mechanical properties. This may suggest that permeability is more sensitive than mechanical performance of concrete to certain levels of damage and microcracking; permeability tests thus provide more insights into concrete quality and health condition than is possible by only mechanical tests. Given the significant impact of permeability on durability under weathering effects, this finding indicates that mechanical test results alone may not truly reflect on durability and remaining service life of concrete pavements, and quantitative microcrack data can provide reliable insight into health conditions and durability of concrete.

VI.5- Spatial (3-D) microcrack measurements are more preferred than planar (2-D) measurements to investigate the degree of damage distribution along concrete structures. Microcrack specific surface area is the most reliable measurement to be used as the viable probe of condition assessment of concrete. Spatial (3-D) data provide a more thorough assessment of concrete damage conditions than planar (2-D) data.

VI.6- The proposed statistical approach to determine the sufficient number of sub-regions and number of cores per sub-region was successful applied to achieve the targeted power of experiment and precision of the results. However, statistical analyses, using microcrack specific surface area indicated that the selected number of cores and sub-regions are reasonable (with some minor compromise) to meet the targeted levels of confidence, precision and power.

VII-Concrete Microcrack-Property Relationships

Concrete specimens from two concrete mixtures were subjected to different damaging effects; damaged specimens were tested to assess the effects of damaging phenomena on concrete engineering properties and quantified microcrack attributes. The following conclusions were drawn:

VII.1- Different damaging effects reduced concrete flexural strength and increased its permeability; these effects were more pronounced for the concrete mix with lower compressive strength.

VII.2- Fire treatment and exposure to 80% compressive stress followed by fire caused the most severe damage to concrete microcrack system. Fire increased the microcrack specific surface area of normal-strength prismatic and cylindrical concrete specimens by 37% and 85%, respectively, and increased microcrack volume fraction by 50% and 75%, respectively. Fire also increased the microcrack specific surface area of prismatic and cylindrical high-strength concrete specimens by 45% and 50%, respectively, and increased microcrack volume fraction by 35% and 28%, respectively.

VII.3- Exposure to freeze-thaw cycles caused the least severe changes in microcrack attributes when compared with other damage phenomena considered in this study. Freeze-thaw increased the microcrack specific surface area of normal-strength prismatic and cylindrical concrete specimens by 9% and 37%, respectively, and increased microcrack volume fraction by 10% and 30%, respectively. Freeze-thaw also increased microcrack specific surface area of the high-strength prismatic and cylindrical concrete specimens by 5% and 26%, respectively, and increased microcrack volume fraction by 8% and 10%, respectively.

VII.4- Exposure of concrete to 80% of its compressive strength prior to exposure to freeze-thaw cycles caused similar damage to microcrack system as the case where freeze-thaw cycles were applied alone; this may give an indication that the combination of compression and freeze-thaw damage treatments imposed a biaxial loading on concrete specimens which reduced the severity of individual damaging effects.

VII.5- Changes in microcrack tortuosity and degree of orientation in space under different damage treatments were least correlated with the corresponding changes in concrete flexural strength and permeability. This provides an indication that these measurements could be excluded form efforts to relate concrete performance to microcrack attributes.

VII.6- Nonlinear regression analyses were used to develop empirical models between changes in flexural strength and permeability of concrete versus the corresponding changes (under damaging phenomena) in microcrack characteristics; specific surface area, width, volume fraction and spacing. Further work in this area can provide deep insight into microstructure-property relationships of concrete.

VII.7- A theoretical model developed to predict permeability in rocks was modified and used to evaluate the developed experimental model. There was a good agreement between the two models. The two models can be satisfactorily used separately or together to relate concrete microstructure to its performance.

LITERATURE CITED

1. Van Mier, J.G.M., "Fracture Processes of Concrete," CRC Press, 1996, pp.4-6, 38-53, 88-116 & 215-234.

2. Nilsen, A.U., and Monteiro, P.J.M., "Concrete: A Three Phase Material," Cement and Concrete Research, V.23, No.1, January 1993, pp.147-151.

3. Mehta, P.K., and Monteiro, P.J.M., "Concrete, Microstructure, Properties, and Materials," Prentice-Hall, 1993, pp.27-33, 80-83, & 129-132.

4. Mehta, K., "High-Performance Concrete Durability Affected by Many Factors," Concrete Construction, V.37, No.5, May 1992, pp.367-370.

5. Victor, C. Li, and Mohamed M., "Toughening in Cement Based Composites. Part I: Cement, Mortar, and Concrete," Cement and Concrete Composites, V.18, 1996, pp.223-237.

6. Rober, H., and Campbell-Allen, D., "Handbook of Structural Concrete," Edited by Kong, F.K., Evans, R.H., Cohen, E., and Roll, F., Chapter 4, 1983, pp.4.4-6.6 and .5.4-5.8.

7. Young, J.F., "The Microstructure of Hardened Portland Cement Paste," Creep and Shrinkage in Concrete Structures, Edited by Bazant, Z.P., and Wittmann, F.H, John, Wiley & Sons Ltd.1982,pp.3-22.

8. Diamond, S., "Cement Paste Microstructure in Concrete," Microstructural Development During Hydration of Cement, Materials Research Society, Symposia Proceedings, Boston, Massachusetts, U.S.A., V.85, December 2-4,1986, pp.21-31.

9. Winslow, D., and Liu, D., "The Pore Structure of Paste in Concrete," Cement and Concrete Research, V.20, No.2, 1990,pp.227-235.

10. St John, D.A., Polle, A.W., and Sims, I., "Concrete Petrography," John Wiley & Sons Inc., 1998, pp.10-46, 223-246, 283, 286-287, 289.

11. Lange, D.A., Jennings, H.M., and Shah, S.H., "The Influence of Pore Structure on the Properties of Cement Paste: Initial Observations about Research-in-Progress," Pore Structure and Permeability of Cementitious Materials Research Society, Symposia Proceedings, Boston, Massachusetts, U.S.A., V.137, November1999, pp.47-54.

12. Popovics, S., "Strength and Related Properties of Concrete, A Quantitative Approach," John Wiely & Sons, Inc., 1998, pp.306-309.

13. Lange, D.A., Jennings, H.M., and Shah, S.H., "The Relationship Between the Porosity of the Surface Layer of Concrete and the Ingress of Aggressive Ions," Pore

Structure and Permeability of Cementitious Materials Research Society, Symposia Proceedings, Boston, Massachusetts, U.S.A., V.137, November1999, pp.279-284.

14. Dequiedt, A. S., Coster, M., Chermant, L., and Chermant, J. L., "Study of Phase Dispersion in Concrete by Image Analysis," Cement & Concrete Composits, V.23, 2001, pp.215-226.

15. Taylor, F.H.W., "Bound Water in Cement Pastes and its Significance for Pore Solution Compositions," Microstructural Development During Hydration of Cement, Materials Research Society, Symposia Proceedings, Boston, Massachusetts, U.S.A., V.85, December 2-4,1986, pp.47-54.

16. Diamond, S., and Huang, J., "The ITZ in Concrete – A Different View Based on Image Analysis and SEM Observations," Cement & Concrete Composites, V.23, 2001, pp.179-188.

17. Diamond, S., "Considerations in Image Analysis As Applied to Investigation of The ITZ in Concrete," Cement & Concrete Composites, V.23, 2001, pp.171-178.

18. ACI Manual of Concrete Practice, 1995, Part 1, "Materials and General properties of Concrete," ACI 201./R-92.

19. Mindess,S., and Young, J.F., "Concrete," Prentice-Hall, Inc., 1981, pp.364-372.

20. Nemati, K.M., Monteiro, J.M., and Scrivener, K.L., "Analysis of Compressive Stress-Induced Cracks in Concrete," ACI Materials Journal, V.98, No.5, September-October 1998, pp.617-630.

21. Zhang, M.H., "Microstructure, Crack Propagation, and Mechanical Properties of Cement Pastes Containing High Volume of Fly Ashes," Cement and Concrete Research V.25, No.6, 1995, pp.1165-1178.

22. Loo, Y.H., "Propagation of Microcracks in Concrete under Uniaxial Compression," Magazine of Concrete Research, V47, No.170, March 1995, pp.83-91.

23. Xuanhui, C. and Yongqi, L., "Damage Process in Hardened Cement Paste," ACI Materials Journal, V.93, No.4, July-August 1996, pp.378-385.

24. Najjar, W.S., and Hover K.C., "Neutron Radiography for Microcracking Studies of Concrete Cylinders Subjected to Concentric and Eccentric Compressive Loads," ACI Materials Journal, V.86, No.4, July-August 1989, pp.354-359.

25. Li, Z., and Shah, S.P., "Localization of Microcracking in Concrete under Uniaxial Tension." ACI Materials Journal, V.91, N0.4, July-August, 1994, pp.372-381.

26. Tjiptobroto, P., and Hansen, W., "Tensile Strain Hardening Composites Containing Discontinuous Fibers," ACI Materials Journal, V.90, No.1, January-February, 1993, pp.16-25.

27. Van Mier, J.G.M., "Mode I Fracture of Concrete: Discontinuous Crack Growth and Crack Interface Grain Bridging," Cement and Concrete Research, V.21, No.1, 1991, pp.1-15.

28. Wang, J., Navi, P., and Huet, P., "Numerical Analysis of Crack Propagation in Tension Specimens of Concrete Considered as a 2D Multicracked Granular Composite," Materials and Structures, V.30, January-February 1997, pp.11-21.

29. Mishashi, H., and Nomura, N., "Microcracking and Tension-Softening Properties of Concrete," Cement & Concrete Composites, V.14, 1992, pp.91-103.

30. Li, Z., "Microcrack Characterization in Concrete under Uniaxial Tension," Magazine of Concrete Research, V.48, No.176, September 1996, pp.219-228.

31. Giuriani, E., and pLizzari, G., "Interrelation of Splitting and Flexural Cracks in R.C. Beams," Journal of Structural Engineering, V.124, No.9, September 1998, pp.1032-1040.

32. Lubin, G., and Cheng-Tzu, H., "Fatigue of Concrete under Uniaxial Compression Cyclic Loading," ACI Materials Journal, V.95, No.5, September-October 1998, pp.575-581.

33. Hideyuki, H., Hak, S., and Tirath, M., "Mechanism of Fatigue Crack Growth in Concrete," Cement & Concrete Composites, V.14, 1992, pp.83-89.

34. Schlangen, E., and Van Mier, J.G.M., "Experimental and Numerical Analysis of Micromechanisms of Fracture of Cement-Based Composites," Cement & Concrete Composites V.14, 1992, pp.105-118.

35. Reinhardt, H. W., Cornelissen, H. A. W., and Hordijk, D.A., "Tensile Test and Failure Analysis of Concrete," Journal of Structural Engineering, ASCE, V.112, 1986, pp.2462-2477.

36. Mazars, J., Verthaud, Y., and Ramatani, S., "The Unilateral Behavior of Damaged Concrete," Engineering Fracture Mechanics V.35, N.4/5, 1990, pp.629-635.

37. Weisu, Y., and Thomas, H., "Fatigue Behavior of Steel Fiber Reinforced Concrete in Uneasily and Biaxial Compression," ACI Materials Journal, V.92, No.1, January-February 1995, pp.71-81.

38. Jacobsen, S., Marchand, J., and Hornain, H., "SEM Observations of the Microstructure of Frost Deteriorated and self-Healed Concretes," Cement and Concrete Research, V.25, No.8, 1995, pp.1781-1790.

39. Jacbsen, S., Gran, H.C., Sellevold, E.J., and Bakke, J.A., "High Strength Concrete-Freeze/Thaw testing and Cracking," Cement and Concrete Research, V.25, No.8, 1995, pp.1775-1780.

40. Selleck, S.F., Landis, E.N., "Peterson, M.L., and Shah, S.P., "Ultrasonic Investigation of Concrete with Distributed Damage," ACI Materials Journal, V.95, No.1, January-February 1998, pp.27-36.

41. Goltermann, P., "Mechanical Predictions of Concrete Deterioration-Part2: Classification of Crack Patterns," ACI Materials Journal, V.92, No.1, January-February 1995, pp.58-63.

42. Shah, S.P., Weiss, W.J., and Yang, W., "Shrinkage Cracking-Can It Be Prevented?," Concrete International, April 1998, pp.51-55.

43. Soroushian, P., and Ravanbakhsh, S., "Control of Plastic Shrinkage Cracking With Specialty cellulose Fibers," ACI Materials Journal, V.95, No.4, July-August 1998, pp.429-435.

44. Zongjin, L., Faming, L., Allan, Z., Eric, L., and Shah, S.P., "Application of Acoustic Emission Technique to Detection of Reinforcing Steel Corrosion in Concrete," ACI Materials Journal, V.95, No.1, January-February 1998, pp.68-76.

45. Mehta, K.P., "Durability-Critical Issues for the Future," Concrete International, July 1997, pp. 27-33.

46. Shayan, A., and Quick, G.W., "Microscopic Features of Cracked and Uncracked Concrete Railways Sleepers," ACI Materials Journal, V.89, No.4, July-August, 1992, pp.348-361.

47. Gillot, J.E., and Soles, J.A., "Petrography of Concrete Cores from New Brunswick, Relating to the Durability Problem," Cement & Concrete Composites, V.15, 1993, pp.101-114.

48. Samah, H.R., and Hover K.C., "Influence of Microcracking on the Mass Transport Properties of Concrete," ACI Materials Journal, V.98, No.4, July-August, 1992, pp.416-424.

49. Fu, Y., and Beaudoin, J.J., "Microcracking as a Precursor to Delayed Ettringite Formation in Cement Systems," Cement and Concrete Research, V.26, No.10, 1996, pp.1493-1498.

50. Sahu, S., Badger, S., Osgood, B., and Taulow, N., "Petrographic Analysis of Concrete Deterioration by Feature Relocation," Transportation Research Broad 80th Annual Meeting, January 7-11, 2001, Washington, D.C.

51. Rossi, P., Godart, N., Robert, L., Gervais, P.J., and Bruhat, D., "Investigation of the Basic Creep of Concrete by Acoustic Emission," Materials and Structures, V.27, 1994, pp. 510-514.

52. Bazant, P.Z., and Yunping, X., "Drying Creep of Concrete: Constitutive Model and New Experiments Separating Its Mechanisms," Materials and Structures, V. 27, 1994, pp.3-14.

53. Castel, A., Francois, R., and Arilguie, G., "Effect of Loading on Carbonation Penetration in Reinforced Concrete Elements," Cement and Concrete Research, V.29, 1999, pp.561-565.

54. Francois, R., and Arliguie, G., "Effect of Microcracking and Cracking on the Development of Corrosion in Reinforced Concrete Members," Magazine of Concrete Research, V.51, April 1999, pp.143-150.

55. Arya, C., and Ofori-Darko, F.K., "Influence of Crack Frequency on Reinforcement Corrosion in Concrete," Cement and Concrete Research, V.26, No.3, 1996, pp.344-353.

56. Chermant, J., L., "Why Automatic Image Analysis? An Introduction to This Issue," Cement & Concrete Composites, V.23, 2001, pp.127-131.

57. John, C. Russ, "The Image Processing Handbook," CRC Press, 1992, pp.1-7.

58. Mouret, M., Ringot, E., and Bascoul, A., "Image Analysis: A Tool For The Characterization of Hydration of Cement in Concrete-Metrological Aspects of Magnification on Measurement," Cement & Concrete Compoistes, V.23, 2001, pp.201-206.

59. Mishashi, H., and Nomura, N., "Microcracking and Tension-Softening Properties of Concrete," Cement & Concrete Composites, V.14, 1992, pp.91-103.

60. Selleck, S.F., Landis, E.N., "Peterson, M.L., and Shah, S.P., "Ultrasonic Investigation of Concrete with Distributed Damage," ACI Materials Journal, V.95, No.1, January-February 1998, pp.27-36.

61. Sakata, Y., and Ohtsu, M., "Crack Evaluation in Concrete Members Based on Ultrasonic Spectroscopy," ACI Materials Journal, V.92, No.6, November-December, 1995, pp.686-698.

62. Ping, G., Zhongzi, X., Ping, X., and Beaudoin, J., "An A.C. Impedance Spectroscopy Study of Micro-Cracking in Cement-Based Composites During Compressive Loading," Cement and Concrete Research, V.23, 1993, pp.675-682.

63. Zongjin, L., Faming, L, Allan Z., Eric, L., and Shah, S.P., "Application of Acoustic Emission Technique to detection of Reinforcing Steel Corrosion in Concrete," ACI Materials Journal, V.95, No.1, January 1998, pp.68-76.

64. Nilleson, K., and Broderesen, K., "Pores and Cracks in Cemented Waste and Concrete," Cement and Concrete Research, V.22, 1992, pp.405-417.

65. Peterson, K.W., Swartz, R.A., Sutter, L.L., and Van Dam, T.J., "Air Void Analysis of Hardened Concrete with a Flatbed Scanner," Transportation Research Board, 80th Annual Meeting, Washington, D.C., January 7-11, 2001, pp.1-24.

66. Becker, J., M., Grousson, S., and Jourlin, M., "Surface State Analysis by Means of Confocal Microscopy," Cement & Concrete Composites, V.23, 2001, pp.255-259.

67. Livingston, R.A., Manghnani, M., and Prasad, M., "Characterization of Portland Cement Concrete Microstructure Using the Scanning Acoustic Microscope," Cement and Concrete Research, V.29, 1999, pp.278-291.

68. Diamond, S., and Mindess, S., "SEM Investigation of Fracture Surfaces Using Stereo Pairs: III Fracture Surfaces of Mortars," Cement and Concrete Research, V.24, No.6, 1994, pp.1140-1152.

69. Danilatos, G.D., "Introduction to the ESEM Instrument," Microscopy Research and Technical Journal, V.25, 1993, pp.354-361.

70. ElectroScan Corporation, "ESEM Model 2020, Environmental Scanning Electron Microscopy, Orientation Guide to Operations Display Interface Reference," V.1, V.2, and V.4, September 1994, pp.1.1-1.35, 2.41-2.46, and 2.1-2.6.

71. Marusin, S.L., "Sample Preparation-the Key to ESM Studied of Failed Concrete," Cement & Concrete Composites, V.17, 1995, pp. 311-318.

72. Stutzman, P., Nist. Specimen Preparation.
[Online] Available
http://www.cee.ee.uiuc.edu/lange/micro,
December 13, 1999.

73. Hornain, H., Marchand, J, Ammouche, A., Commene, J.P., and Moranville, M., "Microscopic Observations of Cracks in Concrete- A new Sample Preparation Technique Using Dye Impregnation," Cement and Concrete Research, V.26, No.4, 1996, pp.573-583.

74. Gran, H.C., "Fluorescent Liquid Replacement Technique, A means of Crack Detection and Water: Binder ratio Determination in High Strength Concretes," Cement and Concrete Research, V.25, No.5, 1995, pp.1063-1074.

75. Russ, J.C., "Image Analysis of the Microstructure of Materials: Images of Materials," Edited by David, B.W., Alan, R.P., and Ronald, G., Oxford University Press, 1991,pp.338-373.

76. Stang, H., Mobasher, B., and Shah, S.P., "Quantitative Damage Characterization in Polypropylene Fiber Reinforced Concrete," Cement and Concrete Research, V.20, 1990, pp.540-558.

77. Russ, J.C., "Computer-Assisted Microscopy, the Measurement and Analysis of Images," Plenum Press, 1990, pp. 20-25, 105-115 & 134-148.

78. Coster, M., and Chermant, J.L., "Image Analysis and Mathematical Morphology for Civil Engineering Materials," Cement & Concrete Composites, V.23, 2001, pp.133-151.

79. Ammouche, A., Riss, J., Breysse, D., and Marchand, J., "Image Analysis for the Automated Study of Microcracks in Concrete," Cement & Concrete Composites, V.23, 2001, pp.267-278.

80. Chermant, J.L., Chermant, L., Coster, M., and Dequiedt, A. S., "Some Fields of Applications of Automatic Image Analysis in Civil Engineering," Cement & Concrete Composites, V.23, 2001, 157-169.

81. Chiaia, B., Mier, van, J.G.M., and Vervuurt, A., "Crack Growth Mechanisms in Four Different Concretes: Microscopic Observations and Fractal Analysis," Cement and Concrete Research, V.28, No.1, 1998, pp.103-114.

82. Konin, A., Francois, R., and Arliguie, G., "Analysis of Progressive Damage to Reinforced Ordinary and High Performance Concrete in Relation to Loading," Materials and Structures, V.31, January-February, 1998, pp.27-35.

83. Kose, S., Guler, M., Bahia, H., and Masad, E., "Distribution of Strains Within Asphalt Binders in HMA Using Imaging and Finite Element Techniques," Transportation Research Board 79th Annual Meeting, Washington, D.C., January 11-15, 2000, pp.1-21.

84. Garboczi, E.J., Bentz, P.D., Quenard, D.A., Kunzel, H.M., Baruchel, J., Peyrin, F., and Martys, N.S., "Microstructure and Transport Properties of Porous Building Materials. II: Three-Dimensional X-ray Tomographic Studies," Materials and Structures, V.33, 2000, pp.147-153.

85. Jourlin, M., Roux, Bernard, and Faure, R., "Recognition of Clinker Phased by Automatic Image Analysis, " Cement & Concrete Composites, V.23, 2001, 207-214.

86. Ringot, E., and Bascoul, A., "About the Analysis of Microcracking in Concrete," Cement & Concrete Composites, V.23, 2001, pp.261-266.

87. Lange, D.A., "Image Analysis Techniques for Characterization of Pore Structure of Cement-Based Materials," Cement and Concrete Research, V.24, No.5, 1994, pp.841-853.

88. Underwood, E. E., "Quantitative Stereology," Addison-Wesley Publishing Company, 1970, pp.48-79& 80-105.

89. Kuo, C.Y., and Freeman, R.B., "Imaging Indices For Quantification of Shape, Angularity, and Surface Texture of Aggregate," Transportation Research Board, 79th Annual Meeting, Washington, D.C., January 9-13, 2000, pp.1-22.

90. Aligizaki, K.K., and Cady, P.D., "Air Content and Size Distribution of Air Voids in Hardened Cement Pastes Using The Section-Analysis Method," Cement and Concrete Research, V.29, 1999, pp.273-280.

91. Pleau, R., Pigeon, M., and Laurencot, J.L., "Some Findings on The Usefulness of Image Analysis For Determination The Characteristics of The Air-Void System on Hardened Concrete," Cement & Concrete Composites, V.23, 2001, 237-246.

92. Dequiedt, A.S., Coster, M., Chermant, L., and Chermant, J.L, "Distances Between Air-Voids in Concrete by Automatic Method," Cement & Concrete Composites, V.23, 2001, 247-254.

93. Mowar, S., Zaman, M., Stearns, D.W., and Roegiers, J.C., "Micro-Mechanisms of Pore Collapse in Limestone," Journal of Petroleum Science and Engineering, V.15, 1996, pp.221-235.

94. Russ, J.C., "Practical Stereology," Plenum Press, New York, 1986, pp.103-120.

95.Weibel, R. W., "Stereological Methods; Practical for Biological Morphometry," Volume 1, Academic Press, 1979, pp.1-3 & 40-45.

96.Underwood, E. E., "Basic Stereology; Fourth International Congress for Stereology," National Bureau of Standards, Gaithersburg, Maryland, U.S.A., September 4-9, 1975, pp.509-512.

97. Petrov, I., and Schlegel, E., "Application of Automatic Image Analysis for the Investigation of Autoclaved Aerated Concrete Structure," Cement and Concrete Research, V.24, N.5, 1994, pp.830-840.

98. Dehoff, R. T., and Rhines, F., N., "Quantitative Microscopy: Surface Area and Length in Volume," McGraw-Hill, Inc., 1968, pp.102-125 & 149,196.

99. Stroeven, P., Stroeven, A. P., and Dalhuiesn, D. H., "Image Analysis if Natural Concrete Samples by Automated and Manual Procedures," Cement & Concrete Composites, V.23, 2001, pp.227-236.

100. Chermant, J. L., Chremant, L., Coster, M., and Dequiedt, A. S., "Some Fields of Applications of Automatic Image Analysis in Civil Engineering," Cement & Concrete Composites, V.23, 2001, pp.157-169.

101. Mobasher, B., Stang, H., and Shah, S.P., "Microcracking in Fiber Reinforced Concrete," Cement and Concrete Research, V.20, 1990, pp.665-676.

102. Weibel, R. W., "Stereological Methods; Theoretical Foundations," Volume 2, Academic Press, 1980, pp.116-125 & 261-263.

103. Dehoff, R.T., "The Determination of the Size Distribution of Ellipsoidal Particles From Measurements Made on Random Plane Sections," Transactions of the Metallurgical Society of AIME, V.224, June 1962, pp.474-477.

104. ASTM C 183-97, " Practice for Sampling and the Amount of Testing of Hydrauic Cement," Annual Book of ASTM Standards, V.4, 2000.

105. Li, K.S., "A Compound Sampling Scheme for Accepting of Concrete," Materials and Structures, V.26, 1993, pp.517-521.

106. ASTM C 295-98, "Guide for Petrographic Examination of Aggregates for Concrete," Annual Book of ASTM Standards, V.4, 2000.

107. ASTM C 856-95$^{\varepsilon 1}$, " Practice for Petrograhic Examination of Hardened Concrete," Annual Book of ASTM Standards," V.4, 2000.

108. ASTM C 457-98, " Test Method for Microscopical Determination of Parameters of the Air-Void System in Hardened Concrete, " Annual Book of ASTM Standards, V.4, 2000.

109. ASTM C 1356M-96, "," Test Method for the Quantitative Determination of Phases in Portland Cement Clinker by Microscopical Point-Count Procedure [Metric]," Annual Book of ASTM Standards," V.4, 2000.

110. Tabsh, S.W., and Aswad, A., "Statistics of High-Strength Concrete Cylinders," ACI Materials Journal, V. 94, No.5, September-October 1997, pp.361-364.

111. Kriviak, G.J., and Scanlon, A., "Estimation of Compressive Strength of Concrete in Existing Structures Based on in Situ Test Data," ACI Materials Journal, V. 84, No.3, May-June, 1987, pp. 235-245.

112. Netter, J., Wasserman, W., and Whitmore, G.A., "Applied Statistics," Simon & Schuster Inc., 4th ed., 1993, pp.218-294 & 651-664.

113. Milton, J.S., and Arnold, J.C., "Probability and Statistics in the Engineering and Computing Science," McGraw-Hill, Inc., 1986, pp.633-639 & 590-591.

114. Devore, J.L., "Probability and Statistics for Engineering and The Sciences," Duxbury Press, 1990, pp. 371-385 & 679-680.

115. Aimin, X., and Ahmad S., "Investigation of Concrete From Bridge Structures Made With Blended Cements," Proceedings-Conference of the Australian Road Research Board, ARRB, V. 17, No.4, 1994, pp. 156-180.

116. Shayan, A., Morris, H., and Doolan, T., "Investigation of Cracking of Precast Concrete Bridge Piles Submerged in Tidal River in Northern NSW," Proceedings-Conference of the Australian Road Research Board, ARRB, V. 17, No.4, 1994, pp. 118-141.

117. Tay, D.C.K., and Tam, C.T., "In Situ Investigation of the Strength of Deteriorated Concrete," Construction ad Building Materials, V.10, No.1, Feb 1996, pp.17-26.

118. Ringot, E., "Automatic Quantification of Microcracks Network by Stereological Method of Total Projection in Mortars and Concretes," Cement and Concrete Research, V.18, No. 1, 1988, pp.35-43.

119. Emmanuel, K., and David D., "Submicrocracking in Cement Paste and Mortar," ACI Materials Journal, V. 84, No. 6, November-December 1987, pp. 491-500.

120. Worting, D., Baladi, G., Buch, N., and Bower, S., "Pavement Distress and Selection of Rehabilitation alternatives: Michigan Practice," Transportation Research Record, No. 1629, Nov. 1998, pp.214-225.

121- Vepa, T.S., George, K.P., and Shekharan, A. Raja, "Prediction of Pavement life," Transportation Research Record, No.1524, Sep.1996, pp.137-144.

122- McNerney, M.T., and McCullough, B.F., "Fatigue Cracking in Rigid Airfield Pavements at Large Commercial-Service Airports," Transportation Research Record, No.1703, 2000, pp.65-71.

123- Al-Qadi, I.L., and Abo-Qudais, S.A., "Joint Width and Freeze/Thaw effects on Joint Sealant Performance," Journal of Transportation Engineering, V.121, No.3, May-Jun 1993, pp. 262-266.

124- Cuttell, G.D., Snyder, M.B., Vandenbossche, J.M., and Wade, M.J., "Performance of Rigid Pavements Containing Recycled Concrete Aggregates," Transportation Research Record, No.1574, Nov.1996, PP.89-98.

125- Ramsamooj, D.V., "Fracture of Highway and Airport Pavements," Engineering Fracture Mechanics, V.44, No.4, Mar.1993, pp.609-626.

126- Heath, A.C., and Roesler, J.R. "Top-down Cracking of Rigid Pavements Constructed with Fast-setting Hydraulic Cement Concrete," Transportation Research Record, No.1721, 2000, pp.3-12.

127- Tayabji, S.D., Steohanos, P.J., and Davis, W.P., "Evaluation and Rehabilitation Design of I-495 in Delware," Transportation Research Record, No.1449, Dec. 1994, pp.159-168.

128- Chamberlin, W. P., "Long-Term Evaluation of Unprotected Concrete Bridge Decks," Research Report, New York State Department of Transportation, Engineering Research and Development Bureau, Nov. 1985, pp. 1-10.

129- Rengaswamy, N. S., Balasubramanian, T. M., Srinivasan, S., Mahadeva L. Y., and Bapu, R. H., "Corrosion Survey of Bridges," Indian Concrete Journal, V.61, No.6, June 1987, pp. 147-151.

130- Weyers, R. E., "Service Life Mode for Concrete Structures in Chloride Laden Environments," ACI Materials Journal, V.95, No.4, Jul-Aug 1998, pp. 445-453.

131- Val, D.V., Stewart, M., G., and Melchers, R. E., "Effect of Reinforcement Corrosion on Reliability of Highway Bridges," Engineering Structures, V. 20, No. 11, Nov. 1998, pp. 1010 – 1019.

132- Paulsson, J., and Silfwerbrand, J., "Durability of Repaired Bridge Deck Overlays," Concrete International, V.20, No.2, Feb. 1998, pp. 76-82.

133- Babaei, K., "Solutions to Concrete Bridge Deck Cracking," Concrete International, V. 19, No. 7, July 1997, pp. 34-37.

134- Carse, A., "Measurements of Concrete Expansive Strains Due to Alkali-Silica Reaction in Australian Concrete Structures," Cement and Concrete Research, V. 20, No. 3, May 1990, pp. 376-384.

135- Mohammad, M. S., and Floyd, O. S., "Microcracking of High and Normal Strength Concretes Under Short- and Long- Term Loadings," ACI Materials Journal, V. 86, No.2, March-April 1989, pp. 117-127.

136- Ramon, L. C., Floyd, O. S., and Arthur H. N., "Microcracking and Behavior of High Strength Concrete Subject to Short-Term Loading," ACI Materials Journal, V. 11, May-June 1981, pp. 179-186.

137- Scrivener, K. L., "The microstructure of Concrete," Material Science of Concrete I, Edited by Skalny, J.P., The American Ceramic Society, Inc., 1989, pp. 127-161.

138- Garboczi, E.J. and Bentz, D.P., "Microstructure-Property Relationships in Concrete: From Nanometers to Centimeters," 2nd CANMET/ACI International Symposium,

"Advances in Concrete Technology," Los Angeles, Nevada, June 11-14, 1995, pp. 573-585.

139- Gettu, R., Aguado, A., and Oliveira, M.O.F., "Damage in High-Strength Concrete Due to Monotonic and Cyclic Compression-A Study Based on Splitting Tensile Strength," ACI Materials Journal, V.93, No.6, Novermber-December 1996, pp.519-523.

140- Saito, M., Ohta, M., and Ishimori, H., "Chloride Permeability of Concrete Subjected to Freeze-Thaw Damage," Cement & Concrete Composites V.16, 1994, pp.233-239.

141- Konin, A., Francois, R., and Arliguie, G., "Analysis of Progressive Damage to Reinforced Ordinary and High Performance Concrete in relation to Loading," Materials and Structures, V.31, January-February 1998, pp.27-35.

142. Zhang, B., "Relationship Between Pore Structure and Mechanical Properties of Ordinary Concrete Under Bending Fatigue," Cement and Concrete Research, V.28, No.5, 1998, pp.699-711.

143- Gueguen, Y., and Dienes, J., "Transport Properties of Rocks from Statistics and Percolation," Mathematical Geology, V. 21, No. 1, 1989, pp. 1-13.

144- Gueguen, Y., David, C., and Darot, M., "Models and Time Constants for Permeability Evolution," Geophysical Research Letters, V. 13, No.5, May 1986, pp. 460-463.

MICHIGAN STATE UNIVERSITY LIBRARIES
3 1293 02551 6836